PhD-FSTC-2012-02

The Faculty of Sciences, Technology and Communication

DISSERTATION

Defense held on 19/01/2012 in Luxembourg

to obtain the degree of

DOCTEUR DE L'UNIVERSITÉ DU LUXEMBOURG
EN PHYSIQUE

by

Johannes Benedikt FISCHER

Born on 1st of June 1982 in Trier (Germany)

$CuInSe_2$ Thin Film Solar Cells Synthesised From Electrodeposited Binary Selenide Precursors

Dissertation defense committee

Dr. Phillip DALE, Dissertation supervisor
Université du Luxembourg

Dr. Susanne SIEBENTRITT, Deputy chairman
Professor, Université du Luxembourg

Dr. Laurence PETER
Professor, University of Bath

Dr. Susan SCHORR
Professor, Helmholtz Zentrum Berlin

Dr. Roland SANCTUARY, Chairman
Professor, Université du Luxembourg

1. Abstract

In this thesis the fabrication of a $\mathrm{CuInSe_2}$ thin film solar cell from an electrodeposited precursor stack consisting of indium selenide and copper selenide layers is demonstrated. A best conversion efficiency of 5.5% was achieved, a higher efficiency than previously reported in the known literature for the selenisation of precursors prepared from indium selenide and copper selenide. The thesis focuses on three main parts, (i) the electrochemistry of indium selenide, (ii) the phase evolution during the annealing and (iii) identifying the loss mechanisms in the finished solar cell.

(i) For the studied conditions (a low concentrated electrolyte at elevated temperature) it is experimentally verified for the first time that indium selenide electrodeposition is induced by the reduction of selenium species at the electrode surface, as has been proposed by Massaccesi et al. [1]. The obtained film consists of both amorphous $\mathrm{In_2Se_3}$ and elemental Se. The deposition is mass transport controlled depending on the selenium ion concentration. The amount of deposited $\mathrm{In_2Se_3}$ cannot simply be obtained from the mass flux due to the presence of the second competing phase, elemental Se. The composition of the films is surprisingly found to be determined by the applied potential. It is suggested that the voltage controls the balance of reduction kinetics between the $\mathrm{In_2Se_3}$ and elemental Se and both compete for the same intermediate selenium species. Smooth and uniform $\mathrm{In_2Se_3}$ deposits can be plated with the use of a rotating disc electrode. Conditions for the electrodeposition of a porous copper selenide film containing amounts of amorphous Se have been established.

(ii) Single phase $\mathrm{CuInSe_2}$ is obtained from annealing the stacked binary selenide precursor. The absorber layer has a larger grain size than a coelectrodeposited $\mathrm{CuInSe_2}$ precursor annealed under the same conditions. The small interface area between the indium selenide and the copper selenide slows down the interdiffusion during the annealing process. It corresponds to the previous reported results that the reaction of binary selenides is diffusion limited. Therefore the temperature required to react the precursor is higher than reported for similar binary selenide stacks in literature. The suppressed diffusion of copper selenide retains this phase at the surface during the annealing process, where it undergoes the transitions ($\mathrm{CuSe_2} \rightarrow \mathrm{CuSe} \rightarrow \mathrm{Cu_2Se}$) which are expected from its phase diagram. A higher Cu/In ratio in the precursor increases the tetragonal splitting of the (220) and (204) reflection in the X-ray diffractogram of the absorber. It is expected that the composition affects the strain inside the thin film causing the observed splitting.

(iii) The highest efficiency of the analysed solar cells is obtained from a stoichiometric precursor (atomic Cu/In ratio equals 1), because it compromises the advantages and disadvantages of Cu-poor and Cu-rich growth. The Cu-poor grown absorber has shown a n-type ordered vacancy compound at the back due to an incomplete reaction of the stack. This causes a reverse junction at the backcontact and reduces the performance. The efficiency of the Cu-rich grown solar cell was limited by the high interface recombination.

Promising results have been recorded for a binary selenide stack annealed under a higher background gas pressure which slows down the Se diffusion from the reaction zone. The absorber consists of grains with a lateral extension of several microns. Photoluminescence measurements have confirmed superior optoelectronic properties for this absorber. So far it is not suited for a solar cell, because the backcontact massively selenises during the annealing rendering it unusable. Optimisation of the annealing conditions will probably solve this issue in future.

Contents

2. Introduction to chalcopyrite thin film solar cells

2.1. General

Chalcopyrite solar cells consist of a I-III-VI_2 compound semiconductor (with I = Cu, Ag; III = In, Ga, Al; VI = Se, S, Te) [2]. Especially the compound Cu(In,Ga)Se_2 has shown the highest potential of all recent thin film solar cells [3]. Solar cell efficiencies above 20% have been achieved (table 2.1).

Several properties qualify $\mathrm{CuInSe_2}$ (CISe) and Cu(In,Ga)Se_2 (CIGSe) chalcopyrites as excellent semiconductors for thin film solar cells.

- The absorption coefficient is high ($10^4 - 10^5\,\mathrm{cm}^{-1}$ [4]) and the typically used absorber thickness of 2 micron is sufficient for complete absorption of photons with energies above the band gap.
- It tolerates variations in composition due to the facile formation of copper vacancies (chapter 14).
- The band gap energy in Cu(In,Ga)Se_2 can be tuned between 1.0 and $1.7\,\mathrm{eV}$ by varying the ratio between In and Ga [4]. This allows to adjust the band gap to the optimum values of $1.15\,\mathrm{eV}$ or $1.35\,\mathrm{eV}$ given by the Schockley-Queisser limit for maximum solar power conversion of a single junction solar cell [5, 6].
- Chalcopyrite thin film solar cells have proved radiation hardness and long-term stability [7, 8].
- The efficiency loss due to recombination at grain boundaries is low in chalcopyrite solar cells in contrast to other semiconductors (e.g. Si) [9].

Figure 2.1 shows the typical structure of a thin film Cu(In,Ga)Se_2 solar cell as it is also reviewed in [15]. The conventional substrate is soda-lime glass. Beside its function as a substrate it also provides a source of sodium by diffusion in the thermal processing of the absorber. Sodium is known to have several beneficial effects on the growth of Cu(In,Ga)Se_2 (chapter 20). Metal foils and polyamide foils have been studied as alternative substrate being suitable for roll-to-roll processing. The backcontact of the solar cell is typically made from molybdenum, because it is relatively stable against selenisation and does not form alloys with Cu or In. Its contact resistance with CIGSe is low. Several groups have reported the presence of a thin $\mathrm{MoSe_2}$ interface layer between Mo and CIGSe, which is supposed

System	deposition	area / cm^2	η/ %	Ref.
Cu(In,Ga)Se_2	PVD	0.50	20.3	[10]
$\mathrm{CuInSe_2}$	PVD	0.40	15.0	[11]
Cu(In,Ga)Se_2	sputtered	9703	15.7	[3]
Cu(In,Ga)Se_2	ED	0.48	13.76	[12]
Cu(In,Ga)Se_2	ED	102	12.25	[13]
Cu(In,Ga)Se_2	ED	10700	10.0	[13]
$\mathrm{CuInSe_2}$	ED	0.06	8.8	[14]

Table 2.1.: Record efficiencies η for chalcopyrite solar cells and modules. The devices have been fabricated by physical vapour deposition (PVD), sputtering or electrodeposition (ED).

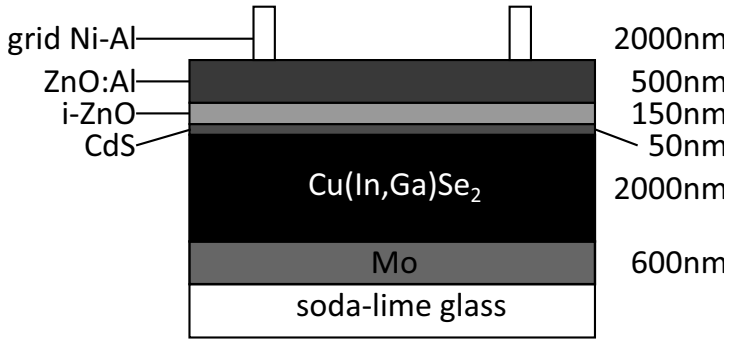

Figure 2.1.: Typical structure of a Cu(In,Ga)Se_2 thin film solar cell in substrate configuration. i-ZnO is an undoped ZnO layer, while ZnO:Al is n-doped with aluminium. The stated thicknesses can vary.

to form an ohmic contact [15]. Cu(In,Ga)Se_2 is the p-type absorber layer where the charge carriers are generated. It is expected that a Ga gradient along the depth profile can increase the solar cell performance [16]. A higher Ga content at the junction will decrease recombination due to the larger band gap. An enhanced Ga content at the backcontact causes an electric field that prevents the diffusion of electrons into the contact. Between the absorber and the front contact is the thin buffer layer, usually prepared from CdS. Its main purpose is the electrical band alignment between the absorber and the front contact (section 23.1). It also provides a protection of the absorber layer against oxidation or damage during the deposition of the ZnO layer and compensates the lattice mismatch between CIGSe and the front contact [17]. The best solar cell performance is reached for CdS from chemical bath deposition. Alternative materials (e.g. $\mathrm{In_2S_3}$) have been screened as possible buffers, because of the toxicity of Cd [15]. The layer of intrinsic ZnO (i-ZnO) has a comparatively high resistance. A real thin film solar cell is often not perfectly uniform, but contains spots acting as recombination centres or short-cuts between back and front contact. The intrinsic ZnO layer can "insulate" these spots, because of its high resistance and thus increases the V_{OC} [18]. The Al-doped ZnO layer acts as an transparent conductive oxide (TCO) layer forming the front contact. The ZnO layers are usually deposited by sputtering. Finally, laboratory-sized solar cells are often contacted by a grid of Ni/Al.

2.2. Electrodeposited chalcopyrite solar cells

The highest efficient Cu(In,Ga)Se_2 thin film solar cells are prepared by physical vapour deposition (PVD) (table 2.1). An alternative route is the electrodeposition of precursors followed by annealing in a selenium containing atmosphere. Although the efficiency is lower than in PVD, the process has several advantages [19].

- Electrodeposition requires only low-cost equipment, because there is no need for a high vacuum system.
- It is comparatively easy to upscale the electrodeposition process and a roll-to-roll fabrication is possible [13]. Depending on the process electroplating can provide a high throughput.
- Electrodeposition provides an effective material use and easier waste handling.
- Electrodeposition includes an automatic purification of chemicals in the deposition process and thus lower purity chemicals can be used.
- Electrodeposition is a low temperature process allowing the use of polymer substrates and reduces energy consumption.

The advantages of electrodeposition are partly compromised by the necessity of a succeeding selenisation step. Nevertheless this selenisation is a non-directional low-vacuum process and therefore still advantageous in comparison to PVD.

There are in principle three different routes to prepare $\mathrm{CuInSe_2}$ by a combination of electrodeposition and annealing [20]:

1. Coelectrodeposition: All elements are simultaneously electrodeposited. The precursor consists of low-crystalline $\mathrm{CuInSe_2}$ containing possible binary or ternary phases [21, 22, 23]. Therefore an annealing in Se atmosphere is necessary to recrystallise the absorber [24, 25]. Despite the selenisation the final grain size does sometimes not exceed $200\,\mathrm{nm}$ and the film stays porous (figure 18.1) [21, 26, 27]. The plating process is susceptible to fluctuation in deposition potential or electrolyte concentration, because three elements are involved.

2. Metal stack electrodeposition: A contrary approach is the electroplating of a stack of elemental Cu and In layers or a Cu-In alloy [28]. The stack is selenised to form the $\mathrm{CuInSe_2}$. The electroplating of metal layers is often a fast and comparatively simple process. The easier electrodeposition is compensated by a more complicate annealing. An additional selenisation step is required to ensure Se incorporation into the precursor, before forming the $\mathrm{CuInSe_2}$ [29, 30]. The metal stack route usually results in large grains. A disadvantage is the expansion of the layer during the selenisation due to the large difference between the densities of Cu ($8.94\,\mathrm{g/cm^3}$) or In ($7.29\,\mathrm{g/cm^3}$) and $\mathrm{CuInSe_2}$ ($5.74\,\mathrm{g/cm^3}$). It causes pinholes and delamination of the film.

3. Binary selenide electrodeposition: In this route copper selenide (Cu-Se) and indium selenide (In-Se) are electrodeposited and annealed to $\mathrm{CuInSe_2}$. It is a compromise between the previous routes. In contrast to coelectrodeposition the composition control of the binary selenide compounds is easier, because less elements are involved. The electroplating of binary selenide compounds is also advantageous for the deposition of elements like In and Ga which require a very negative potential. The deposition potential of the binary compound can be shifted towards more positive potentials (section 5.6), i.e. further away from the evolution of hydrogen. Further advantages of binary selenide precursors in general are given in the next section 2.3. Despite these benefits the binary selenide electrodeposition route has hardly been studied in literature. Hermann et al. are the only ones who reported the annealing of an electroplated Mo/In-Se/Cu-Se precursor [23, 31, 32]. The selenisation of a Mo/Cu/In-Se precursor was studied by Guillen and Herrero [33, 34]. The lack of interest in the binary route can probably be explained by the experience that the electrodeposition process itself is not easier than for the other routes. Although the electrochemistry of coelectrodeposition is more complex, the process itself is not more difficult once the correct settings have been found [20]. Despite the very negative deposition potential of elemental indium it can still be electrodeposited, before hydrogen evolution occurs. The binary selenide electrodeposition process might play out its strength going from $\mathrm{CuInSe_2}$ to Cu(In,Ga)$\mathrm{Se_2}$. The addition of Ga further complicates the coelectrodeposition process and its elemental electroplating requires an even more negative potential than In. Therefore first experiments of gallium selenide electrodeposition have been recently performed [35]. Also the deposition if a Ga-In-Se alloy was reported [32].

2.3. Motivation of binary selenide precursors

The annealing of $\mathrm{CuInSe_2}$ nanoparticles often leads to an insufficient recrystallisation resulting in a porous absorber layer with a lot of grain boundaries [36, 37]. The same effect can sometimes be observed for coelectrodeposited precursors, which also contain nanocrystalline $\mathrm{CuInSe_2}$ grains (figure 18.1) [21]. It can be expected that precursors from binary selenides show a better crystallisation and lead to larger grain size. A $\mathrm{CuInSe_2}$ precursor is already in the thermodynamically stable phase. The only driving force that promotes a recrystallisation is the ambition to minimise Gibbs energy by

Precursor	deposition	η/ %	Ref.	remarks
In-Se/Cu-Se				
Mo/InSe/CuSe	MEE	5.08	[45]	
Mo/In_2Se_3/Cu_2Se	PVD	0.9	[46]	1
Mo/In_2Se_3/Cu_2Se	PVD	5.4	[46]	1,2
CdS/In-Se/Cu-Se	sputtered	low	[47]	
Mo/In_2Se_3/Cu-Se	ED	5.5	this thesis	
In-Se/Cu				
Mo/(In,Ga)-Se/Cu	PVD	4.2	[48]	3
Mo/In-Se/Cu/In-Se	PVD	> 10	[41]	
Mo/In_2Se_3/Cu	PVD	13.7	[40]	4
Mo/In_2Se_3/Cu/Ga	PVD	14.5	[49]	
Cu-Se/In				
Mo/$Cu_{2-x}Se$/In/Ga	PVD	10.2	[48]	3

1: active area
2: In_2Se_3 layer evaporated at surface of absorber
3: (In,Ga)-Se or $Cu_{2-x}Se$ formed by combination of PVD and selenisation
4: precursor formation at 200 °C

Table 2.2.: Efficiencies of selenised absorbers from binary selenide containing precursors. Precursors have been fabricated by physical vapour deposition (PVD), migration enhanced epitaxy (MEE), sputtering or electrodeposition (ED).

reaching single crystal configuration. For a binary selenide precursor the reaction to $CuInSe_2$ involves a complete rearrangement of atom positions. In this context it can be supposed that the atoms will preferentially arrange closer to their ideal lattice configuration resulting in a larger grain size. If the binary selenide precursor is grown with an overall Se excess, it is also possible that a liquid selenium phase forms during annealing and promotes grain growth by liquid phase sintering (chapter 18).

The most often used precursor for selenisation is a stack of elemental Cu and In layers or a Cu-In alloy [15]. Sometimes the stack is capped with an elemental Se layer to provide an additional source of Se in the selenisation. These precursors usually lead to a large absorber grain size above 1 micron which often extend from the backcontact to the front [21, 38, 39]. The drawback of the pure metal precursors is a low adhesion with the Mo substrate being probably linked to the large expansion during selenisation. It has been shown that the inclusion of binary selenides improves the adhesion [40, 41]. The densities of indium selenide and copper selenide are closer to $CuInSe_2$. Therefore expansion causes less stress during the annealing. The formation of the volatile In_4Se_3 must be avoided, because it leads to a loss of indium [42]. On the other hand In_4Se_3 has been observed as a first intermediate phase in the selenisation of stacked elemental layers [43]. Starting with a Se-rich binary (e.g. In_2Se_3) avoids this intermediate phase. Additionally the segregation of Cu-In phases can be prevented by the incorporation of Se in the precursor [41].

Kerr et al. have motivated the synthesis of $CuInSe_2$ from binary selenides as a low-temperature process [44, 45]. According to the ternary phase diagram of Cu-In-Se $CuInSe_2$ coexists with a Se-rich liquid phase, if the overall sample composition is Se-rich. The Se-rich liquid is already expected at temperatures above 220 °C. Therefore already at low temperature the benefits of a liquid assisted growth (e.g. high diffusion rates) can be reached. Starting from binary selenides is expected to avoid the formation of high temperature melting compounds during the reaction process [44].

Several groups have reported the fabrication of solar cells from binary selenide precursors (table 2.2). The efficiencies of solar cells from indium selenide and copper selenide is $5 - 6\%$. If a binary selenide is combined with an elemental metal, it reaches above 10%. It is not clear if the difference has a physical reason or if it is simply caused by different level of process optimisation.

The first solar cell from a completely electrodeposited binary selenide precursor is presented in this thesis. Preceding work on the selenisation of electroplated Mo/In-Se/Cu-Se precursors has been performed by Hermann et al. [23, 31, 32]. They obtained single phase $\mathrm{CuInSe_2}$ of high crystallinity. The surface is roughness is significantly less compared to other absorber fabrication methods (e.g. coelectrodeposition and annealing) [31].

2.4. Thesis outline

The objective of this thesis is the synthesis and understanding of a $\mathrm{CuInSe_2}$ thin film solar cell from an electrodeposited binary selenide precursor. The outline of this thesis follows the fabrication steps of the solar cell. It consists of three major parts: (i) the electrodeposition of the stack, (ii) the compositional and structural characterisation of the annealed absorber, and (iii) the optoelectronic characterisation.

(i) The part on electrochemistry is focused on indium selenide. The electrochemistry of copper selenide has been comprehensively studied by Thouin and Massaccesi [50, 51]. In contrast to this only a few experiments have been performed to understand the electrochemistry of indium selenide. Studying the electrochemistry of indium selenide requires knowledge of the single elements. Therefore the electrochemistry of indium and especially selenium is discussed in the previous chapters. The electroplating of copper selenide is investigated empirically. Finally appropriate conditions for the electroplating of a Mo/In-Se/Cu-Se precursor are given.

(ii) The second part is dedicated to the structural and compositional properties of the annealed absorber. The formation of $\mathrm{CuInSe_2}$ is verified and its uniformity is examined. The recrystallisation of different precursors and different annealing conditions are compared. Ex-situ and In-situ XRD measurements have been applied to identify the phase reactions in the absorber during the annealing process. Several cation impurity sources have been identified in the absorber fabrication process.

(iii) The optoelectronic properties of the absorber and the completed solar cell devices are presented. A Cu-poor, a stoichiometric, and a Cu-rich absorber/cell are analysed. Absorbers/cells annealed at different conditions are added to the comparison. Photoluminescence provides an indicator for the electronic quality of the semiconductor. Standard JV measurements are performed to judge the performance of the solar cells. Possible loss mechanisms are further studied by temperature dependent JV analysis and voltage dependent quantum efficiency measurements.

Every part ends with the conclusions of its results. At the end of the thesis an outlook of future research topics motivated from this thesis is presented.

3. General characterisation techniques

This chapter gives a short summary of commonly used characterisation techniques which have been applied in this thesis. It is not intended to provide a complete discussion of the methods but will restrict to its general principle. Further information on the techniques can be found in standard text books. The discussion is focused on the use of the methods in this thesis.

3.1. Scanning Electron Microscopy (SEM) / Energy Dispersive X-ray Spectroscopy (EDX)

The SEM provides the possibility to record pictures of specimens beyond the resolution limit of optical microscopes. An electron beam is focused on the sample by magnetic lenses. The incident electrons generate secondary electrons in the sample and are partly back-scattered (figure 3.1). The emitted electrons are collected by a detector. Scanning the incident electron beam over the sample surface allows to record its topography [52].

In the present case secondary electron pictures with incident electron energies of $3 - 20\,\mathrm{keV}$ have been recorded. Secondary electron pictures show better resolution, because they are more surface sensitive than backscattered electrons. Their higher count rate reduces the noise in the picture. On the other hand backscattered electrons provide information on the composition of the sample. In general a lower incident electron energy is preferred in SEM pictures to keep the penetration volume small and thus increase resolution.

During the scattering process electrons from the inner electron shells of the atoms in the sample are removed. The shell is filled again by radiative recombination of electrons from the outer shells. The energy of the emitted X-rays is characteristic for each element. This allows the determination of the sample composition by energy dispersive X-ray spectroscopy (EDX or EDS). In the thesis an incident electron energy of $20\,\mathrm{keV}$ was applied to record the EDX spectra. It ensures sufficient signal for the transition with the highest energy (Se K line at about $11\,\mathrm{keV}$). The composition was averaged over an area of $0.2\,\mathrm{mm}^2$. For the EDX maps in chapter 10.2.4 the electron energy was reduced to $7\,\mathrm{keV}$ in order to avoid damaging the sample. The EDX analysis software has been calibrated with a $\mathrm{CuInSe_2}$ standard to increase accuracy. The standard was a Cu-rich grown $\mathrm{CuInSe_2}$ absorber grown by PVD which has been etched to remove secondary copper selenide phases. Under these conditions the sample can be assumed to consist of single phase $\mathrm{CuInSe_2}$ (compare phase diagram 14.3).

3.2. X-ray Diffraction (XRD)

The wavelength of X-rays is in the same order of magnitude as the distance between lattice planes in a solid state crystal. Therefore diffraction of an incident X-ray beam is observed. In most directions the diffracted signal of the atoms will interfere destructively and no signal is observed in total. Constructive interference can only be obtained for directions which satisfy Bragg's law

$$\sin\left(\theta_{hkl}\right) = \frac{n \cdot \lambda}{2 d_{hkl}} \tag{3.1}$$

θ_{hkl} is the diffraction angle (figure 3.2), n is the order of the diffracted reflex (usually $n = 1$) and λ is the X-ray wavelength. d_{hkl} is the distance between lattice planes which are described by the Miller indices hkl. If the lattice shows certain symmetries (e.g. a simple cubic lattice), it is possible that not all reflexes satisfying Bragg's law can be observed (extinction rules).

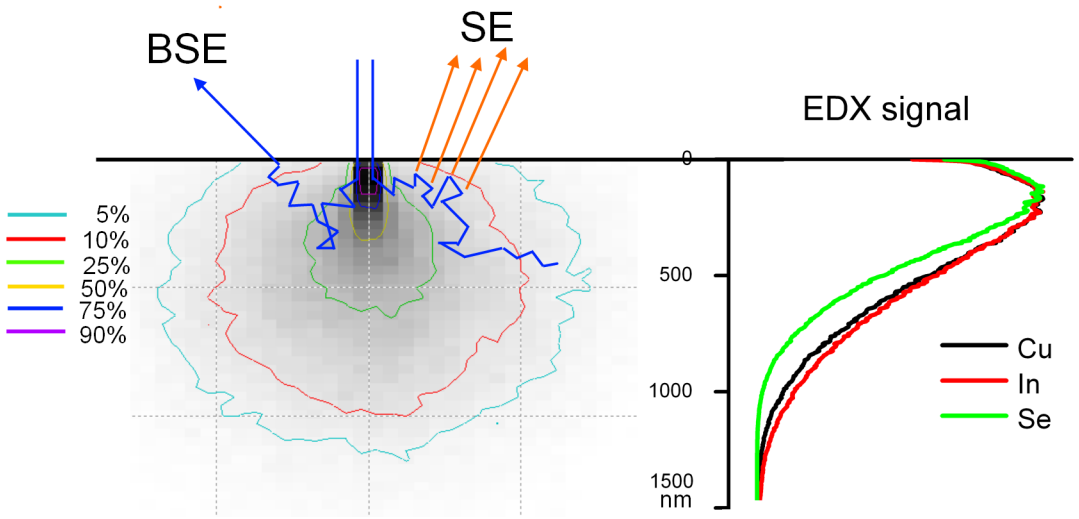

Figure 3.1.: Electron-Matter interaction used in SEM and EDX analysis. The incoming electrons (blue) are partly reflected as back-scattered electrons (BSE). Scattering in the material generates secondary electrons (SE). The remaining holes recombine and emit characteristic X-ray radiation. The X-ray strength versus depth is plotted in the right graph. The further the electron has travelled from the spot of incidence, the less of its initial energy is left (coloured contours). The scattered path of the incident electrons is schematic; energy contours and X-ray signal have been simulated for $20\,\mathrm{keV}$ electron energy in $\mathrm{CuInSe_2}$ with the software CASINO [53].

In a standard XRD set-up (figure 3.2a) the position of the X-ray source and the detector are symmetrically moved to scan the diffraction angle. Due to the symmetry of the set-up this will only take into account lattice planes which are perpendicular to the symmetry axis between source and detector. The samples measured in this thesis are polycrystalline. Therefore it can be assumed that for a pair of θ_{hkl} and d_{hkl} satisfying Bragg's law there will always be crystallites which are oriented in the right way to fulfil the symmetry restrictions of the set-up.

Thus it is possible to reconstruct the crystal structure of the sample from the number and position of the recorded reflections in the diffractogram. It includes the determination of the lattice parameters. There are databases available (e.g. the Powder-Diffraction-Database (PDF) from the International Centre of Diffraction Data (ICDD)) which contain the X-ray diffractograms of numerous phases. This simplifies the analysis of unknown diffractograms, especially if several phases are mixed. The XRD pattern used in this thesis are listed in appendix D.

For the measurement of thin films it is recommended to use grazing incidence XRD [54]. In this set-up the position of the tube is fixed at a shallow angle and only the detector is scanned (figure 3.2b). The shallow incidence angle enlarges the path of the X-ray beam within the thin film and increases the signal coming from the film. For very small incidence angles ($a < 0.05 - 1.5\,°$, depending on material and X-ray energy) the X-ray beam experiences total reflection at the film surface and only an evanescent wave can penetrate into the film. In this regime the surface sensitivity is further increased but the position of the reflections must be corrected [54].

A Cu anode was used as X-ray source in this thesis emitting the wavelengths $\lambda_{Cu,K\alpha1} = 0.1540523\,\mathrm{nm}$ and $\lambda_{Cu,K\alpha2} = 0.1544427\,\mathrm{nm}$ [55]. All XRD measurements have been done with a parallel X-ray beam predetermined by the instrument owner. Initial XRD measurements (figures 9.3, 19.1) have been performed in $\theta - 2\theta$ configuration (figure 3.2a) with a scan time between $30\,\mathrm{min}$ and $2\,\mathrm{h}$. The instrument resolution in this set-up was about $0.13 - 0.22\,°$ (FWHM at $2\theta \approx 27\,°$). Later measurements (figures 17.2, 17.3) were taken in grazing incidence mode with an incidence angle of $4\,°$

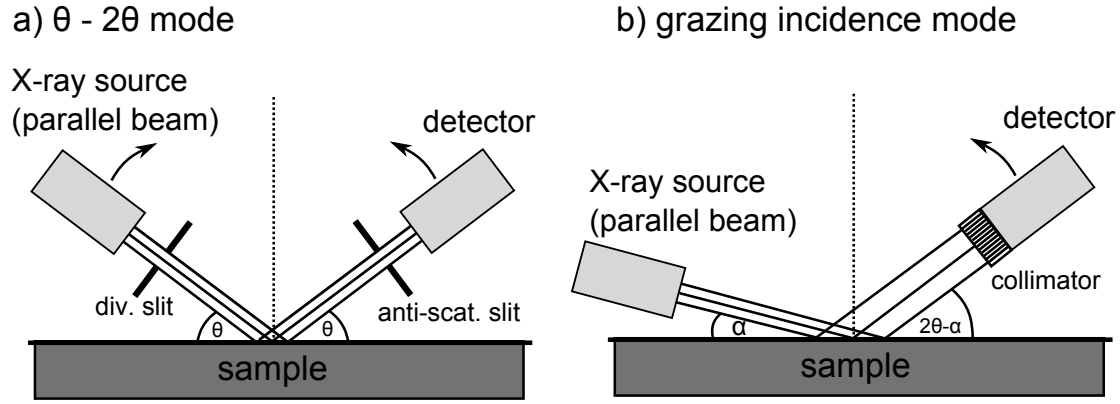

Figure 3.2.: Experimental set-up of XRD measurements in a) $\theta - 2\theta$ configuration and b) grazing incidence configuration.

and a scan time of $2\,\mathrm{h}$ (figure 3.2b). The incidence angle has been adjusted to show a weak Mo reflection of the substrate which ensures probing of the complete absorber thickness. The shallow incidence angle leads to a large illuminated area on the sample decreasing the angular resolution of the instrument. This effect is compensated by the use of a parallel Cu plate collimator which confines the acceptance angle of the detector. Nevertheless the instrument resolution in grazing incidence mode is limited to $2\theta = 0.10\,°$. High resolved measurements of single peaks (figures 17.4, 18.2) have been recorded in $\theta - 2\theta$ configuration with small divergence and anti-scatter slits of $0.1\,\mathrm{mm}$ and a slow scan rate of $0.01\,°/\mathrm{min}$. With these setting an instrument resolution of $0.05\,°$ (FWHM at $2\theta \approx 30\,°$) could be reached.

The set-up and conditions for in-situ XRD measurements during annealing will be presented in section 15.3.1.

3.3. Inductively-Coupled Plasma Mass Spectroscopy (ICP-MS)

Inductively-Coupled Plasma Mass Spectroscopy (ICP-MS) is an accurate measurement technique to determine the composition of a solution. The solution is nebulised and afterwards ionised by a plasma. The plasma is obtained by passing the nebulised sample and a carrier gas (e.g. Ar) through a coil connected to a radio-frequency generator. The ionised sample is finally analysed in a mass spectrometer (figure 3.3) [56].

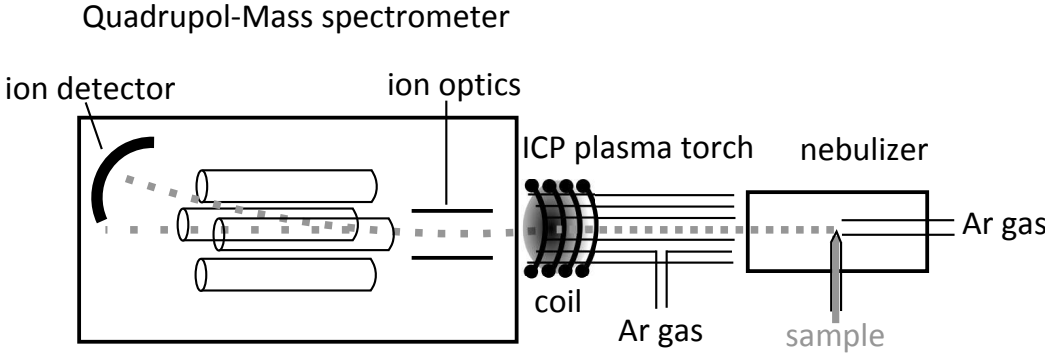

Figure 3.3.: Principal set-up of an ICP-MS system [56]

In this thesis ICP-MS has mainly been used to determine the composition of solid thin films. The films have been dissolved in aqua regia ($\mathrm{HNO_3}$: HCl volume ratio 1 : 3) and the solution was diluted to the concentration regime accepted by the ICP-MS apparatus. The detector output was compared to a standard calibration solution with known composition to calculate the concentration

of the sample solution.

The detection limit by ICP-MS for the elements of interest (Cu, In, Se) is about $1\,\mathrm{ppt}$. The error in the ICP-MS quantification process mainly results from the error of the standard calibration solution and errors in the dilution process. The accuracy of the obtained masses is about $1-3\%$. The determination of trace impurities by ICP-MS is described in section 15.3.2.

Part I.

Electrochemistry and Electrodeposition

4. Introduction

In this part of the thesis procedures for the electrodeposition of indium selenide and copper selenide will be developed. Beyond the pure plating of the film the intention is to get a deeper insight into the electrochemistry of the binary selenide. This part will concentrate on indium selenide, because an excellent discussion of the electrochemistry of copper selenide has already been published by Massaccesi et al. and Thouin et al. [51, 50]. Massaccesi et al. have also worked on indium selenide and proposed that In_2Se_3 electrodeposition is induced by selenium [1]. On the contrary the work by Mishra and Rajeshwa ascribes the deposition of In_2Se_3 to an indium induced process [57]. Both studies have been performed under different conditions (e.g. temperature) and are typical representatives of two routes of indium selenide electrodeposition existing in the literature. This work follows the route which also Massaccesi et al. have studied [1]. It verifies it and supports the results by additional experiments. Moreover new aspects of indium selenide electrochemistry are outlined.

At the beginning of the part a short introduction to the basics of electrochemistry is given. The understanding of the indium selenide electrochemistry requires the understanding of the electrochemical behaviour of its elements. The case of indium will be discussed as an introductory example. It is followed by the characteristics of selenium electrochemistry (e.g. the dominant species at different potentials, the slow electrode kinetics, a passivating deposit on the electrode). The diffusion coefficient of both ions is determined since it is required for the calculation of mass fluxes in the indium selenide bath. Appropriate conditions for the electroplating of a copper selenide film are presented.

The possible deposition potential range for indium selenide electrodeposition will be determined from cyclic voltammetry. Thermodynamic considerations by Massaccesi et al. predict that the deposit from the indium selenide bath consists of In_2Se_3 and elemental Se [1]. It was claimed that the amount of elemental Se is mass transport controlled. These consideration will be checked by composition measurements of samples deposited under various potentials and mass fluxes. The mass fluxes involved in the deposition of In_2Se_3 and elemental Se are quantified. Se precipitation in the bath is an unwanted side reaction. It is quantified and a possible incorporation in the deposit is examined.

In the end a stable process for the uniform plating of a binary selenide precursor is outlined.

5. Introduction to electrochemistry

This section introduces basic principles of electrochemistry. For a more detailed description the reader is referred to standard textbooks on electrochemistry [58, 59, 60, 61, 62].

5.1. Standard electrode potential and Nernst equation

A voltage is measured between two electrochemical half cells. Consider one of the half cells is the standard hydrogen electrode (SHE) following the reaction $\frac{1}{2}\mathrm{H_2} \rightleftharpoons \mathrm{H^+} + \mathrm{e^-}$ at standard conditions (i.e. the activity of all species equals 1; the temperature is $298.15\,\mathrm{K}$ and the pressure is $1013\,\mathrm{mbar}$). Its potential is defined as zero. Then the voltage between the half cells corresponds to the standard electrode potential E^0 of the second half cell (redox reaction $\mathrm{O} + n \cdot \mathrm{e^-} \rightleftharpoons \mathrm{R}$ with O being the oxidised species and R being the reduced species), if the measurement is performed under standard conditions. The overall reaction is

$$\mathrm{O} + \frac{n}{2} \cdot \mathrm{H_2} \rightleftharpoons \mathrm{R} + n\mathrm{H^+} \tag{5.1}$$

The change of Gibbs energy ΔG^0 for this reaction is linked to the standard potential by

$$\Delta G^0 = -nFE^0 \tag{5.2}$$

with F being the Faraday constant. If the activities of the reduced and oxidised species (a_R and a_O) differ from unity the electrode potential is given by the Nernst equation:

$$E = E^0 + \frac{RT}{nF} \cdot \ln \frac{a_O}{a_R} \tag{5.3}$$

R denotes the ideal gas constant.

5.2. Electrode kinetics

According to the Nernst equation a reduction of the oxidised ions in reaction 5.3 (species O) should set in, when the applied potential is more negative than the standard potential of the electron transfer. Nevertheless it is often observed that a significantly more negative potential is needed to obtain a considerable current. The Nernst equation describes the equilibrium case and does not take electrode kinetics into account which can significantly slow down a reaction even if it is thermodynamically possible.

It can be considered that the reduction process and the oxidation process have to overcome different activation Gibbs energies. The difference in activation energy can be controlled by the applied potential. This consideration leads to the Butler-Volmer equation relating the applied overpotential $\eta = E^\circ - E$ to the observed current density i :

$$i = i_0 \left\{ \exp\left(-\frac{\alpha n F \eta}{RT} \right) - \exp\left(\frac{(1-\alpha)\, nF\eta}{RT} \right) \right\} \tag{5.4}$$

i_0 is the exchange current density, α the transfer coefficient. The meaning of these coefficients is explained in figures 5.1a and 5.1b. The exchange current density i_0 equals the reducing current and the oxidising current if the system is in equilibrium at potential E°. If i_0 is high the system reacts

with a current response immediately when the standard potential E° is passed (figure 5.1a, curve 1). Such a system is called "reversible". If i_0 is low the system is "sluggish". A high overpotential is needed to drive a considerable current (figure 5.1a, curve 4). Such a system is called "irreversible". The transfer coefficient is between 0 and 1 and is usually close to 0.5. In this case the reduction and oxidation side of the current characteristic are symmetrical (figure 5.1b, curve 2). If α differs from 0.5 the curve becomes asymmetric and either the reduction or oxidation process needs a high overpotential to start (figure 5.1b curve 1 and 3).

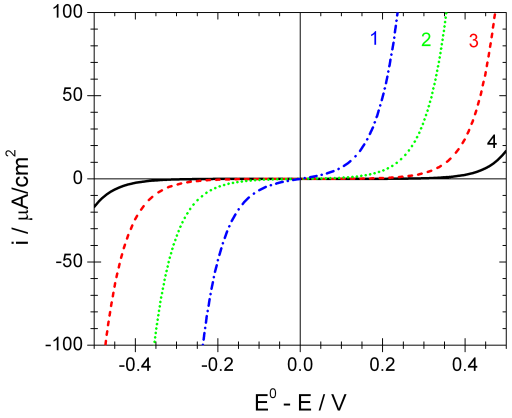

(a) Varying exchange current density i_0 for a constant transfer coefficient of $\alpha = 0.5$: 1) $1\,\mu\mathrm{A/cm^2}$, 2) $0.1\,\mu\mathrm{A/cm^2}$, 3) $0.01\,\mu\mathrm{A/cm^2}$, 4) $0.001\,\mu\mathrm{A/cm^2}$

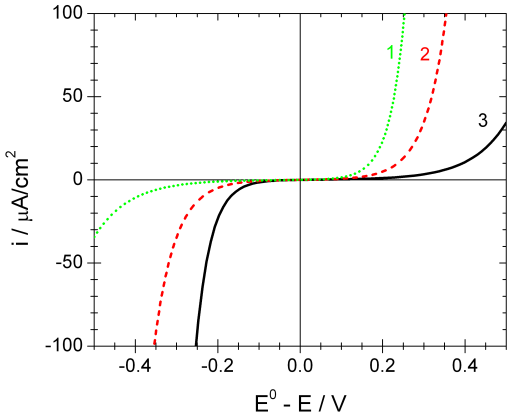

(b) Varying transfer coefficient α for a constant exchange current density of $i_0 = 0.1\,\mu\mathrm{A/cm^2}$: 1) 0.3, 2) 0.5, 3) 0.7

Figure 5.1.: Butler-Volmer equation ($T = 298\,\mathrm{K}$ and $n = 1$)

5.3. Rotating disc electrode

The Butler-Volmer equation 5.4 is only valid under the assumption that the concentration of the electrolyte at the electrode surface is constant in time. This assumption is only justified if the diffusion within the electrolyte is fast enough to compensate any concentration change at the surface caused by the electrode reaction. In many cases the diffusion is too slow and the electrolyte at the electrode is depleted with time.

In these cases the current density transient $i(t)$ at constant applied potential can be estimated by

the Cottrell equation [59, 58, 60]

$$i(t) = \frac{nFD^{1/2}c_0}{\sqrt{\pi \cdot t}} \tag{5.5}$$

D is the diffusion coefficient of the active species, n the number of electrons involved in the redox process and c_0 the concentration of the educt in the bulk. The equation is valid for a planar electrode without edge effects, a fast electron-transfer reaction, and very negative potential ($E \ll E^\circ$). It is obvious from equation 5.5 that the current density $i(t)$ decreases with time meaning that the electrolyte is depleted.

A simple way to apply a controlled mass transport of the electrolyte to the electrode surface is the use of a Rotating Disc Electrode (RDE).

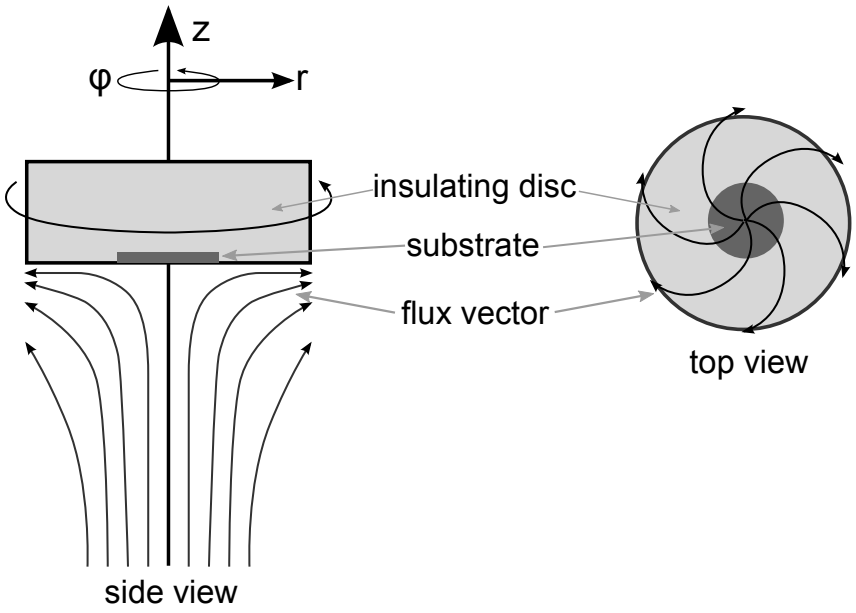

Figure 5.2.: Set-up and flow pattern of a RDE

The RDE consists of an electrode embedded in a disc made from a non-conductive material. The disc has usually a much larger diameter than the electrode in order to avoid possible turbulences at the disc edge effecting the flow at the electrode. The disc is rotated along its symmetry axis to force a flow within the electrolyte (figure 5.2).

At the disc the electrolyte is accelerated towards the edge. This causes the flow towards the electrode surface that is sketched in figure 5.2. Along the surface the rotation of the electrolyte causes a spiral flow pattern. The hydrodynamics of the RDE can be solved analytically in cylindrical coordinates (φ, r, z, see figure 5.2). It turns out that the velocity component along the z-direction is independent of the r and φ. That means the flow of fresh electrolyte towards the electrode is uniform over the electrode surface. Knowing the velocities of the flow the problem of combined diffusion and forced convection can be solved. It results in the Levich equation [60, 63]

$$i_l = 0.62 \cdot nF\nu^{-1/6}D^{2/3}c_0 \cdot \sqrt{\omega} \tag{5.6}$$

i_l is the limiting current density, i.e. the current density being observed if the kinetics are fast enough that the current density is limited by the mass transport. n, c_0, D, ν are the number of electrons transferred in the reaction, the bulk concentration, the diffusion coefficient and the kinematic viscosity[1] of the medium. ω is the angular rotation speed of the RDE. The limiting

[1] The dynamic viscosity η is related to the force F which is necessary to pull a plate (area A) with the speed v through a liquid in a distance d to a wall: $\eta = \frac{Fd}{Av}$. The dynamic viscosity η is linked to the kinematic viscosity ν by the density ρ of the liquid through $\eta = \nu \cdot \rho$. The density ρ, absolute and kinematic viscosity (η and ν) of water at

current density can be either obtained from the cyclic voltammogram or the current density value recorded by deposition at a fixed potential.

In a Levich plot the limiting current density is plotted versus $\sqrt{\omega}$. If the system is mass transport controlled the Levich equation 5.6 is valid and the plot is a line through the origin. Its slope depends on the diffusion coefficient and the electron transfer coefficient n of the reaction. If the diffusion coefficient is known n can be determined giving information on the redox reaction.

The diffusion coefficient $D(T)$ of ions depends on the temperature of the medium. As a rule of thumb the temperature dependency can be calculated by the Walden product[2][59, 65]

$$\frac{D(T_1) \cdot \eta(T_1)}{k_B T_1} = \frac{D(T_2) \cdot \eta(T_2)}{k_B T_2} = \text{const} \tag{5.7}$$

$\eta(T)$ is the dynamic viscosity (table in footnote on the preceding page).

5.4. Linear sweep voltammetry and cyclic voltammetry

Linear sweep voltammetry and cyclic voltammetry are methods to study electrochemical processes, e.g. the electrode potential required for a redox reaction. In linear sweep voltammetry the potential applied to the working electrode is linearly decreased or increased with time and the current is recorded. Cyclic voltammetry is an extension to it, where the voltage scan is reversed again. The shape of the cyclic voltammogram (CV) can be calculated for simple examples. It requires a solution of the hydrodynamics for the reduced and oxidised species (R and O). These are given by Fick's first and second law [61]

$$j = -D \frac{\partial}{\partial x} c_{O/R}(x,t) \tag{5.8}$$

$$\frac{\partial c_{O/R}(x,t)}{\partial t} = D \frac{\partial^2}{\partial x^2} c_{O/R}(x,t) \tag{5.9}$$

j denotes the mass flux, D the diffusion coefficient, $c_O(x,t)$ and $c_R(x,t)$ the concentrations of the oxidised and reduced species, respectively. Several boundary and initial conditions must be chosen according to the experimental set-up and procedure (e.g. $c_O(x, t=0) = \text{const}$ with respect to x).

In a reversible system the ratio between the concentrations of the reduced and oxidised species at the electrode surface ($x = 0$) is given by the Nernst equation 5.3 (assuming that the activity can be approximated by the concentration):

$$\frac{c_O(x=0,t)}{c_R(x=0,t)} = \exp\left(\frac{nF}{RT}\left(E\left(t\right) - E^0\right)\right) \tag{5.10}$$

$E\left(t\right)$ denotes the time dependent potential. The current can be calculated from the redox reaction rate that is necessary to fulfil equations 5.8 - 5.10 and the boundary conditions.

If the system is irreversible (e.g. $\mathrm{O} + \frac{n}{2} \cdot \mathrm{H_2} \rightarrow \mathrm{R} + n\mathrm{H^+}$) the Nernst equation is not longer valid and the electrode kinetics must be considered (compare to Butler-Volmer equation 5.4) [61]

$$D \cdot \frac{\partial c_O(x=0,t)}{\partial x} = k_O \cdot \exp\left[-\frac{\alpha n F}{RT}\left(E(t) - E^0\right)\right] \tag{5.11}$$

k_O is the reaction rate constant (units $\mathrm{m} \cdot \mathrm{s}^{-1}$) of the reduction process. The current at the electrode can be calculated from the reaction rate.

different temperatures are [64]:

	ρ	η	ν
	$\mathrm{g/cm^3}$	$10^{-3}\,\mathrm{g/(s \cdot cm)}$	$10^{-3}\,\mathrm{cm^2/s}$
25 °C	0.9970	8.904	8.931
80 °C	0.9712	3.547	3.652

[2]The original Walden product is not formulated with the diffusion coefficient D but with the related ion mobility u. It is $u \cdot \eta = \text{const}$.

5.5. Nucleation and growth

The electrodeposition of a metal on a different substrate requires a supersaturated solution at the electrode. The presence of nuclei is needed to initialise the crystallisation from this metastable state. The time dependence of nuclei formation depends on the studied system. It is possible to observe an instantaneous nucleation where all nuclei are formed directly at the beginning of the process. Such an instantaneous nucleation can be initialised by a short very negative potential pulse [62]. Under different conditions the number of nuclei can increase with time (progressive nucleation). In the simplest case the rate of nuclei formation is constant. The nuclei grow with time and the increasing surface area leads to a rise in current. The time dependency of the current depends on the type of growth. If the nuclei are hemispherical the current at the nuclei will increase proportional with t^2. If the nuclei are two-dimensional circles and only growing along the edges the increase is proportional with t. So far it has been assumed that the growth was limited by the reaction kinetics. If the process is limited by diffusion the Cottrell equation 5.5 must be considered. An overview on the current time dependence is given in table 5.1.

	kinetically limited		diffusion limited	
	instantaneous	progressive	instantaneous	progressive
hemispherical	2	3	0.5	1.5
2D circles	1	2		

Table 5.1.: Time dependence of current $I \propto t^x$ for different nuclei growth. The exponent x is tabulated [62, 61].

The overpotential that is needed to deposit a metal on a foreign substrate is usually higher than the one needed for depositing on the same substrate. In the cyclic voltammetry of metals it is therefore often observed that the current in the forward scan when the substrate is blank is lower than in the backward scan when the substrate is covered by nuclei which initiate the deposition. This causes a crossing of forward and backward scan in the cyclic voltammogram ("nucleation loop") [66, 67].

5.6. Electrodeposition of binary compounds

A bath contains two species $\mathrm{M}^{\mathrm{m+}}$ and $\mathrm{N}^{\mathrm{n+}}$ with different standard deposition potentials E°_M and E°_N. The element N with the more positive potential $E^\circ_N > E^\circ_M$ is called the "noble" element. It is assumed that there is a compound $\mathrm{M_rN_s}$ which is formed by an exoenergetic reaction, i.e. $G^\circ_{M_rN_s} < 0$. This additional driving force makes it now possible to plate the compound at a potential above E°_M, where the less noble element M cannot be deposited otherwise.

This effect follows directly from the relation between the standard potential and the Gibbs energy (equation 5.2). It is discussed for the example of $\mathrm{In_2Se_3}$ which is conceptually the product of the following reactions:

$$2\mathrm{In}^{3+} + 3\mathrm{H_2} \rightarrow 2\mathrm{In} + 6\mathrm{H}^+ \qquad 2 \cdot \Delta G^0_{\mathrm{In}^{3+}/\mathrm{In}} \tag{5.12}$$

$$3\mathrm{Se} \rightarrow 3\mathrm{Se} \qquad \Delta G^0_{\mathrm{Se/Se}} = 0 \tag{5.13}$$

$$2\mathrm{In} + 3\mathrm{Se} \rightarrow \mathrm{In_2Se_3} \qquad \Delta G^0_{f,\mathrm{In_2Se_3}} \tag{5.14}$$

The total reaction in the electrochemical cell is

$$2\mathrm{In}^{3+} + 3\mathrm{H_2} + 3\mathrm{Se} \rightarrow \mathrm{In_2Se_3} + 6\mathrm{H}^+ \tag{5.15}$$

The total change in Gibbs energy for this reaction is

$$\Delta G^0_{total} = \Delta G^0_{f,\mathrm{In_2Se_3}} - 2\Delta G^0_{\mathrm{In}^{3+}/\mathrm{In}} - \Delta G^0_{\mathrm{Se/Se}} \tag{5.16}$$

	H_2SeO_3	In^{3+}	$\alpha - In_2Se_3$	$H_2Se(aq)$	H_2O
$\Delta G_f^\circ / kJ \cdot mol^{-1}$	-426.22	-97.9	-306	+22.2	-237.1
Reference	[68]	[68]	[69]	[68]	[70]

Table 5.2.: Gibbs free energies of indium and selenium species

The standard electrode potential[3] for In_2Se_3 follows from relation 5.2

$$E^0 = -\frac{1}{6F} \cdot \Delta G^0_{f,In_2Se_3} + \frac{1}{3F} \cdot \Delta G^0_{f,In^{3+}/In} = +0.19\,V \tag{5.17}$$

The reduction of In^{3+} to elemental In can be treated analogous: $E^0 = \frac{1}{3F} G^0_{f,In^{3+}/In} = -0.34\,V$. That means the formation of In_2Se_3 has shifted the standard deposition potential by $-\frac{1}{6F} G^0_{f,In_2Se_3} = +0.53\,V$ in positive direction [20].

In the used In-Se bath H_2SeO_3 and In_3^+ are the relevant selenium and indium species (see section 7.1 and 8). One could conclude the reaction:

$$3\,H_2SeO_3 + 2\,In^{3+} + 9\,H_2 \longrightarrow In_2Se_3 + 9\,H_2O + 6\,H^+ \tag{5.18}$$

This results in a potential of $E^\circ = +0.56\,V$ and is even more positive than in reaction 5.15. However it is not compatible to the assumption of equilibrium. At equilibrium there is no more H_2SeO_3 available at $+0.56\,V$, because it has already been reduced to elemental Se. Above $+0.19\,V$ it is favourable with respect to Gibbs energy if any In_2Se_3 created by reaction 5.18 further decomposes to Se and In^{3+} by the reverse reaction 5.15.

In summary the electrodeposition of a compound M_rN_s from M^{m+} and N^{n+} can take place at a potential G/rmF more positive than the standard potential of the less noble compound M. This is of practical importance, because it provides a self-controlled mechanism for the formation of the compound. One chooses a high concentration of the less noble species M^{m+} and a low concentration of the noble species N^{n+} . A potential is applied that is slightly more positive than the one necessary for the direct deposition of M. At this potential only N and M_rN_s can be obtained. Since the concentration of N^{n+} is lower than M^{m+} it is likely that every deposited N will enable the reduction of M^{m+} in order to form the compound. That means the final film will mainly consist of M_rN_s [71].

The previous argumentation is simplified, because it does not consider the role of activities in the deposition process. A more elaborated model has been proposed by Kröger [71]. The electrodeposition potentials are given by the Nernst equation 5.3

$$E_M = E_M^0 + \frac{RT}{mF} \ln\left(\frac{a_{M^{m+}}}{a_M}\right) \tag{5.19}$$

$$E_N = E_N^0 + \frac{RT}{nF} \ln\left(\frac{a_{N^{n+}}}{a_N}\right) \tag{5.20}$$

In equilibrium

$$E_M = E_N \tag{5.21}$$

$a_{M^{m+}}$ and $a_{N^{n+}}$ are the activities of the ions in solution. a_M and a_N are the activities of M and N in the deposit. In case of single element deposition the activities a_M and a_N usually equal unity, because the pure element is the standard state. This is not longer true for the simultaneous electrodeposition of elements, because the alloy is not the standard state. Only in the limiting case that the deposit mainly consists of one element the corresponding activity will be close to unity (e.g. if $(M/N)_{deposit} \gg 1$ then $a_M \approx 1$). The activities of both elements inside the deposit are linked by the Gibbs energy ΔG_f of the compound

[3] The potentials in this section refer to the standard hydrogen electrode.

$$a_M^r a_N^s = \exp\left(\Delta G_f / RT\right) \tag{5.22}$$

In equilibrium the activities will arrange in a way that both equations 5.21 and 5.22 are satisfied. There are two possible classes depending on the relation between the Gibbs energy of the compound G and the difference in standard potential of the single elements [71]

1. Class I: $(E_N^\circ - E_M^\circ) > |\Delta G_f / mrF|$. The redox potential of the alloy is determined by the activity of the less noble species $a_{M^{m+}}$ according to equation 5.19 for all compositions of the deposit. The activity $a_{N^{n+}}$ of the noble species is then adjusted by a forced reduction to satisfy equations 5.20 and 5.21. In the limiting case of $a_N = 1$ (deposit consists mainly of noble element N) the potential calculated by equations 5.19 and 5.22 is shifted $|\Delta G_f / rmF|$ more positive than the standard potential E_M° (assuming standard activity $a_{M^{m+}} = 1$ for species M^{m+} in solution). This corresponds to the result of the simple calculation from Gibbs energy. In the other limiting case $a_M = 1$ (deposit consists mainly of less noble element M) the deposition potential of the compound will be E_M°. Despite the Gibbs energy of the compound the deposition potential does not shift. That means "Class I"-alloys can experience a positive potential shift between 0 and $|\Delta G_f / rmF|$ depending on the activities of its elements in the deposit. $\mathrm{In_2Se_3}$ belongs to this class.

2. Class II: $(E_N^\circ - E_M^\circ) < |\Delta G_f / mrF|$. The redox potential of the alloy is determined by the less noble species (equation 5.19) if $a_M \gg a_N$ (i.e. deposit consists mainly of M). If $a_N \gg a_M$ (i.e. deposit consists mainly of N) the noble element determines the potential by equation 5.20. In the intermediate regime the potential is determined by both species and the deposition of the compound can even take place at potentials more positive than the noble element.

6. Experimental

6.1. Electrodeposition bath

6.1.1. Indium, selenium, and indium selenide bath

The indium bath (chapter 7.2) and selenium bath (chapter 8) are both based on the indium selenide electrodeposition bath (chapter 10.2) in which the non-relevant species has been left out. $100\,\mathrm{mM}$ K_2SO_4 has been added as background salt [1]. It reduces the specific resistivity of the solution and shields the electrostatic interaction between the ions. A buffer from sulfamic acid and potassium biphthalate stabilised the pH value to 2 (at $80\,°C$). In the following "background electrolyte" will always mean K_2SO_4 or $LiCl$ and the pH buffer. The correct choice of the pH value is critical, because In^{3+} ions tend to form hydroxide complexes if the pH value is not acidic enough (section 7.1). In the current pH buffer In^{3+} concentrations up to $10\,\mathrm{mM}$ are stable. Above $20\,\mathrm{mM}$ indium hydroxide will fall out in the bath as a white precipitate. The concentrations of indium sulphate and selenous acid have been varied in the various experiments between $0.4\,\mathrm{mM}$ and $10\,\mathrm{mM}$. The composition of the plating bath that has been used for the preparation of finished solar cells is given in table 6.1. All experiments with the indium, selenium or indium selenide bath have been performed at an elevated temperature of $80\,°C$ if not stated otherwise. Before the experiments oxygen was removed from the bath, because it can lead to the formation of indium oxide phases in the electrodeposition process. The oxygen was removed by bubbling nitrogen gas through the bath. Additionally the bath was heated up to $95\,°C$ to drive out the dissolved gas and afterwards cooled to the working temperature of $80\,°C$ under nitrogen atmosphere.

Ultrapure water ($18.2\,\mathrm{M\Omega \cdot cm}$) was used for the electrodeposition baths. All chemicals had a purity of 99.99% and above except for the potassium biphthalate which was only 99.95% pure.

6.1.2. Copper selenide bath

The plating bath for copper selenide (chapter 9.2) has been adopted from a plating bath for copper indium diselenide in which the indium compound was left out (table 6.1) [21]. Its pH is buffered at 3. All experiments with the copper selenide plating bath have been performed at room temperature.

6.2. Electrodeposition set up

A standard 3-electrodes set-up has been used for all experiments (figure 6.1). The counter electrode was a platinum sheet at the bottom of the reaction vessel. An Ag | AgCl | $3\,\mathrm{M}$ KCl electrode served as reference electrode (reference potentials given in appendix C). The working electrode was a RDE facing downwards. Two types of working electrodes were used. The "fixed-RDE" consisted of a metal (Mo or Cu) rod with $5\,\mathrm{mm}$ diameter that was permanently embedded in a PEEK cylinder of $10\,\mathrm{mm}$ diameter. The "sample-RDE" was a $25 \times 25\,\mathrm{mm^2}$ substrate mounted onto a polymer cylinder of $50\,\mathrm{mm}$ diameter. The substrate consisted of a Mo layer ($\approx 600\,\mathrm{nm}$ thick) sputtered onto a soda-lime glass substrate. At the corners the substrate was contacted by thin wires. The "fixed-RDE" was

[1] The abbreviation "mM" is usually used for the molarity ($10^{-3}\,\mathrm{mol/l}$) of a solution. In this thesis the solutions have been prepared by molality ($10^{-3}\,\mathrm{mol}$ per kg of solvent) instead. For all concentrations referring to experiments in this thesis "mM" stands for $10^{-3}\,\mathrm{mol}$ per kg of solvent. In case of concentration cited from the literature "mM" means $\mathrm{mmol/l}$. Since the used concentrations are usually low the values between both variables are similar and can be compared.

	Indium selenide	Copper selenide
bath	$1.89\,\mathrm{mmol/kg}$ $In_2(SO_4)_3{\cdot}9\,H_2O$ (*)	$2.6\,\mathrm{mmol/kg}$ $CuCl_2{\cdot}2\,H_2O$
(active species)	$1\,\mathrm{mmol/kg}$ H_2SeO_3	$5.9\,\mathrm{mmol/kg}$ H_2SeO_3
bath	$100\,\mathrm{mmol/kg}$ K_2SO_4	$232\,\mathrm{mmol/kg}$ $LiCl$
(background electrolyte)	$5.5\,\mathrm{g/kg}$ sulfamic acid	$8.55\,\mathrm{g/kg}$ sulfamic acid
	$4.5\,\mathrm{g/kg}$ potassium biphthalate	$1.55\,\mathrm{g/kg}$ potassium biphthalate
pH	2	3
temperature	$80\,°C$	$25\,°C$
RDE rotation	$400\,\mathrm{rpm}$	$100\,\mathrm{rpm}$
potential (vs. $3\,M$ KCl Ag|AgCl)	$-0.60\,V$	$-0.30\,V$

(*) In the preparation of the electrolytes a coordination number of $In_2(SO_4)_3$ of $x = 9$ was assumed [72, 73, 74].

Table 6.1.: Standard conditions for indium selenide and copper selenide electrodeposition. All samples in parts II and III have been plated with these settings.

used for CVs and short depositions to determine the limiting current. CVs in a stationary bath have also been recorded with this RDE if no rotation was applied. The "sample-RDE" was used for the deposition of films that could be further characterised or processed into an absorber.

All experiments with the indium, selenium, and indium selenide bath have been performed in a closed vessel (figure 6.1). This closed environment was necessary to avoid evaporation of the bath and to prevent the interference with oxygen in the bath. Although the set-up was not completely gas tight, it has been kept under a slight nitrogen overpressure to keep out oxygen. A nitrogen bubbler in the bath allowed the removal of oxygen from the bath (section 6.1.1). A condenser at the vapour outlet side reduced the loss by evaporation. A water trap closed the exit against air. The vessel was surrounded by a water-jacket to control the temperature of the system.

In case of the "fixed-RDE" a small vessel ($55\,\mathrm{mm}$ diameter) was used that contained around $90\,\mathrm{ml}$ of bath. The "sample-RDE" was operated in a larger vessel ($100\,\mathrm{mm}$ diameter) containing around $250\,\mathrm{ml}$ bath. In the larger vessel it was possible to bring a pipette close to the RDE (not drawn in figure 6.1). Its opening was directed towards the electrode surface and a flush of electrolyte could be manually applied to the surface. This was necessary to remove possible gas bubbles evolving during the deposition that could cause pinholes in the layer (section 11). In case of the Se film platings in section 8.2.1 a "sample-RDE" for small substrates ($12 \times 12\,\mathrm{mm}^2$) was used in the small vessel set-up.

The electrodeposition of the copper selenide is not sensitive to oxygen. Evaporation is negligible, because the bath is at room temperature. Therefore the plating was not done in a closed vessel but in a simple crystallising dish using the same 3-electrodes set-up as in the other cases.

In all platings and cyclic voltammograms the working electrode was inserted in the bath at open circuit potential. It was ensured that no bubbles were trapped at the electrode surface before the actual deposition potential was applied or the potential scan started. The time between electrode insertion and plating or measurement was about $20\,\mathrm{s}$.

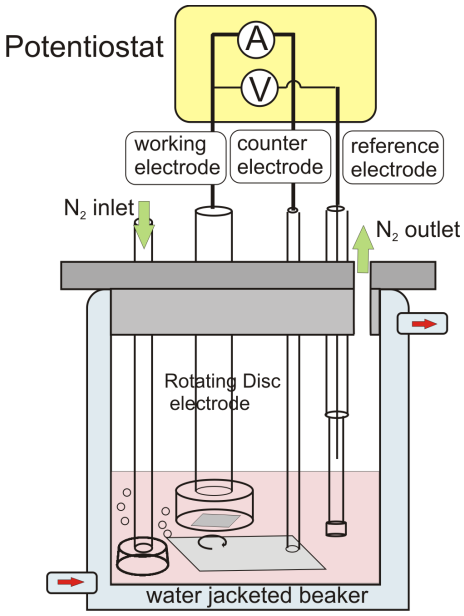

Figure 6.1.: Closed vessel electrodeposition set-up for Se and In_2Se_3 experiments

6.2.1. Substrate preparation

The "fixed-RDE" was consecutively cleaned in detergent, water and ethanol (each step ca. $5\,\mathrm{min}$) inside an ultrasonic bath at the beginning of the experimental series. Before each experiment it was polished with a 1 micron alumina powder for $1-2\,\mathrm{min}$ and afterwards cleaned in water inside an ultrasonic bath.

The Mo substrates used in the "sample-RDE" consisted of a $\approx 600\,\mathrm{nm}$ thick Mo layer which has been sputtered on soda lime glass. For samples that have been finished into solar cells (table 16.1) the substrates have been annealed in vacuum at $500\,°\mathrm{C}$ for $30\,\mathrm{min}$. This should release possible strain inside the Mo layer. All substrates have been consecutively cleaned in detergent, water and ethanol (each step ca. $10\,\mathrm{min}$) inside an ultrasonic bath. Before the deposition the substrates have been etched for $7-9\,\mathrm{min}$ in a 28% ammonia solution to remove possible oxides from the surface. The substrate size of the "sample-RDE" is typically $25\times 25\,\mathrm{mm}^2$ (except for the plating of Se in section 8). Fixing the substrates into the holder by a polyamide tape left an area of $20\times 20\,\mathrm{mm}^2$ for plating.

6.3. Etching of elemental Se

The presence of elemental Se can be examined by a selective etching with $Na_2S{\cdot}9\,H_2O$ [75, 76]. The samples are etched in a $100\,\mathrm{mM}\ Na_2S$ solution for $30\,\mathrm{min}$ under soft shaking. This has been done in the case of copper selenide and indium selenide (chapter 9.2 and 10.2). The Se content before and after etching was measured by ICP-MS to obtain the mass of elemental Se. The electrodeposited copper selenide layer has a porous morphology (figure 9.2).

6.4. Se precipitation

In chapter 10.2.4 the Se precipitate occurring during the deposition of indium selenide was removed to analyse its composition and to quantify its formation rate. Depositions were done at $-0.60\,\mathrm{V}$ and a RDE rotation rate of $400\,\mathrm{rpm}$ in a bath containing $9.47\,\mathrm{mM}\ In^{3+}$ and $1\,\mathrm{mM}\ H_2SeO_3$ as active species ($T = 80\,°\mathrm{C}$). After each deposition (deposited charge $2.2\,\mathrm{C}\cdot\mathrm{cm}^{-2}$ which corresponds to $1000\,\mathrm{nm}\ In_2Se_3$) an electrolyte sample was taken from the bath (mass of each electrolyte sample:

$6 - 8\,\mathrm{g}$). The total mass of the electrolyte was $260\,\mathrm{g}$ and each deposited film contained in average $900\,\mu\mathrm{g}$ In and $1230\,\mu\mathrm{g}$ Se. The mass of the electrolyte sample was then replaced by fresh electrolyte. The precipitate in the electrolyte sample was removed by a centrifuge ($10\,\mathrm{min}$ at $4000\,\mathrm{rpm}$) and the remaining indium and selenium concentration in the electrolyte was determined by ICP-MS (section 3.3). Also the composition of the plated samples has been measured by ICP-MS. The Se^{4+} concentration in the bath is expected to decrease with progressive depositions, because some Se is plated in the sample and afterwards removed with it. Therefore the bath composition has been calculated from the mass balance of the experiment and been compared to the experimental value measured by ICP-MS. The difference between these values is assigned to the loss of Se by precipitation.

$$m_{Se-precipitate} = m_{Se-bath,before} - m_{Se-bath,after} - m_{Se,sample} + m_{Se,refill} \tag{6.1}$$

After the deposition of the 6th indium selenide sample the complete bath was centrifuged to remove the Se precipitate. The precipitate was afterwards rinsed with water and analysed by ICP-MS. Afterwards the bath was used again for further depositions (samples 7 - 9).

7. Electrochemistry of Indium

The purpose of this chapter is the determination of the indium electrode potential under the present conditions. This is necessary to identify in the following chapters on indium selenide if the incorporation of indium shifts to more positive potentials when a binary compound is deposited. Additionally the diffusion coefficient of In^{3+} in the studied bath is determined. A comprehensive review on the electrochemistry of indium was done by Piercy and Hampson [77, 78].

7.1. Background

In^{3+} is the only stable ion of indium in aqueous solutions. It has a strong tendency to undergo hydrolysis. The ion reacts with a water molecule of its hydration sheath and forms an indium hydroxide complex $\mathrm{In(OH)}^{2+}$ by releasing a proton [78]. In^{3+} favours the hydrolysis reaction, because of its high cation charge. The reaction can occur multiple times and furthermore $\mathrm{In(OH)}_2^+$ and $\mathrm{In(OH)}_3$ are formed [79]. Indium hydroxide $\mathrm{In(OH)}_3$ is uncharged and has a low solubility and therefore tends to form a white precipitate if the In^{3+} and hydroxide ion concentrations are high. For an ion concentration of $0.01\,\mathrm{M}$ precipitation at room temperature occurs if the pH value exceeds 3.4 - 3.9 [78, 80]. At an elevated temperature of $100\,°\mathrm{C}$ this critical pH value decreases and hydroxide formation already sets in at a pH value above 2.3 for infinite dilutions [79].

The standard electrode potential of In^{3+} is given by [1] [68]

$$\mathrm{In}^{3+}_{(aq)} + 3\,\mathrm{e}^- \longrightarrow \mathrm{In}_{(s)} \qquad E^\circ = -0.548\,\mathrm{V} \tag{7.1}$$

$$\mathrm{d}E^\circ/\mathrm{d}T = +0.040\,\mathrm{V} \quad \text{(at 298K)} \tag{7.2}$$

The direct three electron transfer process in reaction 7.1 is unlikely and the reduction of In^{3+} takes place in multiple one-electron transfer steps via the unstable species In^+ and In^{2+} [77].

Valderrama et al. studied cyclic voltammograms (at a scan rate of $8\,\mathrm{mV/s}$) of indium from a $8\,\mathrm{mM}$ In^{3+} bath at pH 3 on copper coated Mo substrates at room temperature [81]. They determine the onset of indium deposition between $-0.73\,\mathrm{V}$ and $-0.67\,\mathrm{V}$. They observe a nucleation loop and assign it to a three-dimensional growth under instantaneous nucleation limited by diffusion (section 5.5). The reverse scan shows two anodic peaks. The one at $-0.57\,\mathrm{V}$ belongs to the oxidation of In to In^{3+} and the one at $-0.48\,\mathrm{V}$ can be assigned to the dissolution of indium from the CuIn alloy.

7.2. Results and Discussion

The cyclic voltammogram of In^{3+} on a polished Cu substrate shows a reduction maximum at $-0.65\,\mathrm{V}$ and an oxidation maximum at $-0.59\,\mathrm{V}$ (see figure 7.1a). They can be assigned to the overall reactions $\mathrm{In}^{3+} + 3\,\mathrm{e}^- \longrightarrow \mathrm{In}$ and $\mathrm{In} \longrightarrow \mathrm{In}^{3+} + 3\,\mathrm{e}^-$. Although this three-electron transfer is unlikely and supposed to consist of multiple one-electron transfers (section 7.1) these cannot be clearly resolved in the observed voltammogram. The shoulder at the onset of the reduction maximum ($-0.63\,\mathrm{V}$) may indicate such a one-electron transfer. A nucleation loop is observed being typical for the deposition of a metal on a foreign substrate (section 5.5). At the reduction potential the

[1] All potentials in this thesis cited from the literature have been converted to an Ag | AgCl | $3\,\mathrm{M}$ KCl reference electrode at $25\,°\mathrm{C}$. The conversion is given in Chapter C. Since the experiments in this thesis are done at $80\,°\mathrm{C}$ this can cause a potential shift of $-0.05\,\mathrm{V}$ for the high temperature potentials.

deposition of a silver-white film is observed on the working cathode. Below $-0.70\,\mathrm{V}$ bubbles appear at the cathode caused by the hydrogen evolution reaction (HER), when H^+ ions are reduced. On the reverse scan the deposit is not completely stripped at the oxidation maximum as the films stays visible until the end of the scan. The further oxidation maxima at $-0.44\,\mathrm{V}$ and $-0.28\,\mathrm{V}$ can be assigned to the dissolution of indium from the copper indium alloy formed during deposition [81]. In summary the same results for the indium electrochemistry are observed as it has been reported by Valderrama et al. (section 7.1) [81].

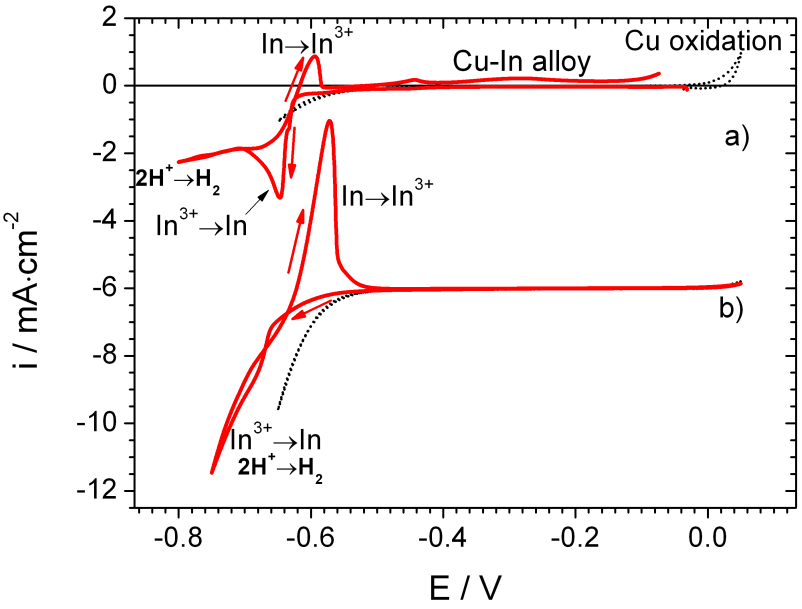

Figure 7.1.: Cyclic voltammograms of $3.79\,\mathrm{mM}\ \mathrm{In}^{3+}$ on a a) Cu and b) Mo electrode. The dotted voltammograms have been recorded in the background electrolyte ($100\,\mathrm{mM}\ \mathrm{K_2SO_4}$; pH 2 buffer, table 6.1) without In^{3+}. The scanning speed of all voltammograms was $10\,\mathrm{mV/s}$.

Changing the substrate to molybdenum leads to some changes in the cyclic voltammogram (figure 7.1b). There is no longer a distinct maximum of In^{3+} reduction, because it smoothly integrates into the hydrogen evolution reaction. It is known that a higher overpotential is needed to form hydrogen on copper in comparison with molybdenum [82]. The onset of HER on Mo is suppressed by the addition of indium in comparison to the pure background electrolyte. In^{3+} reduction needs a slightly higher overpotential on Mo in comparison to Cu. The deposition potential of indium is about$-0.67\,\mathrm{V}$ on Mo and $-0.65\,\mathrm{V}$ on Cu (neglecting the shoulder). Despite the interference with HER a nucleation loop is observed as it has been the case on the Cu surface. After the indium oxidation maximum the current density approaches zero until oxidation of the Mo substrate sets in.

The diffusion coefficient of $\mathrm{In}^{3+}$was determined from cyclic voltammograms measured on a Cu-RDE (figure 7.2, inset). The current density of the plateau at $-0.80\,\mathrm{V}$ was plotted against the square root of the rotation speed to check the linearity of i_l versus $\sqrt{\omega}$ according to the Levich equation 5.6 (figure 7.2). The applicability of the Levich equation is a proof that in the studied system indium electrodeposition is controlled by mass transport and not by the kinetics of the charge transfer. The linear regression of figure 7.2 leads to a slope of $11.3\,\frac{\mathrm{C}}{\mathrm{m}^2\sqrt{\mathrm{s}}}$ and for the In^{3+} reduction process with $n = 3$ one obtains an In^{3+} diffusion coefficient of $(15.7 \pm 1.2) \cdot 10^{-6}\,\mathrm{cm}^2/\mathrm{s}$ at $80\,°\mathrm{C}$ from equation 5.6. That corresponds to a Walden product $\eta \cdot D \cdot \frac{1}{k_B T}$ (see equation 5.7) of $1.11 \cdot 10^8\,\mathrm{m}^{-1}$. In table 7.1 the Walden product is compared to values from the literature. The diffusion value measured in this thesis is a little bit lower than the reported values due to the different bath composition.

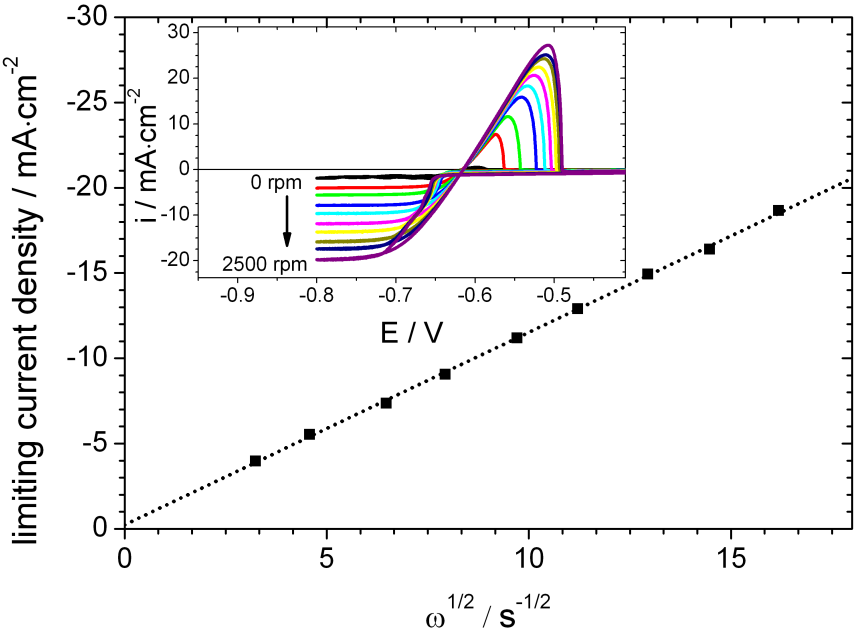

Figure 7.2.: Levich plot of a $3.79\,\mathrm{mM}$ In^{3+} bath. The limiting current densities have been taken from the plateau of the cyclic voltammograms at $-0.80\,\mathrm{V}$ and corrected for the background current density at $-0.60\,\mathrm{V}$. The onset shows the cyclic voltammograms of $3.79\,\mathrm{mM}$ In^{3+}on a Cu RDE at several rotation speeds (0, 100, 200, 400, 600, 900, 1200, 1600, 2000, 2500 min^{-1}), temperature: $80\,°\mathrm{C}$, scan rate: $5\,\mathrm{mV/s}$.

ref	bath	method	D	$\eta \cdot D \cdot (k_B T)^{-1}$
			$10^{-6}\,\mathrm{cm^2 s^{-1}}$	$10^{8}\,\mathrm{m^{-1}}$
this work	$3.79\,\mathrm{mM}$ $\mathrm{In_2(SO_4)_3}$, $100\,\mathrm{mM}$ $\mathrm{K_2SO_4}$, pH2 buffer, $T = 80\,°\mathrm{C}$	Levich plot	17.0 ± 1.3	1.20
[83]	mixture $\mathrm{HNO_3}$ / $\mathrm{KNO_3}$, pH 1.4, ionic strength 0.04, $T = 25\,°\mathrm{C}$	electrophoresis of ^{111}In	7.4 ± 0.1	1.60
[84]	$1\,\mathrm{M}$ KSCN, pH3, $T = 25\,°\mathrm{C}$	Ilkovic equation	6.0	1.30

Table 7.1.: Diffusion coefficient D and Walden product $\eta \cdot D \cdot \frac{1}{k_B T}$ of In^{3+} in aqueous solution determined by Bozhikov et al. [83], Timmer et al. [84] and this thesis.

In summary the observed electrochemical behaviour of In^{3+} under the conditions used in this thesis agrees with the one reported in the literature [81]. The reduction sets in around $-0.64\,\mathrm{V}$ on Cu and $-0.67\,\mathrm{V}$ on Mo under the applied conditions. On a Mo substrate it coincides with the splitting of water. The diffusion coefficient of In^{3+} in the used bath is $(17.0 \pm 1.3) \cdot 10^{-6}\,\mathrm{cm}^2/\mathrm{s}$ at $80\,°\mathrm{C}$.

8. Electrochemistry of Selenium

The electrochemistry of indium selenide is based on the electrochemistry of selenium. This chapter will introduce the characteristics of selenium electrochemistry like the formation of a passive layer on the electrode and the slow electrode kinetics. The potential ranges of the different Se species will be determined under the present conditions and also the Se diffusion coefficient. One section in this chapter will look into the passivation occurring during the electrodeposition of a Se film. The influence of the deposition temperature is studied. These results are the motivation for the elevated bath temperature used in indium selenide electrodeposition. The parameters for thin film Se deposition are given.

8.1. Background

8.1.1. Electrochemsitry of selenium

Selenium has the oxidation states -2, 0, $+4$, and $+6$ [68]. Taking into account the hydrolysis with water the species in figure 8.1 are present. Most of the experiments in this thesis were done at $pH = 2$ where $\mathrm{H_2Se}$, Se and $\mathrm{H_2SeO_3}$ are the stable species [1]. Solid Se is stable over a large pH range from -2 to 16. $\mathrm{H_2Se}$ is in equilibrium between the gas phase and the dissolved phase. The solubility of H_2Se in water at room temperature is given by $\log(\mathrm{H_2Se(aq)}) = -1.03 + \log p_{\mathrm{H_2Se(g)}}$ [80].

$\mathrm{Se^{4+}}$compounds are the usual precursors for Se electrodeposition. $\mathrm{Se^{4+}}$ can be reduced to elemental Se according to

$$\mathrm{H_2SeO_3 + 4\,H^+ + 4\,e^- \longrightarrow Se + 3\,H_2O} \tag{8.1}$$

At more negative potentials $\mathrm{Se^{4+}}$ can also be reduced to $\mathrm{Se^{2-}}$. The reaction is as a direct 6-electron transfer [85]:

$$\mathrm{H_2SeO_3 + 6\,H^+ + 6\,e^- \longrightarrow H_2Se(aq) + 3\,H_2O} \tag{8.2}$$

The standard potentials for reactions 8.1 and 8.2 are $+0.53\,\mathrm{V}$ and $+0.24\,\mathrm{V}$ (see figure 8.1). However the 6-electron transfer is only observed for low concentrations of $\mathrm{Se^{4+}}$ (e.g. $0.5\,\mathrm{mM}$ H_2SeO_3). At higher $\mathrm{Se^{4+}}$ concentrations the following reaction is likely [86]:

$$\mathrm{H_2SeO_3 + 2\,H_2Se \longrightarrow 3\,Se + 3\,H_2O} \tag{8.3}$$

Elemental Se is formed in a comproportionation reaction between $\mathrm{Se^{4+}}$ ions from the bath and $\mathrm{Se^{2-}}$ ions from reaction 8.2. Since reaction 8.3 does not require external electrons it is not restricted to the electrode surface but rather forms a precipitate of red Se [1]. In case of the RDE where such a precipitate is carried away by the hydrodynamic flux a red deposit of Se can be observed at the periphery of the electrode [86]. Reactions 8.2 and 8.3 are competitive processes for the reduction of $\mathrm{Se^{4+}}$ and the dominant one depends on the potential (since it influences the concentration of $\mathrm{Se^{2-}}$) and the concentration of $\mathrm{Se^{4+}}$. At low $\mathrm{Se^{4+}}$ concentrations the 6-electron transfer 8.2 dominates. If the concentration of $\mathrm{Se^{4+}}$ is higher the comproportionation reaction 8.3 is accelerated and the combination of both processes (8.2 followed by 8.3) corresponds to a net charge transfer of four electrons per deposited Se atom. Kazacos showed this in a RDE study where the slopes of the limiting currents (vs. $\sqrt{\omega}$) for a high and low diluted $\mathrm{H_2SeO_3}$ solution give the ratio $6/4$ [86].

[1] For simplicity the ions $\mathrm{Se^{4+}}$ and $\mathrm{Se^{2-}}$ are sometimes written instead of $\mathrm{H_2SeO_3}$ and $\mathrm{H_2Se}$ in the further discussion, although they are not the stable species in the used bath.

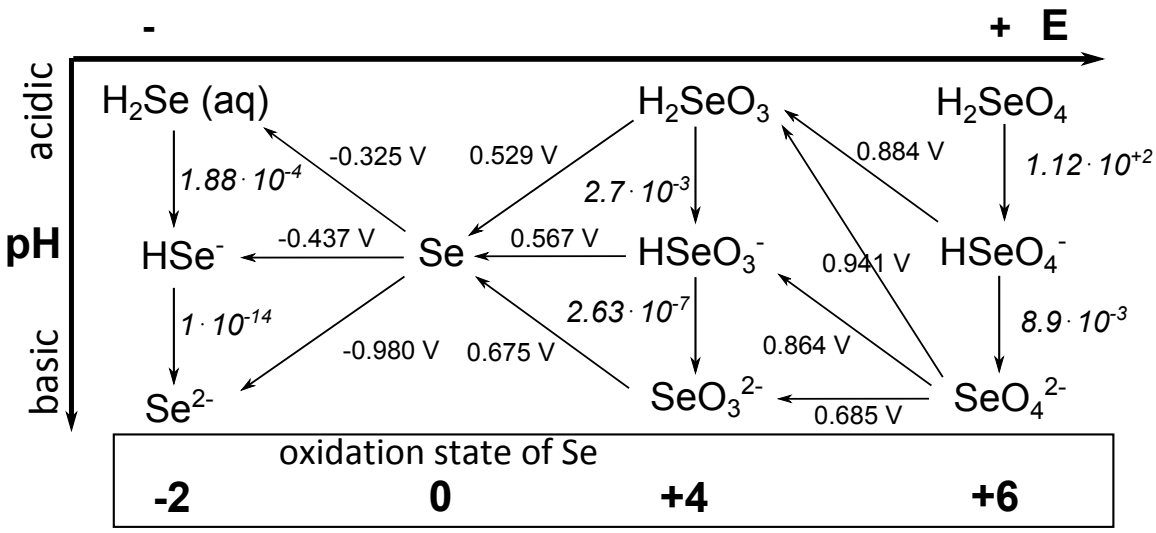

Figure 8.1.: Selenium species in aqueous solution. The bold numbers show the oxidation state of the column. Species on the top left are dominant at acidic conditions and negative potentials, whereas species on the bottom right are dominant in alkaline solutions at positive potentials. Dissociation constants K are italic. The concentration of the species is described by K through $\log \frac{[H_{(x-1)}A^{n-}]}{[H_xA^{(n+1)-}]} = \log K + \mathrm{pH}$ because each step is a single proton transfer [80]. The standard reduction potentials are in normal font and have been taken from [68]. They refer to a Ag | AgCl | $3\,\mathrm{M}$ KCl reference electrode at $25\,^\circ\mathrm{C}$ (appendix D).

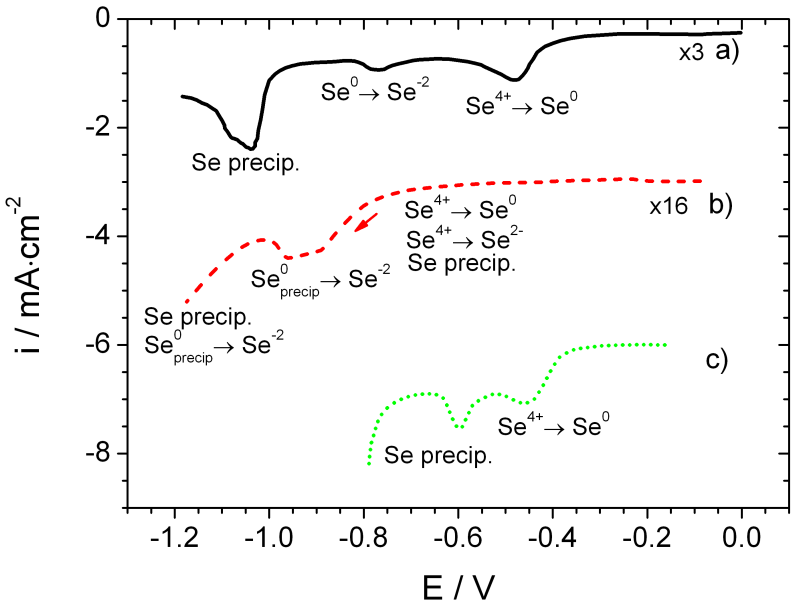

Figure 8.2.: Linear sweep voltammograms of $\mathrm{H_2SeO_3}$ from literature. a) Wei et al., $4\,\mathrm{mM}$ $\mathrm{SeO_2}$ in $500\,\mathrm{mM}$ $\mathrm{Na_2SO_4}$ on Au, $5\,\mathrm{mV/s}$ [85]; b) Pezzatini et al., $0.8\,\mathrm{mM}$ $\mathrm{Na_2SeO_3}$ in pH 9.3 buffer ($\mathrm{HClO_4}$, $\mathrm{NH_3}$) on Ag, $2\,\mathrm{mV/s}$ [87]; c) Massaccesi et al., $1\,\mathrm{mM}$ $\mathrm{H_2SeO_3}$ in $100\,\mathrm{mM}$ $\mathrm{K_2SO_4}$ at pH 3.45 on tin oxide, $10\,\mathrm{mV/s}$, $80\,^\circ\mathrm{C}$ [1]. The current densities of a) and b) have been multiplied by 3 and 16. $-3\,\mathrm{mA/cm^2}$ offset between CVs.

For the interpretation of cyclic voltammograms the orientation of the working electrode is important. In case of a "face-down" geometry the red Se precipitate by reaction 8.3 sediments away from the electrode and does not further contribute to the current whereas in case of a "face-up" set up the red Se precipitate sediments onto the working electrode and will be involved in further reduction and oxidation processes [85].

Wei et al. studied cyclic voltammograms in combination with a electrochemical quartz crystal microbalance (EQCM) or a rotating ring disc electrode (RRDE) onto a gold surface at room temperature in a face-up geometry (figure 8.2, curve a) [85]. Their bath contains $4\,\mathrm{mM}\ \mathrm{SeO_2}$ in $0.5\,\mathrm{M}$ $\mathrm{Na_2SO_4}$ and the scan rate was $5\,\mathrm{mV/s}$. At more positive potentials they observe a mass augmentation due to underpotential electrodeposition of Se by the 4-electron transfer 8.1. At $-0.48\,\mathrm{V}$ an increase of current density is accompanied with a stronger mass uptake. This is attributed to the ongoing 4-electron reduction 8.1 and additionally the onset of the 6-electron transfer reaction 8.2 which is coupled with the comproportionation reaction 8.3 and provides a further channel of Se "deposition" by sedimentation in a "face-up" geometry. Another wave in the CV occurs at $-0.77\,\mathrm{V}$ when the red Se is further reduced to Se^{2-}. At first this reaction is well balanced with reaction 8.3 in which Se^{2-} is consumed and red Se is created and in sum little mass change is detected. Below $-1.04\,\mathrm{V}$ Se reduction dominates and the film is stripped completely. It is noted that the anodic stripping of Se into Se^{4+} requires very positive potentials above $+1.0\,\mathrm{V}$. The visual appearance of films deposited at more negative potentials changes from grey to red and supports the onset of formation reaction 8.3. RRDE experiments show the importance of reaction 8.3. Se^{2-} ions that have been cathodically stripped of the RRDE disc are oxidised at the RRDE ring when no Se^{4+} is added in the electrolyte. Addition of Se^{4+} enables reaction 8.3, consumes Se^{2-}, and the oxidation current at the ring drops [85].

So far only "noble" substrates (e.g. Au, Pt) have been considered which are not involved in the Se reactions. For reactive substrates (e.g. Cu, Ag, Hg) the reduction of Se^{4+} includes the electrode material [86, 87]:

$$2\,\mathrm{M} + \mathrm{H_2SeO_3} + 4\,\mathrm{H^+} + 4\,\mathrm{e^-} \longrightarrow \mathrm{M_2Se} + 3\,\mathrm{H_2O} \tag{8.4}$$

with M = Cu or Ag. The metal selenide is formed by reaction 8.4 until the rate of metal ion diffusion through the selenide film limits the process and the known Se^{4+} reductions 8.1 and 8.2 take over. The potential of Se^{4+} reduction is shifted to more positive potentials in the presence of reactive metals since the chemical reaction provides an additional driving force [86]. In addition also a corrosion of the non-noble substrate can be observed (section 8.1.2).

Cyclic voltammograms of $0.8\,\mathrm{mM}\ \mathrm{Se}^{4+}$ in a pH 9.3 ammonia buffer on silver substrates have been recorded by Pezzatini et al. and combined with EQCM measurements (figure 8.2, curve b) [87]. The scan rate was $2\,\mathrm{mV/s}$. The principle results are in agreement with Wei et al. [85]. Additionally Pezzatini et al. observed the formation of $\mathrm{Ag_2Se}$ when they kept the electrode at $-0.10\,\mathrm{V}$ prior the CV scan. This film is reduced to Ag and $\mathrm{H_2Se}$ at the beginning of the CV for potentials between $-0.10\,\mathrm{V}$ and $-0.60\,\mathrm{V}$. Below $-0.60\,\mathrm{V}$ current density and deposited mass increase which is assigned to Se deposition by the 4-electron process 8.1 and the sedimentation of Se formed by the chemical reaction 8.3 which follows the 6-electron transfer 8.2. The red Se is stripped by reduction to Se^{2-} around $-1.0\,\mathrm{V}$. For potentials below $-1.4\,\mathrm{V}$ no mass change is observed anymore, because all red Se is directly reduced to Se^{2-}.

A cyclic voltammogram at $82\,^\circ\mathrm{C}$ for a $1\,\mathrm{mM}\ \mathrm{H_2SeO_3}$ in $100\,\mathrm{mM}\ \mathrm{K_2SO_4}$ and $10\,\mathrm{mM}\ \mathrm{H_2SO_4}$ on tin oxide was recorded with a scan rate of $10\,\mathrm{mV/s}$ by Massaccesi et al. (figure 8.2, curve c) [1]. In comparison to the CV at room temperature having just one wave at $-0.56\,\mathrm{V}$ they observe two waves at $-0.46\,\mathrm{V}$ and $-0.60\,\mathrm{V}$ at the elevated temperature. Depositions show a grey adhesive deposit without electrode passivation at $-0.46\,\mathrm{V}$ for $82\,^\circ\mathrm{C}$ suggesting the formation of an elemental Se film by reaction 8.1. At $-0.76\,\mathrm{V}$ a red suspension in the electrolyte is observed attributed to the comproportionation reaction 8.3 while the grey deposit on the electrode stays very thin with time. Deposition at $-0.46\,\mathrm{V}$ for $22\,^\circ\mathrm{C}$ results in a very thin orange deposit and a fast passivation of the electrode.

In summary all authors report the deposition of elemental Se by the 4-electron-transfer (reaction 8.1) at less negative potentials. Going further negative the formation of Se^{2-} by the 6-electron-transfer (reaction 8.2) sets in which forms elemental Se by reaction 8.3. Any elemental Se deposited or sedimented on the electrode can be reduced into Se^{2-} at very negative potentials and react again with Se^{4+} to form further elemental Se. The dominant reaction depends on the concentration of each Se species.

8.1.2. Corrosion of copper in selenous acid solutions

The reduction of Se^{4+} on a non-noble electrode material like Cu is given by reaction 8.4 [51]. However it is also possible that Cu will corrode in a selenous acid solution. In corrosion an anodic and a cathodic reaction happen at the electrode surface at the same time. Therefore the oxidation of a metal can proceed without an external current.

The corrosion of Cu in selenous acid solutions has been studied by Villalvilla and Velasco [88]. They determined the dependence of the corrosion rate with $\mathrm{H_2SeO_3}$ concentration, pH value, and temperature. The corresponding coefficients are

$$\left(\frac{\delta \lg\left(\tau^{-1}\right)}{\delta \lg c_{\mathsf{H}^+}}\right)_{c_{Se},T} = 1 \qquad \left(\frac{\delta \lg\left(\tau^{-1}\right)}{\delta T^{-1}}\right)_{c_{Se},c_{H^+}} = -1.74 \qquad \left(\frac{\delta \lg\left(\tau^{-1}\right)}{\delta \lg c_{\mathsf{Se}}}\right)_{c_{H^+},T} = 1.3 \quad (8.5)$$

τ is the time in s for the complete reaction of a $4.9\,\mu\mathrm{m}$ thick film of copper. T is the temperature in $10^{-3}\,\mathrm{K}$. c_{H^+} and $c_{\mathsf{Se}}$are the concentrations of H^+ and $\mathrm{H_2SeO_3}$ in $\mathrm{mol/l}$. The reaction time for $c_{\mathsf{Se}} = 1\,\mathrm{mM}$, $T = 298\,\mathrm{K}$, pH $= 1.8$ is about $87000\,\mathrm{s}$. At high reaction rates $\alpha - \mathrm{Cu_2Se}$ is the dominant phase which is formed. At slower rates a mixture $\alpha -$ CuSe and $\mathrm{Cu_{2-x}Se}$ dominates [88].

8.1.3. Electrodeposition of selenium

Selenium exists in several allotropes [89]. The most stable allotrope at ambient conditions is hexagonal (or also called trigonal) selenium which has a grey colour. It is a semiconductor with a bandgap of $1.8\,\mathrm{eV}$ at room temperature and often applied in optoelectronic devices due to its photoconductivity. The resistivity at room temperature is between 10^5 and $10^6\,\Omega\mathrm{cm}$ [90]. Hexagonal Se consists of spiral Se chains that are oriented along the c-axis of the hexagonal unit cell [91, 92]. Another allotrope is monoclinic Se which shows 3 polymorphs (α, β, and γ). They are red and form Se_8 rings which differ in their bond lengths [92]. Further crystalline allotropes are rhombohedric Se_6 rings, orthorhombic and cubic Se [89]. Despite the crystalline allotropes Se also exists in amorphous forms that can be red, brown or black. Amorphous Se is also a semiconductor with a bandgap of $1.7\,\mathrm{eV}$ and a high ohmic resistivity between 10^{12} and $10^{16}\,\Omega\mathrm{cm}$ [91][2]. Another non-crystalline allotrope of Se is vitreous Se which is formed by rapid cooling of the melt. It is black and consists of mixture of different sized rings and chains. This is the ordinary commercial form of Se [92, 89].

The formation of purely crystalline grey films without amorphous red Se is dependent on the appropriate choice of electrodeposition conditions. Von Hippel and Bloom presented possible parameter ranges for the deposition of crystalline grey Se films [94, 95]. They use $\mathrm{SeO_2}$ as selenium source. The concentration of $\mathrm{SeO_2}$, the pH value, and the temperature are key parameters in the deposition of hexagonal Se. The tendency to form crystalline Se is increased at high $\mathrm{SeO_2}$ concentrations (above $1\,\mathrm{M}$), very low pH values (e.g. $18\,\mathrm{N}\ \mathrm{H_2SO_4}$), and high temperatures close to $100\,°\mathrm{C}$. Although grey Se can also be electrodeposited without the addition of acid at temperatures higher than $50\,°\mathrm{C}$ the increase of acidity is in general preferred, because it allows the electrodeposition of crystalline Se at higher current densities. On the other hand it is also possible to deposit grey Se at room

[2] The specific resistivities of hexagonal and amorphous seem to be strongly dependent on the deposition conditions, because for electrodeposited films a resistivity of $1\,\Omega\mathrm{cm}$ for hexagonal Se and $10^5\,\Omega\mathrm{cm}$ for amorphous Se have been reported [93]. Since hexagonal Se is a semiconductor the large deviation in resistivity could be explained by a larger defect density for electrodeposited material.

temperature if the pH value is sufficiently low, but again the allowed current density is lower than in case of an optimisation of pH value and temperature. If the current density in the galvanostatic deposition mode exceeds a critical value an additional deposition of red amorphous Se is observed or the formation of hydrogen bubbles cause pits on the surface.

Graham et al. studied the electrodeposition of amorphous selenium films [96]. They restricted temperatures to $5 - 45\,°C$ in order to avoid the formation of crystalline phases. The bath includes $1\,g/l$ sodium lauryl sulphate as a wetting agent that must be dissolved in water before $350\,g/l\ SeO_2$ is added. The pH value of the final bath is $0.7 - 0.9$. Best deposits could be obtained if the cathode was previously plated with a $250\,\mu m$ thick bright nickel coating and galvanostatic deposition was carried out at current densities between 1 and $4\,mA/cm^2$. The amorphous Se deposits appeared smooth, glossy black and well adherent. A thickness of $30\,\mu m$ could be obtained without indication for a further restriction. A certain amount of red Se precipitate formed in the bath during plating.

The Se plating bath used in this thesis is similar to the one of Massaccesi et al. [1]. Instead of a pH 2 buffer they added $0.01\,M$ sulphuric acid as background electrolyte. At room temperature deposits were orange and insulating whereas at $82\,°C$ they looked grey and no passivation was observed. Cattarin et al. did a detailed study on the passivation process of Se electrodeposition on titanium substrates [93]. They assign the passivation in the Se electrodeposition process to the high resistivity of the Se film. The conductivity of Se depends on the conditions of the plating process (e.g. electrolyte temperature or addition of a surfactant influencing the morphology). In contrast to typical anodic passivation which requires the transport of an ionic species across the film, the passivation caused by the Se layer requires only the transport of electrons through the film. While the passivising layer in typical anodic passivation processes is only a few nanometres, the thickness of the Se film can reach several hundred nanometres. Cattarin et al. obtained limiting thicknesses from $25\,nm$ (at $25\,°C$) to $650\,nm$ (at $60\,°C$) until the current seized due to electrode passivation [93]. Since they were working with a much higher concentration of $3\,M\ SeO_2$ their current density drops to zero in less than a minute. The deposition charge at $90\,°C$ increases to 55 times the room temperature value before passivation.

8.2. Results and Discussion

8.2.1. Electrochemistry of selenium

Although the electrochemistry of selenium is complex due to its several oxidation states, the recorded cyclic voltammogram shows only a few features (figure 8.3). A continuous darkening of the Mo surface can be observed when scanning the voltage from open circuit potential ($+0.05\,V$) to $-0.50\,V$. Grey Se films are deposited at these potentials (figure 8.6). In accordance with the literature (see section 8.1.1) [85, 87, 1] the Se electrodeposition is a result of the 4-electron transfer $Se^{4+} + 4\,e^- \longrightarrow Se^0$ (reaction 8.1). The onset of Se deposition at $+0.05\,V$ shows the necessity of a high overpotential, because the standard potential for $H_2SeO_3 + 2\,H_2 \longrightarrow Se + 3\,H_2O$ is $+0.53\,V$ (figure 8.1). Below $-0.50\,V$ a shoulder can be seen in the CV before hydrogen evolution dominates. This shoulder is accompanied by a red precipitate that evolves at the electrode. At the same time the appearance of the electrode surface changes back to molybdenum. At these potentials no Se films can be deposited and the molybdenum surface stays blank. The cathodic stripping of the Se film is caused by a further reduction of Se^0 into Se^{2-}. The resulting Se^{2-} ions can react with further Se^{4+} ions from the bath and form elemental red Se by the comproportionation reaction 8.3. This is the explanation for the parallel occurrence of a red colloidal precipitate [1].

The existence of a Se film on the electrode is not necessary for the formation of the precipitate in solution. It is also observed on a blank Mo substrate. In this case the presence of Se^{2-} is either explained by the ongoing Se^0 deposition through the 4-electron transfer followed by a further reduction into Se^{2-} or by direct reduction of Se^{4+} into Se^{2-} via the 6-electron transfer 8.2. Previous studies in the literature of cyclic voltammograms in combination with an EQCM have proposed the

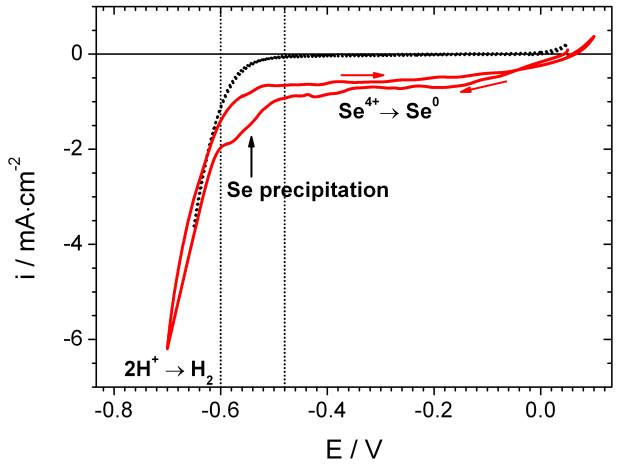

Figure 8.3.: Cyclic voltammogram of $1\,\mathrm{mM}\ \mathrm{Se}^{4+}$ at $80\,°\mathrm{C}$ on a stationary Mo substrate (scanning speed $10\,\mathrm{mV/s}$) . The dotted voltammogram has been recorded in the background electrolyte ($100\,\mathrm{nm}\ \mathrm{K_2SO_4}$, pH 2 buffer, table 6.1) without Se precursor. The shallow waves can be assigned to thermal convection in the bath due to the elevated temperature. Three ranges can be identified. At potentials above $-0.49\,\mathrm{V}$ Se is electrodeposited. Below this potential red Se precipitate is formed by reaction 8.3. Further negative hydrogen evolution sets in.

presence of both mechanisms at very negative potentials (section 8.1.1) [87, 85]. From the standard potentials it is expected that the mechanism $\mathrm{Se}^{4+} + 6\,\mathrm{e}^- \longrightarrow \mathrm{Se}^{2-}$ already sets in at $+0.24\,\mathrm{V}$ whereas the mechanism $\mathrm{Se}^0 + 2\,\mathrm{e}^- \longrightarrow \mathrm{Se}^{2-}$ requires a potential of $-0.33\,\mathrm{V}$ (see figure 8.1). That means if both mechanisms are present between $-0.50\,\mathrm{V}$ and $-0.60\,\mathrm{V}$ a large activation overpotential is necessary for the 6-electron transfer reaction to take place. This has already been observed for the plating of elemental Se and therefore it can be concluded that the kinetics of Se^{4+} reduction are very sluggish. When the deposited Se film is completely consumed the current density decreases and a maximum is observed at $-0.60\,\mathrm{V}$ which is degenerated to a shoulder, because hydrogen evolution rises sharply for more negative potentials. The hydrogen evolution reaction is confirmed by the observation of bubbles. The current density of the reverse scan above $-0.50\,\mathrm{V}$ is close to the forward scan and corresponds again to Se electrodeposition by Se^{4+} reduction.

	100 s	**10 s**	**5 s**
charge deposited before CV	56	25	4
charge between -0.4 V and 0 V	34	61	71
total charge of Se deposition	90	86	75

Table 8.1.: Charge densities in $\mathrm{mC/cm^2}$ for the cyclic voltammograms in figure 8.4. The first row shows the passed charge when Se was deposited at $-0.30\,\mathrm{V}$ before the CV was started. The second row shows the charge passed during the Se deposition maximum around $-0.20\,\mathrm{V}$ in the CV.

Cathodic stripping is confirmed in figure 8.4. Se films of several thicknesses have been electrodeposited on a Mo substrate before the CV starts. At the beginning of the scan a maximum appears around $-0.20\,\mathrm{V}$ when Se is electrodeposited in the 4-electron transfer process. It will be shown in section 8.2.3 that elemental Se passivises the surface which causes the decrease of current for potentials more negative than $-0.20\,\mathrm{V}$. Due to the 10 times higher Se^{4+} concentration in the bath than in figure 8.3 the Se film grows faster and the surface is passivated already before the stripping

potential is reached. The amount of charge that passes during the Se deposition maximum seems to be higher without initial Se coating. Adding the charge that passed in the initial coating of the sample and the charge of the $-0.20\,\mathrm{V}$ deposition maximum in the CV leads to similar values for all samples (table 8.1). This confirms the passivising effect of the Se layer. Although one sample has been kept at the deposition potential several times longer than the other sample the same amount of material has been electrodeposited for both, because passivation ends the process when a certain thickness is reached. At $-0.46\,\mathrm{V}$ a sharp increase of current is observed, when the Se film is cathodically stripped. This is accompanied by strong Se precipitation from the electrode surface.

In summary the cyclic voltammograms of Se under the studied conditions behave similar to the ones from the literature (section 8.1.1). At more positive potentials elemental Se can be electrodeposited by the 4-electron transfer 8.1 [1, 85]. Below $-0.50\,\mathrm{V}$ Se^0 is further reduced to Se^{2-} which forms red Se precipitate through reaction 8.3. Additionally the 6-electron reduction 8.2 of Se^{4+} might be present. Our voltammograms show less features than other works [87, 85], because our electrode is mounted "face-down" and the red precipitate does not interfere in the further scan. The kinetics of Se electrochemistry are slow and an overpotential of several hundred mV is necessary for $\mathrm{H_2SeO_3}$ reduction. In addition the electrodeposited Se film passivates the electrode surface and decelerates the kinetics further.

8.2.2. Diffusion coefficient of Se^{4+}

A Mo electrode is not the best choice to determine the diffusion coefficient of Se. In the potential range of Se deposition the passivation of the electrode makes the determination of a limiting current difficult. Measuring in the range of cathodic stripping has other disadvantages. First it is already close to hydrogen evolution that might interfere. Second it has to assume all Se^{2-} formed by the 6-electron process is consumed in reaction 8.3 to allow the description by an effective 4-electron process. If the reaction is incomplete the effective charge transfer per Se atom is undefined between $4\,\mathrm{e}$ and $6\,\mathrm{e}$ [86].

Therefore the diffusion coefficient was determined with a Cu electrode, because its reaction with Se^{4+} according to 8.4 makes it possible to determine the limiting current over a wide potential range (see figure 8.5) [51]. However it must be considered that the copper substrate will also corrode in the selenous acid bath. Therefore a part of the incoming Se^{4+} will be consumed without giving a current response at the electrode. The reaction rate of corrosion can be estimated from the coefficients in section 8.1.2. In a $1\,\mathrm{mM}$ $\mathrm{H_2SeO_3}$ solution at $80\,°\mathrm{C}$ and pH $= 2$, a $4.9\,\mu\mathrm{m}$ thick copper film will corrode in about $17000\,\mathrm{s}$. The current density in figure 8.5 is at least $2\,\mathrm{mA/cm^2}$. According to this current and reaction 8.4 it will take about $5200\,\mathrm{s}$ to consume a $4.9\,\mu\mathrm{m}$ thick film of copper. For higher rotation speeds of the electrode meaning higher current density the time will be shorter. It is expected that the corrosion rate will decrease if the competitive reaction 8.4 occurs at the same time. Therefore it can be assumed that reaction 8.4 is still dominant and valid to calculate the diffusion coefficient. This is supported by the fact that the current density in figure 8.5 is linear with a small intercept.

Above $-0.70\,\mathrm{V}$ the cyclic voltammogram shows the formation of $\mathrm{Cu_2Se}$ described by reaction 8.4. Below $-0.70\,\mathrm{V}$ the surface becomes light grey and red Se precipitation occurs. That could indicate a further reduction of $\mathrm{Cu_2Se}$ leading to elemental copper and Se^{2-} ions which cause the red precipitate by reaction with Se^{4+}. Additionally the appearance of gas bubbles could indicate the onset of the hydrogen evolution reaction. Between $-0.45\,\mathrm{V}$ and $-0.50\,\mathrm{V}$ the average limiting current density has been determined. A diffusion coefficient of $(25 \pm 2) \cdot 10^{-6}\,\mathrm{cm^2/s}$ results from the slope of the Levich plot for Se^{4+} at $80\,°\mathrm{C}$. This translates into a Walden product $\eta \cdot D \cdot \frac{1}{k_B T}$ of $1.8 \cdot 10^{8}\,\mathrm{m^{-1}}$. Massaccesi et al. determined the diffusion coefficient of Se^{4+} at room temperature by using a Cu-RDE. Instead of the pH 2 buffer in our case they adjusted the pH value to 2.45 with sulphuric acid. The obtained diffusion coefficient was $(9.2 \pm 0.5) \cdot 10^{-6}\,\mathrm{cm^2/s}$ or a Walden product of $2.0 \cdot 10^{8}\,\mathrm{m^{-1}}$ that is close to our value [51].

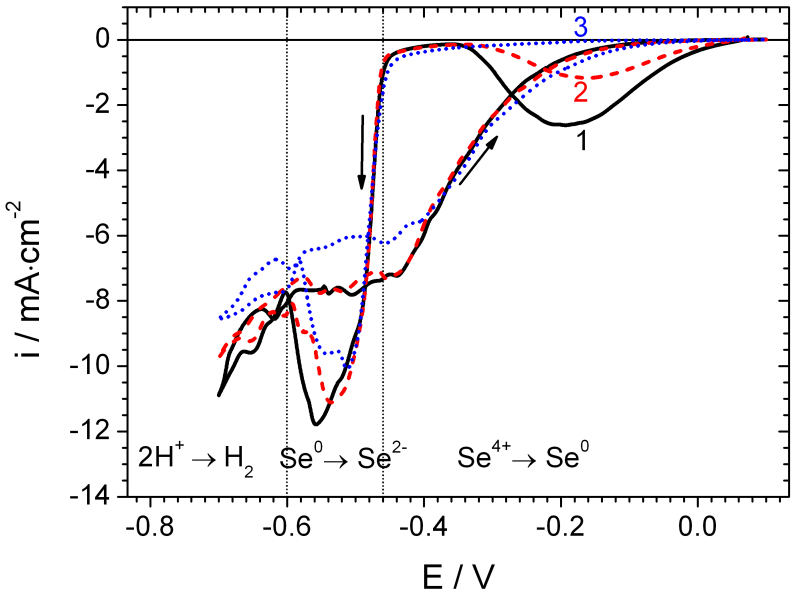

Figure 8.4.: Cyclic voltammograms of $10\,\mathrm{mM}\ \mathrm{Se}^{4+}$ at $80\,°\mathrm{C}$ on a Se capped Mo electrode (scan rate $10\,\mathrm{mV/s}$). The Se film has been plated onto the Mo substrate in the same bath at a potential of $-0.30\,\mathrm{V}$ for 1) $5\,\mathrm{s}$, 2) $10\,\mathrm{s}$ and 3) $100\,\mathrm{s}$. Depositions and CVs were performed without rotation of the electrode. The shallow waves at negative potentials are due to thermal convection.

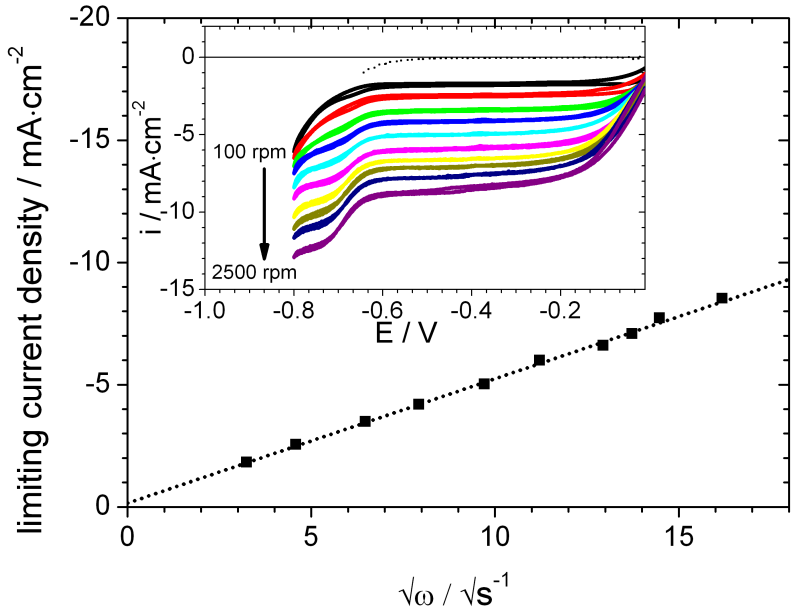

Figure 8.5.: Levich plot of $1\,\mathrm{mM}\ \mathrm{Se}^{4+}$ on a Cu RDE. The copper substrate reacts with Se^{4+} according to reaction 8.4. The limiting current densities have been obtained from the average current density between $-0.50\,\mathrm{V}$ and $-0.45\,\mathrm{V}$ of the cyclic voltammograms shown in the onset. The dotted line shows the current density in the background electrolyte. The rotation speeds are 100, 200, 400, 600, 900, 1200, 1600, 1800, 2000, 2500 min^{-1}. temperature: $80\,°\mathrm{C}$, scan rate: $50\,\mathrm{mV/s}$

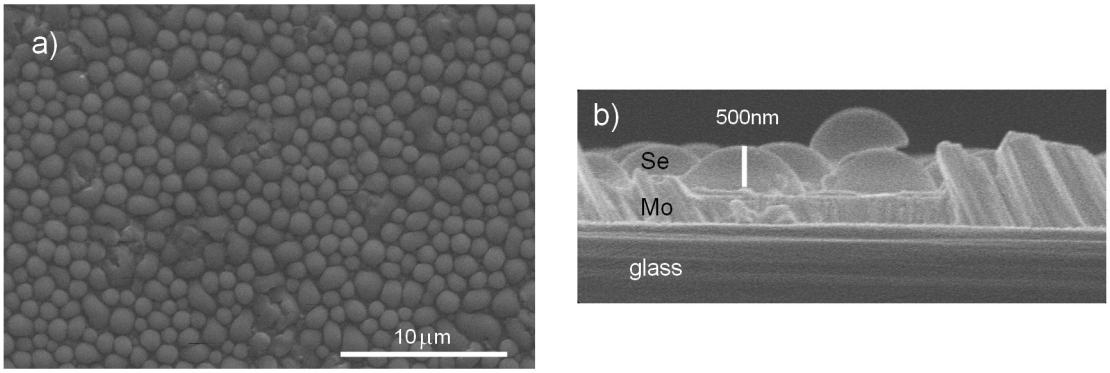

Figure 8.6.: SEM pictures of selenium films on glass / Mo substrates, deposited at $-0.30\,\mathrm{V}$ from $1\,\mathrm{mM}\ H_2SeO_3$ bath at $80\,°\mathrm{C}$. Deposition were done on a RDE at $100\,\mathrm{rpm}$. (a) top view and (b) cross section. The structured pieces on the left and right side in b) are remains from the breaking of the substrate.

8.2.3. Electroplating of selenium

The passivation observed in the cyclic voltammograms of Se (e.g. figure 8.4) directly effects the electroplating of Se films. In a standard metal electrodeposition the current density reaches a steady state value after a certain time. For Se deposition from the present deposition bath the current density decreases continuously with time until it is close to zero (figure 8.7). At $80\,°\mathrm{C}$ the deposited mass calculated from the charge is $120\,\mu\mathrm{g/cm^2}$. The film has a brownish colour with aspects of grey and red. The results differ from the observation of Massaccesi et al. who report no electrode passivation at $80\,°\mathrm{C}$ when depositing on a stationary electrode (section 8.1.3) [1]. This discrepancy can be explained by the fact that the passivation at $1\,\mathrm{mM}$ without rotation is slow. In this case (not shown) it takes about $30\,\mathrm{min}$ until the current density has decreased from its initial value ($0.7\,\mathrm{mA/cm^2}$) below $0.1\,\mathrm{mA/cm^2}$ and thus Massaccesi et al. would not see an electrode passivation.

The microscopic morphology of the film deposited under rotation consists of hemispheres (figure 8.6). The film thickness is about $500 - 550\,\mathrm{nm}$ determined from SEM cross sections which roughly agrees with $490\,\mathrm{nm}$ calculated from the deposited charge[3] .

The deposited charge limited by passivation of the electrode increases when the temperature of the deposition bath rises from room temperature to $80\,°\mathrm{C}$ (figure 8.7). However the increase in deposition charge with higher temperature is less pronounced then reported by Cattarin et al. (section 8.1.3) [93]. In figure 8.7 the deposited charge at $80\,°\mathrm{C}$ is 8 times more than at room temperature, while Cattarin et al. observe 55 times more charge at a similar temperature. Above $80\,°\mathrm{C}$ the deposited charge decreased again. The higher temperature can lead to a different growth of the layer that effects the morphology of the film. A different morphology can influence the passivation. The colour of the films changes with their deposition temperature. At room temperature they were shiny blue, which is probably an interference effect due to their small thickness ($30 - 40\,\mathrm{nm}$ are calculated from the deposition charge, assuming a compact film). At $60\,°\mathrm{C}$ the films were dull and dark red with some grey aspect. At $80\,°\mathrm{C}$ and above the films where light grey and dull. The expectation that the red and grey films are different allotropes of Se is confirmed by XRD diffractograms (not shown). The layers deposited at $80\,°\mathrm{C}$ show the reflections of trigonal Se. The ones plated at $60\,°\mathrm{C}$ do not show any reflections meaning that they are amorphous.

In summary it has been shown that the passivation of the electrode during the Se plating limits the thickness of the film which can be obtained under the given conditions. The passivation is slow and takes several minutes depending on the bath temperature. It can be assumed that the passivation is caused by the high resistivity of the deposited Se layer which causes a potential drop

[3]The thickness was calculated using the density of trigonal Se $4.82\,\mathrm{g/cm^2}$ [89] and considering that the volume ratio between a hemisphere and its surrounding cuboid is $\pi/6$.

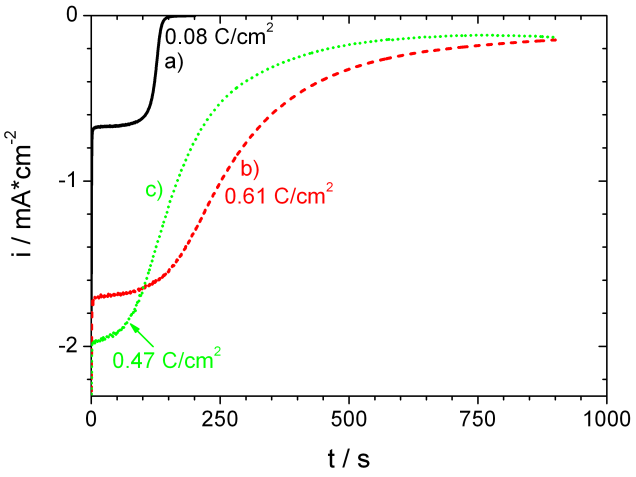

Figure 8.7.: Transient current densities of selenium films on glass / Mo substrates, deposited from $1\,\mathrm{mM}$ H_2SeO_3 at $-0.30\,\mathrm{V}$. The bath temperature is a) $25\,°\mathrm{C}$, b) $80\,°\mathrm{C}$, and c) $93\,°\mathrm{C}$. All platings were done at a RDE rotation speed of $100\,\mathrm{rpm}$. The electrode rested at open circuit potential for about $20\,\mathrm{s}$ before the deposition potential was applied.

across the film (section 8.1.3). The resistivity of the film is dependent on the plating conditions, e.g. the temperature of the electrolyte. Especially the phase transition from amorphous Se deposited at $60\,°\mathrm{C}$ to hexagonal Se deposited at $80\,°\mathrm{C}$ will decrease the resistivity of the film (section 8.1.3) which reduces the potential drop across the film and thus allows the plating of thicker layers. The results in this section are in agreement with the literature. Massaccesi et al. have reported the change from an amorphous red Se film at room temperature to a conductive grey Se film at $80\,°\mathrm{C}$ deposition temperature [1]. Hexagonal Se can be plated from the bath described in table 6.1 (without $In_2(SO_4)_3$) at a potential of $-0.30\,\mathrm{V}$ and a rotation rate of $100\,\mathrm{rpm}$ at $80\,°\mathrm{C}$. The deposit consist of densely packed Se hemispheres.

9. Copper selenide plating

A layer of copper selenide is part of the electrodeposited binary selenide precursor stack. This chapter studies possible plating conditions for the formation of copper selenide. The composition, structure and phase of the films are analysed and a candidate for the complete binary selenide stack is identified.

9.1. Background

The phases of copper selenide exist with the following compositions: $\mathrm{CuSe_2}$, CuSe , $\mathrm{Cu_3Se_2}$ [1], and $\mathrm{Cu_{2-x}Se}$ (section 14.2).

The formation of copper selenide is linked to a negative change in Gibbs energy. This enables its electrodeposition at potentials which are more positive than the less noble element (section 5.6). In the present case $\mathrm{Se^{4+}}$ is the noble element (standard potential $+0.53\,\mathrm{V}$) and $\mathrm{Cu^{2+}}$ the less noble one ($+0.13\,\mathrm{V}$) [68]. Indeed a shift of the onset potential towards more positive values is observed, when $\mathrm{Se^{4+}}$ is added to a $\mathrm{Cu^{2+}}$ solution. The shift increases the more $\mathrm{Se^{4+}}$ is added and the deposition of copper selenide can take place at positive potentials where neither $\mathrm{Cu^{2+}}$ nor $\mathrm{Se^{4+}}$ can be reduced alone [98, 57]. In case of Se this is an effect of the high overpotential which is necessary for deposition. From the very positive standard potential of $\mathrm{Se^{4+}}$ one would assume that it is possible to reduce $\mathrm{Se^{4+}}$ at potentials above the onset of copper selenide. However a deposition of Se is not observed, because of its sluggish kinetics and the fast passivation of the electrode at room temperature. The presence of Cu seems to be necessary to allow Se reduction [51, 50]. The high overpotential of selenium even allows the reduction of $\mathrm{Cu^{2+}}$ or $\mathrm{Cu^{+}}$ (standard potential $+0.31\,\mathrm{V}$ [68]) to take place at more positive potentials than the reduction of $\mathrm{Se^{4+}}$ although this is not expected from the standard equilibrium potentials. In contrast to the plating of selenium the electrodeposition of copper selenide does not suffer from passivation (section 8.2.3). Murali and Xavier determined the resistivity of a $\mathrm{Cu_2Se}$ thin film electroplated at $80\,°\mathrm{C}$ to be $0.09\,\Omega\mathrm{cm}$ [99] and therefore significantly lower than for amorphous or hexagonal Se (section 8.1.3). $\mathrm{Cu_2Se}$ is a mixed electronic - ionic conductor. The ionic conduction results from the high mobility of Cu-ions in the structure [100].

.

The phase and composition of copper selenide is dependent on the applied potential (figure 9.1). For negative potential below $-0.45\,\mathrm{V}$ $\mathrm{Cu_2Se}$ is the only electrodeposited copper selenide phase [57]. At this potential excess $\mathrm{Se^{4+}}$ is reduced to $\mathrm{Se^{2-}}$ [51] and excess $\mathrm{Cu^{2+}}$ is reduced to elemental Cu [98]. Further negative below $-0.57\,\mathrm{V}$ the deposit is not adherent to the substrate anymore [50]. At potentials above $-0.45\,\mathrm{V}$ the film composition is controlled by the mass fluxes [51]. Finally above $-0.15\,\mathrm{V}$ the reaction kinetics slow down and start to limit the process [50]. In the mass flux controlled regime between $-0.35\,\mathrm{V}$ and $-0.15\,\mathrm{V}$ and for bath concentrations $[\mathrm{Cu^{2+}}]$ and $[\mathrm{Se^{4+}}]$ between $0.1\,\mathrm{mM}$ and $2\,\mathrm{mM}$ Thouin et al. obtain a film composition at room temperature of [50]:

$$\left(\frac{\mathsf{Cu}}{\mathsf{Se}}\right)_{\mathsf{solid}} = 0.69\frac{[\mathsf{Cu}^{2+}]}{[\mathsf{Se}^{4+}]} \tag{9.1}$$

In a similar bath a proportionality factor of 0.80 instead of 0.69 is given [51]. For low flux ratios $r = [\mathrm{Cu^{2+}}]/[\mathrm{Se^{4+}}] < 1.5$ the film consists of CuSe and elemental Se. If $\mathrm{Cu^{2+}}$ is increased the

[1] According to [97] $\mathrm{Cu_3Se_2}$ is outdated and must be replaced by $\mathrm{Cu_5Se_3}$. However even the new diffraction pattern database PDF-4 (2010) from the International Centre for Diffraction Data (ICDD) assigns this phase to $\mathrm{Cu_3Se_2}$. Therefore we stay with $\mathrm{Cu_3Se_2}$ as this is in line with most of the literature.

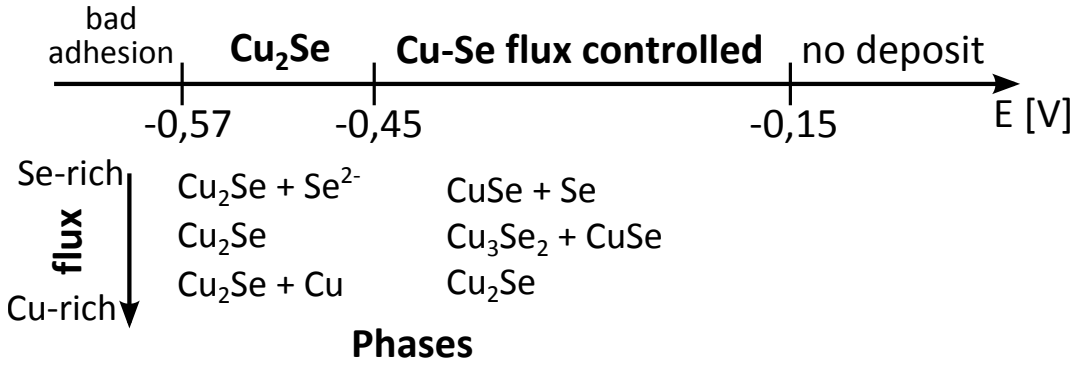

Figure 9.1.: Electrodeposited phases of copper selenide dependent on potential and flux ratio. Above the potential axis the different regimes of copper selenide electrodeposition are labelled. Below the axis the deposited phases are given for Se-rich to Cu-rich fluxes (based on [50, 51]). The existence of a $\mathrm{CuSe_2}$ phase has not been considered in the reference.

formation of $\mathrm{Cu_3Se_2}$ becomes possible and at fluxes $r > 2.2$ also $\mathrm{Cu_2Se}$ is present. The phase of the deposit is also influenced by the electrodeposition temperature. For $r = 2$ Lippkow and Strehblow report only $\mathrm{Cu_3Se_2}$ reflections in XRD if the film is deposited at $25\,°\mathrm{C}$. After some exposure time in the laboratory the film converts into $\mathrm{Cu_2Se}$. In a layer plated at $80\,°\mathrm{C}$ from the same bath $\mathrm{Cu_2Se}$ is already the dominant phase in the as-deposited film. They conclude the electrodeposition of amorphous Se which can react with the deposited $\mathrm{Cu_3Se_2}$ either in the hot bath or during a longer exposure time [101]. Furthermore the pH value can influence the composition of the film. Layers deposited at pH 2.4 from a bath containing $50\,\mathrm{mM}\ \mathrm{CuSO_4}$ and $50\,\mathrm{mM}\ \mathrm{H_2SeO_3}$ consist of $\mathrm{Cu_2Se}$ for all potentials between $-0.77\,\mathrm{V}$ and $-0.17\,\mathrm{V}$. At pH 1.4 the composition changes from Cu/Se $= 0.90$ at $-0.57\,\mathrm{V}$ to Cu/Se $= 0.74$ at $-0.07\,\mathrm{V}$ [22].

A detailed study on the electrochemistry of copper selenide has been performed by Massaccesi et al. who determined the diffusion coefficients of Cu and Se and the kinetic constants of their possible reduction processes. Knowing the kinetics and the mass transport they are able to calculate the phase composition in dependence of the applied voltage for various bath compositions [51].

9.2. Results and Discussion

In contrast to Se plating the deposition of copper selenide can be performed at room temperature, because no electrode passivation is observed. Copper selenide films have been plated from the copper selenide bath given in table 6.1 at $-0.10\,\mathrm{V}$, $-0.20\,\mathrm{V}$, and $-0.30\,\mathrm{V}$ with and without rotation. SEM pictures show a change in surface morphology taking place at $-0.20\,\mathrm{V}$ in the not rotated case (figure 9.2). At more positive potentials the morphology shows a fine grained background with plates of several microns at the surface. For more negative potentials the film consists of a random packing of $0.5\,\mu\mathrm{m}$ sized platelets. This morphology has also been reported by [22].

The morphology of randomly stacked platelets at $-0.30\,\mathrm{V}$ is preserved if the electrode is rotated. Rotation at more positive potentials leads to a film consisting of Cu-rich particles.

For all samples plated between $-0.10\,\mathrm{V}$ and $-0.30\,\mathrm{V}$ the Cu content in the deposit rises in the transition from a stationary to a rotated electrolyte. Since the composition of copper selenide between $-0.45\,\mathrm{V}$ and $-0.15\,\mathrm{V}$ is mass transport controlled (section 9.1) it can be assumed that this due to the change in the ratio of mass flux between $\mathrm{Cu^{2+}}$ and $\mathrm{Se^{4+}}$ if the mass fluxes are controlled by convection instead of diffusion.

Due to the open surface morphology all copper selenide films in figure 9.2 appear completely black. Not all of them turned out as valid candidates for the solar cell precursor. Samples deposited at $-0.10\,\mathrm{V}$ showed insufficient nucleation if the sample diameter exceeded $1\,\mathrm{cm^2}$. In that case the middle of the substrate stayed blank. Rotation of the substrate speeds up the plating, because

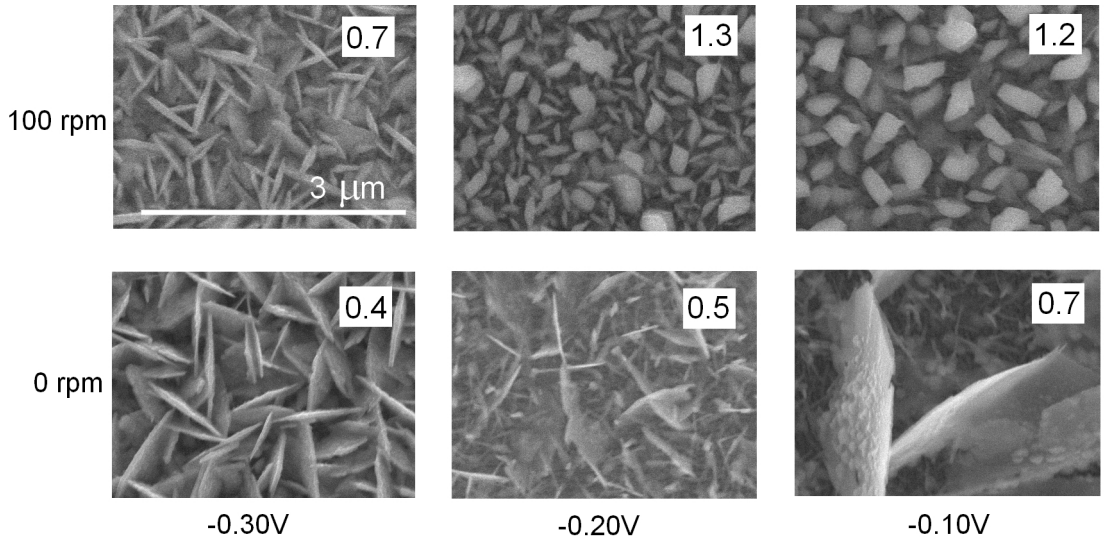

Figure 9.2.: Morphology and composition of copper selenide electrodeposited onto sputtered Mo substrates from a bath containing $2.6\,\mathrm{mM}\ \mathrm{CuCl_2}$ and $5.9\,\mathrm{mM}\ \mathrm{H_2SeO_3}$. Rotation speed of the RDE (rows) and applied potential (columns) have been varied. The scale bar is valid for all pictures. In the corner of each picture is the Cu/Se ratio noted which has been determined by EDX.

the system is mass transport limited. Therefore copper selenide films deposited at $-0.30\,\mathrm{V}$ and a rotation speed of $100\,\mathrm{rpm}$ have been used in the solar cell precursors. The as-deposited films consist of a $\mathrm{Cu_{2-x}Se}$ phase (figure 9.3). The Se-rich composition (figure 9.2) indicates the presence of amorphous Se in the film. An accurate determination of the Cu/Se ratio by inductive coupled plasma - mass spectroscopy (ICP-MS) gives 0.76 ± 0.03 and confirms the value of EDX. The film has been etched in a $0.1\,\mathrm{M}\ \mathrm{Na_2S{\cdot}9\,H_2O}$ solution for $30\,\mathrm{min}$. This etching is known to remove elemental Se phases [75, 76]. Afterwards the Cu/Se ratio has increased to 1.25 ± 0.03 which proves the existence of amorphous Se in our copper selenide layers. Obviously the etching was incomplete and the Cu/Se atomic ratio does not reach the value 1.8 expected from the phase identified in XRD (figure 9.3). It has been reported previously that $\mathrm{Cu_2Se}$ is the only copper selenide phase deposited at very negative potentials. In case of a Se-rich bath excess Se^{4+} is expected to be reduced to Se^{2-} or to be deposited as elemental Se in the layer (section 9.1) [51, 50, 101]. In the first case Se^{2-} and Se^{4+} could react to elemental Se precipitation which is trapped in the open structure of the film. Thus our results are in line with the previous literature.

In summary the composition and morphology of electroplated copper selenide depends on the reduction potential and if the electrode is rotated or stationary. Stable conditions for plating have been found at $-0.30\,\mathrm{V}$ and $100\,\mathrm{rpm}$ RDE rotation. For these parameters the film consists of randomly stacked $\mathrm{Cu_{2-x}Se}$ platelets covered with amorphous Se.

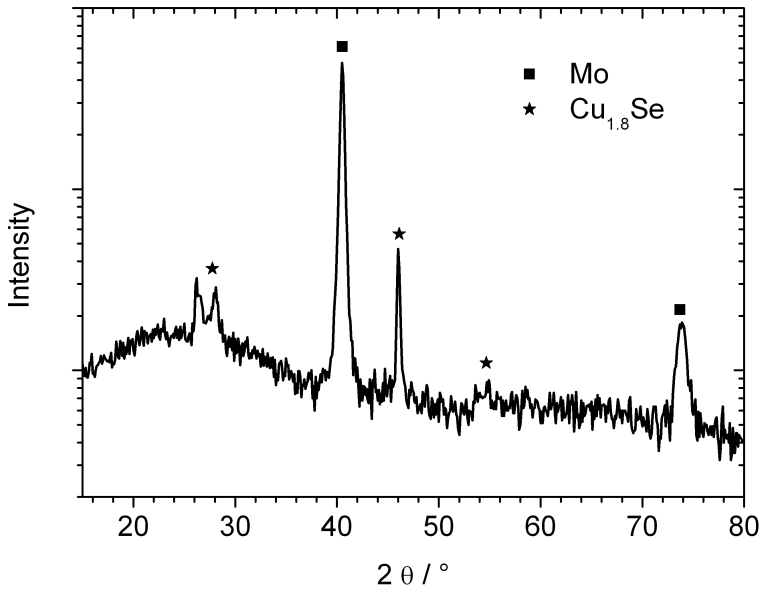

Figure 9.3.: XRD diffractogram of copper selenide electrodeposited at $-0.30\,\mathrm{V}$ and a RDE rotation speed of $100\,\mathrm{rpm}$. The peak at $26.2\,^\circ$ cannot be identified.

10. Electrochemistry of Indium Selenide

Although several procedures for the electroplating of indium selenide have been reported (section 10.1.2) the knowledge of the electrochemistry of indium selenide is still limited (section 10.1.3). Moreover the proposed deposition mechanisms disagree. While Massaccesi et al. propose that indium incorporation is induced by selenium according to the Kröger mechanism (section 5.6) [1], Mishra et al. claim the presence of indium as a prerequisite for indium selenide deposition [57].

The experiments in this chapter provide new insight into the electrochemistry of indium selenide. First the cyclic voltammogram of indium selenide is compared to the ones of the single elements and the interference between the elements is studied. This will be supported by varying the In^{3+} concentration. CVs on a rotating electrode will test the hypothesis if indium selenide is mass transport limited which has been claimed by Massaccesi et al. [1].

The composition of the deposit at different plating conditions (potential, bath composition) will be analysed. The elemental Se content in the films will be a focus, because it allows conclusions on the side reactions in the plating process. The rate of indium selenide formation, elemental Se deposition and Se precipitation in the bath will be evaluated.

10.1. Background

10.1.1. Phases of indium selenide

Indium selenide can occur in the following phases: $\mathrm{In_4Se_3}$, InSe, $\mathrm{In_6Se_7}$, $\mathrm{In_9Se_{11}}$, $\mathrm{In_5Se_7}$, and $\mathrm{In_2Se_3}$ (phase diagram in figure 14.1). Small changes in the composition can lead to a change in structure, because the Se/In atomic ratio of some phases are very close. While $\mathrm{In_4Se_3}$, InSe, and $\mathrm{In_2Se_3}$ are the most studied phases, the structures of $\mathrm{In_9Se_{11}}$ and $\mathrm{In_5Se_7}$ are still unknown [102, 103]. $\mathrm{In_2Se_3}$ [104, 105], InSe [106], $\mathrm{In_4Se_3}$ [107] or a mixture of these phases [108] have been reported for electrodeposited indium selenide films. In addition to these crystalline phases also amorphous indium selenide layers have been obtained by electrodeposition [1, 109].

In contrast to the crystalline phases with well-defined Se/In atomic ratios the composition of amorphous indium selenide can continuously vary in a wide range [110]. Several authors have reported that the local structure in amorphous indium selenide is similar to the structure of an indium selenide crystal with an equivalent composition. Raman measurements of amorphous $\mathrm{In_2Se_3}$ ($\mathrm{a{-}In_2Se_3}$) revealed a short-range structure that is in principal identical with the structure of $\alpha{-}\mathrm{In_2Se_3}$ [111, 112]. This explains their similar electronic behaviour in photoemission experiments.

10.1.2. Indium selenide electrodeposition

Indium selenide electrodeposition is motivated by several applications in the synthesis of $\mathrm{CuInSe_2}$ solar cells. It is either used as part of the precursor stack [31, 23, 34, 35] or it is plated on top of electrodeposited CIGS in order to obtain a Cu-poor surface [113, 114]. It is also applied as an alternative Cd-free buffer layer especially in superstrate cell configuration [115, 116].

There are two major routes for indium selenide electrodeposition. The first one uses a bath containing $25\,\mathrm{mM}$ $\mathrm{H_2SeO_3}$ or $\mathrm{SeO_2}$ and $25-50\,\mathrm{mM}$ In^{3+} ions from $\mathrm{InCl_3}$ or $\mathrm{In_2(SO_4)_3}$ at a pH around 1.5. The advantage of this route is a fast growth of ca. $200\,\mathrm{nm/min}$ even without stirring the bath. The deposition is carried out at room temperature and potentials between $-0.67\,\mathrm{V}$ and $-1.30\,\mathrm{V}$ [22, 23, 109]. The Se/In ratio in the as-deposited film is close to the $\mathrm{In_2Se_3}$ stoichiometric value of 1.5 for a deposition potential of $-1.07\,\mathrm{V}$ in a bath containing $25\,\mathrm{mM}$ $\mathrm{H_2SeO_3}$ and $25\,\mathrm{mM}$

$In_2(SO_4)_3$. At more positive potentials the film is Se-rich whereas for more negative potentials it is growing In-rich[1] [22]. The increase of indium content with more negative potentials is confirmed for several bath compositions [109]. It is furthermore increasing if $In_2(SO_4)_3$ is replaced by $InCl_3$. At a potential of $-1.17\,V$ the Se/In ratio decreases from 1.67 for sulfate to 1.08 for chloride. It is not clear if it takes into account that indium sulfate is providing twice as much In^{3+} ions for the same salt concentration [22]. Layers with a composition close to InSe can be obtained at $-1.12\,V$ from a bath containing $25\,mM\ InCl_3$ and $12.5\,mM\ SeO_2$ [109]. The deposited indium selenide films are amorphous and consists of round particles in the order of $800\,nm$ whose size increases with more negative deposition potentials [22].

The second route of indium selenide electrodeposition uses lower concentrations of $1-2\,mM$ H_2SeO_3 or SeO_2 and $1-2\,mM\ In_2(SO_4)_3$ at pH values between 1.5 and 3.5 [115, 117, 116, 113, 1]. A background electrolyte of $100-300\,mM\ K_2SO_4$ or Na_2SO_4 is added to improve solution conductivity. The potential is between $-0.75\,V$ and $-0.60\,V$ and the deposition is in general done at an elevated temperature of $60-80\,°C$. The as deposited films are also amorphous and their Se/In ratio is between 1.2 [113] and 1.53 [1].

For the low temperature deposition route several authors report insufficient adhesion of the indium selenide film on Mo substrates. They solve this issue by depositing a $50\,nm$ thick copper underlayer on the Mo prior to the In-Se plating [22, 23, 34, 31]. It is likely that the bath temperature is the decisive parameter for the issue of low adhesion, because the indium selenide films plated in this thesis show a superior adhesion on Mo substrates. It has also been reported that the formation of In_2Se_3 directly on Mo is not possible at room temperature due to hydrogen evolution [1].

10.1.3. Indium selenide electrochemistry

Although several recipes of indium selenide electrodeposition are available (subsection 10.1.2), most of them are empirical and do not consider the reduction processes.

The most detailed study of indium selenide electrochemistry has been done by Massaccesi et al. [1]. They propose the formation of In_2Se_3 through a reduction of Se^{4+} to Se^{2-} followed by a subsequent electroless reaction with In^{3+}. Additionally they calculate the standard potentials of possible reduction processes by the Gibbs energies of the different indium selenide phases[2]. From this they concluded the existence of three potential domains until the reduction of H^+ into H_2 marks the negative potential limit where water is split (figure 10.1). In the first domain at very positive potentials only In^{3+} and H_2SeO_3 ions can exist. In the second domain at more negative potentials elemental Se can be deposited but indium can only exist in the form of In^{3+}. In the third domain at potentials close to the splitting of water In_2Se_3, elemental Se and In^{3+} are the allowed species. Therefore the deposit can only consist of In_2Se_3 and possible elemental Se. Assuming the system is mass-transport controlled this means that the Se/In ratio of the as-deposited film is 1.5 if the Se flux is lower than 1.5 times the In flux, because no elemental indium can be deposited (equation 10.1) . In case of a higher Se flux the film composition is given by the flux ratio (equation 10.2).

$$\frac{flux(\mathsf{Se})}{flux(\mathsf{In})} \leq \frac{3}{2}: \quad \left(\frac{\mathsf{Se}}{\mathsf{In}}\right)_{\mathsf{deposit}} = \frac{3}{2} \tag{10.1}$$

$$\frac{flux(\mathsf{Se})}{flux(\mathsf{In})} > \frac{3}{2}: \quad \left(\frac{\mathsf{Se}}{\mathsf{In}}\right)_{\mathsf{deposit}} = \frac{flux(\mathsf{Se})}{flux(\mathsf{In})} \tag{10.2}$$

[1] Reference [22] is ambiguous in this point. Although it is stated that the sample deposited at $-1.17\,V$ is In-rich, the noted Se/In ratio is 1.67 which might be a misprint.

[2] An error occurred in the calculation of the standard potentials in [1]. The Gibbs energy of $H_2(g)$ was assumed to be negative, although it must be 0, because it is the stable elemental form of hydrogen. This leads to a shift in the zero potential. This shift is corrected afterwards and therefore the transition potentials between the domains in figure 10.1 agree with the ones calculated from table 5.2.

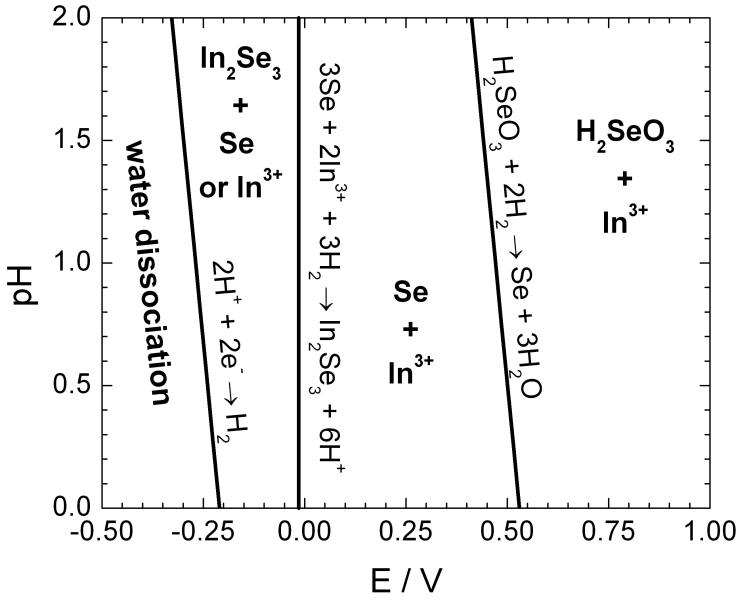

Figure 10.1.: Stable species in an aqueous solution containing Se and In in dependence of pH and applied potential. The stable species of every domain are in bold print. The borders between the domains are labelled with the corresponding reaction. The graph is recalculated from [1] with the thermodynamic data from table 5.2.

These considerations have not been experimentally verified. In their experimental section Massaccesi et al. compared the cyclic voltammogram of a bath containing only $\mathrm{H_2SeO_3}$ as active species to a bath containing $\mathrm{H_2SeO_3}$ and $\mathrm{In^{3+}}$. Indium selenide can be deposited around the potential, where Se precipitation occurred in the pure $\mathrm{H_2SeO_3}$ bath. At room temperature a red passivising Se film is obtained at $-0.61\,\mathrm{V}$ and grey indium selenide with a share of red Se is deposited at $-0.80\,\mathrm{V}$. At $80\,°\mathrm{C}$ grey indium selenide is deposited with an atomic Se/In ratio of 1.43 (at $-0.60\,\mathrm{V}$) and 1.53 (at $-0.75\,\mathrm{V}$). For low indium concentration additional red precipitate of elemental Se appeared in the bath.

The potentials of the reactions in figure 10.1 must be considered with care. There are several effects which limit the applicability of a simple potential calculation from Gibbs energy.

- The potentials are calculated from thermodynamical data in table 5.2, i.e. they are only valid in the equilibrium case. One needs to consider the overpotential. It might be necessary to apply a potential more negative than the equilibrium value to obtain a significant current. Since a profound overpotential is required to deposit Se, it is also likely for the deposition of indium selenide.

- The Gibbs energy of $\mathrm{In_2Se_3}$ in table 5.2 is valid for a crystalline phase. It will be shown that the electrodeposited indium selenide is amorphous, which will change the value of the Gibbs energy. The composition of amorphous indium selenide is not restricted to discrete Se/In ratios any more but can vary continuously (section 10.1.1). In this case the formation reaction of $\mathrm{In_2Se_3}$ in figure 10.1 needs to be adapted and thus also the calculated potential will change.

- As it has been shown in section 5.6 the simple calculation of the compound deposition potential from the Gibbs energy does not consider the activity of the elements inside the deposit. The deposition potential of $\mathrm{In_2Se_3}$ (at $\mathrm{pH} = 0$) in figure 10.1 is $530\,\mathrm{mV}$ more positive than the standard reduction potential of $\mathrm{In^{3+}}$. According to the description by Kröger [71] this is an

upper limit (if the activity of In^{3+} is at a standard value of 1). Dependent on the exact film composition the onset of In_2Se_3 can be between $0\,mV$ and $530\,mV$ more positive than the standard reduction potential of In^{3+}.

From these arguments it is obvious that the absolute values of the potentials in figure 10.1 will probably differ from the observed ones. Nevertheless the predicted domains can still be right.

The experimental results of Mishra et al. contradict the considerations of Massaccesi et al., because they conclude the electrodeposition of elemental indium reacting with Se species from the electrolyte [57]. In their cyclic voltammogram they observed a cathodic wave at $-0.36\,V$ on a glassy carbon substrate in $50\,mM\ In_2(SO_4)_3$ and $25\,mM\ SeO_2$ which they do not assign. It is followed by a sharp increase in current probably caused by H_2 evolution. On the reverse scan a nucleation loop occurs at $-0.36\,V$ indicating the necessity for a large overpotential for In^{3+} reduction. A strong anodic peak is observed at $-0.16\,V$ which they ascribe to the oxidation of excess elemental indium deposited in forward direction. From the fact that there is still elemental In on the reverse scan they conclude slow kinetics for the reaction between In and Se species.

The anodic stripping peak is confirmed in the cyclic voltammogram of a $25\,mM\ InCl_3$ and $12.5\,mM$ SeO_2 bath on Ti coated glass substrates [107]. It is also observed in the pure indium bath and corresponds to the oxidation of elemental indium. In the presence of Se the stripping peak is shifted slightly positive. The electrodeposition of elemental indium is in contradiction with Massaccesi et al. who states that for all potentials above water splitting the only stable form of indium is In^{3+} (figure 10.1 and [1]). The reason for this discrepancy are the different modes of indium selenide electrodeposition (compare section 10.1.2). While Massaccesi et al. studies a bath with low H_2SeO_3 concentration at high temperature, the studies that state a deposition of elemental indium are at higher concentrations and room temperature [57, 107]. It seems as if both electrodeposition routes of indium selenide are based on a different deposition mechanism.

10.2. Results and Discussion

10.2.1. Electrochemistry of Indium Selenide

10.2.1.1. Potential ranges

The cyclic voltammogram of a bath containing Se^{4+} and In^{3+} is shown in figure 10.2 for different negative vertex potentials. In principle three waves are visible on the forward scan. The first one sets in around $-0.10\,V$ (C_1), the second one at $-0.57\,V$ (C_2) and the third one at $-0.75\,V$ (C_3). Samples have been electrodeposited for different potentials to study the composition of the deposit. The first wave C_1 corresponds to the electrodeposition of elemental Se similar to the CV in figure 8.3. Films deposited below $-0.57\,V$ (C_2) have an atomic Se/In ratio close to 1.5 and can be assigned to In_2Se_3. In contrast to the pure Se bath no red Se precipitation is observed in the potential range of the second wave. The third wave C_3 is accompanied by the appearance of gas bubbles and is assigned to hydrogen evolution.

If the vertex stays above $-0.60\,V$, i.e. just at the beginning of indium selenide electrodeposition, the current density in the reverse scan shows a small anodic stripping peak A_2 at $-0.37\,V$ before it drops again to the current value of the forward scan. The current of this anodic oxidation peak is not reaching positive values, because ongoing Se deposition at these potentials lowers the baseline to ca $-1\,mA/cm^2$. Accordingly if the current density in the reverse scan above $-0.30\,V$ is close to zero it is not caused by passivation but it is an extended anodic stripping peak of indium selenide that compensates the Se deposition current. If the negative vertex is more negative, more indium selenide is deposited during the forward scan and the anodic stripping peak reaches positive current values. This behaviour is different to the one observed for selenium. While electrodeposited elemental selenium cannot be oxidised again in the available potential range, it is possible to oxidise the indium selenide.

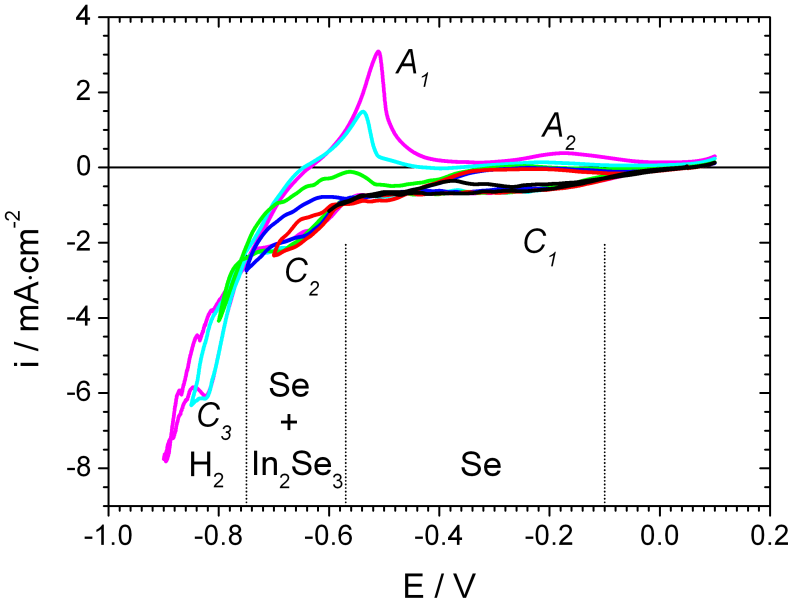

Figure 10.2.: Cyclic voltammograms with different negative potential limits of $1\,\mathrm{mM}\ \mathrm{H_2SeO_3} + 4.74\,\mathrm{mM}\ \mathrm{In_2(SO_4)_3}$ in background electrolyte ($100\,\mathrm{mM}\ \mathrm{K_2SO_4}$, pH 2, table 6.1) at $80\,°\mathrm{C}$; scanrate $10\,\mathrm{mV/s}$; the perturbations on the signal are caused by thermal convection. A_1-A_2 and C_1-C_3 label the cathodic and anodic peaks.

At $-0.75\,\mathrm{V}$ another step can be observed and reduction below this potential causes an oxidation peak A_1 at $-0.51\,\mathrm{V}$. For indium selenide baths with higher concentrations the most prominent oxidation peak in the cyclic voltammogram at room temperature is often assigned to the oxidation of elemental In^0 into In^{3+} [107, 57]. From the cyclic voltammogram in an In^{3+} single element bath (figure 7.1) it is known that elemental indium can be deposited at this potential. Another possible explanation is the oxidation of $\mathrm{H_2}$ that is present in the form of bubbles trapped on the electrode surface. When the cyclic voltammogram is paused on the reverse scan at $-0.75\,\mathrm{V}$ and the hydrogen bubbles are removed by rotating the electrode, the oxidation peak disappears in the continued scan. However no platings have been done in the potential regime more negative than $-0.75\,\mathrm{V}$, because hydrogen evolution prohibited the deposition of a uniform film.

The domains identified in figure 10.2 have been plotted in figure 10.3 together with the dominant species from the single element baths.

It is obvious that the domains in figure 10.3 correspond to the ones that have been obtained from thermodynamic calculations of the Gibbs energy in figure 10.1. No film can be deposited above $-0.10\,\mathrm{V}$. Above $-0.57\,\mathrm{V}$ only Se can be electrodeposited, whereas below this potential also the deposition of indium selenide is possible. If the potential is more negative than $-0.75\,\mathrm{V}$ water splits up and the formation of elemental indium can be present. The onset of $\mathrm{In_2Se_3}$ deposition is about $100\,\mathrm{mV}$ more positive than the deposition potential of In in the single element bath. (The latter value is unsure due to the interference with hydrogen evolution.) This potential gain can be attributed to the Gibbs energy of the compound. However this potential shift is considerably lower than the value of $+530\,\mathrm{mV}$ which has been calculated in section 5.6. Possible reasons for the discrepancy between the observed potential onset and the calculated one have been discussed in the context of figure 10.1. According to the formalism of Kröger $+530\,\mathrm{mV}$ is an upper limit for the potential shift, because the activity of the less noble element inside the deposit must be considered. It is also very likely that slow kinetics demand a high overpotential in the case of indium selenide. The sluggish kinetics of Se have already been recognised in the Se-bath where a high overpotential is necessary for

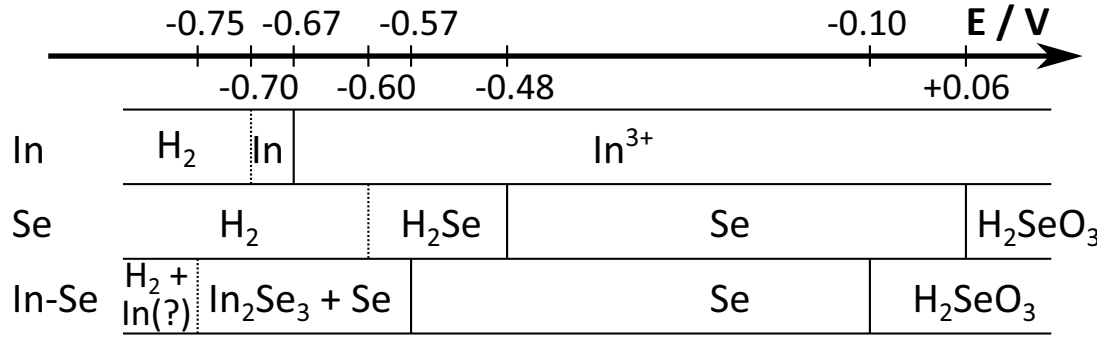

Figure 10.3.: Potential ranges of predominate species on a Mo electrode in the In-bath, Se-bath and In-Se bath (section 6.1.1). The ranges have been defined by the cyclic voltammograms in figures 7.1, 8.1, 10.2. If two ranges are separated by a dotted line the species at the more positive side of the line are also stable on the more negative side of the line.

the formation of Se^{2-}. Therefore it is likely that also $\mathrm{In_2Se_3}$ will suffer from slow kinetics, especially if a pure Se reduction step is involved in the deposition of the compound.

Figure 10.3 does also show that the electrochemistry of indium selenide is not just a simple superposition of the In and Se electrochemistry enhanced by the formation of $\mathrm{In_2Se_3}$. According to the CV of the In-bath it should be possible to deposit elemental indium below $-0.67\,\mathrm{V}$. Since the concentration of In^{3+} is several times higher than the one of Se^{4+} it would be expected that a significant amount of elemental indium is deposited below $-0.67\,\mathrm{V}$ in the In-Se bath. This is not observed in composition measurements (figure 10.6). Therefore the onset of elemental indium deposition must be shifted negative by the presence of Se-ions in the bath or the change of electrode surface. A similar observation is made for the reduction of elemental Se into Se^{2-}. According to the CV of pure Se it is expected that the Se film electrodeposited on the electrode will be cathodically stripped before the formation of $\mathrm{In_2Se_3}$ sets in. This is not observed and in figure 10.4 it will be discussed that the cathodic stripping of the Se film takes place within the potential range of $\mathrm{In_2Se_3}$ deposition. Therefore the reduction of elemental Se is either affected by the presence of In^{3+} ions or the change of electrode surface.

In conclusion the cyclic voltammogram agrees qualitatively with the dominant species calculated from thermodynamic considerations (figure 10.1). As it is predicted by the Kröger mechanism indium can be incorporated in the deposit at a potential $+100\,\mathrm{mV}$ more positive than its electrode potential in a bath containing only In^{3+}as active species.

10.2.1.2. Mass transport control

According to Massaccesi et al. the film composition of the $\mathrm{In_2Se_3} + \mathrm{Se}$ deposit is given by equations 10.1 and 10.2 . These equations assume a mass flux controlled system, which has not been experimentally proved in the literature so far. If the assumption is justified can be easily verified with the RDE. Figure 10.4 shows cyclic voltammograms recorded with a RDE at several rotation speeds, i.e. several mass fluxes. Two regimes can be distinguished. For potentials above $-0.55\,\mathrm{V}$ the current density is the same for all rotation rates above $200\,\mathrm{rpm}$. That means above $200\,\mathrm{rpm}$ not mass flux but electrode kinetics are the limiting step of the deposition process. The potential range corresponds to the deposition of elemental Se. Since Se has a tendency to passivate the surface it is not surprising to observe slow electrode kinetics. For potentials below $-0.60\,\mathrm{V}$ the current density increases with higher rotation rate. That verifies mass transport control as the limiting step in indium selenide electrodeposition as it has been assumed for equations 10.1 and 10.2 in [1].

The subplot in figure 10.4 shows a CV recorded on a RDE at a rotation rate of $400\,\mathrm{rpm}$. At the beginning of the CV elemental Se starts to deposit. Its electrode passivation leads to a current decrease for potentials below $-0.35\,\mathrm{V}$. Around $-0.55\,\mathrm{V}$ a small nucleation peak marks the beginning

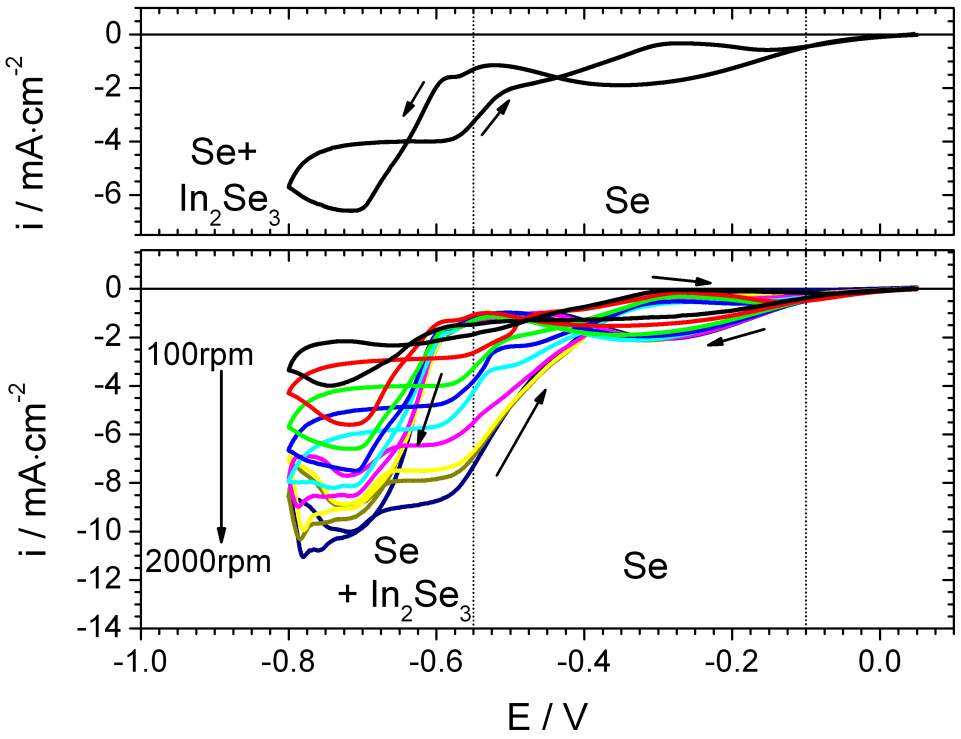

Figure 10.4.: Cyclic voltammograms for different RDE rotation rates of $1\,\mathrm{mM}\ \mathrm{H_2SeO_3} + 2\,\mathrm{mM}\ \mathrm{In_2(SO_4)_3}$ in pH 2 background electrolyte at $80\,°\mathrm{C}$; scanrate $10\,\mathrm{mV/s}$; rotation rates are 100, 200, 400, 600, 900, 1100, 1400, 1600, and $2000\,\mathrm{rpm}$; The upper subplot shows the scan at $400\,\mathrm{rpm}$.

of indium incorporation. In addition the deposited Se film is reduced to Se^{2-} similar to the case of the pure Se bath. This reduction provides a reservoir for Se^{2-} ions which can react with In^{3+} ions in order to form $\mathrm{In_2Se_3}$. Below $-0.73\,\mathrm{V}$ the supply of Se^{2-} ceases as the elemental Se film is consumed. That is why a broad peak is observed at $-0.73\,\mathrm{V}$ instead the typical current plateau for a mass transport limited system. On the reverse scan the initial Se film has been completely consumed and the indium selenide electrodeposition is only determined by the RDE mass fluxes of In^{3+} and Se^{4+}. As a result a current plateau is observed between $-0.70\,\mathrm{V}$ and $-0.60\,\mathrm{V}$ on the reverse scan. The current step between $-0.60\,\mathrm{V}$ and $-0.50\,\mathrm{V}$ can be assigned to the end of indium selenide electrodeposition, when the potential is above the formation of Se^{2-}. At more positive potentials Se electrodeposition and a partial oxidation of indium selenide are the only processes. The latter causes a weak oxidation peak at $-0.28\,\mathrm{V}$. This principal shape is true for all scans up to a RDE rotation rate of $1000\,\mathrm{rpm}$. At higher rotation speeds deviations occur at the negative potential limit. They can probably by assigned to hydrodynamic effects not considered in the Levich equation (e.g. turbulences or effects from the limited size of RDE and beaker).

In conclusion it has been verified that indium selenide electrodeposition under the recent conditions is controlled by the mass flux. The domains calculated from thermodynamic data in figure 10.1 are also present in case of the RDE.

10.2.1.3. Varying In^{3+} concentration

In case of a RDE the mass flux of each species in the bath is separately described by the Levich equation . The flux is proportional to $\sqrt{\omega}$ for all species. That means the ratio of the Se^{4+} and In^{3+} fluxes is constant for all rotation rates although the absolute value of the fluxes changes with ω. The ratio between both fluxes can be varied by changing the concentration in the bath. Cyclic voltammograms have been recorded for the following bath compositions (figure 10.5): The Se^{4+}

concentration was kept constant at $1\,\mathrm{mM}$ and the In^{3+} concentration has been varied from high In^{3+} excess of $9.47\,\mathrm{mM}$ to a concentration of $0.81\,\mathrm{mM}$ where the ratio of the Se^{4+} and In^{3+} fluxes correspond to 1.5 which is the stoichiometric ratio of $\mathrm{In_2Se_3}$. In the following bath compositions will be noted as (x; y) where x is the concentration of In^{3+} and y is the concentration of Se^{4+} in mM. The composition of the (0.81; 1) bath has been calculated by the Levich equation to result in a ratio of the Se^{4+} and In^{3+} flux towards the electrode equal to 1.5. The diffusion coefficients of In^{3+} and Se^{4+} obtained from figures 7.2 and 8.5 have been used.

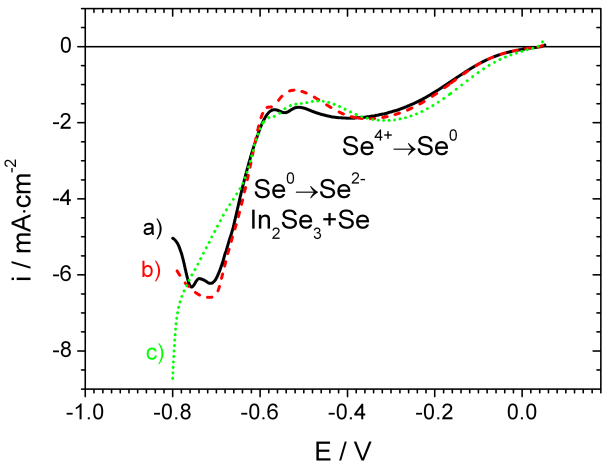

Figure 10.5.: Linear sweep voltammograms onto a Mo RDE at $400\,\mathrm{rpm}$ for $1\,\mathrm{mM}\ \mathrm{H_2SeO_3}$ + varying concentrations of $\mathrm{In_2(SO_4)_3}$ in pH 2 background electrolyte at $80\,°\mathrm{C}$; scanrate $10\,\mathrm{mV/s}$; $\mathrm{In_2(SO_4)_3}$ concentration: a) $4.74\,\mathrm{mM}$ b) $1.89\,\mathrm{mM}$ c) $0.41\,\mathrm{mM}$

The voltammograms of the $(9.47;\ 1)$ and $(3.79;\ 1)$ baths show a very similar behaviour (figure 10.5) which has already been explained in the context of figure 10.4. In both cases In^{3+} is present in excess. The high In^{3+} excess of $(9.47;\ 1)$ has been motivated by the observation of a red Se precipitate in the $(3.79;\ 1)$ bath when depositing indium selenide for several hours (see chapter 10.2.4). It has been assumed that the side reaction forming the red Se precipitate (reaction 8.3) can be suppressed when more In^{3+} ions are present to react with the Se^{-2} ions in solution. However the voltammogram 10.5 shows that an increase in In^{3+} excess does not significantly change the reaction and indeed red Se precipitation is also observed when depositing from a $(9.47;1)$ bath.

The fact that the voltammograms are similar although the In^{3+} concentration is augmented gives a first hint on the reaction mechanism of In-Se electrodeposition. In general three cases are possible:

1. Indium and selenium are reduced independently.
2. Indium induces the deposition of selenium. This route has been proposed by Mishra and Rajeshwar [57].
3. Selenium induces the deposition of indium. This route is predicted by the Kröger mechanism [71] and proposed by Massaccesi et al. [1].

In the first two routes it is expected that the current will increases with a higher In^{3+} concentration, because more indium can be deposited. This is not observed in figure 10.5 and thus the third route applies as it has already turned out in the interpretation of figure 10.3. This will also be supported by composition measurements from figure 10.6. Therefore it can be concluded from several experiments that the Kröger mechanism holds true for the electrodeposition of $\mathrm{In_2Se_3}$, which predicts a potential range in which In cannot be plated alone but only if it is induced by simultaneous Se deposition. It has already been mentioned why the second route is observed by Mishra et al. [57] but not in our

case (section 10.1.3). The experiments of Mishra et al. have been performed at higher concentration of $100\,\mathrm{mM}\ \mathrm{In}^{3+}$ and $20\,\mathrm{mM}\ \mathrm{Se}^{4+}$ at room temperature. Especially the change in temperature can influence the electrochemical reactions, because it effects the properties of the electrodeposited Se (chapter 8.2.3).

The voltammogram of the $(0.81;\ 1)$ bath follows the ones obtained with In^{3+} excess above a potential of $-0.57\,\mathrm{V}$ in forward direction. This potential range has been assigned to the deposition of selenium and therefore it is expected to see no effect of the In^{3+} concentration. This holds even true for the onset of indium selenide electrodeposition down to a potential of $-0.63\,\mathrm{V}$. Below this potential the current density rises considerably slower than for the baths with In^{3+} excess. In this range In^{3+} becomes the limiting species. Since the same Se film has been deposited in the previous part of the scan for all baths, it can be concluded that the Se^{2-} concentration is equal in all cases, when the film is reduced. This additional source of Se^{2-} ions cannot be included in the indium selenide electrodeposition process as it is the case for the $(9.47;\ 1)$ and $(3.79;\ 1)$ baths, because there is no excess In^{3+} flux for the $(0.81;\ 1)$ bath. The excess Se^{2-} ions will react with Se^{4+} to elemental red Se by reaction 8.3. This reaction consumes a part of the incoming Se^{4+} flux and therefore decreases the current density. Below $-0.78\,\mathrm{V}$ current density increases sharply which is probably caused by the onset of hydrogen evolution. Already in figure 10.3 it was seen that hydrogen evolution in the Se bath requires a higher overpotential if indium is added to the system. Then the onset of hydrogen formation should be less negative in case of a $(0.81;\ 1)$ bath in comparison with a $(3.79;\ 1)$ bath.

In conclusion it has been shown that the incorporation of indium in the deposit requires the presence of selenium at the studied conditions. Excess In^{3+} in the bath cannot be reduced to elemental indium in the potential range until hydrogen evolution sets in.

10.2.2. Indium selenide electrodeposition

10.2.2.1. Standard indium selenide plating conditions

A uniform indium selenide film can be electrodeposited from a $(3.79;\ 1)$ bath at a potential of $-0.60\,\mathrm{V}$ onto a Mo RDE rotating at $400\,\mathrm{rpm}$. The film has an atomic Se/In ratio of 1.51 ± 0.08 which is close to the stoichiometric composition of $\mathrm{In_2Se_3}$. No reflections are visible in XRD indicating an amorphous structure. This is supported by its appearance in the SEM cross section (figure 11.1) which shows a compact structureless layer. There are no grains visible that could indicate a polycrystalline structure of the film. The amorphous nature of electrodeposited indium selenide films has previously been reported [1, 113, 22]. Although there is no profound red Se precipitation visible at $-0.60\,\mathrm{V}$ in the cyclic voltammogram of indium selenide (figure 10.2), it does occur during a long deposition. After 2 hours of deposition the bath has a light orange clouding and red precipitate forms a thin cover at the bottom of the beaker. Although In^{3+} ions are present in excess, a certain part of the synthesised Se^{2-} ions does not react to $\mathrm{In_2Se_3}$ but forms the red colloidal Se precipitate according to reaction 8.3.

10.2.2.2. Composition at different potential and In^{3+} concentration

The influence of the bath composition has been examined in figure 10.6. Layers have been plated from baths with different In^{3+} concentrations at various potentials. In general the deposited charge was $2.2\,\mathrm{C}\cdot\mathrm{cm}^{-2}$ resulting in a layer thickness of one micron after about $12\,\mathrm{min}$ of deposition. At $-0.50\,\mathrm{V}$ the current density has been lower and only $0.5\,\mathrm{C}\cdot\mathrm{cm}^{-2}$ have been deposited. Several results follow from this experiment.

It is not necessarily true that a higher In^{3+} concentration in the bath leads to a higher indium content in the deposit. For example at $-0.70\,\mathrm{V}$ the atomic Se/In ratios of a deposit from a $(9.47;\ 1)$ or $(0.81;\ 1)$ bath are 1.69 and 1.49. That means although the In^{3+} concentration is more than 10 times higher, there is not more In in the compound (it is even less as it will be explained later).

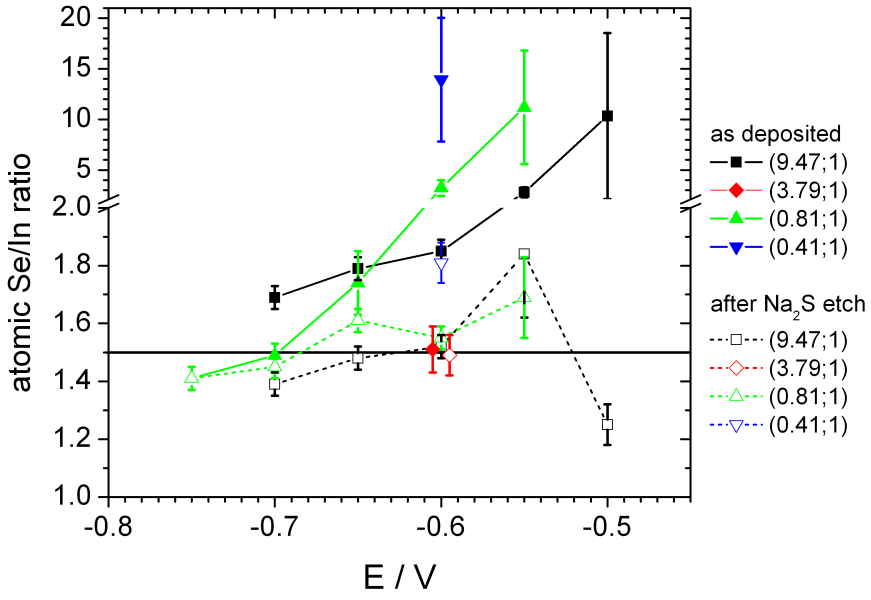

Figure 10.6.: Composition of indium selenide samples electrodeposited from baths with different Se/In ratios at a RDE rotation rate of $400\,\mathrm{rpm}$. The composition of as-deposited samples (solid symbols) has been measured by ICP-MS for the $(9.47;1)$ bath and by EDX for the other baths. The deviation between both techniques is about 5% (relative). The composition was measured again after $30\,\mathrm{min}$ etching in $\mathrm{Na_2Se}$ in order to remove elemental Se (open symbols). Notice the different scaling for Se/In ratios below and above 1.5. The error has been determined from variation between several samples (if available), variation in uniformity; and standard deviation of the measurement. The highest error has been chosen for the error bar. The large error bars at the most positive potentials can be explained by the small absolute indium content.

It is another verification that the deposition is neither an independent deposition of indium and selenium nor can it be induced by indium. Otherwise the indium content would increase with In^{3+} concentration. Thus indium incorporation must be induced by selenium.

For a given bath the Se/In ratio of the deposit decreases for more negative potentials, which is not expected for a mass flux controlled system. This is once more an indication that indium can only be incorporated in the presence of Se species in the covered potential range. From figure 10.4 it has been shown that indium selenide electrodeposition is mass flux controlled. In this case the composition should be independent of the potential and only given by the flux ratio of the single elements, if both elements have an independent deposition path. Since the composition is dependent on potential in figure 10.6, it means that $\mathrm{In_2Se_3}$ and Se deposition are competing processes. It seems that both depositions rely on the same selenium species. If the potential becomes more negative the kinetics of the $\mathrm{In_2Se_3}$ deposition becomes faster in relation to Se deposition and the Se/In ratio of the complete $\mathrm{In_2Se_3} + \mathrm{Se}$ deposit decreases.

Comparing the curve of the $(9.47;\,1)$ and $(0.81;\,1)$ bath in figure 10.6 it seems that the first one is shifted towards more positive potentials. This is also expected by the Kröger mechanism, in which the activity of the less noble ion determines the deposition potential of the compound by equation 5.19. Under the given conditions the increase of In^{3+} activity by a factor of 10 would cause a shift of $+23\,\mathrm{mV}$. It is not enough to explain the difference between the curves and maybe additional interactions of the In^{3+} concentration (e.g. formation of complexes) must be considered.

In conclusion it has been confirmed again that the incorporation of indium in the deposit requires

the presence of Se. Although the system is mass transport controlled the composition depends on the applied potential. This can be explained if Se deposition and In_2Se_3 deposition are competing for the same intermediate Se species.

10.2.2.3. Se content

Most as-deposited samples in figure 10.6 have an atomic Se/In ratio above 1.5. If the composition is below this value the difference is only small and can be explained by the difficulty of absolute composition measurements. A Se/In ratio above 1.5 supports the idea that the deposit consists of $In_2Se_3 + Se$ (or pure Se if the deposition potentials is above the onset of In_2Se_3). In the $(9.47;\ 1)$ bath the films consist mainly of Se for potentials above $-0.55\,V$. Towards more negative potentials In can be incorporated as In_2Se_3 and the amount of elemental Se is reduced. Therefore the Se/In ratio of the as-deposited $In_2Se_3 + Se$ film decreases. The onset of elemental In deposition is shifted to the potential range of hydrogen evolution and not show in figure 10.6. Although the curve is shifted for the $(0.81;\ 1)$ bath, the trend is the same. However in case of the $(9.47;\ 1)$ bath the atomic Se/In ratio is higher than the In_2Se_3 value 1.5, because additional elemental Se is present. This can be verified by a selective etching of Se. A solution of Na_2S is known to be an appropriate etching agent for the removal of elemental Se (section 6.3) [75, 76]. The atomic Se/In ratio after etching is close to the stoichiometric value of 1.5 (figure 10.6 and table 10.1). Some samples have a Se/In ratio below 1.5 which is in conflict with the explanation of an $In_2Se_3 + Se$ film. In case of the etched sample deposited at $-0.50\,V$ this can be explained as an artifact of the small absolute mass, because most of the film has been etched away (table 10.1). For the other films the stoichiometric Se/In ratio 1.5 is still in the error range of the measurements. Although several films with compositions between 1.39 and 1.50 have been measured, the variation between different samples deposited under the same conditions and different characterisation techniques (EDX and ICP-MS) do not allow a reliable proof of In-rich samples. Samples with a slightly In-rich composition do not contradict the explanation of $In_2Se_3 + Se$ films any more, if the amorphous nature of the layer is considered. The composition of amorphous indium selenide is not fixed to the distinct values of it its crystalline phases but can continuously vary (refer to subsection 10.1.1).

If the samples consist only of the phases In_2Se_3 and elemental Se, the amount of the latter can be calculated from the total mass m_{Se} of Se in the sample and the mass m_{In} of In. These masses can be determined from the as-deposited sample by ICP-MS (section 3.3).

$$m_{Se,elemental} = m_{Se} - \frac{3}{2} \cdot m_{In} \cdot \frac{M_{Se}}{M_{In}} \tag{10.3}$$

M_{Se} and M_{In} are the molar masses of Se and In. In Table 10.1 the results from equation 10.3 are compared to the mass of elemental Se which is removed by Na_2S etching. Both values are in good agreement, supporting again the hypothesis of $In_2Se_3 + Se$ films.

Massaccesi et al. proposed that the composition of the $In_2Se_3 + Se$ film is given through the ratio of the Se^{4+} and In^{3+} fluxes by the equations 10.1 and 10.2. It has already been proved that the system is mass transport controlled in figure 10.4 which is a prerequisite for the validity of equations 10.1 and 10.2.

Equation 10.1 predicts a constant sample composition of Se/In $= 1.5$ if the In^{3+} flux is sufficient. It does not longer hold in case of strong In^{3+} excess. The $(9.47;\ 1)$ and $(3.79;\ 1)$ baths both contain In^{3+} in excess, but the Se/In ratios at $-0.60\,V$ are 1.51 and 1.85. Under these conditions an increase of In^{3+} concentration leads to a higher Se content in the sample. This effect has already been observed in the context of figure 10.5. It is probably restricted to a strong In^{3+} excess. A film plated from a $(0.81;\ 1)$ bath has a Se/In ratio of 3.2 and in comparison with the $(3.79;\ 1)$ bath confirms the expectation that less In^{3+} in the bath leads to more Se in the film. The effect can probably be explained by the complexation of Se species with In^{3+} ions. Complexation can change the kinetics of the competitive processes of In_2Se_3 and Se deposition in a way that the latter one is favoured and therefore the Se content in the film is increased. In other works the indium content

	$-0.50\,\mathrm{V}$	$-0.55\,\mathrm{V}$	$-0.60\,\mathrm{V}$	$-0.65\,\mathrm{V}$	$-0.70\,\mathrm{V}$
Se/In atomic ratio as-deposited	10.3 ± 8.2	2.8 ± 0.5	1.85 ± 0.04	1.79 ± 0.04	1.69 ± 0.04
Se/In atomic ratio after $\mathrm{Na_2S}$ etch	1.25 ± 0.07	1.84 ± 0.22	1.52 ± 0.04	1.48 ± 0.04	1.39 ± 0.04
Se mass as-deposited / $\mu\mathrm{g/C}$	169 ± 8	159 ± 11	137 ± 7	115 ± 5	119 ± 5
Se mass after $\mathrm{Na_2S}$ etch / $\mu\mathrm{g/C}$	23 ± 13	100 ± 29	114 ± 6	96 ± 4	97 ± 4
Mass of etched Se / $\mu\mathrm{g/C}$	146 ± 17	60 ± 40	23 ± 8	19 ± 6	22 ± 7
Calculated elemental Se / $\mu\mathrm{g/C}$	135 ± 24	73 ± 20	26 ± 6	19 ± 5	14 ± 5
plating efficiency	96 ± 4	99 ± 4	94 ± 4	80 ± 4	84 ± 4

Table 10.1.: Composition of indium selenide films electrodeposited from a $(9.47;\ 1)$ bath onto a RDE with $400\,\mathrm{rpm}$ at several potentials. The data is plotted in figure 10.6. In addition to the Se/In ratio the absolute deposited Se mass has been determined by ICP-MS. The samples have been etched in $\mathrm{Na_2S}$ in order to remove elemental Se. The mass of elemental Se has also been calculated by equation 10.3. In the as-deposited case the deposition charge has been calculated from the masses by assuming a 3-electron transfer for $\mathrm{In^{3+}}$and a 4-electron transfer for $\mathrm{Se^{4+}}$. The plating efficiency of $\mathrm{In_2Se_3}$+Se is the quotient of the calculated and the measured charge.

in the film increases when the $\mathrm{In^{3+}}$ concentration is augmented [35, 22, 109]. These depositions were done with higher $\mathrm{In^{3+}}$ and $\mathrm{Se^{4+}}$ concentrations at room temperature. It has already been discussed that under these conditions the deposition mechanism of $\mathrm{In_2Se_3}$ changes. Therefore the observations cannot be compared to our compositions.

Equation 10.2 predicts that the Se/In ratio of a $\mathrm{In_2Se_3 + Se}$ film is given by the corresponding flux ratio if Se is in excess. The $(0.41;\ 1)$ bath and the $(0.81;\ 1)$ should both follow equation 10.2, because the concentrations have been chosen to result in a Se/In ionic flux of 3.0 and 1.5, respectively. At $-0.60\,\mathrm{V}$ the atomic Se/In ratio in the deposit is 13.9 ± 6.2 in the $(0.41;\ 1)$ bath and 3.2 ± 0.8 in the $(0.81;\ 1)$ bath. Although the $\mathrm{Se^{4+}/In^{3+}}$ flux ratio in the (0.41; 1) bath is double as high as in the (0.81; 1) bath, the Se/In ratio in the film is more than 4 times larger. There are more indications that equation 10.2 is probably not valid. The concentrations in the (0.81; 1) bath have been calculated from the diffusion coefficients in figures 7.2 and 8.5 to result in a $\mathrm{Se^{4+}/In^{3+}}$ flux ratio of 1.5. Above $-0.70\,\mathrm{V}$ the Se/In ratios of its films are significantly higher than 1.5. A third argument is the fact that the composition of the films is potential dependent. It has already been discussed that this points out competitive processes of $\mathrm{In_2Se_3}$ and Se deposition. Equation 10.2 is based on the assumption that the complete $\mathrm{In^{3+}}$ and $\mathrm{Se^{4+}}$ fluxes are deposited which does not allow competitive processes. Finally the potential dependent composition and its disagreement with the calculated flux ratio plus a possible counter-example confirm that equation 10.2 is not valid under the applied conditions.

In summary it has been confirmed that the deposited films consist of $\mathrm{In_2Se_3}$ and elemental Se. The amount of elemental Se cannot be directly calculated from the ratio of the $\mathrm{H_2SeO_3}$ and $\mathrm{In^{3+}}$ fluxes as it has been claimed in the literature [1]. It was shown that a higher excess concentration of $\mathrm{In^{3+}}$ can lead to a higher Se content in the deposit. $\mathrm{In_2Se_3}$ and Se deposition are competitive processes, which means that they rely on a common intermediate species (e.g. $\mathrm{Se^{2-}}$ or elemental Se). Both processes are balanced by their kinetics. If the kinetics are changed (e.g. example by varying the potential) it effects the film composition. It has been observed that a high $\mathrm{In^{3+}}$ excess can raise the Se content in the sample. This can be explained by complex formations of the excess

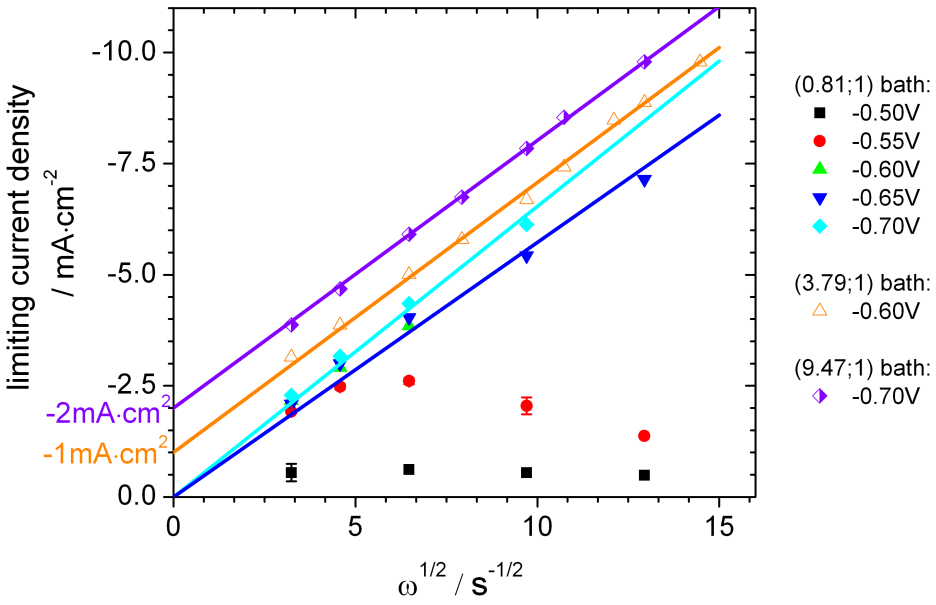

Figure 10.7.: Levich plots for different indium selenide baths at various potentials. The limiting current has been measured after depositing $3-5\,\mathrm{min}$ onto a Mo RDE. If the current did not converge but showed oscillations or decays it has not been considered in the plot. Only in case of the $(3.79;1)$ bath the limiting current density has been determined from the current plateau in the reverse scan of the cyclic voltammograms in figure 10.4. Some exemplary error bars have been derived from the variation between repeated runs. The data for the $(9.47;1)$ and $(3.79;1)$ baths have been shifted by a constant offset ($-2\,\mathrm{mA}\cdot\mathrm{cm}^{-2}$ and $-1\,\mathrm{mA}\cdot\mathrm{cm}^{-2}$) to avoid overlapping. Several data sets have been fitted by a line through the origin.

In^{3+} ions which disturbs the kinetic balance between the processes.

10.2.2.4. Charge transfer coefficient

A Levich plot is a useful measurement to obtain further information on the reaction mechanism, because the Levich equation contains the transferred charge nF per mol (equation 5.6).

Figure 10.7 contains Levich plots of indium selenide electrodeposited under several conditions. In case of a $(0.81;\ 1)$ bath the applied potential has been varied between $-0.50\,\mathrm{V}$ and $-0.70\,\mathrm{V}$. At $-0.50\,\mathrm{V}$ the current density is constant and does not depend on the mass flux. This backs up the result of the cyclic voltammogram 10.4 that Se electrodeposition is controlled by electrode kinetics and not by mass transport. At $-0.55\,\mathrm{V}$ the regime is mixed. Up to $200\,\mathrm{rpm}$ the current is proportional to the ion flux towards the electrode. If the rotation rate is increased further, the electrode kinetics start to limit the charge transfer and the limiting current levels. It even decreases again at higher rotation speeds, perhaps caused by passivation of the surface. For potentials equal or below $-0.60\,\mathrm{V}$ the system is controlled by mass transport and the limiting current is proportional to the flux ($j \propto \sqrt{\omega}$). At $-0.60\,\mathrm{V}$ the current density of the depositions did not stabilise with time at high rotation speeds and not enough data points could be obtained to fit the slope. The linear fits of the Levich plot at $-0.65\,\mathrm{V}$ and $-0.70\,\mathrm{V}$ show a slightly steeper slope at more negative potential. According to the Levich equation 5.6 this corresponds to a higher charge transfer.

Since the deposited film seems to consist of $\mathrm{In_2Se_3} + \mathrm{Se}$, there are the two effective charge transfer reactions

$$2\,\mathrm{In}^{3+} + 3\,\mathrm{Se}^{4+} + 18\,\mathrm{e}^- \longrightarrow \mathrm{In_2Se_3} \tag{10.4}$$

$$\mathrm{Se}^{4+} + 4\,\mathrm{e}^- \longrightarrow \mathrm{Se} \tag{10.5}$$

A third charge transfer reaction $\mathrm{Se}^{4+} + 6\,\mathrm{e}^- \longrightarrow \mathrm{Se}^{2-}$ is also possible which is a 6-electron transfer in the absence of In^{3+} ions. However it can be assumed that the product Se^{2-} will react with the incoming flux of Se^{4+} according to reaction $2\,\mathrm{Se}^{2-} + \mathrm{Se}^{4+} \longrightarrow 3\,\mathrm{Se}$. Therefore this reaction path also results in an effective charge transfer of 4 electrons per Se atom.

In reaction 10.4 In^{3+} does not change its oxidation state. The Levich plot cannot distinguish intermediate reaction steps. Therefore it is possible to assign the charge transfer completely to the Se ions. Then all elemental Se in the film can be assigned to the 4-electron transfer 10.5. Even if it is created through a 6-electron reduction (reaction 8.2) with a subsequent reaction between Se^{4+} and Se^{2-} (reaction 8.3), it will effectively result in a transfer of 4 electrons per deposited Se atom. Since $\mathrm{In_2Se_3}$ requires 6 electrons per deposited Se atom and elemental Se requires just 4, it is possible to distinguish both reaction 10.4 and 10.5 in the Levich plot. The steeper the slope the more $\mathrm{In_2Se_3}$ is involved in the charge transfer.

If Se is the limiting species and the system is mass transport limited, it is sufficient to consider only the Se^{4+} flux in the Levich equation. Then the charge transfer coefficient n can be calculated straightforward from the slope of the Levich plot by the Levich equation 5.6 with the known concentration of Se^{4+} $c_{Se} = 1\,\mathrm{mmol/l}$[3] and its diffusion coefficient (see chapter 8). In case of the (0.81; 1) bath one obtains $n = 4.3 \pm 0.3$ at $-0.65\,\mathrm{V}$ and $n = 5.0 \pm 0.3$ at $-0.70\,\mathrm{V}$ from figure 10.7. Both values are between 4 and 6 indicating a parallel electrodeposition of $\mathrm{In_2Se_3}$ and elemental Se. The larger n at $-0.70\,\mathrm{V}$ indicates a higher ratio of $\mathrm{In_2Se_3}$ deposition at more negative potentials. For the $(9.47;1)$ and $(3.79;1)$ bath $n = 4.6 \pm 0.3$ in both cases, although the potential was different. From figure 10.6 one expects n values close to 6, because the film compositions are close to 1.5 and contain only little elemental Se. Therefore it must be considered that a part of the elemental Se is not deposited on the surface but causes the red precipitate in the bath that is observed during long plating runs (see chapter 10.2.4).

In summary it was shown that the charge transfer coefficient n of the studied depositions is between 4 and 6. This is within the limits given by Se and $\mathrm{In_2Se_3}$ deposition.

10.2.3. Quantification of In-Se electrodeposition

Combining the film compositions in figure 10.6 and the Levich plots in 10.7 makes it possible to quantify the three major processes of indium selenide electrodeposition: electrodeposition of $\mathrm{In_2Se_3}$, electrodeposition of elemental Se in the film, and Se precipitation in the bath. Capacitive currents are neglected. The calculations are based on the following considerations:

- Se^{4+} is the limiting species and its flux j_{Se} can either be reduced to $\mathrm{In_2Se_3}$ or elemental Se [4]

$$j_{Se} = j_{Se,In_2Se_3} + j_{Se,Se} \tag{10.6}$$

[3] Although the bath has been prepared by $10^{-3}\,\mathrm{mol/kg}$(solvent) and not "mM" the value is assumed to be equal, because the concentration is low.

[4] The fluxes / concentrations are indexed in a way that the first index assigns the species of the flux / concentration (i.e. Se or In) and the second index describes the product of this flux / concentration.

variable	description
j_{Se}	complete RDE flux of Se^{4+} ions
$j_{Se,Se}$	part of j_{Se} which is reduced to elemental Se
$j_{Se,Se-film}$	part of $j_{Se,Se}$ that is incorporated in deposited film
j_{Se,In_2Se_3}	part of j_{Se} which reacts to $\mathrm{In_2Se_3}$

The indices are corresponding for concentrations and indium fluxes.

The first reaction is a 6-electron transfer (reaction 10.4) the latter one a 4-electron transfer per Se ion (reaction 10.5). The current density i [5] is then given by the Levich equation

$$\frac{i}{\sqrt{\omega}} = 0.62 \cdot F\nu^{-1/6} \cdot D_{Se}^{2/3} \cdot (6 \cdot c_{Se,In_2Se_3} + 4 \cdot c_{Se,Se}) \tag{10.7}$$

Only a part of the elemental Se is incorporated in the film. The rest forms Se precipitation in the bath

$$j_{Se,Se} = j_{Se,Se-film} + j_{Se,Se-bath} \tag{10.8}$$

- The flux of In^{3+} that is incorporated into $\mathrm{In_2Se_3}$ j_{In,In_2Se_3} is controlled by the corresponding Se^{4+} flux

$$j_{In,In_2Se_3} = \frac{2}{3} \cdot j_{Se,In_2Se_3} \tag{10.9}$$

- The atomic Se/In ratio r in the deposited film is the ratio of the fluxes that contribute to the film

$$r = \left(\frac{\mathrm{Se}}{\mathrm{In}}\right)_{\mathrm{at}} = \frac{j_{Se,In_2Se_3} + j_{Se,Se-film}}{j_{In,In_2Se_3}} \tag{10.10}$$

- The plating efficiency $\eta_{plating}$ is determined by the percentage of Se that is incorporated in the film either as elemental Se or as $\mathrm{In_2Se_3}$. A possible reduction of In^{3+} and $\mathrm{H}^{+}$is neglected in the studied potential range.

$$\eta_{plating} = \frac{j_{Se,Se-film} + j_{Se,In_2Se_3}}{j_{Se}} \tag{10.11}$$

With these equations it is possible to calculate all relevant fluxes, if the slope from the Levich plot $\frac{i}{\sqrt{\omega}}$, the rotation speed ω, the Se^{4+} concentration c_{Se}, and the film composition r are known.

$$j_{Se} = 0.62 \cdot \nu^{-1/6} D_{Se}^{2/3} \cdot \sqrt{\omega} \cdot c_{Se} \tag{10.12}$$

$$j_{Se,Se} = 3 \cdot j_{Se} - \frac{i}{2F} \tag{10.13}$$

$$j_{Se,In_2Se_3} = \frac{1}{2}\left(\frac{i}{F} - 4 \cdot j_{Se}\right) \tag{10.14}$$

$$j_{Se,Se-film} = \frac{1}{3} \cdot \left(r - \frac{3}{2}\right) \cdot \left(\frac{i}{F} - 4 \cdot j_{Se}\right) \tag{10.15}$$

$$j_{In,In_2Se_3} = \frac{1}{3}\left(\frac{i}{F} - 4 \cdot j_{Se}\right) \tag{10.16}$$

$$\eta_{plating} = \frac{r}{3} \cdot \left(\frac{i}{F j_{Se}} - 4\right) \tag{10.17}$$

From the fluxes and the deposition time it is possible to calculate the deposited masses[6]. In case of the sample deposited at $-0.70\,\mathrm{V}$ from the $(9.47;\,1)$ the mass of Se in the sample is calculated to be $132\,\mu\mathrm{g/cm^2}$ while ICP-MS measures $259 \pm 8\,\mu\mathrm{g/cm^2}$ (table 10.2). In order to fulfil the constraints given by the Se/In ratio in the final film and the current density from the Levich plot the solution of equations 10.12-10.16 results in a process, where 68% of the Se^{4+} flux is converted into Se

	$(9.47;1)\ -0.70\,\mathrm{V}$	$(9.47;1)\ -0.70\,\mathrm{V}$	$(0.81;1)\ -0.70\,\mathrm{V}$	$(3.79;1)\ -0.60\,\mathrm{V}$
input				
Se^{4+} concentration / mM	1	0.865	0.850	0.795
Levich slope / $\mathrm{C/(m^2 \cdot \sqrt{s})}$	6.023	6.023	6.541	6.073
film composition r	1.69	1.69	1.54	1.53
calculated				
Se mass as-deposited / $\mu\mathrm{g/cm^2}$	132	257	305	486
Se mass after etching / $\mu\mathrm{g/cm^2}$	111	217	293	472
mass of Se precipitate / $\mu\mathrm{g}$	1257	397	72	176
plating efficiency / %	41.8	81.6	96.8	94.6
measured				
Se mass as-deposited / $\mu\mathrm{g/cm^2}$	259 ± 8	259 ± 8	306 ± 10	489 ± 28
Se mass after etching / $\mu\mathrm{g/cm^2}$	223 ± 8	223 ± 8	288 ± 16	465 ± 22
plating efficiency / %	84 ± 3	84 ± 3	97 ± 4	95 ± 4

Table 10.2.: Comparison of Se masses and plating efficiency calculated by equations 10.12-10.17 and the corresponding values measured by ICP-MS. The Se mass after Na_2S etching was calculated by equation 10.10 neglecting the flux $j_{Se,Se-film}$. In the first column the Se^{4+} concentration was fixed the concentration in the prepared bath ($1\,\mathrm{mM}$). In the second column the concentration was varied to mimic the depletion of the electrolyte and allow a better description of experimental values.

precipitation in the bath. This percentage of Se precipitation is far more than the actual measured one (compare chapter 10.2.4).

The calculations can be corrected if the concentration of Se^{4+} in the bath is not fixed but allowed as a fitting parameter (compare first and second column in table 10.2). If the concentration is reduced in a way that the calculated as-deposited Se mass fits the measured one, also the Se mass of the Na_2S etched sample and the plating efficiency fit the experimental results (table 10.2). The necessary reduction of the initial concentration Se^{4+} has a physical meaning. Several samples have been deposited consecutively, i.e. the Se concentration has already decreased in the last depositions. The sample deposited from a $(0.81;1)$ bath in table 10.2 was the 4th sample of a series. Assuming three similar samples have been deposited before ($250\,\mu\mathrm{g/cm^2}$, $4.5\,\mathrm{cm^2}$, $250\,\mathrm{ml}$ electrolyte), a concentration of $0.83\,\mathrm{mM}\ Se^{4+}$ is left which is in agreement with the fitted value. The decreased bath concentration also explains why the current density in the deposition experiments is

[5] In this section i will denote the current density, while j will denote the flux in $\frac{\mathrm{mol}}{\mathrm{m^2 \cdot s}}$. They are correlated by $i = nFj$

[6] The current densities in the Levich plot (figure 10.7) are about 25% higher than the ones observed during electrodeposition. With every deposition the content of the active species in the bath decreases, because of its low concentration. While this is negligible for the small area and short deposition times onto the RDE, it has an effect in case of complete plated samples. Later a correction for the depletion will be introduced that reduces the discrepancy between the current densities to less than 10%. Due to the lower current density in the plating experiments it is preferred not to use the experimental deposition time. Instead the deposition time is calculated from the deposited charge and the Levich current density in order to be consistent.

lower than the value from the Levich plot (see footnote 6). Corrected with the depleted concentration the fluxes in figure 10.8 are calculated.

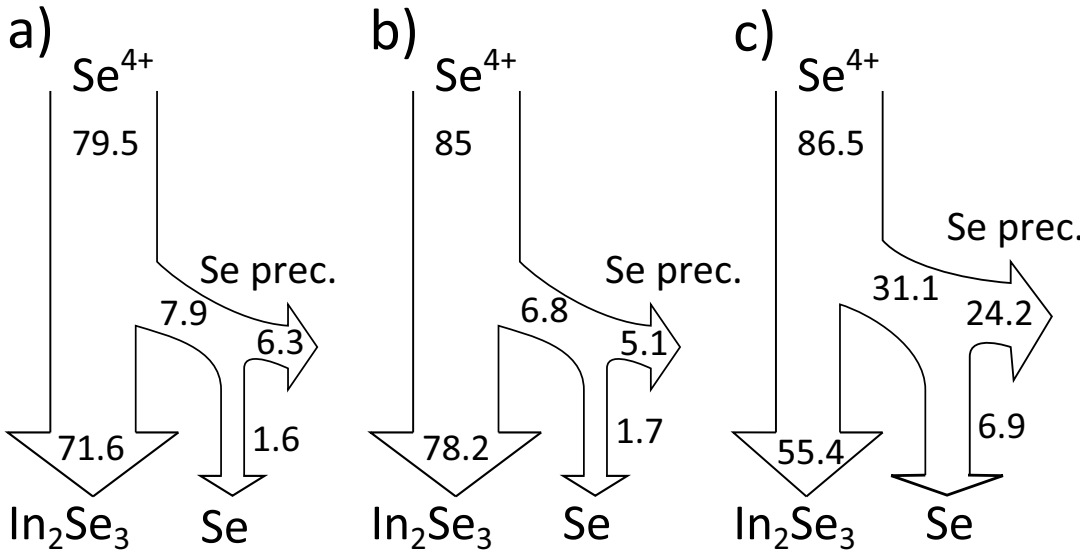

Figure 10.8.: Se fluxes in the indium selenide electrodeposition process a) $(3.79;1)$ bath at $-0.60\,\mathrm{V}$, b) $(0.81;1)$ bath at $-0.70\,\mathrm{V}$, c) $(9.47;1)$ bath at $-0.70\,\mathrm{V}$. The main flux results in $\mathrm{In_2Se_3}$ deposition while the flux of elemental Se splits into a part of plated Se and a part of Se forming a precipitate in the bath. The values denote the percentage of flux referred to the RDE flux of a $1\,\mathrm{mM}\ \mathrm{Se^{4+}}$ bath at $400\,\mathrm{rpm}$, giving $j_{Se} = 88.5\,\frac{\mu\mathrm{mol}}{\mathrm{m^2 \cdot s}}$. It is considered that the bath is already slightly depleted at the time of the deposition (table 10.2).

The depositions from the $(3.79;1)$ and (0.81;1) baths have a similar flux distribution. The main part of the incoming $\mathrm{Se^{4+}}$ flux contributes to the formation of $\mathrm{In_2Se_3}$. Most of the elemental Se forms the precipitation in the bath and only a small fraction is incorporated into the film. The plating efficiency calculated by equation 10.17 is close to the one that has been derived from ICP-MS measurements (table 10.2). Therefore Se precipitation is the main side reaction reducing the plating efficiency, because this assumption was made in deriving formula 10.17. The composition of the as-deposited sample is close to $\mathrm{In_2Se_3}$ stoichiometry, which has been a constraint in the calculation. The film deposited at $-0.70\,\mathrm{V}$ from a $(9.47;1)$ bath contains more elemental Se. In the flux calculation it turns out that this results in a pronounced increase in Se precipitation. Indeed it is observed in the plating experiments that the $(9.47;1)$ bath turns orange-red after a shorter time than the $(3.79;1)$ and (0.81;1) bath. However the different colour appearance is not a sufficient proof for an increased Se precipitation, because it can also be explained by a different size of the Se precipitate particles. The different ionic strengths of the baths effect the coagulation rate of the particles, that means the duration until they merge [118, 119]. The link between the elemental Se in the final film and in the bath is given by the similar slopes of the electrodeposition processes in the Levich plots of figure 10.7. The slopes of the $(9.47;1)$ bath at $-0.70\,\mathrm{V}$ and the $(3.79;1)$ bath at $-0.60\,\mathrm{V}$ are very close, i.e. the total charge transfer is similar. But the first sample contains more elemental Se in the film, which is connected to a lower charge transfer process than $\mathrm{In_2Se_3}$ deposition (reactions 10.4 and 10.5). This can only be compensated if additional elemental Se is formed that is not incorporated in the film.

Thus the quantification of the deposition processes confirms the effect that the Se/In ratio in the deposit can increase if the $\mathrm{In^{3+}}$ excess is higher. For the limited number of examined samples the quantification also predicts that a higher Se content in the sample is linked to a higher rate of Se precipitation in the bath. It is known that the existence of $\mathrm{Se^{2-}}$ is a prerequisite for the reaction of Se precipitation (reaction 8.3). If Se precipitation is linked to the deposition of elemental Se in

the film it is likely that both will depend on the same species. This species could be Se^{2-} forming elemental Se by reaction 8.3 either on the the electrode or in the bath. It is also possible that the link between both mechanism contains intermediate steps. Elemental Se could also act as the link between precipitation and elemental Se deposition. One part of it could stay on the electrode while another part is reduced to Se^{2-} which forms the precipitate.

In summary a good quantitative agreement between film composition and Levich plot has been observed. It allows to calculate the deposition rates of $\mathrm{In_2Se_3}$ or Se deposition and Se precipitation (figure 10.8). In the limited number of measured samples it seems that the latter two fluxes have the same source and an increase of Se precipitation is linked to more elemental Se deposition in the film.

10.2.4. Se precipitation

The precipitation of red Se seems to be an unavoidable side reaction of indium selenide plating under the given conditions. Its quantification allows to verify the calculation in section 10.2.3 and to determine its importance in the electrodeposition process of indium selenide. The precipitation might not only be a Se^{4+} loss mechanism that limits the lifetime of the deposition bath but could also effect the sample composition, if its particles can be incorporated in the deposited film.

Although the precipitate is formed by the comproportionation reaction 8.3, it requires the presence of an electrode to generate the necessary Se^{2-} ions. Nine indium selenide samples have been plated from a $(9.47;1)$ bath at $-0.60\,\mathrm{V}$ and $400\,\mathrm{rpm}$ RDE rotation speed. After each deposition a sample of the electrolyte has been taken. In order to study a possible incorporation of Se precipitate particles in the sample, the complete bath was centrifuged after the deposition of the 6th sample. The centrifuged red particles have been rinsed with water and afterwards analysed in ICP-MS (details of the experimental procedure in section 6.4) .

The atomic Se/In ratio of the precipitate is 4.6 ± 0.1. If the precipitate consists of $\mathrm{In_2Se_3 + Se}$ like the deposit it contains 55% (atomic) Se and 45% $\mathrm{In_2Se_3}$. If $\mathrm{In_2Se_3}$ is present it does not necessarily have to form at the electrode, but could be from a slow reaction with In^{3+} ions in the bath. It is also likely that residues of the bath stayed despite the washing of the precipitate and cause the indium contamination, because only about $100\,\mu\mathrm{g}$ of precipitate have been analysed. Therefore it is assumed that the In content in the precipitate does not influence the calculations in section 10.2.3.

The results of the bath and sample composition are shown in figure 10.9. The measured Se concentration is close to the calculated value. Therefore most of the Se is plated on the sample and Se precipitation is only a small perturbation to it. Since the atomic In^{3+} concentration is ten times higher than for Se^{4+} it is nearly constant throughout the depositions. The slight increase in the measured In^{3+} concentration can result from some evaporation of electrolyte. The deviation of Se^{4+} from its calculated concentration can be used to estimate the amount of Se precipitation, because it is the only Se loss that has not been considered in the calculation. After the 6th sample the measured Se^{4+} concentration is $4.9 \pm 1.2\,\mathrm{mg/l}$ below the calculated value. Considering a constant Se precipitation for all samples this results in $212 \pm 52\,\mu\mathrm{g}$ Se precipitate per sample. This result is in the same order of magnitude as it has been predicted by the calculation in table 10.2. Since the table does not include a sample deposited at $-0.60\,\mathrm{V}$ from a $(9.47;1)$ bath, it can be assumed that its value is between the $(9.47;1)$ / $-0.70\,\mathrm{V}$ sample with $400\,\mu\mathrm{g}$ Se precipitate and the $(3.79;1)$ / $-0.60\,\mathrm{V}$ sample with $180\,\mu\mathrm{g}$ Se precipitate. Despite the aggregating amount of Se precipitate the plated sample does not show significantly more Se until the 6th sample which conflicts with a possible incorporation of Se precipitate in the bath. Instead the Se content rises after the Se precipitate has been removed from the bath. It could be another indication of the effect of an increasing Se content in the sample with decreasing relative Se concentration in the bath. For the last sample the bath concentration has already changed from the initial (11.1; 1.1) bath[7] to a (11.8; 0.6) bath. On the

[7] The (11.1; 1.1) composition has been determined by ICP-MS. This bath was designed to be a $(9.47;\ 1)$ bath. The discrepancy can be explained by the hygroscopic property of $\mathrm{H_2SeO_3}$ and a wrong coordination number of $\mathrm{In_2(SO_4)\cdot xH_2O}$. In this thesis $x = 9$ was assumed as it has been reported in literature [72, 73, 74]. The higher

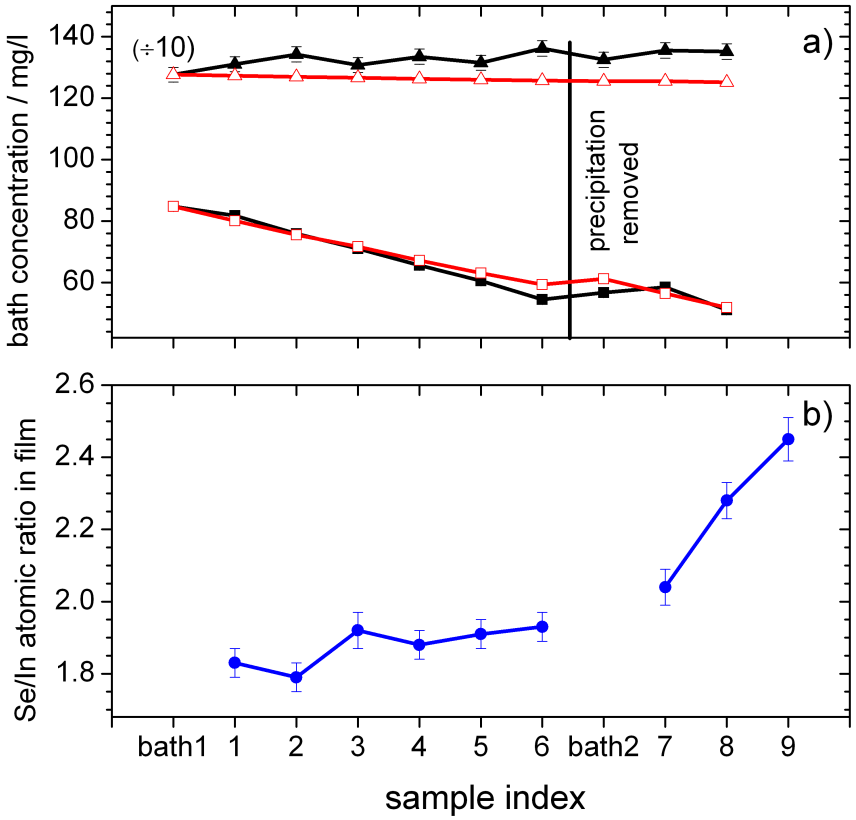

Figure 10.9.: Series of indium selenide samples deposited from a $(9.47;\ 1)$ In-Se bath at $-0.60\,\mathrm{V}$, $400\,\mathrm{rpm}$, and $80\,^{\circ}\mathrm{C}$. Figure a) records the Se (squares) and In (triangles) concentrations in the bath after deposition of the sample noted on the x-axis. The open symbols are values calculated from the mass balance of material in the bath. The solid symbols have been measured by ICP-MS. The indium concentrations have been divided by 10 to fit on the same scale. The datapoint "bath1" is the fresh bath before samples were plated; "bath2" has been measured after Se precipitate has been removed by centrifuging and electrolyte loss has been replaced with fresh electrolyte. Figure b) notes the atomic Se/In ratio of the electrodeposited films measured by ICP-MS.

other hand the removal of Se precipitate by centrifuging has been a considerable disturbance to the bath, because it had to be cooled down to room temperature, was refilled several times and heated up again. This could explain the unexpected behaviour of increasing Se concentration after deposition of the 7th sample. Therefore the data points after precipitate removal must be interpreted with care.

The constant composition of the film until the 6th sample is still not a proof that particles of Se precipitate are not incorporated in the sample. Adsorbed particles could further react with In^{3+} ions to $\mathrm{In_2Se_3}$ and would not change the film composition. The question of particle incorporation is of practical interest, e.g. Hirono plated indium layers in a suspension of fine Se powder. The resulting film contained 35% (at) Se [120]. In our case the visual appearance of the obtained films changed during the series. The samples got darker from the 1st to the 6th run indicating a change in surface morphology. After removing the Se precipitate sample 7 appeared light grey again. The surface morphology can be identified in the SEM pictures in figure 10.10. Sample 6 has a loose

concentration measured by ICP-MS can be explained if the actual coordination number of the used indium sulphate is smaller.

surface structure with pronounced round particles as they are expected, if Se precipitate adsorbs to the surface. The morphology of the 1st and 7th sample is more compact but also in this case particles are visible. EDX maps with an electron high voltage of $7\,\mathrm{kV}$ were recorded to determine the composition of the top $150\,\mathrm{nm}$ in the indium selenide layer [53]. Sample 6 in figure 10.10 shows an increased Se content in the EDX map at the spots where the round particles are located. Sample 7 that has been plated after the removal of Se precipitate shows a uniform composition of $\mathrm{In_2Se_3}$ instead. Therefore the spots of Se concentration in sample 6 are not a quantification artifact of the rough morphology but a real indication for the adsorption of Se particles on the surface.

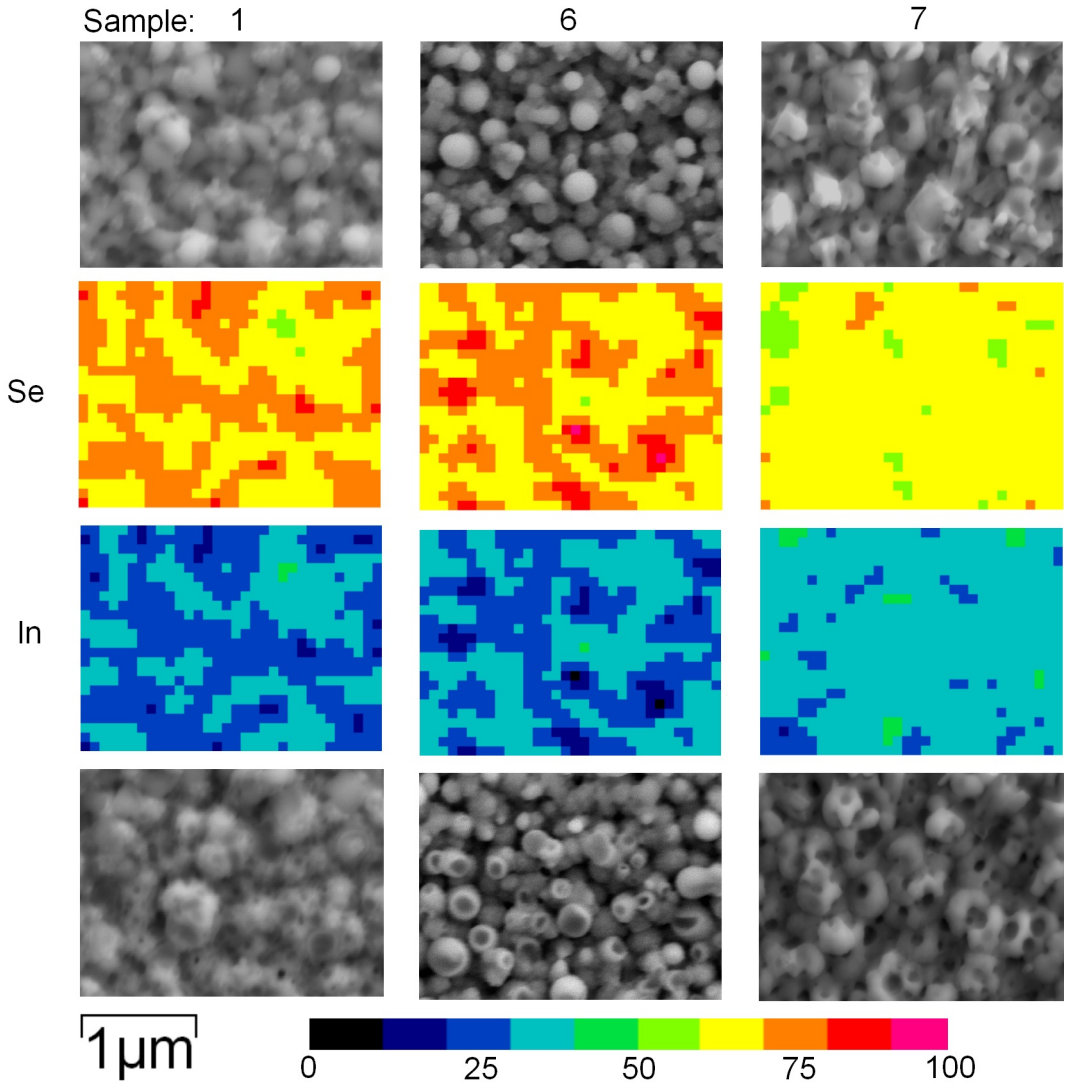

Figure 10.10.: SEM pictures and EDX composition maps of chosen indium selenide samples from the plating series in figure 10.9. The column label corresponds to the sample index in figure 10.9. The first row shows SEM pictures before the EDX mapping, the last row shows the same spot after the EDX measurement. Although a reduced electron voltage of $7\,\mathrm{kV}$ has been applied to record the EDX map, parts of the surface start to evaporate. The EDX maps show the atomic composition of Se and In.

It is surprising that the first sample also shows variations in the surface composition, because the amount of Se precipitate is low at the beginning of the series. This indicates that the particles are perhaps incorporated at the moment when they are formed near the surface and the precipitate in the bath does not longer contribute. In this case the absence of Se particles in sample 7 is not

caused by the removal of precipitate from the bath. It is possible that the storage of the bath and the removal procedure of the precipitate have changed the formation kinetics of the precipitate.

In summary it could be shown that Se particles can be adsorbed to the sample surface. Nevertheless the total composition of the plated film is not effected. It means either the particles only stick to the surface and are not incorporated in the indium selenide film, or if they are incorporated, they have previously reacted with In^{3+} to indium selenide. Additionally it has been shown that due to the low bath concentration of Se^{4+} its composition is changed during plating. This depletion can effect the film composition.

11. Precursor formation and characterisation

Based on the experience from the plating experiments in chapters 9 and 10 the standard conditions in table 6.1 have been established for the electrodeposition of indium selenide and copper selenide.

The (3.79;1) bath has been chosen for indium selenide electrodeposition, because the excess of In^{3+} ensures the formation of In_2Se_3 but the Se precipitation is not so pronounced as in the (9.47;1) bath. At $-0.60\,V$ In_2Se_3 is already formed and the rate of hydrogen evolution is still low. Even a low rate of hydrogen evolution can be an issue in the plating of a uniform film, because evolving bubbles cannot escape in the RDE geometry. If the bubbles are small and stick to surface, they create a pinhole in the film. Larger bubbles can circulate at the film surface and ruin its uniformity. For a smooth film it is therefore necessary to remove any bubbles by directing a flush of electrolyte (e.g. using a bend pipette) to the surface every few minutes. This results in a shiny light blue-grey film.

Several authors report the necessity of a $50-100\,nm$ thin Cu underlayer between the Mo substrate and the indium selenide film in order to improve adhesion [31, 22, 34, 23]. The indium selenide film electrodeposited according to the conditions in table 6.1 has an excellent adhesion to the Mo substrate and can even not be removed by soft scratching. This difference is probably an effect of electrodeposition temperature, because all cited sources [31, 22, 34, 23] deposit at room temperature. Another advantage of the Cu underlayer is the suppression of hydrogen evolution (compare chapter 7 and [82]). In order to obtain a compact Cu layer a thickness of more than $50\,nm$ is required using the copper plating bath from [121]. However the Cu underlayer has also disadvantages. It roughens the the surface of the indium selenide film, which results in an opaque grey appearance. SEM pictures show a shift from a fine granular, compact structure to micron sized conglomerates if a Cu underlayer is introduced. Precursor stacks on a Cu underlayer have a higher tendency to delaminate during the annealing process. Therefore its use is not recommended.

As mentioned in chapter 9 a deposition potential of $-0.30\,V$ is preferred for copper selenide electrodeposition, because it compromises between the better film nucleation at more negative potentials and the less fragile film structure at less negative potentials. The structure is still brittle and therefore a slow rotation is preferred. For this reason it is also not possible to deposit a Mo/Cu-Se/In-Se precursor stack, because it would peel in the plating process of the indium selenide layer.

Thus a Mo/In-Se/Cu-Se precursor stack was annealed in the following parts of the thesis (part II and III). The thicknesses of its layers were adjusted to result in a final $CuInSe_2$ absorber thickness around $2300\,nm$ (figure 18.1b). The deposited charge density in case of In_2Se_3 was $3.63\,C/cm^2$ resulting in a $1600\,nm$ thick layer. For copper selenide $3.10\,C/cm^2$ have been plated. This deposition charge was chosen to result in an atomic Cu/In ratio of 1. The residence times for indium selenide electrodeposition has been about $15\,min$ and $22\,min$ for copper selenide. In average the following masses are plated: $260\pm9\,\mu g/cm^2$ copper, $455\pm30\,\mu g/cm^2$ indium, and $905\pm40\,\mu g/cm^2$ selenium. That means the Se content is about 42% more than needed for a stoichiometric precursor and provides an additional Se source during annealing.

A SEM cross section (figure 11.1) of the precursor shows the compact amorphous indium selenide film underneath the layer of randomly stacked copper selenide platelets.

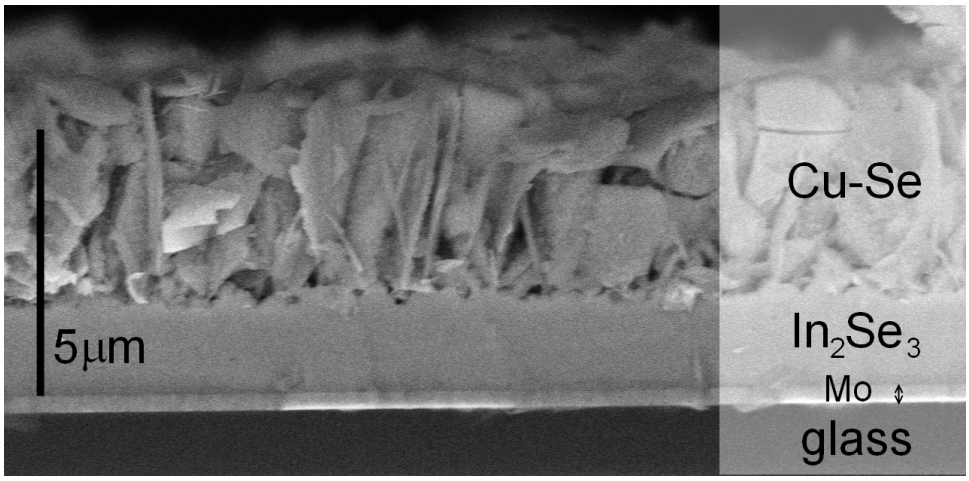

Figure 11.1.: SEM cross section of an electrodeposited Mo/In_2Se_3/Cu-Se stack

12. Conclusion

The two main routes for electrodeposition of indium selenide films in the literature have been discussed in particular with respect to the different deposition mechanisms. For the work in this thesis it was decided to develop the low concentration bath deposited at elevated temperatures rather than the high concentration bath deposited at room temperature. This route was chosen because it profits from the Kröger mechanism as an intrinsic composition control. The electrodeposition of indium selenide is preferred in a potential range where it is induced by selenium through the Kröger mechanism, before the onset of hydrogen evolution.

Experimentally it was shown that the kinetics of only selenium electrodeposition are sluggish. High overpotentials are needed and already at low mass fluxes the kinetics become limiting. The passivation of the electrode caused by Se plating becomes less at higher temperature. Additionally Se undergoes a phase change from amorphous to crystalline if the plating temperature exceeds $80\,°\mathrm{C}$. This makes the plating of Se easier at higher temperature. At room temperature the deposition of Se is significantly slowed down.

This thesis has verified the hypothesis of Massaccesi et al. that an $\mathrm{In_2Se_3 + Se}$ film is deposited in the high temperature route by different experiments. Composition measurements of the deposit and the composition change after Se-selective $\mathrm{Na_2S}$ etching confirm the hypothesis of a $\mathrm{In_2Se_3 + Se}$ film. Additionally a charge transfer value between 4 and 6 supports it. We have verified that indium selenide electrodeposition is mass transport controlled. On the other hand it was discussed that the film composition cannot simply be calculated by the ratio of mass fluxes. It is more likely that the composition is determined by the balance between the kinetics of $\mathrm{In_2Se_3}$ and Se deposition. Both mechanisms seem to compete for a common intermediate species.

This can also explain the effect why a high $\mathrm{In^{3+}}$ excess in the bath can lead to more elemental Se in the final film. The additional $\mathrm{In^{3+}}$ ions form complexes with the species in solution and can thus influence the balance between the kinetics in a way that Se deposition is preferred. An increase in elemental Se deposition seems to be linked to a rise in Se precipitation that is the major side reaction in the plating. It could be demonstrated that particles of the Se precipitate can be adsorbed on the surface of the film. Nevertheless they are not changing the composition of the film and are therefore expected to react with $\mathrm{In^{3+}}$ in the further deposition. The incorporation of such particles is probably negligible in our standard $\mathrm{In_2Se_3}$ plating process. The relation between Se precipitation and elemental Se deposition is a sign that both processes rely on the same selenium species. Furthermore it allows to identify processes for which the Se precipitation side reaction can be reduced.

Finally a deposition route was established to form uniform Mo\$\mathrm{In_2Se_3}$\Cu-Se binary selenide precursors for further processing.

Part II.

Structural and Compositional Characterisation of the Absorber

13. Introduction

In the previous part a process to electrodeposited binary selenide precursors was established. These precursors are annealed in the current part to form the desired $\mathrm{CuInSe_2}$ absorber layer. Before completing the precursor into a solar cell device, it is necessary to check its compositional and structural suitability. The verification of chalcopyrite $\mathrm{CuInSe_2}$ and the determination of possible secondary phases is part of this chapter. This was done for Cu-poor, stoichiometric, and Cu-rich growth conditions.

One motivation of the binary selenide precursor is an expected improvement of grain size in the annealed absorber compared to the coelectrodeposited precursor (section 2.3). Therefore the grain and crystallite size of both absorbers is compared by several methods. The grain size was also used as a simple test criterion to optimise the background pressure in the annealing process.

The phase evolution during annealing has not been studied for electrodeposited Mo/In-Se/Cu-Se stacks so far. It is interesting to compare it to the results which are reported for precursors deposited by vacuum methods. Ex-situ and in-situ XRD measurements have been used to study the phase evolution. Ex-situ XRD measurements were taken on samples that have been annealed at several temperatures in the standard oven. This allows conditions which are close to the standard absorber annealing, but the long annealing time does not allow to resolve non-equilibrium phases. In-situ XRD measurements have been recorded during the annealing process. They allow real-time detection of the phases present during annealing, but have to be performed in a special set-up. The different morphology of copper selenide and indium selenide (figure 11.1) makes it possible to support the phase reaction processes from XRD by SEM cross sections.

Electroplating is considered especially sensitive to impurities, because it is a non-vacuum deposition technique. This motivated a short study of the trace cation impurities in the absorber.

14. Phase diagrams

The phase diagrams for the indium - selenium, copper - selenium, and copper - indium - selenium systems will be introduced here. The relevant polymorphs, phases, and transitions within the experimental temperature and composition range of interest will be discussed so as to provide an overall framework for the following results. The phase diagrams will have particular importance when discussing the formation of the absorber layer from the stacked binary precursor (chapter 19).

14.1. Indium - Selenium

Indium selenide can occur in the following phases: In_4Se_3, $InSe$, In_6Se_7, In_9Se_{11}, In_5Se_7, and In_2Se_3 (section 10.1.1 and figure 14.1). The phase diagram of indium selenide is further complicated by several polymorphs that can exist for In_2Se_3 (α, β, γ, δ) and $InSe$ (α and β) [124].

$\gamma - In_2Se_3$ and $\delta - In_2Se_3$ are the stable phase of In_2Se_3 [124]. $\gamma - In_2Se_3$ is an ionic compound of In^{3+} and Se^{2-} ions which are arranged in a defect wurtzite structure [102, 125]. A third of the In^{3+} sites stays vacant in order to fulfil charge neutrality. $\alpha - In_2Se_3$ is metastable below $200\,°C$ and has a layered structure [124, 125].

$InSe$ also shows a layered configuration of In and Se planes hold together by Van-der-Waals forces. Inside the indium layers In^{3+} and In^{+} are covalently bound to $[In]_2^{4+}$ dications. The polymorphs of $InSe$ differ in the stacking order of the layers [125, 102].

The following reactions of indium selenide are within the temperature range of interest ($< 600\,°C$) [124]:

- In_4Se_3 melts with the indium rich liquid $L_1$and forms the liquid L_2 (32% at Se)

$$520\,°C: \qquad In_4Se_3 + L_1 \rightleftharpoons L_2 \tag{14.1}$$

- In_4Se_3 decomposes into $InSe$ and a liquid L (38% at Se)

$$550\,°C: \qquad In_4Se_3 \rightleftharpoons 3InSe + L \tag{14.2}$$

14.2. Copper - Selenium

At standard conditions the following copper selenide phases exist: orthorhombic $CuSe_2$, hexagonal $\alpha - CuSe$ (the corresponding mineral is called klockmannite), tetragonal Cu_3Se_2 (umangite), monoclinic $\alpha - Cu_2Se$ and face-centred cubic $\beta - Cu_{2-x}Se$ (berzelianite). The last phase is a defect compound [124]. Several polymorphs of $CuSe$ (α, β, γ) and $Cu_{2-x}Se$ (α, β) exist.

According to the copper selenide phase diagram (figure 14.2) the following reactions take place in the temperature range of interest [102, 126, 124]

- Cu_3Se_2 decomposes into $CuSe$ above $113\,°C$ according to reaction

$$113\,°C: \qquad Cu_3Se_2 \rightleftharpoons \beta - Cu_2Se + \beta - CuSe \tag{14.3}$$

- $CuSe_2$ is expected to decompose at $332 - 342\,°C$.

$$332 - 342\,°C: \qquad CuSe_2 \rightleftharpoons \gamma - CuSe + Se \tag{14.4}$$

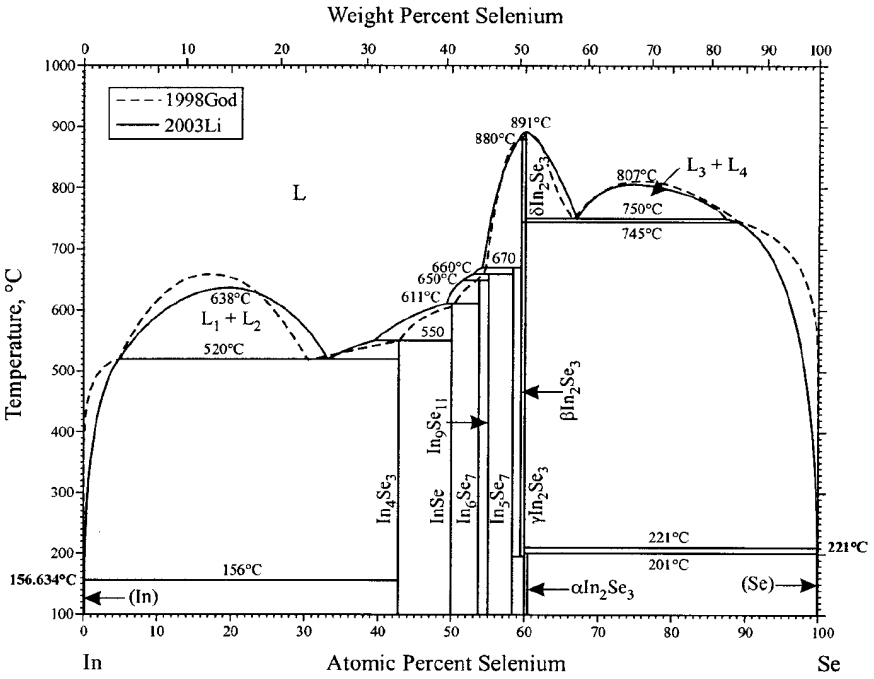

Figure 14.1.: Phase diagram of the indium - selenium binary system. The diagram was taken from the compilation in [103]. The dashed line refers to [122], the solid line to [123].

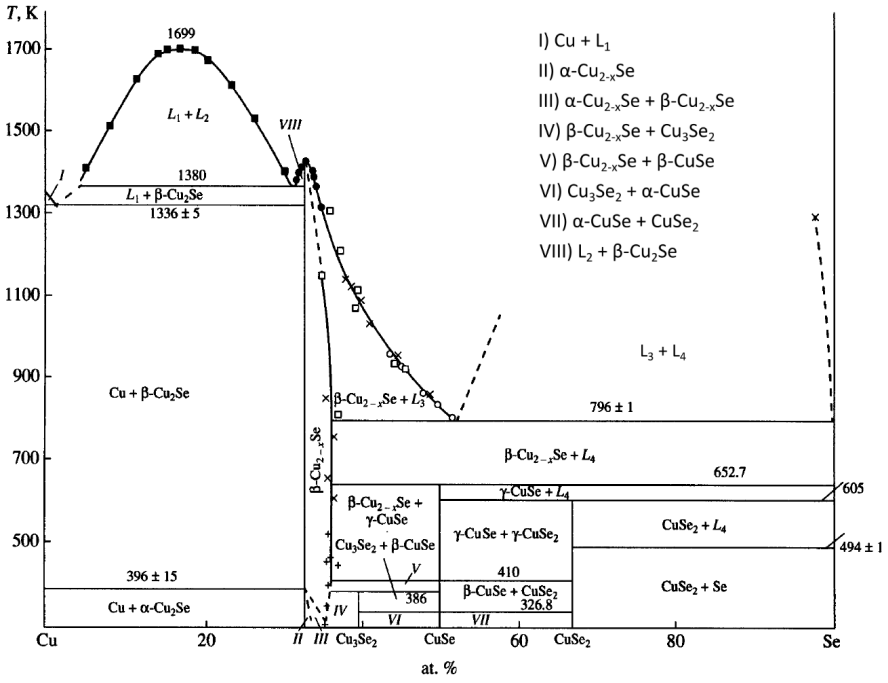

Figure 14.2.: Phase diagram of the copper - selenium system. The diagram was taken from the compilation in [126].

- The product CuSe undergoes another decomposition at $377 - 379\,°\mathrm{C}$.

$$377 - 379\,°\mathrm{C}: \qquad 2\gamma - \mathrm{CuSe} \rightleftharpoons \beta - \mathrm{Cu_2Se} + \mathrm{Se} \tag{14.5}$$

- Above $523\,°\mathrm{C}$ $\mathrm{Cu_2Se}$ melts in the presence of liquid Se and forms liquid $\mathrm{L_3}$ (53% at Se)

$$523\,°\mathrm{C}: \qquad \beta - \mathrm{Cu_2Se} + \mathrm{L_4} \rightleftharpoons \mathrm{L_3} \tag{14.6}$$

14.3. Copper - Indium - Selenium

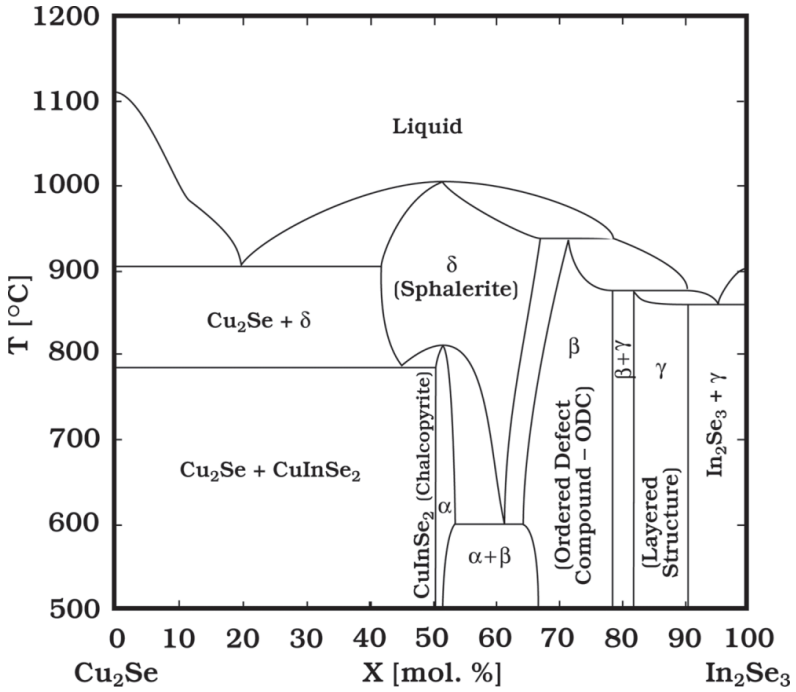

Figure 14.3.: Quasibinary section of the copper - indium - selenium system. The diagram was taken from the review [127]. The Greek letters abbreviate the following phases: α-CISe: $\mathrm{CuInSe_2}$ (chalcopyrite), β-CISe: $\mathrm{CuIn_3Se_5}$, γ-CISe: $\mathrm{CuIn_5Se_8}$, δ-CISe: $\mathrm{CuInSe_2}$ (sphalerite). Below $500\,°\mathrm{C}$ no phase transitions are observed and the diagram can be extrapolated.

The ternary phase diagram of the copper-indium-selenium system has three degrees of freedom. Instead of taking into account the complete three dimensional phase diagram, it is often sufficient to restrict to the section between $\mathrm{Cu_2Se}$ and $\mathrm{In_2Se_3}$ (figure 14.3). Gödecke et al. have confirmed in a comprehensive study that this section is indeed a "quasibinary section" [128]. The term "quasibinary" means that the section can be considered as a two-dimensional phase diagram with the binary compounds $\mathrm{Cu_2Se}$ and $\mathrm{In_2Se_3}$ acting as elements.

The chalcopyrite $\mathrm{CuInSe_2}$ phase is part of the quasibinary section. Due to copper vacancies its composition can vary, i.e. $\mathrm{Cu_{1-x}In_{1+x}Se_{2+x}}$. At equilibrium the copper deficiency x reaches values up to 0.02. In the preparation of thin films the final layer is often a supercooled non-equilibrium state and Cu deficiencies up to $x \approx 0.16$ are observed [128]. Also the addition of sodium impurities can increase the composition range of $\mathrm{Cu_{1-x}In_{1+x}Se_{2+x}}$ to the indium-rich side [102]. If the In-content is further increased, an ordered vacancy compound is formed together with the chalcopyrite $\mathrm{Cu_{1-x}In_{1+x}Se_{2+x}}$. This vacancy compound (phase β in figure 14.3) is usually assigned to $\mathrm{CuIn_3Se_5}$ [127]. A stannite structure and a "P-chalcopyrite" structure (space group $\mathrm{P\bar{4}2c}$) have been proposed for $\mathrm{CuIn_3Se_5}$. The latter one has been supported by determining the bond distances with XRD

refinements [129]. $CuIn_3Se_5$ is usually called an "ordered vacancy compound" or "ordered defect compound". This refers to the ordered lattice sites which the copper vacancies can occupy. It does not mean that there exists a long range order of the copper vacancies [127]. Increasing the indium amount further leads to a $CuIn_5Se_8$ phase. While it is possible to form In-rich $Cu_{1-x}In_{1+x}Se_{2+x}$, it is not possible to form a Cu-rich chalcopyrite containing more than 25% (at) Cu. In this case the excess Cu is consumed in a Cu_2Se phase. If in the following a $CuInSe_2$ absorber is labelled "Cu-rich", it refers to the growth conditions and not to the sample composition.

At high temperatures above $600\,°C$ chalcopyrite $CuInSe_2$ can transform into sphalerite $CuInSe_2$. This transition is not expected for the temperature and composition range applied in this thesis.

15. Experimental

In this chapter the methods of annealing the stacked indium selenide copper selenide precursors and of their structural characterisation are described. Furthermore the synthesis of reference samples prepared by other methods is introduced. The characterisation of both annealed stacked precursors and reference samples allows direct comparison and more knowledge and insight to be gained. All electrodeposited precursors are annealed in a closed tube furnace with elemental selenium, whilst vacuum deposited samples are prepared in a physical vapour deposition machine. Finished absorber layers and absorber formation processes are characterised by SEM, EDX, XRD, AES, and EBSD.

15.1. Synthesis

15.1.1. Electrodeposited stacked binary selenide layers

The main analysis is performed on electrodeposited binary selenide precursors. These precursors have been prepared according to chapter 11. Stacks with different Cu/In ratio will be compared (chapter 16).

15.1.2. Indium selenide + Cu + Se precursors

The in-situ XRD experiments in figure 19.7 have been performed on a precursor where the electrodeposited copper selenide layer has been substituted by an elemental Cu and Se layer. Unfortunately the electrodeposition of a smooth and compact Cu layer on top of an electrodeposited indium selenide film was not successful in this thesis. The obtained films consisted of small particles and the lateral uniformity was insufficient. Therefore the elemental Cu layer was deposited by sputtering, which resulted in a smooth film. An elemental Se layer has been evaporated on top of the Cu layer. Both layers have been deposited by Guillaume Zoppi (Northumbria University). The Se layer was supposed to provide the necessary Se during annealing, because no elemental Se was added in the hotstage experiment. Additionally it protects the sputtered copper film from oxidation. The overall composition of the complete stack is slightly Cu-rich (Cu/In atomic ratio $= 1.14$). The thicknesses of the Cu and Se layer were chosen to match the Cu/Se ratio in the electrodeposited Cu-Se film. The sputtering was done at low temperatures in order to avoid a reaction between Cu and Se. A XRD diffractogram of the complete stack shows a dominating Cu peak. Also some minor reflections of $\mathrm{Cu_3Se_2}$ are observed. The Se capping layer is amorphous.

15.1.3. Coelectrodeposited $\mathrm{CuInSe_2}$ sample

In chapter 18 the grain size and coherence length (section 18.1.1) of $\mathrm{CuInSe_2}$ absorbers prepared from electrodeposited binary selenide precursors are compared to an annealed coelectrodeposited $\mathrm{CuInSe_2}$ sample. The preparation of the annealed coelectrodeposited sample follows the procedure described by Dale et al. [21]. All elements (Cu, In, Se) are simultaneously electroplated at room temperature from a bath containing $2.6\,\mathrm{mM}$ $\mathrm{CuCl_2}$, $9.6\,\mathrm{mM}$ $\mathrm{InCl_3}$, $5.5\,\mathrm{mM}$ $\mathrm{H_2SeO_3}$, $240\,\mathrm{mM}$ LiCl in a pH 3 buffered aqueous solution. The electrodeposition potentials are $-0.476\,\mathrm{V}$ (vs. Ag | AgCl | $3\,\mathrm{M}$ KCl) for $20\,\mathrm{min}$ followed by $-0.576\,\mathrm{V}$ for $50\,\mathrm{min}$. The precursor has been annealed in the same set-up under the same conditions ($30\,\mathrm{min}$ at $550\,°\mathrm{C}$) as the electrodeposited binary selenide precursors described in section 15.2. A background gas (10% $\mathrm{H_2}$ / 90% $\mathrm{N_2}$) pressure of $10\,\mathrm{mbar}$ and excess elemental Se have been applied during the annealing. Sample "co-ED" has been annealed in the

same graphite box as the binary selenide precursors. The annealed absorber is typically single-phase Cu-poor (Cu/In atomic ratio ~ 0.8) $CuInSe_2$ chalcopyrite.

15.1.4. PVD deposited $CuInSe_2$ absorbers

For comparison purpose samples prepared by physical vapour deposition (PVD) have been added. The sample labelled "PVD-Cu-poor" (table 16.1) has been prepared in a "3-stage-process" that is usually applied for chalcopyrite solar cells with the highest efficiency [130]. In the first stage In and Se are evaporated onto the substrate having a temperature around $350\,°C$. In the second stage the substrate temperature is increased to $540\,°C$ while Cu and Se are evaporated. The substrate temperature is kept constant during the last step, when again In and Se are evaporated. The absorber composition is Cu-poor.

In the preparation of the absorber labelled "PVD-Cu-rich" constant fluxes of Cu, In, and Se have been evaporated ending up with an atomic Cu/In ratio of 1.55. The substrate temperature during the deposition has been $540\,°C$. The Cu excess is contained in copper selenide phases at the surface and can be removed by KCN etching [131, 132].

15.2. Annealing of electrodeposited precursors

The electrodeposited precursors have been annealed under Se atmosphere inside a quartz tube furnace. The samples were placed in a graphite box (together with $100\,mg$ Se powder (figure 15.1)) [133, 30, 21]. The volume inside the box was reduced by a glass slide and a graphite slide to about $20\,cm^3$. The graphite slide was placed on top of the Se powder to fix it during the pumping of the chamber. The graphite box fitted tightly into a quartz tube which contained a mixture of 10% H_2 and 90% N_2 as background gas. The pressure of the background gas was usually set to $10\,mbar$ at the beginning of the experiment and the annealing was done in a stationary atmosphere without a gas flow. The presence of hydrogen gas during in the annealing process was motivated by the idea to remove oxides from the sample. It has been shown for metal precursor stacks that annealing in a hydrogen atmosphere can prevent indium loss [134]. It has further been reported that annealing in hydrogen changes the defect concentrations in the absorber [135].

In the initial step the sample was heated to $100\,°C$ for $30\,min$ which was supposed to remove adsorbates from the surface. The actual annealing followed at $550\,°C$ for $30\,min$. At the end the sample slowly cooled down to room temperature (figure 15.2). The thermal inertia of the oven and heat losses cause a derivation of the real temperature profile of the graphite box from the ideal steps programed in the temperature controller (figure 15.2). The actual annealing temperature in °C is about 4% lower than the stated controller temperature. This was determined with an additional thermocouple directly connected to the graphite box.

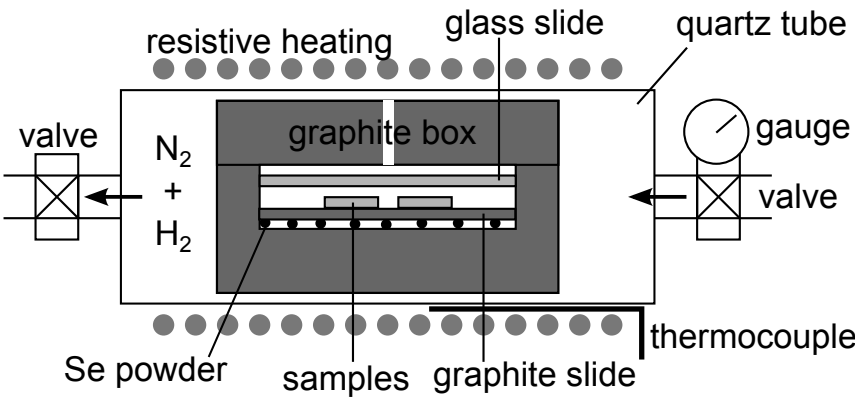

Figure 15.1.: Annealing set-up

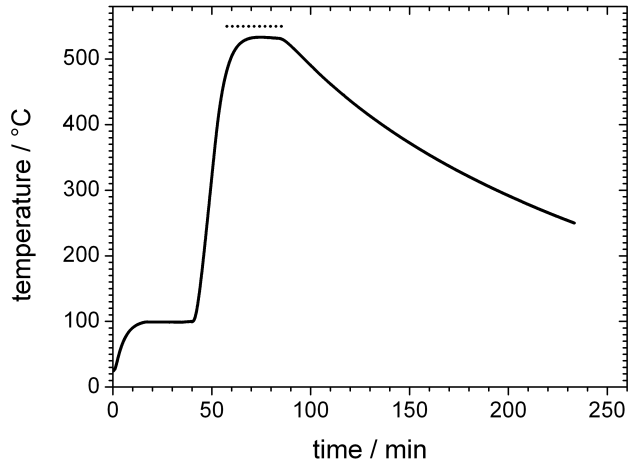

Figure 15.2.: Typical annealing temperature profile measured at the graphite box. The controller temperature is indicated by the dotted line.

15.3. Characterisation techniques

A general introduction to SEM, EDX, XRD, and ICP-MS is given in chapter 3. This chapter will discuss specific issues of the techniques related to this part of the thesis and further introduce the principles of AES and EBSD.

15.3.1. Ex-situ and in-situ XRD

The samples measured by ex-situ XRD in chapter 19.2.1 have been annealed in the oven described in the previous section 15.2. The standard conditions of $100\,\mathrm{mg}$ Se powder and a H_2/N_2 background gas pressure of $10\,\mathrm{mbar}$ have been applied. The temperature of the actual annealing step was varied between $250\,°C$ and $550\,°C$. Afterwards the annealed absorbers were analysed in a $\theta - 2\theta$ configured XRD set-up (section 3.2).

For in-situ XRD measurements the samples were annealed in a special sample stage which could be mounted to the XRD goniometer (figure 15.3). Grazing incidence configuration with an incidence angle of $4\,°$ was used to record the diffractograms (section 3.2). The sample was covered by a thin graphite dome which is transparent to X-rays, but causes additional reflections at $28.6\,°$ and $26.1\,°$. The graphite dome allows to maintain an inert atmosphere during annealing. The pressure is adjusted by an overpressure valve opening at $250\,\mathrm{mbar}$ above atmosphere. No elemental Se has been added in the annealing to avoid contamination and reaction of the stage. The temperature was linearly ramped up from $40 - 50\,°C$ to $550\,°C$ within $77\,\mathrm{min}$. 20 scans of each $4\,\mathrm{min}$ were taken during the heat up process, i.e. during each scan the temperature continuously increased by $27 - 28\,°C$. Afterwards the sample was kept at $550\,°C$ for $30\,\mathrm{min}$. Finally the sample was cooled down to $50\,°C$ again within $58\,\mathrm{min}$. Also during the constant temperature step and the cooling a new scan was recorded every $4\,\mathrm{min}$.

15.3.2. ICP-MS impurity measurements

The trace cation impurities in several samples have been studied by ICP-MS. The samples can be categorised to the following classes:

1. absorbers prepared by PVD in a 3-stage process [130]
2. absorbers prepared by annealing electrodeposited binary selenide precursors

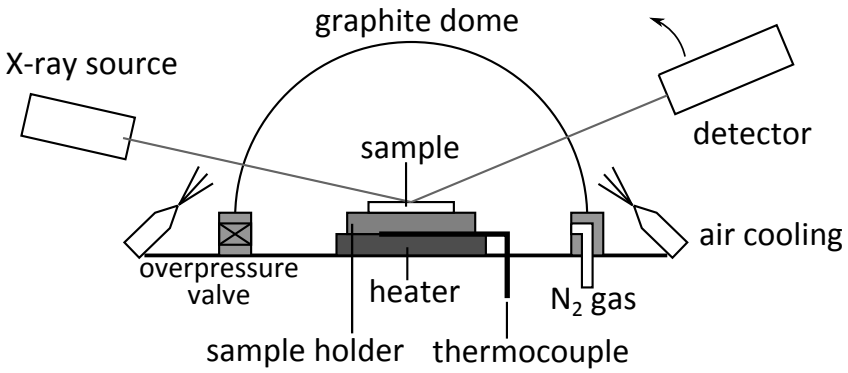

Figure 15.3.: Set-up for in-situ XRD measurements

3. precursor stacks and single layers prepared by electrodeposition

All samples have been prepared on soda-lime glass (SLG) and boro-aluminosilicate glass (BAG).

The measurement of trace cation impurities requires a more careful sample preparation than for a simple determination of film composition. Especially a long contact between the glass substrate and the acids during the dissolution process of the samples must be avoided. Otherwise the dissolution of the glass substrate increases the impurity level. The dissolution rate of Na from soda-lime glass is about $3\,\mu\mathrm{g}/\left(\mathrm{cm}^2 \cdot \mathrm{h}\right)$ at pH 2 and is therefore a significant contribution to a thin film sample of $1.4\,\mathrm{mg/cm}^2$ [136, 137]. In case of the finished absorbers the absorber layer was scraped with a highly pure Cu-plate. The obtained powder was afterwards dissolved in acid to obtain a liquid sample for ICP-MS. Scraping was not successful for samples containing an indium selenide layer, because the latter adheres strongly to the Mo substrate. These precursor stacks have been dipped with the sample side into aqua regia. As soon as the precursor and the Mo had dissolved the remaining glass substrate was taken out again. The dissolved samples were processed by ICP-MS as described in section 3.3. 5 blank solutions have been processed in the same way like the sample solutions and defined the background contamination level of the process. Also Mo coated glass substrates without sample coating have been processed to determine the impurity caused by the dissolved Mo layer. The background contamination level was subtracted from the masses measured by ICP-MS. For the precursor stacks and single layers also the Mo impurities have been subtracted.

Although ICP-MS has a detection limit of $\sim 1\,\mathrm{ppt}$ for many elements [138], the quantification limit can be much less. Its actual value depends on the element, the preparation procedure, concentration limits to avoid instrument contamination, etc. In the recent procedure especially alkali metals have a high quantification limit of $12\,\mu\mathrm{g/sample}$. Nevertheless it is still possible to discuss these results qualitatively as long as they are significantly above the background contamination level.

15.3.3. Auger-Electron Spectroscopy (AES)

Auger-Electron Spectroscopy (AES) is a surface sensitive technique to measure the composition of samples. An electron beam is focused on the sample and removes electrons from the inner shells of the atoms. The remaining hole can be filled again by the relaxation of another electron from an outer shell. The energy that is released in the relaxation process can be emitted as X-ray photon (principle of EDX). Another possibility is the exciton of an Auger electron from an outer shell (figure 15.4). The energy of the Auger electron depends on the energies of the atomic shells and is therefore characteristic for each element. The typical energy of the Auger electrons is $20 - 2000\,\mathrm{eV}$. Taking into account the mean free path of electrons in a solid only electrons generated $0.5 - 5\,\mathrm{nm}$ away from the surface can escape the sample [52]. In order to obtain depth profiles the sample is ablated by sputtering with Ar ions. The ablation is paused to record the AES spectra.

The AES depth profiles in this thesis (figures 16.1a, 16.1b, 19.3) have been recorded with a primary electron beam of $10\,\mathrm{kV}$ acceleration voltage and $1\,\mathrm{nA}$ current. The sample was sputtered with $3\,\mathrm{kV}$

Ar^+ ions and a current of $3\,\mu A$ on an area of $\sim 1\,mm^2$. The sputtering was done at an angle of about $45\,°$ to avoid roughening of the sample. The sensitivity factors of each elemental in the composition analysis have been determined on a PVD $CuInSe_2$ reference sample (Cu-rich grown and KCN-etched).

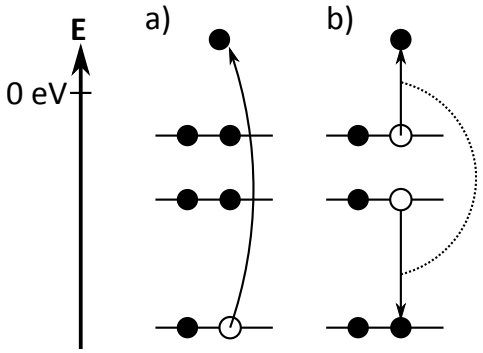

Figure 15.4.: Auger effect: a) An electron vacancy is created at an inner shell. b) When the vacancy is filled again from an outer shell, an Auger electron is emitted that carries the energy from the relaxation process.

15.3.4. Electron Backscatter Diffraction (EBSD)

Electron Backscatter Diffraction (EBSD) is a technique to obtain microscopic resolved information on the structure of a material [139]. Similar to XRD it can be used for phase identification. In this thesis it has been applied to measure the orientation of crystallites (figure 18.3). EBSD measurements can be performed in an extended SEM set-up. The electron beam is diffracted on the sample and a diffraction pattern is obtained on an area detector (figure 15.5). The orientation of the crystallite at the spot of measurement can be calculated from the pattern. The sample is scanned by the electron beam which results in an orientation map (figure 18.3, coloured map). A primary electron voltage of $15\,kV$ and a current of $5\,nA$ were used to record the EBSD maps.

While SEM cross section pictures can be taken on a simple breaking edge, EBSD maps require a more careful sample preparation. The samples have been mechanically polished, afterwards ion polished and in the end coated with a thin carbon film to ensure electrical conductivity [140].

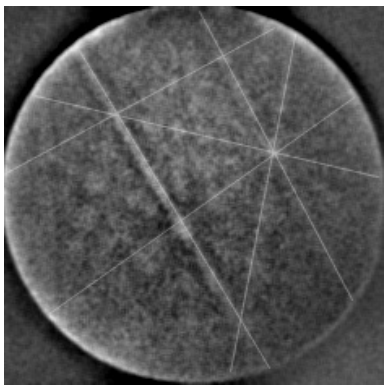

Figure 15.5.: EBSD pattern of $CuInSe_2$. The pattern lines have been redrawn with fine white lines.

16. Chemical compositional characterisation

The aims of this chapter are to define the bulk chemical composition of the samples to be used throughout the rest of this thesis and to examine the in-depth homogeneity. The bulk chemical composition, in particular the Cu/In ratio is of importance when discussing both the structural and opto-electronic properties of the absorber layer. Several absorber layers have the same composition but were annealed under different background gas pressures. Finally the in-depth chemical composition is measured for both copper rich and copper poor absorber layers to demonstrate their differences.

16.1. Sample definition and bulk chemical composition

A Cu-poor, stoichiometric and Cu-rich precursor have been electrodeposited by adjusting the thickness of the plated copper selenide top layer. Additionally two samples have been annealed under higher background gas pressure. Their precursors were intended to have a Cu/In ratio of 1, although sample "ED-stoich-500mbar" slightly deviates from this set value. All precursors have been annealed for $30\,\mathrm{min}$ at $550\,°\mathrm{C}$ (section 15.2). The composition of the annealed absorbers is shown in table 16.1. All precursors contain Se in excess, e.g. the Se/(Cu+In) atomic ratio of a stoichiometric precursor (i.e. Cu/In $= 1$) is 1.42 ± 0.08. During the annealing the excess Se evaporates and the Se/(Cu+In) atomic ratio of all absorbers is close to 1.

The Cu-rich sample shows a higher Cu/In ratio in the as-annealed absorber than has been intended. This is probably caused by an overestimation of Cu in EDX, because the excess Cu forms copper selenide phases at the surface. The absorber is etched in a 5% potassium cyanide (KCN) solution at room temperature for $2\,\mathrm{min}$. It is known that KCN etching selectively etches copper selenide phases [131, 132]. After KCN etching the Cu-rich absorber has a Cu/In ratio of 1 indicating that excess copper was present in a secondary phase. The presence of copper selenide in sample "ED-Cu-rich-10mbar" will be confirmed by XRD in figure 17.3. For comparison purpose samples prepared by physical vapour deposition (PVD) have been added (section 15.1.4).

16.2. Composition Depth Profiles

Composition depth profiles have been recorded by AES to check if the reaction of the precursor stack is complete or if residuals of the initial phases are left.

In case of the KCN etched "ED-Cu-rich-10mbar" precursor the measured composition is constant from the surface to the back contact (figure 16.1a). The elemental ratios correspond to the stoichiometric composition Cu:In:Se $= 1 : 1 : 2$. That means the complete indium selenide layer has reacted into $\mathrm{CuInSe_2}$ and the Cu excess has formed copper selenide phases at the surface (see chapter 17.3) which have been removed by KCN etching. The situation is different for the "ED-Cu-poor-10mbar" precursor. The top $1800\,\mathrm{nm}$ have a constant Cu-poor composition (Cu/In atomic ratio 0.8). However close to the back contact the Cu-concentration drops while In and Se increase. It must be assumed that the back side of the absorber is not completely reacted. Depending on the degree of Cu-incorporation at the back either $\mathrm{In_2Se_3}$, an ordered vacancy compound ($\mathrm{CuIn_3Se_5}$ or $\mathrm{CuIn_5Se_8}$) or a very Cu-deficient $\mathrm{CuInSe_2}$ is formed. The relative composition at the interface is Cu:In:Se $= 1 : 3.3 : 5.8$ (measured at $2150\,\mathrm{nm}$ depth, where the In signal is maximum) which is close to the vacancy compound $\mathrm{CuIn_3Se_5}$. An accurate determination of the composition at the

	preparation	
sample	intended Cu/In	annealing pressure
ED-stoich-10mbar	1	$10\,\mathrm{mbar}$
ED-Cu-rich-10mbar	1.2	$10\,\mathrm{mbar}$
ED-Cu-poor-10mbar	0.85	$10\,\mathrm{mbar}$
ED-stoich-500mbar	1	$500\,\mathrm{mbar}$
ED-stoich-1000mbar	1	$1000\,\mathrm{mbar}$

	after annealing		after KCN etch	
sample	Cu/In	Se/(Cu+In)	Cu/In	Se/(Cu+In)
ED-stoich-10mbar	0.98	0.99	0.98	0.97
ED-Cu-rich-10mbar	1.47 ± 0.12	0.92	1.02	1.00
ED-Cu-poor-10mbar	0.92	1.03	0.91	1.02
ED-stoich-500mbar	0.94	1.04	0.94	0.99
ED-stoich-1000mbar	1.03	1.05	1.03	1.03
PVD-Cu-poor	0.92	1.03		
PVD-Cu-rich	1.55	0.91	1.03	1.03

Table 16.1.: Preparation conditions (first table) and composition (second table) of $\mathrm{CuInSe_2}$ absorbers which are further analysed in parts II and III of this thesis. "ED" denotes electrodeposited precursors and "PVD" absorbers synthesised by physical vapour deposition (section 15.1.4). All atomic ratios are averages of 2-4 EDX measurements. Their error is around ± 0.05 if not otherwise stated. The etching was done for $2\,\mathrm{min}$ in a 5% KCN solution at room temperature.

backcontact is difficult, because the signal drops fast. Nevertheless the Cu content is probably too low to allow a very Cu-deficient $\mathrm{CuInSe_2}$ phase.

In summary the composition of the annealed absorbers can be simply controlled by adjusting the layer thicknesses in the precursor stack, because no major change in Cu/In ratio is observed during the annealing. The uniformity of the samples is sufficient to compare different growth conditions (e.g. Cu content or background gas pressure during annealing). The composition depth profile is constant in the Cu-rich case but an incomplete reaction causes an ordered vacancy phase (probably $\mathrm{CuIn_3Se_5}$) at the back contact for the Cu-poor sample.

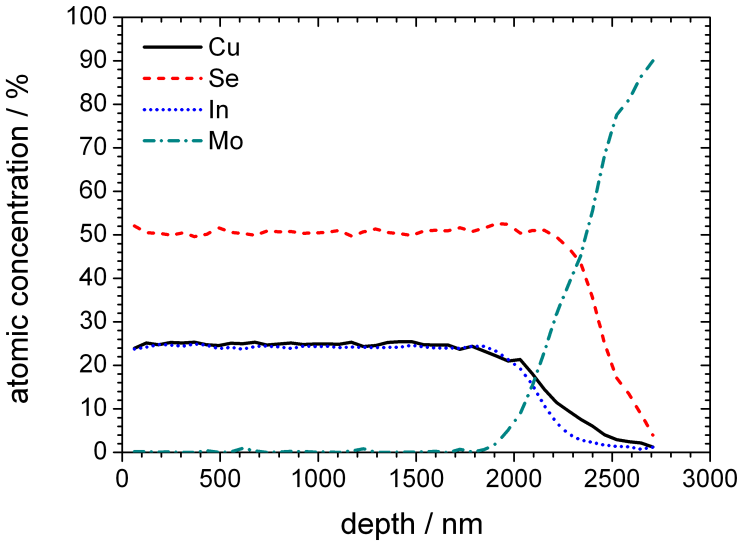

(a) Sample "ED-Cu-rich-10mbar"

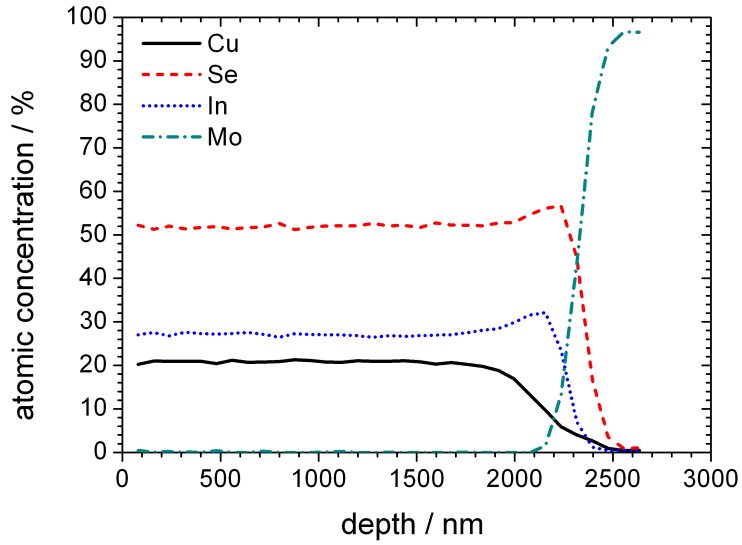

(b) Sample "ED-Cu-poor-10mbar"

Figure 16.1.: Composition depth profiles determined by AES of a) a Cu-rich b) a Cu-poor $CuInSe_2$ absorber after KCN etching. The settings of the AES measurements are given in section 15.3.3.

17. Crystallographic characterisation of the absorber layer

X-ray diffraction is a powerful technique which enables the crystallographic structure of the phases present in a thin film to be measured. Further it can be used to detect secondary phases, estimate crystal sizes, measure unit cell distortions, and show the presence of strain. In this chapter XRD measurements are used to demonstrate that $\mathrm{CuInSe_2}$ was indeed formed from the annealed stacked binary precursors and also a minority copper selenide phase was observed for the copper rich samples. Detailed measurements of the unit cell proportions were made for all samples, including reference samples, to see if the Cu/In ratio or annealing conditions effected the ratio of the dimensions, and hence the unit cell distortion. This chapter begins with a brief discussion of the chalcopyrite $\mathrm{CuInSe_2}$ unit cell and a survey of the literature on unit cell distortions.

17.1. Background

17.1.1. Structure of chalcopyrite

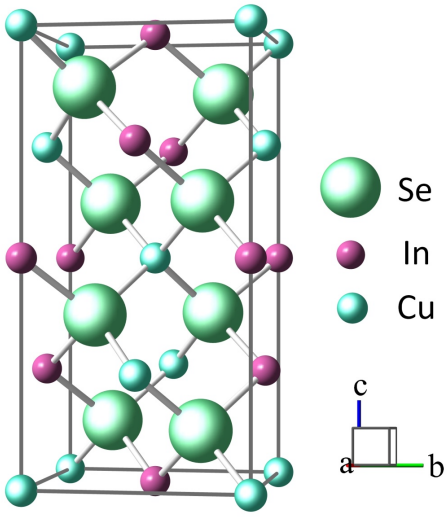

Figure 17.1.: Structure of chalcopyrite $\mathrm{CuInSe_2}$

Chalcopyrite $\mathrm{CuInSe_2}$ belongs to the tetragonal crystal system. Its structure is shown in figure 17.1.

For a tetragonal crystal system the lattice plane distance d_{hkl} in diffraction experiments is connected to the Miller indices (hkl) of the peak by [141]:

$$\frac{1}{d_{hkl}^2} = \frac{1}{a^2}\left(h^2 + k^2 + \frac{a^2}{c^2}l^2\right) \tag{17.1}$$

with a and c being the lattice constants. The diffraction angle θ_{hkl} can be calculated with the knowledge of the wavelength λ of the incident beam by the Bragg condition:

$$\sin\theta_{hkl} = \frac{\lambda}{2d_{hkl}} \tag{17.2}$$

Chalcopyrite $\mathrm{CuInSe_2}$ belongs to space group $\mathrm{I\bar{4}2d}$, i.e. the extinction rules from table on the current page apply for the observed reflection hkl [142, 143].

reflex	hkl	hhl	$hk0$	$0kl$
condition	$h+k+l=2n$	$2h+l=4n$	$h+k=2n$	$k+l=2n$

reflex	$00l$	$h00$	$h\bar{h}l$
condition	$l=4n$	$h=2n$	$h=2n$

Table 17.1.: Extinction rules of the space group $\mathrm{I\bar{4}2d}$ [142, 143]

17.1.2. Tetragonal distortion

From equation 17.1 it is obvious that the (204) and (220) peaks coincide for a chalcopyrite structure with $c = 2a$. For $\mathrm{CuInSe_2}$ the lattice is slightly distorted in a way that the tetragonal distortion parameter $\eta = c/2a$ is above 1. This causes a splitting between the peaks. The extent of the splitting depends on η and also on the value of the lattice parameter a.

The tetragonal splitting in a $\mathrm{CuInSe_2}$ absorber decreases with a lower Cu/In ratio. This has been reported by Merino et al., who grew polycrystalline samples of various Cu/In ratios from a melt [144]. They obtained the lattice parameters a and c from Rietveld refinement of the XRD diffractograms. The splitting can then be calculated by equation 17.1. It is interesting to note that the distortion parameter $\eta = 1.005$ was constant for all compositions. The observation of η being constant has been recently confirmed by refinements from neutron scattering experiments on powder samples with Cu/In ratios between 0.84 and 1.04 [145, 146]. That means the trend in the splitting is not caused by a different distortion of the lattice but the size of the unit cell changes with film composition. The data of Merino et al. can be approximated by linear regression:

$$\Delta d[\mathrm{pm}] = d_{204} - d_{220}\,[\mathrm{pm}] = (0.41 \pm 0.04) + (0.10 \pm 0.05) \cdot (\mathrm{Cu/In}) \tag{17.3}$$

Δd denotes the splitting of the d_{hkl} values for the (204) and (220) reflection in picometres. (Cu/In) is the atomic ratio in the film. It should be noted that the Cu/In ratio in [144] was determined from the occupancy of the Cu sites in the refinement. The Cu/In ratio determined by EDX can deviate from the one obtained by the refinement if Cu ions are located on interstitial sites [144]. Paszkowicz et al. accurately determined the lattice constants of stoichiometric $\mathrm{CuInSe_2}$ by Rietveld refinement of a powder sample [147]. From these values a difference in lattice plane distance of $\Delta d = (0.4922 \pm 0.0006)\,\mathrm{pm}$ can be calculated by formula 17.1.

The distortion parameter η has also been determined for coevaporated thin film absorbers in [148]. In this case η and the lattice constant a both change with Cu/In ratio. A Δd splitting of $1.6\,\mathrm{pm}$ for Cu/In $= 0.86$ and $2.7\,\mathrm{pm}$ for Cu/In $= 1.23$ can be calculated from the reported values. The splitting in the thin film absorber is $3-5$ times larger than in bulk or powder samples and also its change with Cu/In ratio is about 30 times more. Nevertheless this result must be interpreted sceptically, because the lattice parameters have not been determined by an accurate refinement but from a simple Nelson-Riley plot with three or less datapoints [148].

Kötschau determined the lattice constants of coevaporated $\mathrm{CuInSe_2}$ thin film absorbers with various Cu/In ratios by Rietveld refinement. For Cu-poor absorbers he obtained the following dependence of the lattice constants on the atomic Cu/In ratio [149]:

$$a = (5.798 \pm 0.003)\text{Å} - (1 - \mathrm{Cu/In}) \cdot (0.057 \pm 0.007)\text{Å} \tag{17.4}$$

$$c = (11.624 \pm 0.013)\text{Å} - (1 - \mathrm{Cu/In}) \cdot (0.155 \pm 0.032)\text{Å} \tag{17.5}$$

The corresponding splitting of the lattice planes Δd can be calculated from the lattice parameters by equation 17.1.

It has been reported that the tetragonal distortion in Cu-poor Cu-III-VI_2 (with III = In or Ga; VI = Se or S) is linked to the grain size of the material [146]. A deviation from $\eta = 1$ causes strain inside the lattice and promotes the formation of extended defects. These defects lead to a reduced grain size during the crystallisation process. This argumentation is not longer valid for Cu-rich material. A higher Cu content can accelerate the kinetics of grain boundary motion which promotes a homogeneous micro-structure of the bulk material [146].

Balboul et al. state that the best device performance is obtained if the tetragonal splitting vanishes (i.e. $c = 2a$) [150]. They conclude this from a series of samples, where the Ga content is varied from $\mathrm{CuInSe_2}$ to $\mathrm{CuGaSe_2}$. At an atomic ratio of $\mathrm{Ga}/(\mathrm{Ga}+\mathrm{In}) \approx 0.2$ the device efficiency is maximised and the splitting vanishes.

In summary the change of the tetragonal splitting with Cu/In ratio is larger for thin films than for bulk or powder samples. There are indications that a reduced tetragonal splitting ($\eta \approx 1$) is correlated to a better solar cell performance.

17.2. Results and Discussion

The XRD diffractogram in figure 17.2 verifies the formation of the $\mathrm{CuInSe_2}$ chalcopyrite structure for the annealed samples. This is true for all samples mentioned in table 16.1. In case of the Cu-rich precursor additional copper selenide ($\mathrm{Cu_{2-x}Se}$) is formed as a secondary phase. Its peaks are close to the main reflections of $\mathrm{CuInSe_2}$ (figure 17.3). It is expected from the phase diagram of Cu-In-Se that in case of Cu-rich growth conditions stoichiometric $\mathrm{CuInSe_2}$ is formed and the copper surplus leads to the appearance of $\mathrm{Cu_2Se}$ secondary phases (figure 14.3). Etching in a KCN solution removes the peaks in XRD indicating that the copper selenide phases are present at the surface of the absorber [131, 132].

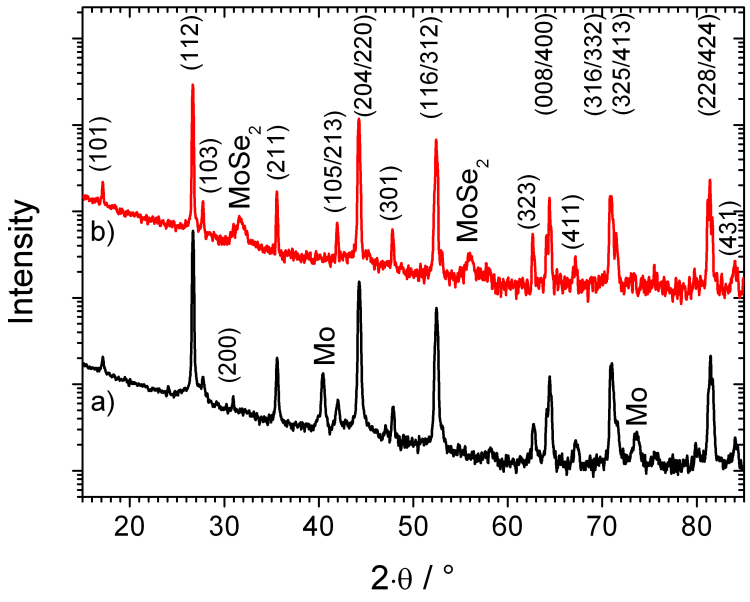

Figure 17.2.: GI-XRD diffractograms of annealed Mo/In-Se/Cu-Se samples after KCN etching. The background annealing pressure has been a) $10\,\mathrm{mbar}$ ["ED-stoich-10mbar"] and b) $1000\,\mathrm{mbar}$ ["ED-stoich-1000mbar"]. The reflections of $\mathrm{CuInSe_2}$ are labelled with their corresponding Miller indices. The grazing tube angle ($4°$) has been chosen to record also a part of the substrate signal.

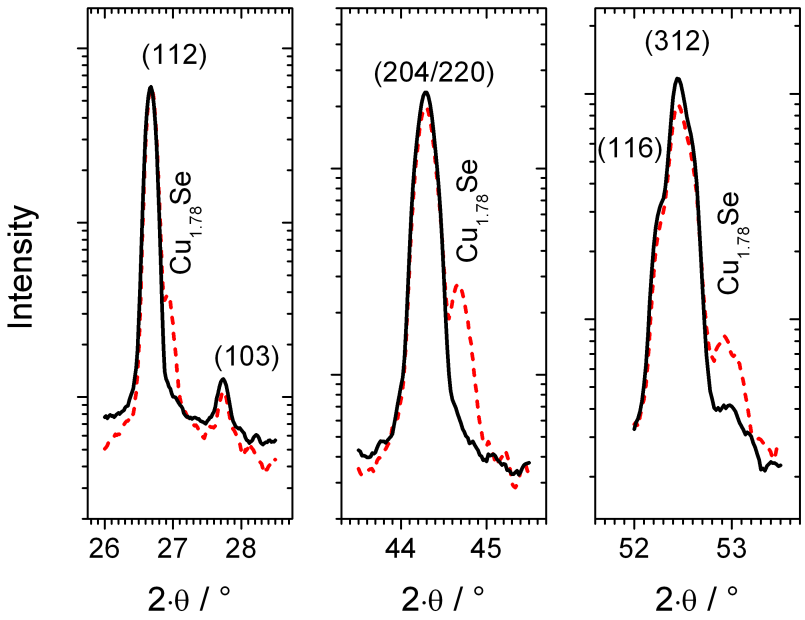

Figure 17.3.: Main XRD reflections of the Cu-rich sample "ED-Cu-rich_10mbar" directly after annealing (dashed line) and after 120 s KCN etching (solid line). The Miller indices refer to directions in $CuInSe_2$. All diffractograms have been normalised to the (112) reflection and slightly smoothed.

The composition depth profile of sample "ED-Cu-poor-10mbar" has shown a secondary phase at the back contact (figure 16.1b). It is interesting to see if this is validated by XRD. There are no additional reflections observed for the sample "ED-Cu-poor-10mbar" in comparison to the stoichiometric sample "ED-stoich-10mbar" (not shown). The prominent (110) and (116) peaks of $\gamma - In_2Se_3$ are located at 24.97 ° and 37.55 °, where they do not interfere with $CuInSe_2$. Also the major reflections of other In_2Se_3 polymorphs have peaks which are clearly separated from the $CuInSe_2$ reflections. This rules out the formation of an In_2Se_3 phase at the back.

The structure of $CuIn_3Se_5$ is similar to $CuInSe_2$ and most reflections are very close to each other. Since the contribution of $CuIn_3Se_5$ is expected to be low, it can probably not be resolved from the $CuInSe_2$ peaks. However due to less restrictive extinction rules several reflections exist for $CuIn_3Se_5$ exclusively[1]. None of them are observed for "ED-Cu-poor-10mbar". In contrast to In_2Se_3 the mentioned reflections are not the most intense peaks but rather weak side peaks. Since the secondary phase is located at the back contact and is only a minor share of the total absorber, it is likely that the reflections disappear in the background noise. Combining the results from the composition profile (figure 16.1b) and the diffractogram it can be assumed that the back contact phase in sample "ED-Cu-poor-10mbar" is an ordered vacancy compound; probably $CuIn_3Se_5$. A very Cu-deficient $CuInSe_2$ phase can be excluded, because of the low Cu content at the back. An

[1]

$2\theta/°$	15.37	21.81	35.25	47.30
reflections	(002)	(102)	(114)	(006)
	(100)	(110)	(212)	(214)
				(222)
				(300)

Reflections of $CuIn_3Se_5$ which are excluded for $CuInSe_2$. The positions have been calculated with the software "Powdercell"[151] from the data in [129]. There are additional exclusive peaks of $CuIn_3Se_5$ which are not mentioned, because their intensity is either very weak or they are interfering with close $CuInSe_2$ reflections.

In_2Se_3 phase can be ruled out, because the major XRD reflections are absent.

The incidence angle of the diffraction set-up was chosen large enough ($4\,°$) to record signal of the Mo substrate. For sample "ED-stoich-1000mbar" annealed at a high background gas pressure no Mo reflection can be observed any more in the diffractogram 17.2b. Instead, peaks of molybdenum selenide $MoSe_2$ appear. The higher background gas pressure has slowed down the outdiffusion of Se vapour from the heating zone in the oven and the increased Se partial pressure selenised the Mo back contact. A similar observation has been made by Volobujeva et al. for coelectrodeposited $CuInSe_2$ absorbers that have been annealed under different Se overpressures. In this case the thickness of the $MoSe_2$ layer at the back increases with the Se pressure [152].

A way to learn more about the lattice parameters of $CuInSe_2$ is to look at the splitting of the (204)/(220) peak doublet. It requires a high resolution but is rather insensitive to height displacement of the sample or a position offset of the detectors. In figure 17.4a and 17.4b the experimental data has been fitted with two peak profiles in order to locate the position of the reflections. Each peak profile is a superposition of two Pseudo-Voigt functions taking into account that two X-ray wavelengths (Cu Kα_1 and Kα_2) are present in the diffraction. It can already be observed in figure 17.4 that the Cu-rich sample "ED-Cu-rich-10mbar" shows a slightly larger splitting than the Cu-poor one ("ED-Cu-poor-10mbar").

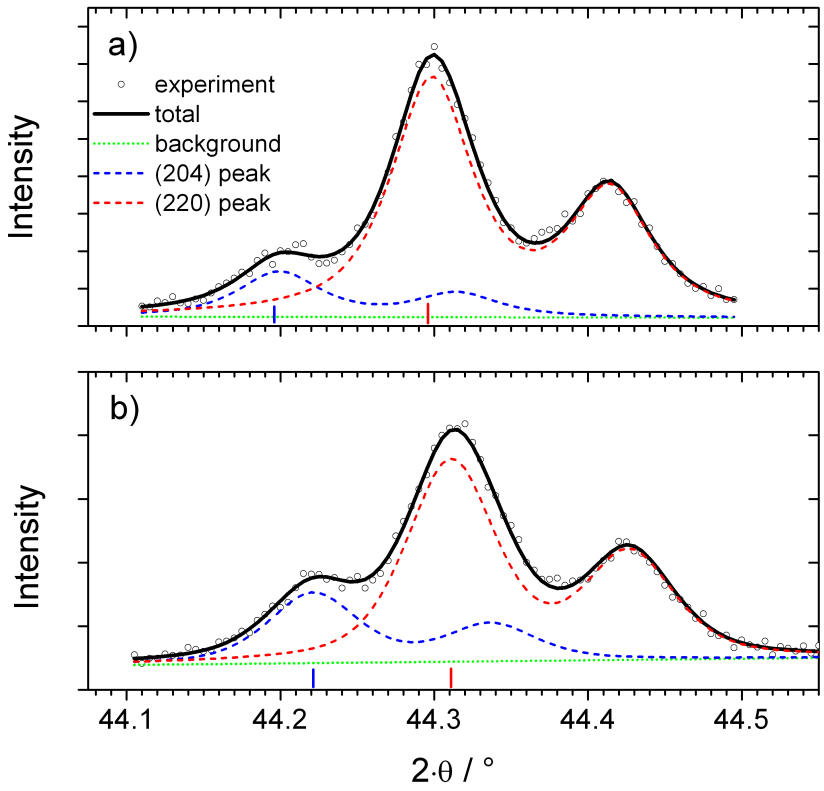

Figure 17.4.: Highly resolved XRD diffractogram of the splitting between (204) and (220) peak in $CuInSe_2$ for samples a) "ED-Cu-rich-10mbar" and b) "ED-Cu-poor-10mbar". The peak doublet has been fitted with a Pseudo-Voigt profile. Each reflection is doubled by the presence of the Cu Kα_1 and Kα_2 line. The positions of the Kα_1 maxima for the (204) and (220) reflection are marked on the axis. The diffractogram has been recorded in Bragg-Brentano configuration with a parallel beam. The x-axis is valid for both subplots. The fitting was done with the software WinPlotr [153].

This trend is confirmed in table 17.2 where the splitting of all samples from table 16.1 is recorded. The splitting of the (204)/(220) is reduced the more Cu-deficient the chalcopyrite absorber is.

		tetragonal splitting		
		(exp.)	(calc. bulk)	(calc. thin film)
sample	Cu/In atomic ratio	$\Delta d/\mathrm{pm}$	$\Delta d/\mathrm{pm}$	$\Delta d/\mathrm{pm}$
ED-Cu-poor-10mbar	0.91	0.394	0.501	0.215
PVD-Cu-poor	0.92	0.384	0.502	0.218
ED-stoich-500mbar	0.94	0.411	0.504	0.225
ED-stoich-10mbar	0.98	0.415	0.508	0.240
ED-Cu-rich-10mbar	1.02	0.435	0.512	0.254
ED-stoich-1000mbar	1.03	0.406	0.513	0.258
PVD-Cu-rich	1.03	0.473	0.513	0.258

Table 17.2.: Splitting between (204) and (220) reflections in XRD for Cu $K\alpha_1$ radiation. The composition after KCN etching has been taken from table 16.1. The experimental splitting was determined from fitting high resolved diffractograms of the (204)/(220) doublet (figure 17.4). The splitting was calculated for bulk absorbers by equation 17.3 [144] and for thin film absorbers by equations 17.4, 17.5, and 17.1 [149]. The latter equations have been reported for Cu-poor absorbers and are extrapolated to an atomic Cu/In ratio of 1.03. The errors are the following: Cu/In ratio ± 0.05, experimental splitting $\pm 0.006\,\mathrm{pm}$, calculated bulk splitting $\pm 0.06\,\mathrm{pm}$, calculated thin film splitting $\pm 0.21\,\mathrm{pm}$.

Table 17.2 also contains Δd values interpolated from the bulk samples of Merino et al. (equation 17.3) [144]. The change of the tetragonal splitting with composition is about eight times more for the thin film absorbers measured in this thesis. Therefore it must be concluded that the change in the composition is not the only cause for the different tetragonal splitting. It is likely that strain in the thin film also affects the lattice constants and the distortion parameter η and thus influences the splitting. Then it can be assumed that Cu-poor growth conditions cause a strain that reduces the lattice distortion and brings it closer to $\eta = 1$. In this way the Cu/In ratio is not directly influencing the splitting but indirectly through a change of strain in the thin film. Since equation 17.3 was approximated for polycrystalline bulk samples it does not include a possible strain effect for thin films.

The tetragonal splitting Δd calculated from the coevaporated thin film samples of Kötschau (equations 17.4 and 17.5) [149] is roughly half the value that has been measured in this thesis (table 17.2). The difference is within the error of the measurement. The statistical error calculated from the errors of the lattice constants is large, because two similar d values are subtracted to obtain the splitting Δd. The error of Δd is mainly determined by the errors of the lattice constants and the Cu/In ratio. If only the errors of the composition dependence of the lattice constants are taken into account the error of Δd decreases to values between $\pm 0.008\,\mathrm{pm}$ and $\pm 0.036\,\mathrm{pm}$. That means although the absolute value of the calculated Δd is uncertain, it is still possible to compare the relative differences between the samples. The change in the tetragonal splitting Δd with absorber composition calculated from the coevaporated thin film samples of Kötschau [149] is about half the value that has been measured in this thesis (table 17.2). Thus the change of Δd with composition measured in this thesis is similar to coevaporated $\mathrm{CuInSe_2}$ thin films but different to bulk absorbers. Therefore it can be concluded that the change in Δd with composition measured for our absorbers is not an effect of the absorber preparation from electrodeposited binary selenides but an effect of the thin film configuration. It supports the hypothesis of composition dependent strain in the thin film.

Strain is also a possible explanation why the high-pressure annealed sample "ED-stoich-1000mbar" does not integrate into the general trend. Its grain size is several times larger than for the other

samples (figure 18.1) which can have stronger effects on the strain (e.g. the absence of stress relieving grain boundaries) than the composition difference in growth.

In summary the formation of chalcopyrite $\mathrm{CuInSe_2}$ has been verified for absorbers annealed from electrodeposited binary selenide stacks. A Cu-rich precursor stack leads to an additional formation of $\mathrm{Cu_{2-x}Se}$ phases. The tetragonal splitting of the (204) and (220) reflection varies with composition. This variation is larger than expected from bulk measurements in literature. It can be explained by composition dependent strain in the thin film.

18. Absorber layer structural crystal quality

High quality absorber layers of Cu(In,Ga)Se_2 normally consist of grain sizes of above one micron that often extend from the back contact to the buffer layer. However, absorber layers produced by electrodeposition and annealing often have smaller grain sizes, if the annealing step does not recrystallise the precursor. The role of grain boundaries in Cu(In,Ga)Se_2 absorber layers is still unclear, but the highest efficiency devices have very few of them, and hence larger grains are preferable. In this chapter the basic principle of grain size determination from x-ray diffraction patters is explained, and applied to all the fabricated absorber layers. Results are compared with measurements obtained from SEM and EBSD measurements. Specifically the hypothesis that stacked binary selenide precursor layers can give larger grains after annealing than precursors where all the elements at once have been deposited is tested.

18.1. Background

18.1.1. Scherrer formula

The grain size of a material is often determined by a SEM picture of its cross section. This method makes use of the fact that a weakly bonded mineral tends to break along its grain boundaries [154]. However it is often difficult to estimate the grain size from SEM cross section. In addition these grains are not necessarily single crystals. Therefore it is helpful to use XRD diffraction data as a complementary method to determine crystal quality. The broadening of the reflections in XRD depends on the number of contributing lattice planes, similar to the diffraction at multiple slits. It is possible to obtain a coherence volume from the breadth of the reflections. Within the coherence volume the material is a perfect single crystal without grain boundaries or stacking faults. The average dimension D of the coherence volume is given by the modified Scherrer formula[1] [155]

$$D = \frac{\lambda}{\beta_{size}(2\theta) \cdot \cos(\theta)} \tag{18.1}$$

λ is the X-ray wavelength, θ the diffraction angle, D the coherence length, and $\beta_{size}(2\theta)$ the integral breadth (peak area divided by maximum height) of the reflection in radians. It must be considered that the measured integral breadth β_{obs} of the XRD reflection contains a contribution β_{instr} of the instrumental broadening which has to be deconvolved before. In case of Pseudo-Voigt profiles this deconvolution can be approximated by the subtraction [156]

$$\beta_{size} \approx \beta_{obs} - \frac{\beta_{instr}^2}{\beta_{obs}} \tag{18.2}$$

The accuracy of β_{size} is improved if the instrumental broadening β_{instr} is reduced as much as possible. In the following measurements the resolution of the XRD instrument has been improved to $\beta_{instr}\,(2\theta \approx 30\,^\circ) = 0.05\,^\circ$ by using a $0.1\,\mathrm{mm}$ small divergence slit and anti-scatter slit (section 3.2).

Micro-strain inside the sample can also contribute to the width of the diffraction peaks. This has been described by Wilson and Stokes [157]:

$$\beta_{strain} = \frac{\cot(\theta)}{\eta_{strain}} \tag{18.3}$$

[1] The original Scherrer formula is $D = \frac{K \cdot \lambda}{\mathrm{FWHM}(2\theta) \cdot \cos(\theta)}$. It is derived for the full-width half-maximum (FWHM) of the reflections and contains a form factor K which depends on the shape of the coherence volume and is usually close to unity [155].

η_{strain} is the "apparent strain" and a measure for the distortion in the lattice. The different angular dependence of β_{size} and β_{strain} allows to separate both contributions. If only a single peak is analysed it is not possible to distinguish size and microstrain broadening.

18.1.2. Influence of Se partial pressure on grain size and coherence length

It has been shown for coelectrodeposited precursors and metal stacks that a higher Se pressure in the selenisation process can considerably increase the grain size [25, 24, 158, 152]. Lopez-Garcia and Guillen annealed Cu/In precursors in a partially closed graphite box containing different amounts of elemental Se [158]. For higher additions of Se they observed a larger coherence length in XRD and a more pronounced (112) orientation. These effects are weakened again if the amount of Se excess is too high. The copper selenide phase detected after annealing changes from $\mathrm{Cu_{2-x}Se}$ to CuSe if more Se is present.

Guillemoles et al. have been the first who studied the improvement of coelectrodeposited precursors by annealing in Se atmosphere [24, 25]. They annealed in a two-temperature-zone furnace that allowed them to vary the sample substrate temperature and the temperature of the Se atmosphere separately and showed that an absorber annealed under high Se pressure gives grains with a lateral extension up to $5\,\mu\mathrm{m}$ [24]. For moderate Se pressures the absorber composition has an influence on the recrystallisation revealing larger grains for Cu-rich samples than for In-rich ones. The presence of Se during annealing is essential to obtain a photoluminescence response, because otherwise non-radiative recombination processes dominate. On the other hand excess Se causes a "dead layer" at the surface that has a high defect density, is very conductive and therefore shunts the finished device. Guillemoles et al. also present a growth model to explain the important role of Se in the recrystallisation process. The model contains two possible mechanisms that can also act together.

The first mechanism explains the recrystallisation by a liquid phase sintering process [25]. A Se-rich liquid phase surrounds the $\mathrm{CuInSe_2}$ grains and attracts them by capillary forces. The liquid allows high interdiffusion rates between the grains resulting in a faster process than solid state sintering [159]. A liquid assisted growth has also been proposed for the rapid thermal annealing of polycrystalline $\mathrm{CuInSe_2}$ absorbers which enhances the grain size [160, 9]. The liquid is supposed to consist of molten copper selenide phases. It can either accelerate the ion diffusion between the grains or serve as a fluxing agent for the dissolution of $\mathrm{CuInSe_2}$. These rapid thermal annealing experiments have been performed at $850\,°\mathrm{C}$. In case of the annealings at $400-450\,°\mathrm{C}$ by Guillemoles et al. the temperature is not sufficient to melt copper selenide (melting point $523\,°\mathrm{C}$ according to reaction 14.6; figure 14.2). Therefore it is assumed that elemental Se forms the liquid phase (melting point $\approx 220\,°\mathrm{C}$ [89]) [25].

The second mechanism explains why Se can also favour recrystallisation in the solid state. Se-rich material has a high density of cation vacancies and therefore promotes the diffusion of copper and indium ions. The higher mobility of the cations improves recrystallisation and diminishes defects in the material. On the other hand negatively charged cation vacancies are trapped at the surface of the $\mathrm{CuInSe_2}$ due to its p-type band bending. This could explain the reason for the observed "dead layer".

Chen and Wang have recently reported that the grain size of $\mathrm{CuInSe_2}$ from a mixture of $\mathrm{Cu_2Se}$ and $\mathrm{In_2Se_3}$ nanoparticles significantly enlarges, if the annealing is done in an elemental Se atmosphere [161]. Similar to Guillemoles they assign the larger grain size to the presence of a liquid during growth. They postulate a low melting Se-rich copper selenide phase as flux agent above $450\,°\mathrm{C}$, but do not give experimental proof for this.

18.2. Results and Discussion

One motivation for the application of binary selenide precursors has been the idea of improved crystallisation during the annealing. The higher reactivity of the binary selenide phases in comparison

to coelectrodeposited precursors provides an additional driving force for (re-) crystallisation (section 2.3). SEM cross section pictures (figure 18.1) confirm this idea. The grain size of an annealed co-electrodeposited sample (section 15.1.3) is estimated below $100\,\mathrm{nm}$ from the SEM cross section. For a binary selenide precursor annealed under the same conditions (figure 18.1b) the average grain size is estimated from the SEM cross section to be around $1\,\mu\mathrm{m}$. This value refers to the bulk of the layer. At the surface also smaller grains (some hundred nm) are scattered, which cannot be explained by copper selenide phases, because the grains resist KCN treatment. The same morphology is observed for all electrodeposited sample in table 16.1 that have been annealed at $500\,\mathrm{mbar}$ background gas pressure or below. A further increase in grain size is observed, when the binary selenide stacks are annealed at a high background gas pressure of $1000\,\mathrm{mbar}$ instead of $10\,\mathrm{mbar}$. In this case grains with a lateral grain size above $5\,\mu\mathrm{m}$ extending from the backcontact to the surface are observed.

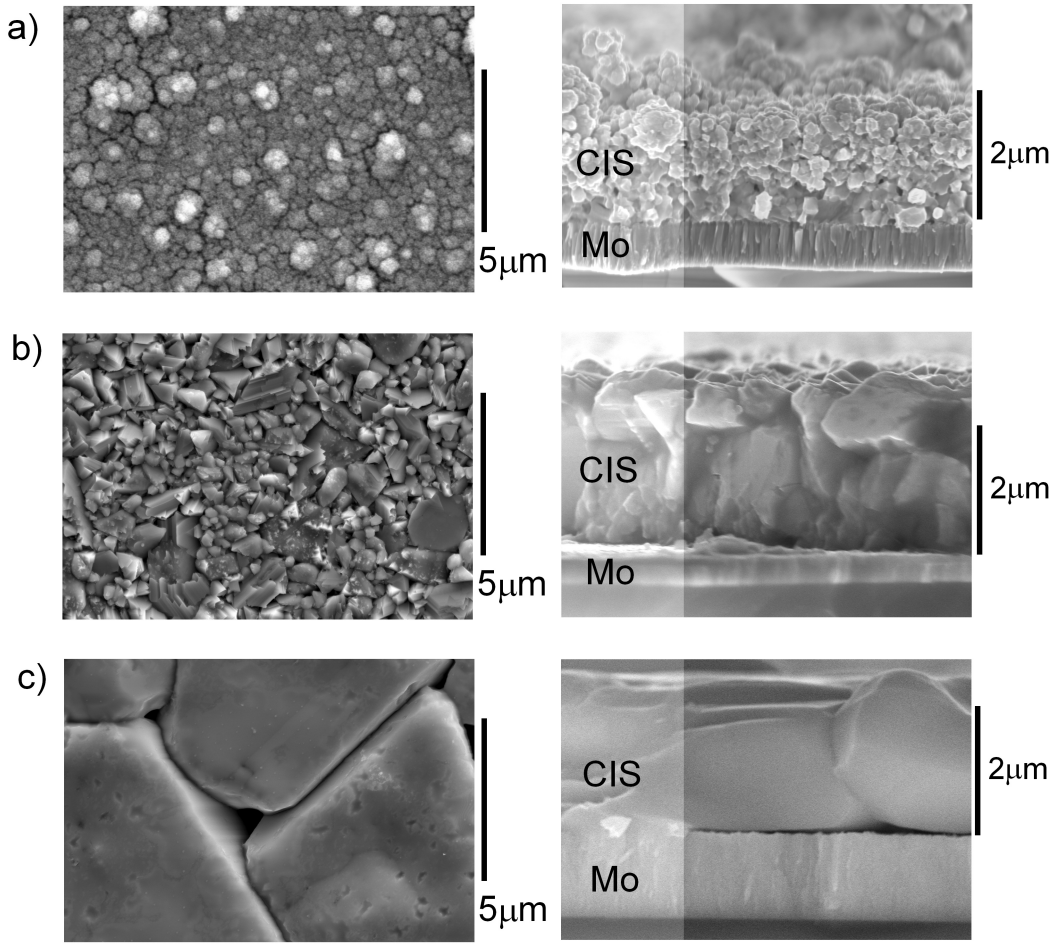

Figure 18.1.: SEM pictures in top view and cross section view of a) a coelectrodeposited $\mathrm{CuInSe_2}$ absorber "co-ED" (section 15.1.3) b) sample "ED-stoich-10mbar" and c) sample "ED-stoich-1000mbar" annealed at high background pressure. The last two samples have been etched in KCN.

Figure 18.2 shows the (112) X-ray reflection for a coelectrodeposited absorber and absorbers from binary selenide stacks annealed at low and high pressure. It is obvious that the annealed binary selenide stacks show a narrower peak width than the coelectrodeposited sample which has been annealed under the same conditions. Thus not only the apparent grain size in SEM but also the coherence length of the crystallites is improved for the binary selenide stacks. The coherence length is further increased for the binary selenide stack annealed under high background gas pressure. Table 18.1 lists the integral breadth β_{obs} and the coherence length of all samples from table 16.1 and the

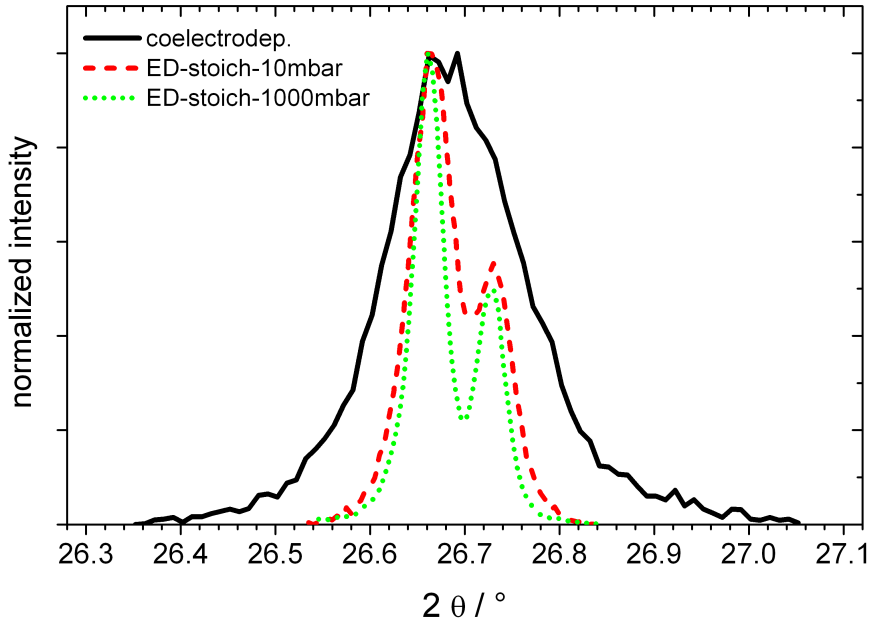

Figure 18.2.: Highly resolved XRD diffractogram of the $CuInSe_2$ (112) reflection for a coelectrodeposited ["co-ED"] and annealed absorber (solid line), a stoichiometric sample annealed at standard conditions ["ED-stoich-10mbar"] (dashed line), and an absorber annealed at high background gas pressure ["ED-stoich-1000mbar"] (dotted line).The double peak is caused by the presence of the Cu Kα_1 and Kα_2 line.

	(112) reflection		(204)/(220) reflection	
sample	$\beta_{obs}(2\theta)/°$	coherence length / nm	$\beta_{obs}(2\theta)/°$	coherence length / nm
ED-stoich-10mbar	0.068	260 ± 50	0.093	220 ± 50
ED-Cu-rich-10mbar	0.074	210 ± 40	0.091	240 ± 60
ED-Cu-poor-10mbar	0.086	150 ± 20	0.090	250 ± 70
ED-stoich-500mbar	0.056	600 ± 30		
ED-stoich-1000mbar	0.049	2000 ± 5000	0.068	∞
co-ED	0.189	50 ± 5		
PVD Cu-poor	0.057*	500 ± 200*	0.083	300 ± 100
PVD Cu-rich	0.052*	1000 ± 900*	0.075	700 ± 600
GaAs	0.047	∞		

Table 18.1.: Integral breadth β_{obs} of the highly resolved $CuInSe_2$ (112) and (204)/(220) reflections. The samples from table 16.1 have been studied plus an annealed coelectrodeposited $CuInSe_2$ absorber ("co-ED", section 15.1.3). Some reflections (marked with *) showed a small asymmetric broadening on the left side that has probably been caused by a misalignment of the diffractometer. In these cases only the right side of the peak and the Kα_2 reflection have been considered in the fit. The integral breadth of a GaAs wafer [(200) reflection] determines the instrumental resolution in case of the (112) reflection. For the (204)/(220) reflection the instrumental resolution is assumed to be close to the integral breadth of sample "ED-stoich-1000mbar". The crystal coherence length has been calculated by the Scherrer formula 18.1. The error of β_{obs} is estimated to be 10%; the error of the coherence length has been calculated by error propagation from the Scherrer formula.

annealed coelectrodeposited sample (section 15.1.3). β_{obs} has been determined from a Pseudo-Voigt fit of the peak shape (see figure 18.2) with the software WinPlotr [153]. The instrumental broadening of the instrument has been subtracted according to equation 18.2 and the crystal coherence length was calculated by the Scherrer formula 18.1. The error of the integral breadth β_{obs} can be estimated by 10%. It must be considered that the Scherrer formula has a singularity, when the observed peak width equals the instrument resolution. Therefore the error of the calculated coherence length becomes large, if the peak width is close to the instrument resolution.

Fitting the (204)/(220) doublet in figure 17.4 does not only provide the tetragonal splitting between the reflections but also their integral breadth, because the measurement has been performed in the highly resolved configuration (section 3.2). The line width of both reflections, (204) and (220), was assumed to be equal in the fitting procedure. The results are summarised in table 18.1, where the coherence length is calculated from the Scherrer formula. As an approximation the integral breadth of sample "ED-stoich-1000mbar" can be used as the instrumental resolution, because this sample shows little line broadening in case of the (112) reflection.

It has already been pointed out in section 18.1.1 that a peak broadening can also result from microstrain within the sample. The line broadening due to a limited coherence length can be separated from the broadening caused by microstrain, because of their different dependence on the diffraction angle θ. If microstrain caused a line broadening in the samples, the calculated coherence length in table 18.1 (which did not considered strain) would be different for different angles θ. Within the error of the measurement the calculated coherence length is the same for the (112) and (204)/(202) reflection for most samples. Only the Cu-poor samples show a deviation between both coherence lengths. That means in the further discussion the effect of microstrain is negligible for most samples. This holds true for the coelectrodeposited samples, although only one reflection has been measured. The coelectrodeposited absorber consists of small grains being loosely packed. It is unlikely that they are strained. Then the peak broadening in figure 18.2 is mainly due to coherence length.

The results in table 18.1 confirm the conclusion from figure 18.2. Binary selenide precursors lead to a larger coherence length in the absorber than for a coelectrodeposited sample annealed under the same conditions. The coherence length of annealed electrodeposited binary selenide stacks ($150\,\mathrm{nm}$ - $260\,\mathrm{nm}$) is still smaller than for absorbers prepared by PVD ($300\,\mathrm{nm}$ - $700\,\mathrm{nm}$). It becomes significantly larger if the background pressure during the annealing of the binary stacks is increased to $1000\,\mathrm{mbar}$.

For the binary selenide stack annealed at $1000\,\mathrm{mbar}$ the breadth of the XRD reflection is very close to the resolution limit. Therefore Electron-BackScatter-Diffraction (EBSD, section 15.3.4) maps have been recorded for samples annealed under similar conditions as "ED-stoich-10mbar" and ED-stoich-1000mbar" (figure 18.3). Theses maps show the orientation and size of each crystallite [162].

The absorber annealed at high background gas pressure shows crystallites with a lateral extension of several microns reaching from the backcontact to the surface of the layer. It turns out that the grains observed in SEM (figure 18.1c) are single crystals. The grain boundaries are parallel to the charge carrier flow through the pn-junction. It is therefore expected that they have only a minor influence on cell performance [163]. There are also grains in the standard annealed sample that extend from the backcontact to the surface. In contrast to the high pressure annealed sample their lateral extension is limited to a micron. Additionally smaller crystallites of $0.5\,\mu\mathrm{m}$ size or below are observed. It seems that some grains determined from SEM cross sections consist of several single crystals. The smaller grain size leads to boundaries which are perpendicular to the charge carrier flow and might act as recombination centres.

Thus three different methods (SEM, XRD, EBSD) confirm the increase of grain size or crystal coherence length for higher background pressure. It can be excluded that this is an effect of the different temperature profile caused by the higher gas pressure. In our oven design the heat is conducted from the resistive heating through a glass tube and the gas atmosphere to the graphite chamber (figure 15.1). A thermocouple that has been connected to one side of the graphite chamber

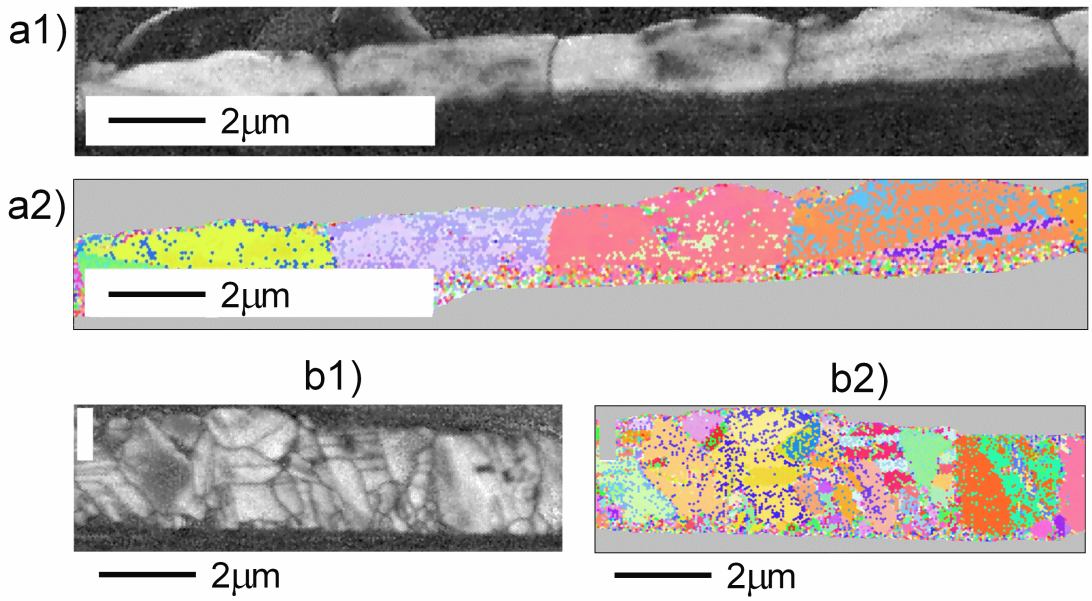

Figure 18.3.: EBSD mapping of a) absorber annealed at high background gas pressure similar to "ED-stoich-1000mbar", b) absorber annealed under same conditions as "ED-stoich-10mbar". Pictures a1 and b1 are "quality contrast maps". Light areas show a strong Kikuchi pattern. Grain boundaries weaken the Kikuchi pattern and appear dark in the "quality contrast map". EBSD maps a2 and b2 show the orientation of each crystallite. Similar colours represent close orientations. The scale bar in all pictures is approximated.

shows different temperature profiles if the background gas pressure is increased from $10\,\mathrm{mbar}$ to $1000\,\mathrm{mbar}$. The graphite chamber heats up 13% faster and reaches a $6\,°\mathrm{C}$ higher temperature at higher pressure. In order to see if the change in temperature profile can explain the different crystallisation two annealings have been performed. A high pressure annealing at a lower heating rate (similar to the one at low pressure) leads to large grains like in figure 18.1c. A low pressure annealing to a $6\,°\mathrm{C}$ higher temperature does not result in such large grains. Thus the change in the temperature profile caused by the different gas pressure is not the reason for the different grain size.

The actual cause for the different grain growth is expected to be the change in the Se partial pressure during the annealing. Although precursor and elemental selenium are placed in a graphite chamber the system is not entirely closed. This is clearly visible during the annealing, when Se vapours start condensing at the glass tube outside the heating zone. It means that the Se overpressure is only contained at the beginning of the annealing until it has diffused out of the graphite chamber. This outdiffusion of Se is slowed down if the background gas pressure in the oven is raised. In the approximation of an ideal gas the diffusion coefficient D is inverse proportional to the particle density n of the gas, i.e. $D \propto \frac{1}{n} \propto \frac{1}{p}$ with p being the pressure of the gas. A rough estimation[2]of partial

[2]Partial pressures inside the oven. The background gas pressure at $550\,°\mathrm{C}$ has been calculated by the ideal gas equation. The partial pressure of Se has been calculated from [164]. In the high pressure system the total pressure is 100 or 17 times larger at room temperature or $550\,°\mathrm{C}$, respectively.

	partial pressure Se / mbar	partial pressure N_2/H_2 / mbar	total pressure / mbar
high pressure, room temp.	0	1000	1000
high pressure, $550\,°\mathrm{C}$	140	2760	2900
low pressure, room temp.	0	10	10
low pressure, $550\,°\mathrm{C}$	140	28	168

pressures shows that the diffusion coefficient and therefore also the diffusion kinetics is between 17 and 100 times slower for $1000\,\mathrm{mbar}$ background gas pressure compared to $10\,\mathrm{mbar}$ background gas pressure. This is not only true for the outdiffusion of Se vapour of the graphite box but also true for the loss of excess Se from the precursor. Therefore the higher background pressure ensures a longer presence of Se overpressure during the annealing process. It is reported in literature that a higher Se partial pressure during annealing leads to larger grains and a longer coherence length (section 18.1.2) [25, 24, 158, 152].

In our annealing set-up a doubling of the elemental Se amount in the chamber $(200\,\mathrm{mg})$ did not change the morphology of the samples. It can be estimated that already $100\,\mathrm{mg}$ Se are enough to obtain a saturated Se vapour pressure in the current graphite box[3]. Increasing the amount of Se will therefore not increase the partial Se pressure, but prolong the presence of Se vapour in the graphite box. It provides a supply of fresh Se that replaces the losses due to outdiffusion from the box. If the absorber benefits from a higher background gas pressure during annealing but not from a doubling of the provided Se amount, it shows that the first way is more efficient to retain the Se pressure during annealing. An increase of background gas pressure is also preferred to an increase of excess Se due to practical considerations, because it reduces the consumption of toxic Se and leads to less contamination of the oven.

The idea of Guillemoles et al. that a higher Se partial pressure during annealing improves the recrystallisation of a coelectrodeposited precursor by liquid phase sintering (section 18.1.2, [25]) is also a promising explanation for the binary selenide precursors. A liquid Se phase can result from the decomposition of copper selenide as it will be discussed in chapter 19.2.1. If the background gas pressure is low, the liquid Se will evaporate, because it partly has to compensate the Se losses caused by outdiffusion from the box. (Another part of the Se losses will be compensated by the excess elemental Se which has been added to the graphite box.) A high background pressure can slow down the evaporation process and thus maintain the liquid Se phase at the surface. The liquid Se phase does not show X-ray diffraction and will not appear in the in-situ diffractograms in figure 19.5 and 19.7.

In summary it has been shown that the annealing of electrodeposited binary selenide stacks leads to a larger grain size and a longer crystal coherence length than the annealing of coelectrodeposited precursors under the same conditions. The grain size and crystal coherence length can be further enhanced, if the background gas pressure during the selenisation process is increased. The conclusion of Guillemoles et al. that an increased Se partial pressure improves recrystallisation of coelectrodeposited precursors [25] can likely be transferred to the case of electrodeposited binary selenide stacks. The higher background gas pressure has shown to be a more efficient way to maintain a high Se overpressure during annealing than an increase of excess Se provided in the annealing chamber.

[3] The dominant vapour species of selenium at $550\,°\mathrm{C}$ is Se_2 [69]. The volume of the graphite box is $20\,\mathrm{cm}^3$. The vapour pressure of selenium at $550\,°\mathrm{C}$ is $140\,\mathrm{mbar}$ [164]. According to the ideal gas equation this corresponds to a Se vapour content of $6.5\,\mathrm{mg}$ in the graphite box.

19. XRD characterisation of phase formation

19.1. Background

19.1.1. Phase reactions in binary selenide precursors

An advantage of the binary selenide precursor is the low annealing temperature necessary for the formation of $\mathrm{CuInSe_2}$ (section 19.1.2). It has been shown for Mo/InSe/CuSe and Mo/$\mathrm{In_2Se_3}$/CuSe binary selenide stacks deposited by migration enhanced epitaxy that already an annealing temperature between $250\,°\mathrm{C}$ and $270\,°\mathrm{C}$ for $1\,\mathrm{h}$ is sufficient for a complete transformation to $\mathrm{CuInSe_2}$. In both cases no intermediate phases have been observed during the reaction [165, 166]. For comparison, a co-sputtered Cu-In alloy precursor annealed at $300\,°\mathrm{C}$ for $45 - 70\,\mathrm{min}$ still contained secondary $\mathrm{In_2Se_3}$ and CuSe phases [38].

The mentioned Mo/InSe/CuSe precursor in the work of Kim et al. was heated up to the reaction temperature ($220 - 270\,°\mathrm{C}$) within $2 - 3\,\mathrm{min}$ and in the following the phase evolution was recorded by in-situ XRD during the constant temperature annealing [166]. No intermediate phases were observed. From the fact that the CuSe phase was consumed faster than the product $\mathrm{CuInSe_2}$ appeared in the diffractogram, they concluded the presence of an amorphous intermediate phase which they expected to be $\mathrm{CuInSe_2}$. The evolution of the $\mathrm{CuInSe_2}$ mole fraction with time was fitted by two models in order to check the applicability of different growth models. The Avrami model and a simple kinetic model could describe the formation rate of $\mathrm{CuInSe_2}$. Both models lead to the conclusion that the growth is one-dimensional diffusion controlled. In summary Kim et al. concluded that a $\mathrm{CuInSe_2}$ layer is formed at the interface of In-Se and CuSe at the beginning of the reaction. This layer acts as a nucleation barrier that partly suppresses the crystallisation of the product and leads to the formation of an intermediate amorphous $\mathrm{CuInSe_2}$ phase. Beside its function as nucleation barrier the $\mathrm{CuInSe_2}$ layer at the interface also acts as a diffusion barrier for the further reaction between InSe and CuSe. Diffusion through this barrier limits the reaction rate. These results have been supported with differential thermal analysis measurements by Purwins et al.[167]. They observe a two-dimensional phase boundary reaction which they ascribe to the nucleation of $\mathrm{CuInSe_2}$ at the interface. The reaction is more pronounced if a multi-layered precursor stack is used, i.e. more interfaces are present. It is followed by the one-dimensional diffusion limited reaction. Similar results have been obtained for a Mo/$\mathrm{In_2Se_3}$/CuSe precursor stack [165]. This time no amorphous $\mathrm{CuInSe_2}$ phase has been assigned and the Avrami model cannot describe the product evolution. The parabolic kinetic growth model is still valid confirming that the reaction is one-dimensional diffusion limited. The applicability of the parabolic growth model for PVD grown Mo/$\mathrm{In_2Se_3}$/CuSe precursors has also been validated in [168]. The influence of sodium incorporation on the reaction mechanism was studied by the use of a soda-lime glass substrate and a sodium free glass substrate. The reaction mechanism was the same on both substrates showing no intermediate phases. The reaction rate of the sodium-free precursor was about 30% faster than on a standard soda-lime glass substrate [168].

The interdiffusion of a $\mathrm{In_2Se_3}$/$\mathrm{Cu_2Se}$ stack has been studied by Park et al. [169]. They prepared a $3\,\mathrm{mm}$ thick stack from binary ingots and annealed it at $550\,°\mathrm{C}$ for several hours. Afterwards they determined the composition across the junction by EDX. From the composition they identified the following phases across the junction: $\mathrm{In_2Se_3}$ / $\mathrm{CuIn_5Se_8}$ / $\mathrm{CuIn_3Se_5}$ / $\mathrm{CuInSe_2}$ / $\mathrm{Cu_2Se}$ [1]. That means the observed phases in principle follow the quasibinary section of the phase diagram (figure 14.3). If the accurate compositions are taken into account, it turns out that the composition gradient

[1] In the original article the compositions of $\mathrm{CuIn_5Se_8}$ and $\mathrm{CuIn_3Se_5}$ are not mentioned but the abbreviations β- and γ-phase from the quasibinary phase diagram in figure 14.3 are used.

along the junction does not precisely follow the quasibinary section $Cu_{1-x}In_{1+x}Se_{2+x}$ but slightly deviates in composition. Again the applicability of the parabolic kinetic model and thus the diffusion limited growth kinetics could be verified. In general Park et al. assign the interdiffusion to Cu atoms moving from Cu_2Se into the In_2Se_3. In addition they observe a fast diffusion of In ions into the Cu_2Se phase causing "peninsulas" of $CuInSe_2$ in the Cu_2Se region. This fast diffusion can be assigned to indium diffusing through copper vacancy sites.

Further in-situ XRD measurements of binary selenide stacks have been performed by Hergert and Jost [102, 170, 43, 171, 172]. In contrast to the in-situ XRD measurements that have been mentioned before the diffractograms are recorded during the heating up and higher temperatures are applied. Hergert identifies 3 major reactions of $CuInSe_2$ formation [43] for binary selenide and stacked elemental precursors:

$$CuSe + InSe \longrightarrow CuInSe_2 \tag{19.1}$$

$$Cu_2Se + 2\,InSe + Se \longrightarrow 2\,CuInSe_2 \tag{19.2}$$

$$Cu_2Se + In_2Se_3 \longrightarrow 2\,CuInSe_2 \tag{19.3}$$

Mo/InSe/CuSe/Se stacks are annealed to $425\,°C$ within $15\,min$. At the melting point of Se ($217 - 221\,°C$) the formation of $CuInSe_2$ sets in by the slow reaction 19.1. At the decomposition of $CuSe$ into Cu_2Se (reaction 14.5) the faster second reaction 19.2 becomes possible. In a stacked elemental precursor $InSe$ is usually completely consumed before it selenises into In_2Se_3. In a binary selenide precursor the formation of In_2Se_3 is possible and reaction 19.3 occurs at high temperatures, when $InSe$ has been completely selenised and thus reactions 19.1 and 19.2 are suppressed.

Reactions 19.2 and 19.3 are also observed during the annealing of electrodeposited precursors [172]. Coelectrodeposited precursors can contain binary selenide phases which depend on its composition. The amount of Se in the precursor decides which reaction occurs [171]. At a high Se content (Se/In atomic ratio > 2) reaction 19.3 dominates. At moderate Se content (Se/In ≈ 1) reaction 19.2 is observed. In both reaction pathways no intermediate phases are detected. Reaction 19.3 leads to smaller grains than reaction 19.2.

An ex-situ XRD study of a binary selenide precursor has been performed by Teheran et al. [173]. The precursors are prepared by PVD deposition of an indium selenide layer followed by coevaporation of Cu and Se. The substrate temperature is kept at $250\,°C$ during the complete PVD process. Already during the precursor deposition they observed the formation of $CuInSe_2$. Due to the absence of copper selenide in XRD they propose a direct reaction of indium selenide with Cu and Se:

$$InSe + Cu + Se \longrightarrow CuInSe_2 \tag{19.4}$$

$$In_2Se_3 + 2\,Cu + Se \longrightarrow 2\,CuInSe_2 \tag{19.5}$$

The reaction is incomplete and the composition (atomic ratio Cu:In:Se) of the precursor is 60:0:40 at the surface and 20:35:45 at the back. The XRD diffractogram of the precursor shows the phases $InSe$ and $CuInSe_2$. Annealing the precursor in a Se containing atmosphere at $350\,°C$ lead to an increase of $CuInSe_2$ but the composition depth profile is still not uniform. If the precursor is annealed at $450\,°C$ the absorber is still slightly Cu-rich (Cu:In:Se = 25:15:60) in the upper third of the layer and additional $CuIn_3Se_5$ is observed in the diffractogram. After $600\,°C$ annealing the composition is slightly Cu-poor in the upper half of the layer (Cu:In:Se = 15:25:60) and the sample basically consists of $CuInSe_2$ with some $CuIn_3Se_5$ [173].

In summary it can be concluded that any combination of $InSe$, In_2Se_3, $CuSe$, Cu_2Se can lead to a direct formation of $CuInSe_2$. Which reaction dominates depends on the initial precursor phases and the annealing conditions. High temperatures or the presence of Se excess can cause phase transitions either due to decomposition or selenisation of a phase.

19.1.2. Onset temperature of $CuInSe_2$ formation from binary selenide precursors

The onset temperature of $CuInSe_2$ formation from binary selenide precursors varies in literature depending on the actual phases and the precursor structure. For Mo/InSe/CuSe and Mo/In_2Se_3/CuSe prepared by migration enhanced epitaxy $CuInSe_2$ could already be detected at a temperature of $210-220\,°C$. At this temperature the reaction was very slow and not completed after $5\,h$. To reach a complete conversion within $1\,h$ a temperature of $250-270\,°C$ was sufficient [165, 166].

In-situ XRD measurements of a PVD deposited Mo/In_2Se_3/CuSe precursor showed the onset of $CuInSe_2$ formation at $290\,°C$ [168]. In this context it was shown that the sodium content of the substrate can effect the reaction rate. The reaction of a glass/Mo/In_2Se_3/CuSe precursor annealed at $300\,°C$ for $20\,min$ was 70% completed on a soda-lime glass and 90% completed on a sodium free glass[168].

Hergert et al. have determined the onset temperature of $CuInSe_2$ formation for a Mo/InSe/CuSe precursor prepared by combined sputtering and coevaporation. The $CuInSe_2$ formation roughly coincides with the melting point of Se at $221\,°C$ [43]. In case of simultaneously electrodeposited copper, indium, and selenium the onset temperature of $CuInSe_2$ formation depended on the initial binary selenide phases that were formed in the as-deposited film. For the binary selenides InSe and $Cu_{2-x}Se$ the reaction started at $200\,°C$. If the precursor consisted of $\gamma-In_2Se_3$ and $Cu_{2-x}Se$ already a temperature of $125\,°C$ was sufficient to form $CuInSe_2$ although this reaction proceeded very slowly [172]. An interesting point is added by Purwins et al. who compared the reaction of a single In-Se/CuSe bilayer and multiple bilayers by differential thermal analysis. In case of the multiple bilayers the reaction starts at $210-220\,°C$. In contrast to this no significant amounts of $CuInSe_2$ are formed below $315\,°C$ if only a single bilayer was present [167]. Chen and Wang annealed a precursor consisting of In_2Se_3 and Cu_2Se nanoparticles. Although this should have a large interface area, a temperature of $350\,°C$ is necessary to convert the precursor into $CuInSe_2$ [161].

In summary the onset temperature of $CuInSe_2$ formation can significantly vary between different precursors but most authors report it around $200-220\,°C$. If diffusion limits the kinetics, higher temperatures are necessary to achieve a complete conversion of the film.

19.1.3. Crystallisation of amorphous indium selenide

In PVD processes the temperature is usually kept below $100\,°C$ to obtain amorphous indium selenide [174]. Annealing a room temperature deposited indium selenide film at $180\,°C$ for $2\,h$ leads to $\alpha-In_2Se_3$ while annealing it at $350\,°C$ for $7-8\,h$ results in $\beta-In_2Se_3$ [175, 176]. Other authors report the transition from the amorphous film to $\beta-In_2Se_3$ at $250\,°C$ [177]. However it is also mentioned in the review by Massalski that the transition temperatures between the In_2Se_3 polymorphs are not unanimous [124]. A high crystallisation temperature of In_2Se_3 has been reported by Hachiuma et al. who claim the deposition of amorphous indium selenide by PVD at a substrate temperature of $400\,°C$ [47].

19.2. Results and Discussion

19.2.1. Ex-situ XRD characterisation of phase formation

The following annealings have been performed on the electrodeposited binary selenide precursors in order to determine the temperature ranges when $CuInSe_2$ formation sets in and when the diffusion kinetics are fast enough to allow a complete reaction of the film. The precursors have been prepared according to chapter 11, i.e. an amorphous layer of In_2Se_3+Se with a Se/In atomic ratio close to 1.5 and a porous layer of $Cu_{2-x}Se$ platelets covered with amorphous Se. This time the precursors contain a $10\,nm$ thin Cu underlayer between the Mo substrate and the indium selenide layer[2]. The

[2]The Cu underlayer has been introduced to reduce hydrogen evolution in the electrodeposition process (see chapter 11). It often leads to delamination of the absorber during annealing and is not recommended. At the time of the

underlayer includes only 4% of the overall Cu content and its effect in the phase reaction is expected to be negligible. The precursors have been annealed for $30\,\mathrm{min}$ at temperatures ranging from $250\,°\mathrm{C}$ to $550\,°\mathrm{C}$. In all cases $100\,\mathrm{mg}$ Se have been added in the graphite box and the N_2/H_2 background gas pressure was $10\,\mathrm{mbar}$.

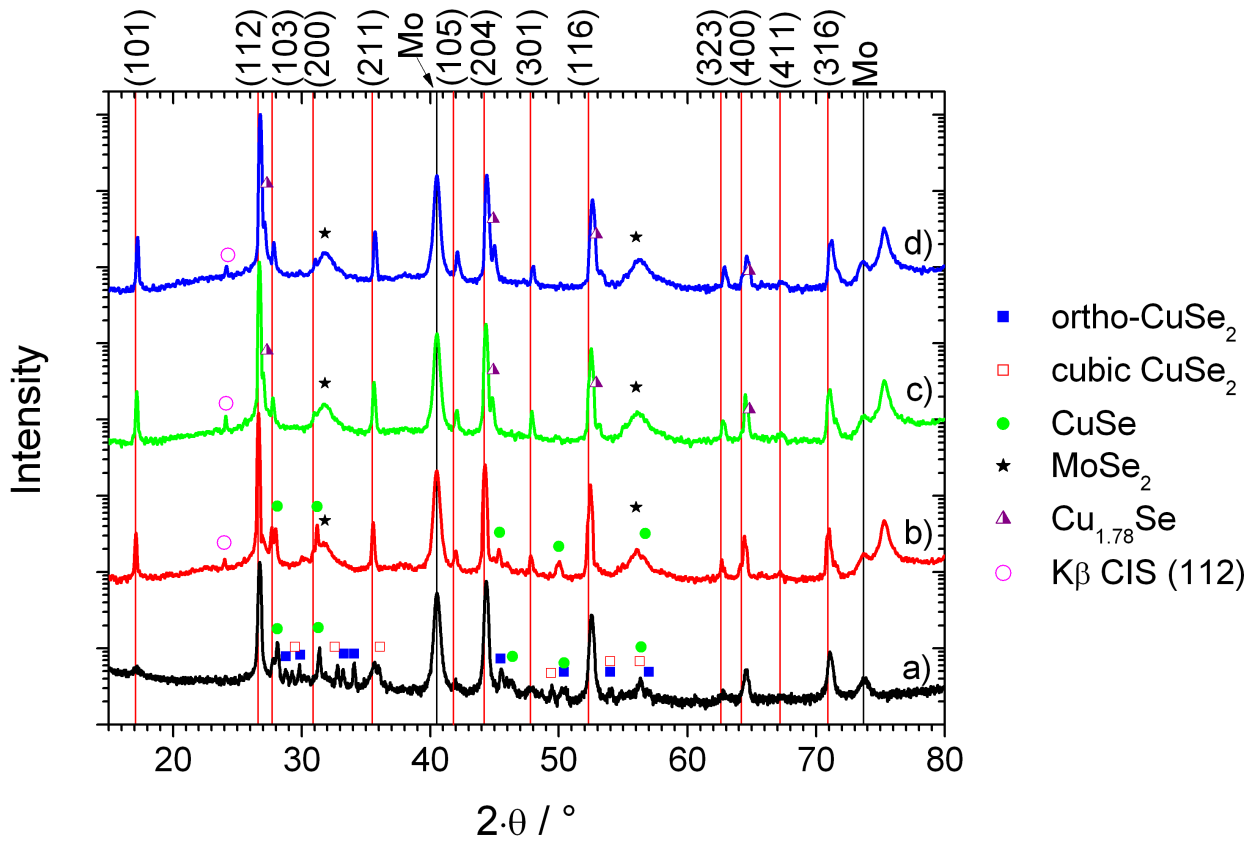

Figure 19.1.: XRD diffractograms of Mo/Cu/In-Se/Cu-Se precursors with a Cu/In atomic ratio of 1.15 after annealing at a) $350\,°\mathrm{C}$, b) $400\,°\mathrm{C}$, c) $450\,°\mathrm{C}$, d) $550\,°\mathrm{C}$. The vertical red lines record the reflections of $CuInSe_2$ and the black ones the Mo substrate. In case of a doublet only the hkl-indices of one peak are noted. The diffractograms have been measured in theta/2-theta mode. The annealing was done at several temperatures for $30\,\mathrm{min}$ inside the quartz tube furnace with $100\,\mathrm{mg}$ Se added and a N_2/H_2 background gas pressure of $10\,\mathrm{mbar}$. A summary of the observed phases is given in table 19.1. At $24.14\,°$ is a replica of the $CuInSe_2$ (112) reflection caused by the Cu Kβ line. The reflection at $75.4\,°$ is a fluorescence artifact.

Figure 19.1 shows the XRD diffractograms of annealed Cu-rich precursors. A Cu/In atomic ratio of 1.15 has been calculated from the deposited charge, the plating efficiency and the composition of the layers. In contrast to the diffractograms in figure 17.2 which were recorded in the more surface sensitive grazing incidence mode, the XRD measurements in this chapter were done in theta/2-theta mode. This mode has a deeper penetration depth and therefore features at the back of the sample (e.g. the $MoSe_2$ phase) are more pronounced. The diffractogram of the precursor is not shown in figure 19.1, because it corresponds to the diffractogram of electrodeposited copper selenide (figure 9.3). Indium selenide is not visible in the diffractogram due to its amorphous structure, nor can any additional phase from a reaction between the electrodeposited layers be detected. At $350\,°\mathrm{C}$ (figure 19.1a) the reflections of $CuInSe_2$ are already dominant in the diffractogram. However there are still

ex-situ XRD study the correlation between delamination and the Cu underlayer has not been clear.

several copper selenide phases present. These phases are cubic and orthorhombic $CuSe_2$, and $CuSe$. Compared to the copper selenide ($Cu_{1.8}Se$) in the as-deposited precursor (figure 9.3) the new phases contain more selenium. Although pure $Cu_{1.8}Se$ is stable up to temperatures above $1000\,°C$, it has changed its phase during the annealing due to an overpressure of Se. It will be shown in figure 19.4 that the Se overpressure is not caused by the additional elemental Se in the graphite box but by the amorphous Se that is electrodeposited together with the copper selenide top layer (section 9.2).

No $CuSe_2$ phases are expected in the diffractogram after the $350\,°C$ annealing, because these phases should have decomposed to $CuSe$ and elemental Se at temperatures above $332 - 342\,°C$ according to reaction 14.4. It must be considered that our oven overestimates sample temperatures by about 4% (referring to the temperature value in °C), because the thermocouple of the controller is installed outside of the quartz tube and the heat transfer through the glass and the low-pressure atmosphere is low (section 15.2). This value has been estimated by measuring the temperature of the graphite box with a second thermocouple directly connected to it. The overestimation of sample temperature is the probable reason why the sample in figure 19.1a was still annealed below the $CuSe_2$ decomposition temperature. After the $400\,°C$ annealing there is no $CuSe_2$ left and $CuSe$ is the dominating copper selenide phase. According to reaction 14.5 $CuSe$ is also not stable at $400\,°C$. Considering again the temperature overestimation of the oven, it is obvious that the sample temperature has just been slightly above the decomposition temperature of $377\,°C$. Therefore the decomposition is supposed to be slow. It can be even slowed down further by the presence of Se vapour. This vapour can either come from the elemental Se added in the graphite box or from the Se that has been released in the decomposition of $CuSe_2$. The overpressure of Se forces reaction 14.5 to the side of the educts and so suppresses the decomposition. For annealings at $450\,°C$ and above the only remaining copper selenide phase is $Cu_{2-x}Se$ as it has already been observed before (figure 17.3). The integral breadth of the (112)-$CuInSe_2$ reflection decreases from $0.21\,°$ (2-theta) at $350\,°C$ to $0.14\,°$ at $400\,°C$. This indicates an improved crystallisation at the higher temperature. A further decrease cannot be observed due to the limited resolution of the XRD set-up. In the current configuration the instrument resolution at this angle is about $0.13\,°$ (section 3.2). Thus figure 19.1 can be summarised by an ongoing crystallisation of $CuInSe_2$ above $350\,°C$ and the phase transformations of copper selenide that are expected from its phase diagram.

In a similar way diffractograms of a Cu-poor and a stoichiometric Mo/Cu/In-Se/Cu-Se annealed at various temperatures have been recorded and evaluated. The observed phases are summarised in table 19.1. Some absorbers peeled during the annealing and could not be analysed. Therefore not all temperatures ($250\,°C$, $350\,°C$, $400\,°C$, $450\,°C$, $550\,°C$) are available for all samples. Some of the phases cannot be determined definitely, because either there are only some of their reflections visible or the assignment is ambiguous. An example of two secondary phases with similar main reflections are $CuIn_3Se_5$ and $Cu_{2-x}Se$. Both of them show reflections which form a shoulder on the $CuInSe_2$ main peaks (see figure 17.3). While in the case of a Cu-rich sample at temperatures above $400\,°C$ this phase is likely to be $Cu_{2-x}Se$, it has been assigned to $CuIn_3Se_5$ in the case of the Cu-poor sample at low temperatures.

Table 19.1 contains analysis of diffractograms from samples annealed at $250\,°C$. Orthorhombic-$CuSe_2$ can be definitely observed and shows that the selenisation of the as-deposited copper selenide phase already starts below $250\,°C$. Reflections at $23.7\,°$ and $29.8\,°$ (the latter overlapping with a $CuSe_2$ peak) indicate the presence of elemental hexagonal Se. It can result from the amorphous Se which has been electrodeposited with the copper selenide layer. The assignment of four reflections ($25.7\,°$, $26.9\,°$, $28.4\,°$, $45.0\,°$) is not sure. They might belong to $InSe$ if a shift of $\pm 0.2°$ is tolerated, but one of the main reflections (006) is missing. Then the amorphous In_2Se_3 does not simply crystallise (section 19.1.3) but also loses Se during the annealing. In the in-situ XRD experiment in figure 19.4 In_2Se_3 does not decompose, but is stable even for an annealing at $550\,°C$. Maybe the low background gas pressure in the ex-situ experiment promotes Se evaporation and can explain the different behaviour.

It is also possible that the $26.9\,°$ and $45.0\,°$ reflections belong to a $Cu_{2-x}Se$ that is still present

composition	Cu/In = 0.85				Cu/In = 1				Cu/In = 1.15			
temperature °C	250	350	450	550	250	400	450	550	350	400	450	550
$\mathrm{ortho{-}CuSe_2}$	A	A	B		A				A			
$\mathrm{cubic{-}CuSe_2}$		C							A			
CuSe									A	A		
$\mathrm{Cu_{1.78}Se}$											A	A
$\mathrm{CuInSe_2}$		A	A	A		A	A	A	A	A	A	A
$\mathrm{CuIn_3Se_5}$		B	B									
InSe	C				C							
$\mathrm{MoSe_2}$				A		A	A	A		A	A	A
hex-Se	B				B							
unknown peaks		25.4°										

Table 19.1.: Phases for annealed Mo/Cu/In-Se/Cu-Se precursors of different compositions. The phases have been determined by XRD in theta/2-theta mode (e.g. in figure 19.1). The letter expresses the confidence of the phase assignment: A) definite, B) likely, C) unsure. At $250\,°\mathrm{C}$ the phase assignment is unsure as it is discussed in the text. The annealing was done at several temperatures for $30\,\mathrm{min}$. The composition of the precursors was varied by adjusting the copper selenide thickness. Some temperatures are missing, because the samples delaminated during annealing.

from the electrodeposited copper selenide. No clear evidence of $\mathrm{CuInSe_2}$ formation can be found at this temperature. Most studies on binary selenide precursors locate the onset of $\mathrm{CuInSe_2}$ formation at $200 - 220\,°\mathrm{C}$ (section 19.1.2). Therefore $250\,°\mathrm{C}$ should just be enough to allow the $\mathrm{CuInSe_2}$ synthesis. It will be later explained in the context of the figure 19.2 why the precursor morphology slows down the reaction kinetics and shifts the onset of $\mathrm{CuInSe_2}$ to higher temperatures.

As in the Cu-rich case also the Cu-poor sample shows definite presence of $\mathrm{CuInSe_2}$ at $350\,°\mathrm{C}$. A shoulder is visible on the high angle side of the $\mathrm{CuInSe_2}$ main reflections. Since the sample is Cu-poor these peaks are probably linked to an ordered vacancy compound (e.g. $\mathrm{CuIn_3Se_5}$). However no exclusive peaks of $\mathrm{CuIn_3Se_5}$ can be detected (see footnote on page 100). It has been shown that $\mathrm{CuIn_3Se_5}$ appears as an initial phase in the interdiffusion of $\mathrm{In_2Se_3}$ and $\mathrm{Cu_2Se}$ (section 19.1.1). It can be presumed that also in the present case the $\mathrm{In_2Se_3}$ goes through the $\mathrm{CuIn_3Se_5}$ phase before finally $\mathrm{CuInSe_2}$ is formed. In case of a Cu-rich or stoichiometric film enough Cu-cations are present to convert $\mathrm{CuIn_3Se_5}$ to $\mathrm{CuInSe_2}$. For the Cu-poor precursor this process seems to be slower and therefore the vacancy compound can be still detected after annealing at $350\,°\mathrm{C}$ and $450\,°\mathrm{C}$. No phases besides chalcopyrite $\mathrm{CuInSe_2}$ are observed for the stoichiometric sample at $400\,°\mathrm{C}$ and above.

It has already been mentioned that diffusion is the limiting step in the reaction of a In-Se/Cu-Se bilayer (section 19.1.1) [167, 165, 166, 169]. SEM cross sections provide a simple tool to observe the morphology change that can be associated with the reaction. It becomes obvious in figure 19.2a why $\mathrm{CuInSe_2}$ has not formed at $250\,°\mathrm{C}$, although it is thermodynamically possible. The indium selenide and the copper selenide layer are still distinct after annealing at that temperature. The open structure of the electrodeposited copper selenide film causes a small interface area between the indium selenide and copper selenide layer (figure 11.1). Therefore the mass transport between the layers is limited and a reaction cannot proceed. It is visible that the reaction of the electrodeposited $\mathrm{Cu_{2-x}Se}$ into $\mathrm{CuSe_2}$ has modified its morphology. The platelets have sintered and dense conglomerates cover the surface. This increases the contact area between both layers. After the $350\,°\mathrm{C}$ annealing $\mathrm{CuInSe_2}$ emerges and the absorber appears as one layer in the SEM cross section 19.2b. Only scattered copper selenide clusters remain on the surface.

The absorber film has a substructure. The surface shows grain boundaries indicating small columnar grains. At the backcontact the morphology conveys the impression of an amorphous phase with some artifacts from breaking. The morphology stays in principle the same after the $450\,°\mathrm{C}$ annealing.

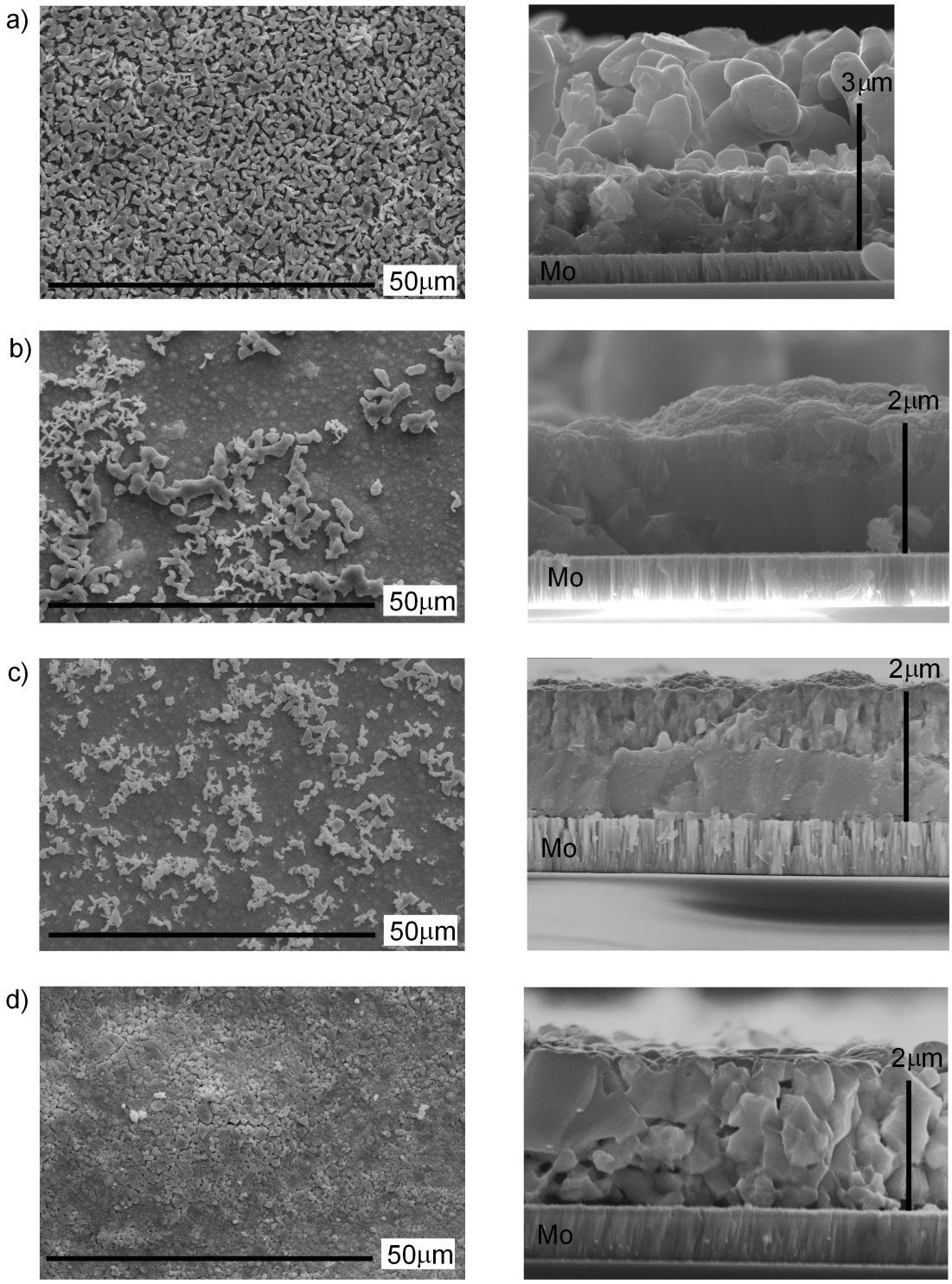

Figure 19.2.: SEM top views and cross sectional views of Mo/Cu/In-Se/Cu-Se precursors with a Cu/In atomic ratio of 0.85 annealed at a) $250\,°C$, b) $350\,°C$, c) $450\,°C$, d) $550\,°C$. The annealing was done for $30\,\mathrm{min}$ inside the quartz tube furnace with $100\,\mathrm{mg}$ Se added and a N_2/H_2 background gas pressure of $10\,\mathrm{mbar}$. A SEM cross section of the as-deposited precursor is shown in figure 11.1.

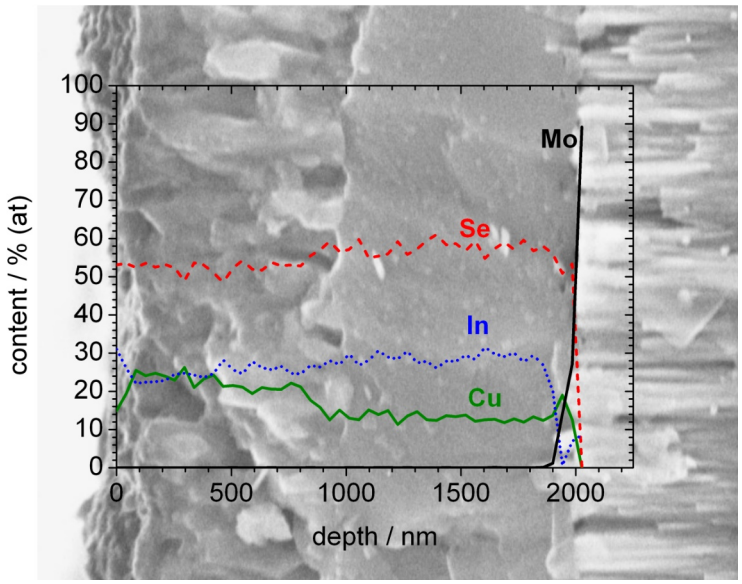

(a) Cu-poor sample (Cu/In ratio = 0.85)

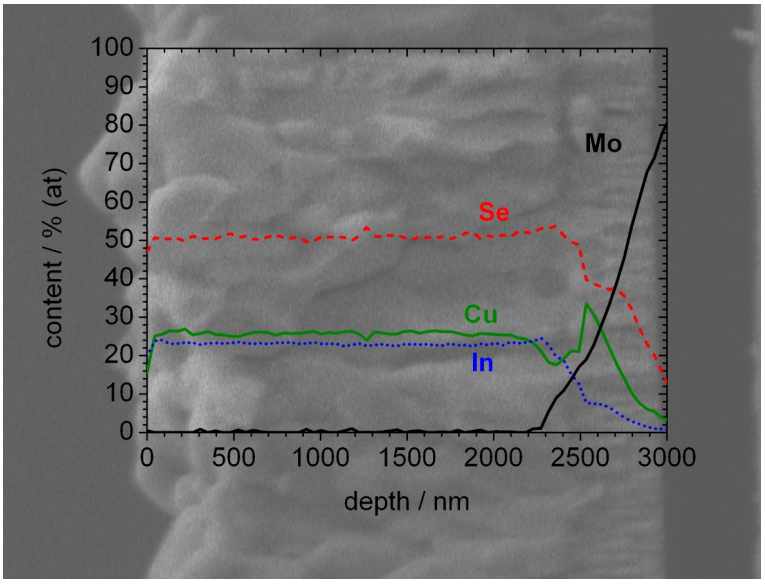

(b) stoichiometric sample (Cu/In ratio = 1)

Figure 19.3.: AES composition depth profiles of Mo/Cu/In-Se/Cu-Se precursors with different Cu/In ratios annealed at $450\,^{\circ}\mathrm{C}$ for $30\,\mathrm{min}$. The corresponding SEM cross section has been underlaid.

An AES composition depth profile (figure 19.3a) reveals that the layered substructure is linked to a different composition. The top $800\,\mathrm{nm}$ have a composition close to stoichiometric $\mathrm{CuInSe_2}$. In the smooth layer at the back the Cu content drops below 15% (at). With the information of table 19.1 one can conclude that the back layer probably consists of $\mathrm{CuIn_3Se_5}$. The overall composition of the precursor (an atomic Cu/In $= 0.85$ ratio was estimated from the current during electrodeposition) should still contain enough Cu to convert the complete film into a Cu-deficient $\mathrm{CuInSe_2}$. The reason why the vacancy compound is still present after annealing is likely a suppressed diffusion of copper. The porous structure of electrodeposited copper selenide slows down the interdiffusion with the indium selenide layer. Therefore even in a Cu-poor film copper selenide phases can be detected at the surface when annealing at intermediate temperature (also see table 19.1). The copper that is trapped in the phases on the surface is missing at the back of the absorber. Similar results have been reported Teheran et al. for a PVD-grown In-Se/Cu-Se precursor (section 19.1.1)[173]. Their samples show still a Cu excess at the surface after an annealing at $450\,°\mathrm{C}$, although the overall composition is Cu-poor. Unfortunately no SEM cross-section have been published in this study providing information on the interface area between indium selenide and copper selenide.

In case of a stoichiometric precursor more copper is available. The AES composition profile of a $450\,°\mathrm{C}$ annealed absorber (figure 19.3b) is uniform throughout the complete depth of the film. The morphology does not show a discontinuity as in the Cu-poor case. At some spots on the cross section (not shown) the grain size at the the surface is slightly larger than at the backside, but the difference is considerably less than in figure 19.3a. Such a variation in grain size might be explained by a different level of sodium along the sample profile or a different concentration of Se during growth. Since the diffusion in the stoichiometric precursor is also hindered by the open copper selenide morphology, one would still expect copper selenide phases to stay at the surface and the bulk to be slightly Cu-poor. However in the studied samples this is not observed, but the composition is close to stoichiometry and no copper selenide phases have been detected at $450\,°\mathrm{C}$ in table 19.1. It seems that there is still some variability in the temperature, where the copper selenide phases are consumed. A repetition of the Cu-poor sample did not show the sharp bilayer structure of figure 19.2c anymore, but showed a similar crystallinity from the surface to the back (similar to the one in figure 19.3b). This can be explained by the fact that the variability of the precursor composition (e.g. samples "ED-stoich-10mbar" and "ED-stoich-500mbar" in table 16.1) and the variability in the Cu diffusion flux add up.

Annealing at $550\,°\mathrm{C}$ accelerates diffusion enough that most of the copper selenide on the surface can finally diffuse into the absorber. Above $523\,°\mathrm{C}$ copper selenide can melt if enough Se is present in the system (reaction 14.6 and phase diagram 14.2). A liquid copper selenide phase would increase the contact surface if it can wet the indium selenide. It would also increase the interdiffusion. However it is not likely to melt the copper selenide phase in the present case, because the temperature is only slightly above the melting point (considering the temperature overestimation of the oven) and excess Se has probably already evaporated. Judging from the SEM cross section the grain size rises to several hundred nanometres and occasional grains extending from the backcontact to the surface are observed.

In summary the following reaction pathway can be concluded from the presented experiments. In a first step the electrodeposited $\mathrm{Cu_{2-x}Se}$ top layer reacts with the simultaneously deposited amorphous Se to $\mathrm{CuSe_2}$. The morphology of the electrodeposited copper selenide is very porous and the interface area with indium selenide is small. This slows down the diffusion kinetics between the amorphous indium selenide and the copper selenide top layer. Therefore the $\mathrm{CuSe_2}$ is localised at the sample surface for a long time. In a Cu-rich precursor the excess Cu will stay as a copper selenide phase at the surface and undergo the transitions expected from the Cu-Se phase diagram. Depending on the annealing temperature the final copper selenide phase will be either $\mathrm{CuSe_2}$, CuSe, or $\mathrm{Cu_{2-x}Se}$.

Between $250\,°\mathrm{C}$ and $350\,°\mathrm{C}$ the reaction between indium selenide and copper selenide into $\mathrm{CuInSe_2}$ will set in. From the performed experiments it is not definite which copper selenide phase is involved in the reaction. This will depend on the annealing temperature, because it determines which copper

selenide phase is stable at the surface. At a temperature of $450\,°C$, for example, the only stable copper selenide phase at the surface is $Cu_{2-x}Se$ and the reaction will follow reaction 19.3. Diffractograms of the annealed Cu-poor sample indicate the presence of the vacancy compound $CuIn_3Se_5$. This supports the reaction path which is expected from the quasibinary section of the Cu-In-Se phase diagram. Cu and Se ions from the copper selenide phase at the surface will diffuse into the In_2Se_3 and react it to $CuIn_3Se_5$. (This is supposed to happen through the intermediate $CuIn_5Se_8$ phase, although this has not been resolved in the measurements.) $CuIn_3Se_5$ will be further converted to $CuInSe_2$ as the diffusion of Cu and Se continues.

The slow diffusion caused by the porous morphology of copper selenide explains why the onset of $CuInSe_2$ formation in this thesis is observed at a higher temperature than usually reported for binary selenide stacks in literature. It can also explain the variation between repeated annealings. The diffusion between copper selenide and indium selenide is effected how both layers change their contact interface. It depends on the sintering process of the copper selenide platelets which is also accompanied by its phase changes expected from the phase diagram. This is a complex process and therefore the temperature until the reaction between the binary phases is completed will certainly vary with parameters like the stacking density of the electrodeposited platelets or the Se overpressure during the annealing.

19.2.2. In-situ XRD characterisation of phase formation

The ex-situ XRD measurements in chapter 19.2.1 are useful to determine the minimum temperature necessary to form a certain phase like $CuInSe_2$. The advantage of these experiments is that the experiments can be performed in the annealing oven under conditions close to the actual annealing. On the other hand it is not certain that the phase evolution during the annealing follows the path that is given in figure 19.1 and table 19.1. The annealing time of $30\,min$ in the previous experiments allows the system to equilibrate. In contrast the annealing of the actual sample does not necessarily pass through states of thermal equilibrium but the kinetics of the process must be considered. It is also possible that additional phase transitions occur in the cooling process of the sample. These issues can be avoided if the XRD diffractograms are recorded in-situ, i.e. during the annealing process. The drawback of the in-situ annealing is that it cannot be performed in our annealing oven but is done in special chamber (in the following called "XRD-hotstage") that requires a modification of annealing conditions (e.g. no additional elemental Se, background gas pressure of about $1\,bar$ above atmosphere; also see section 15.3.1). Moreover the heating rate was reduced to $7\,°C/min$ in order to have sufficient time for the XRD scans.

In a first step the phase evolution of an electrodeposited Cu-Se layer was studied by in-situ XRD (figure 19.4, left column). The well defined phase transitions in the copper selenide phase diagram (reactions 14.4 and 14.5) provide a possible check of the sample temperature. The reduced resolution and the limited angle range of the XRD scans do not allow the determination of the precursor phases. The main peak in the diffractogram at $28.6\,°$ is caused by the graphite dome of the XRD-hotstage that also causes a minor peak at $26.1\,°$. From previous measurements (figure 9.3) it is known that the precursor consists of $Cu_{2-x}Se$ platelets covered with amorphous Se. Between $110\,°C$ and $130\,°C$ the first reflection of hexagonal Se appears at $29.7\,°$. This corresponds to the temperature range $(125-130\,°C)$ reported for the crystallisation of amorphous Se [178]. The melting point of selenium at $217-221\,°C$ [89] cannot be observed, because the peak at $29.7\,°$ is replaced by the (101) reflection of orthorhombic $CuSe_2$ at the same angle above $195\,°C$. This is confirmed by the appearance of the (111) and (120) doublet at $33.2\,°$ and $34.0\,°$. Above $245\,°C$ the first reflections of hexagonal $CuSe$ set in ($26.5\,°$ and $28.0\,°$). At $316-333\,°C$ the $CuSe_2$ phase decomposes according to reaction 14.4. This promotes further $CuSe$ and also its weaker reflections show up ($30.4\,°$ and $31.2\,°$). Reaction 14.5 is observed at $356-365\,°C$, when $CuSe$ decomposes and $Cu_{2-x}Se$ appears. Further heating causes an increase of the lattice constant of $Cu_{2-x}Se$ by thermal expansion and causes a shift of the main reflection towards lower angles. Until the end of the process $Cu_{2-x}Se$ remains the only observed phase. Its lattice parameters shrink again with cooling. The peak shift during the heating is

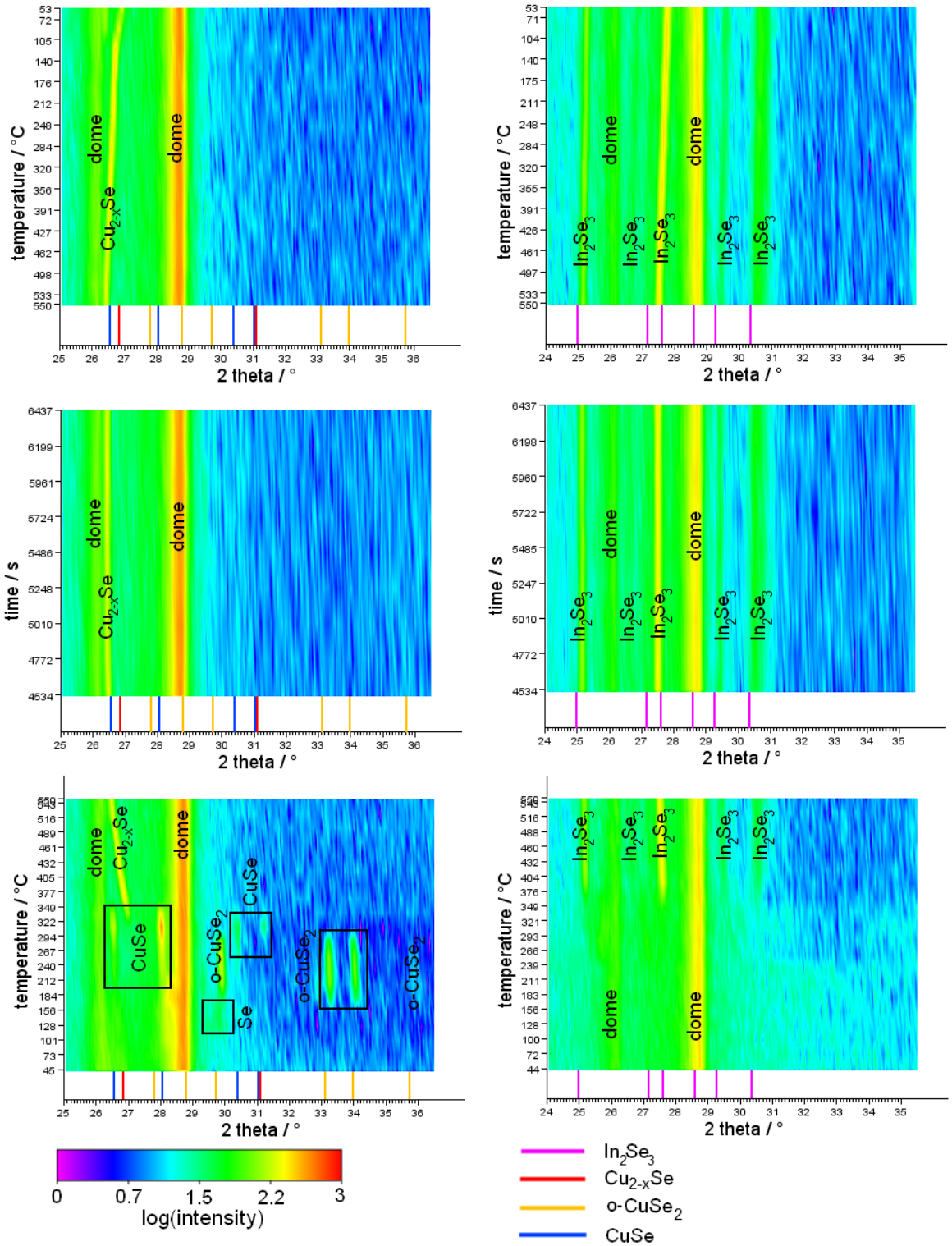

Figure 19.4.: In-situ XRD of electrodeposited Mo/Cu-Se (left column) and Mo/In-Se (right column) precursors heated up to 550 °C (bottom row), annealed at 550 °C (middle row) and cooled again to room temperature (top row). The colour shows the logarithmic intensity of the XRD signal. In the heating and cooling process the start temperature of each scan is plotted on the y-axis. The temperature was ramped continuously. For the annealing at constant temperature the time has been plotted on the y-axis. The coloured lines underneath the map mark the main reflections of important phases. (Colours can be easier separated in the electronic version of this thesis.)

stronger than during the cooling. That means it cannot be solely explained by thermal expansion but also a change in the composition of $Cu_{2-x}Se$ must be considered. The thermal expansion coefficient decreases with increasing x [179]. That means during the heating the $Cu_{2-x}Se$ phase either looses copper or gains selenium and therefore the peak shift is lower in the cooling process. Cu_2Se forms in the decomposition reaction 14.5. A selenium gain is possible, if Cu_2Se reacts with some of the elemental Se product from the decomposition reaction into $Cu_{2-x}Se$. A Cu loss can be explained, if Cu diffuses from the Cu_2Se into the $MoSe_2$ which is formed during the selenisation. This has been reported in literature for the selenisation of coelectrodeposited absorbers [25]. In case of the complete Mo/In-Se/Cu-Se stack it is likely that some Cu from the Cu_2Se phase diffuses into indium selenide and leaves a $Cu_{2-x}Se$ phase behind.

Comparing the reported temperatures of Se crystallisation, $CuSe_2$ and $CuSe$ decomposition ($125-130\,°C$, $332-342\,°C$, $377-379\,°C$) to the observed temperature intervals ($110-130\,°C$, $316-333\,°C$, $356-365\,°C$) it seems that our set-up underestimates the actual sample temperature by roughly 5% (referring to the °C value of the temperature) during the heating process.

Figure 19.4 (right column) shows the in-situ diffractograms of an electrodeposited In-Se layer. It has already been mentioned before that the as-deposited film is amorphous or nanocrystalline. No reflections are observed except the background caused by the graphite dome. At $380\,°C$ the reflections of $\gamma - In_2Se_3$ occur. Until the end of the process no further phases appear. The crystallisation temperature is higher than expected (section 19.1.3). Other authors report a crystalline $\alpha - In_2Se_3$ or $\beta - In_2Se_3$ phase before the $\gamma - In_2Se_3$ formation [175, 176] but Hachiuma et al. showed the presence of amorphous indium selenide up to $400\,°C$ [47] (section 19.1.3).

The diffractograms of a complete electrodeposited Mo/In-Se/Cu-Se precursor are shown in figure 19.5. In order to extend the angle range two annealings have been performed; one at 2θ $25-36.5\,°$ (left column) and the other at $43-54.5\,°$ (right column). Below $150\,°C$ the phase assignment is difficult. The reflection at $45.8°$ can probably be referred to $Cu_{2-x}Se$ as in figure 9.3. A shoulder on the low angle side of the graphite dome peak can indicate the presence of some $CuSe$. At $180\,°C$ orthorhombic $CuSe_2$ sets in. In parallel the formation of cubic $CuSe_2$ is observed. It has already been present in case of the single Cu-Se precursor, but it was less pronounced. Around $200\,°C$ also the shoulder at the low angle side of the graphite dome peak rises to a definite reflection of hexagonal $CuSe$ ($28.0°$). It is accompanied by the appearance of further $CuSe$ reflections. At $314-331\,°C$ the $CuSe_2$ phases decompose according to reaction 14.4. Afterwards $CuSe$ decomposes at $361-378\,°C$ according to reaction 14.5.

Around $270\,°C$ a small peak appears at $44.9°$. It can already be an indicator for the formation of an ordered vacancy compound like $CuIn_5Se_8$ or $CuIn_3Se_5$, but no further definite peaks can be observed confirming this phase (see footnote on page 100). $CuIn_5Se_8$ or $CuIn_3Se_5$ are expected as intermediate phases, when In_2Se_3 and Cu_2Se interdiffuse to form $CuInSe_2$ [169]. At $350\,°C$ the peak has further grown and shifted to $44.4°$. It is probably linked to the reflection at $26.8°$ that is also appearing. It is difficult to assign these reflections definitely, because $CuInSe_2$, $CuIn_3Se_5$ and $Cu_{2-x}Se$ all show these peaks. As it has been pointed out in section 19.2.1 the peaks of these three phases lie very close to each other and overlap. The exclusive $CuIn_3Se_5$ reflections (see footnote on page 100) are probably too weak to appear from the background noise, because of the fast scanning. The thermal expansion makes the assignment even more difficult, because peak positions differ from the referenced values at room temperature. An approach to separate $CuInSe_2$, $CuIn_3Se_5$ and $Cu_{2-x}Se$ can be a detailed look at the onset of the main peak around $26.8\,°$. In figure 19.6 the contour of the $Cu_{2-x}Se$ reflection from figure 19.4 is overlaid with the contour of the main peak of the Mo/In-Se/Cu-Se precursor from figure 19.5. As expected the contour of the complete precursor stack seems to contain the signal of $Cu_{2-x}Se$ and additional parts from further phases. The $Cu_{2-x}Se$ peak is thin and has a pronounced shift with increasing temperature due to its thermal expansion and the change in composition. This feature can also be recognised in the complete stack and is highlighted with a blue box. However it cannot explain the complete contour which is broader and shows a different shift with temperature (highlighted in red). Around $490\,°C$ the contour

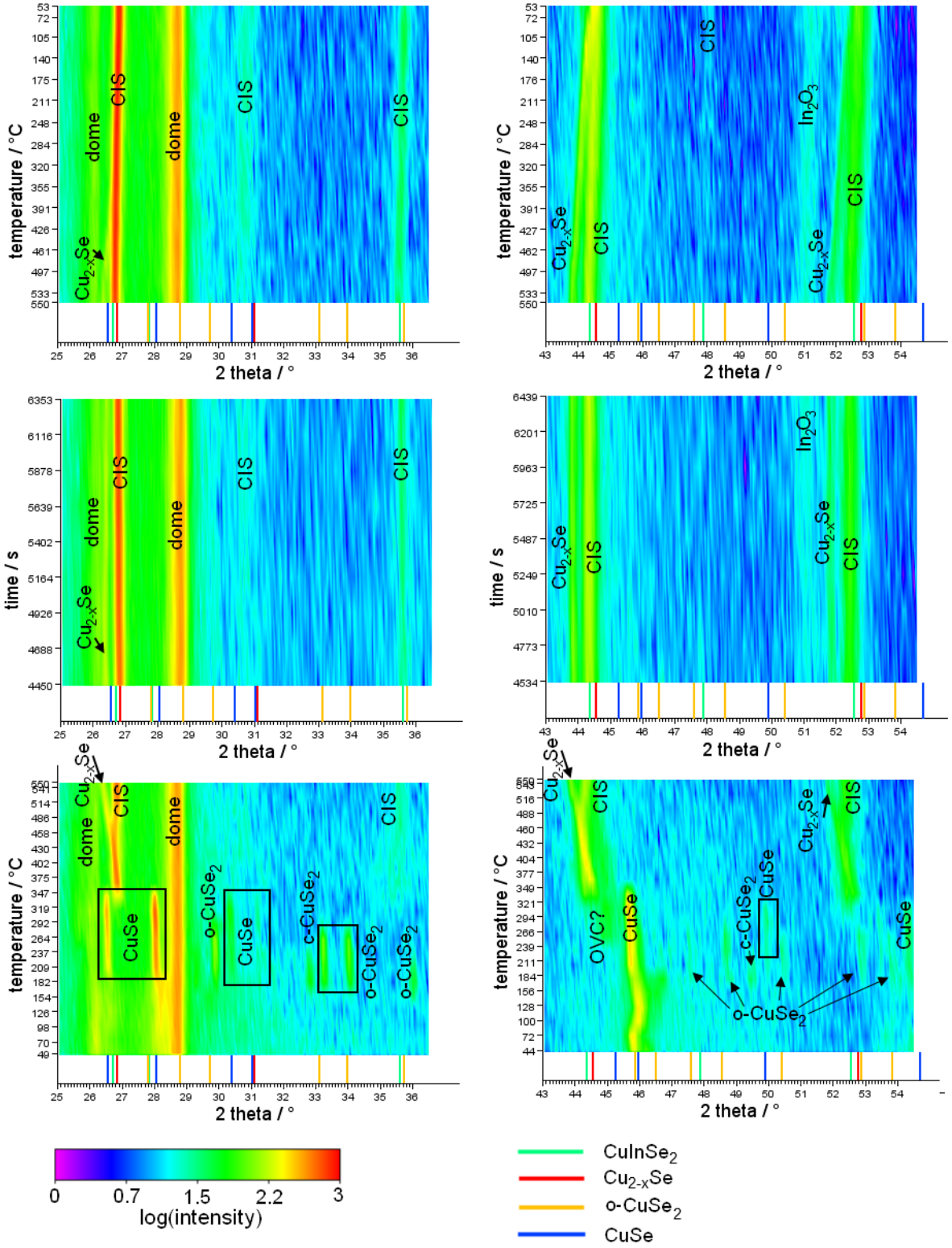

Figure 19.5.: In-situ XRD of an electrodeposited Mo/In-Se/Cu-Se precursor heated up to $550\,°C$ (bottom row), annealed at $550\,°C$ (middle row) and cooled again to room temperature (top row). The Cu/In ratio of the complete precursor is close to 1. Two measurements with pieces of the same precursor have been performed to record the diffractogram in the 2θ-range $25 - 36.5°$ (left column) and $43 - 54.5°$ (right column). (Colours can be easier separated in the electronic version of this thesis.)

has a kink, which can indicate the onset of another phase (highlighted in green). It is obvious to assign the lower temperature signal to $CuIn_3Se_5$ and the higher temperature signal to $CuInSe_2$. The highlighted areas in figure 19.6 are only a rough estimation. They predict that the copper selenide in the precursor stack behaves similar to a single copper selenide layer. In parallel copper can diffuse into the indium selenide layer and form the vacancy compound $CuIn_3Se_5$. With increasing temperature and time more copper diffuses into the layer until $CuInSe_2$ is formed. From figure 19.6 one would locate the onset of $CuInSe_2$ around $470\,°C$. The error of this temperature is high, because the phase assignment is not well-defined. This temperature is considerably higher than the one observed from the equilibrium experiments in the annealing oven. $CuInSe_2$ was detected after $30\,min$ annealing at $350\,°C$ (section 19.2.1). The difference can result from slow reaction kinetics. That means the process is slow and the set-up has already reached a high temperature, when the process is finished. The temperature is ramped from $350\,°C$ to $490\,°C$ within $20\,min$ under the current conditions. The slow reaction kinetics are probably due to the porous morphology of the copper selenide. This causes a small interface area with the indium selenide as it has been discussed at the end of section 19.2.1.

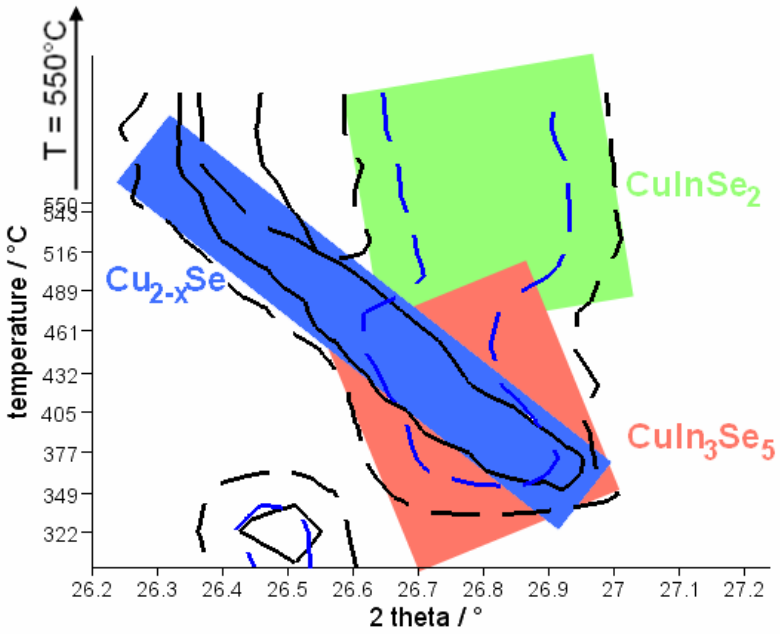

Figure 19.6.: Contour plot of the onset of the dominant peak in the in-situ diffractograms of Mo/Cu-Se and Mo/In-Se/Cu-Se. The heating up and the first three scans at $550\,°C$ are shown. The black lines show the contour of the measured data at $150\,counts$ and the blue line is the contour at $300\,counts$. The solid line belongs to the Mo/Cu-Se stack and the dashed one to Mo/In-Se/Cu-Se. The coloured boxes suggest the phases that are involved in the contour. The plot is a magnified excerpt of the measurement in figure 19.5.

The thermal expansion coefficient of $Cu_{2-x}Se$ is about two times larger than for $CuInSe_2$ [100, 4]. Therefore the main X-ray reflections ($26.7\,°$, $44.1\,°$, $52.1\,°$) separate above $490\,°C$ and can clearly be distinguished during the annealing at constant temperature. At the beginning of the cooling process at $460 - 490\,°C$ the peaks of $CuInSe_2$ and $Cu_{2-x}Se$ merge again. A complete XRD scan after the hotstage experiment does not show $Cu_{2-x}Se$ phases as in figure 17.3 any more. The crystallisation of $\gamma - In_2Se_3$ at $380\,°C$ is not observed in the stack. Therefore it must be considered that the amorphous indium selenide has already been converted to $CuInSe_2$ or an ordered vacancy phase when the sample reaches this temperature.

Although the XRD-hotstage experiment has been performed under a stagnant nitrogen atmosphere,

an In_2O_3 phase is observed in the final absorber that was scanned in the range $43 - 54.5°$. This oxide forms at the beginning of the constant temperature step at $550\,°C$ and indicates a leak in the chamber. For the second sample In_2O_3 reflections (e.g. at $30.6\,°$) are neither observed during the scan in the range $25 - 36.5°$ (figure 19.5) nor afterwards in the final absorber.

In conclusion the Mo/In-Se/Cu-Se precursor reacts in the following way. The copper selenide phase undergoes the transitions that are expected from its phase diagram. The indium selenide layer stays amorphous until its reaction with copper selenide. At the decomposition temperature of $CuSe$ into $Cu_{2-x}Se$ the latter one reacts with indium selenide into $CuInSe_2$. This presumably takes place through a Cu-poor intermediate phase (e.g. $CuIn_3Se_5$). The observed phase reaction pathway differs from the one proposed by the group of Anderson [165, 166]. In their case a glass/InSe/CuSe and a glass/In_2Se_3/CuSe precursor transform directly into $CuInSe_2$ without intermediate phases (section 19.1.1). The difference is caused by the structure of our electrodeposited precursor as it has been discussed in chapter 19.2.1. The precursors stacks of the Anderson group [165, 166] are compact, smooth and thinner than our stacks (stack thickness ca. $800\,nm$). The diffusion between the layers can proceed fast and the reaction is already completed at $310\,°C$, before the decomposition of copper selenide begins. In the electrodeposited case the small contact area between indium selenide and copper selenide slows down the interdiffusion between the layers. Therefore the system proceeds to temperatures where copper selenide decomposes. That is the reason why we do not observe a direct reaction between In_2Se_3 and $CuSe$ although these phases are present at $250\,°C$. The presence of a Cu-poor intermediate phase in our system can also be explained by the higher temperature that our system requires due to the slow kinetics. The higher temperatures can increase the diffusion coefficient of Cu in indium selenide. Instead of sharp interfaces Cu-Se/$CuInSe_2$/In_2Se_3 the fast diffusion of Cu will blur the interface between $CuInSe_2$ and In_2Se_3 and give rise to a Cu-poor intermediate phase.

A comparison between the ex-situ XRD measurements in section 19.2.1 and the in-situ XRD measurements shows differences in both processes. The ex-situ measurements have been performed inside the tube furnace in a Se containing atmosphere and the system had time to equilibrate. In the in-situ XRD the atmosphere did not contain Se and the temperature was continuously ramped to $550\,°C$. The Se excess in the ex-situ experiments favours the formation of the Se-rich $CuSe_2$ phases at temperatures up to $350\,°C$ (table 19.1). Although the last $CuSe_2$ reflection disappears in the in-situ XRD around $320\,°C$ it is not the dominant phase anymore. Already at $200\,°C$ $CuSe$ becomes the major copper selenide phase. Another difference between the in-situ and ex-situ experiments is the onset of $CuInSe_2$. In the ex-situ case $CuInSe_2$ is already present at $350\,°C$. According to the contour plot 19.6 $Cu_{2-x}Se$ and the vacancy phase $CuIn_3Se_5$ set in at this temperature in the in-situ experiment, while $CuInSe_2$ needs a higher temperature to form. It can be explained again by slow reaction kinetics between indium selenide and copper selenide. Therefore the system reaches a higher temperature before the process finishes.

If our reaction mechanism is dominated by structure and slow diffusion, it is interesting to study the phase evolution within a Mo/In-Se/Cu/Se precursor (preparation described in section 15.1.2). Since the copper is now present as an elemental layer and no longer chemically bound as it was the case for the electrodeposited Cu-Se layer, we expect a faster interdiffusion with the indium selenide film. This interdiffusion can be further accelerated if the copper film is smooth and compact, because it enlarges the interface area with the indium selenide in comparison to the electrodeposited Mo/In-Se/Cu-Se stack.

At the beginning of the annealing experiment in the XRD hotstage set-up the reflection of the elemental copper layer is observed at $43.3°$. There are additional weak reflections which probably belong to hexagonal $CuSe$. This means that the initial Cu_3Se_2 phase which has been measured directly after the precursor preparation (section 15.1.2) has been transformed within the two weeks until the XRD measurement was performed. Cu_3Se_2 decomposes into $CuSe$ above $113\,°C$ according to reaction 14.3 [126].

However no clear Cu_2Se peaks can be identified. At $113 - 141\,°C$ a peak appears at $29.7°$ and

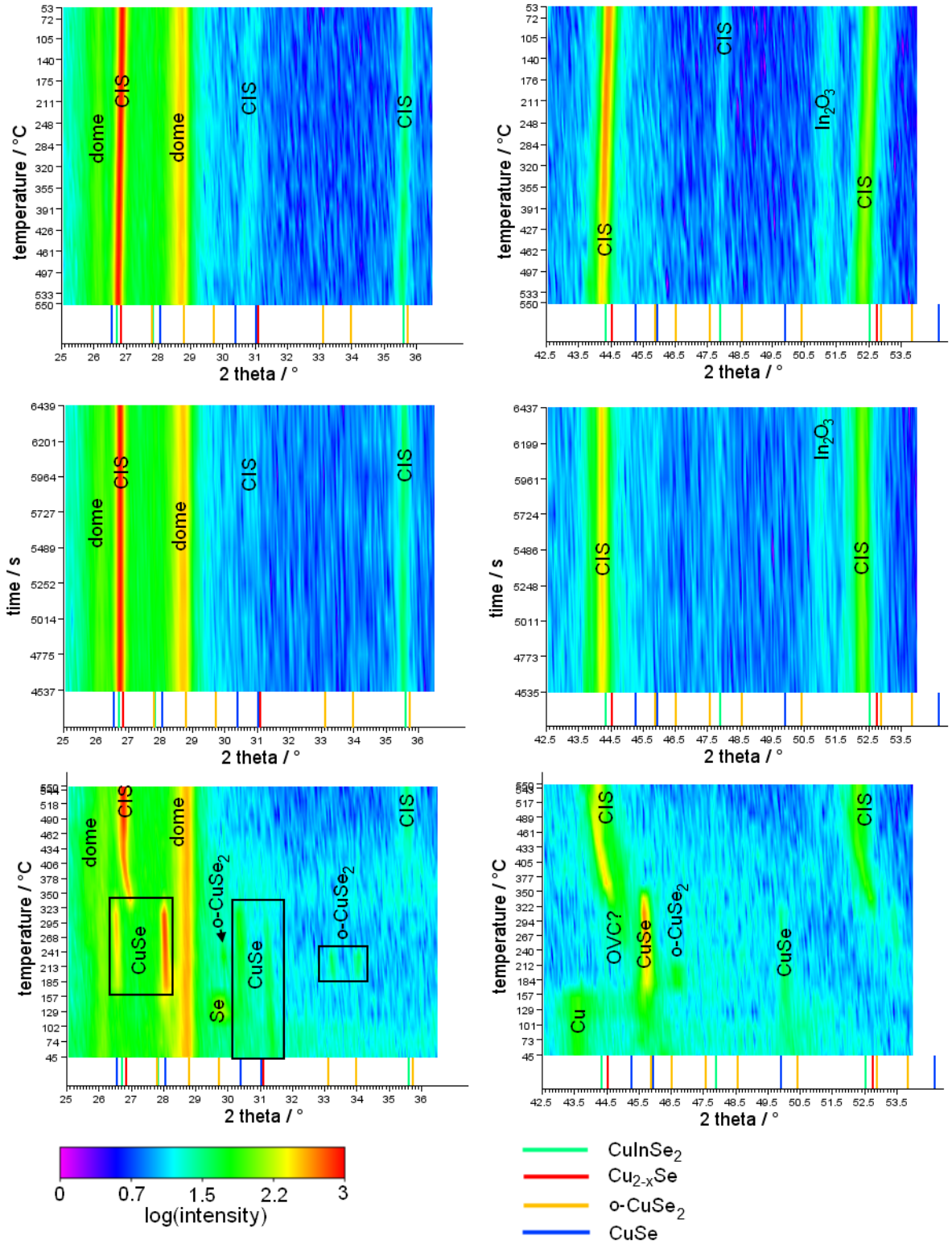

Figure 19.7.: In-situ XRD of a Mo/In-Se/Cu/Se precursor heated up to 550 °C (bottom row), annealed at 550 °C (middle row) and cooled again to room temperature (top row). The In-Se layer was electrodeposited while the Cu and Se layers have been sputtered. The thicknesses of the Cu and Se layer have been chosen to result in a similar Cu/Se ratio as for electrodeposited Cu-Se (section 9.2). The overall film composition is Cu-rich (Cu/In = 1.14).

vanishes again above $168 - 196\,°C$. It corresponds to the crystallisation and melting of hexagonal Se. The melting of Se is linked with the consumption of elemental Cu and a distinct increase of $CuSe$. Between $205\,°C$ and $280\,°C$ also orthorhombic $CuSe_2$ can be detected, but it is less pronounced than in the precursor with electrodeposited Cu-Se. $CuSe$ decomposes according to reaction 14.5 at $357 - 381\,°C$.

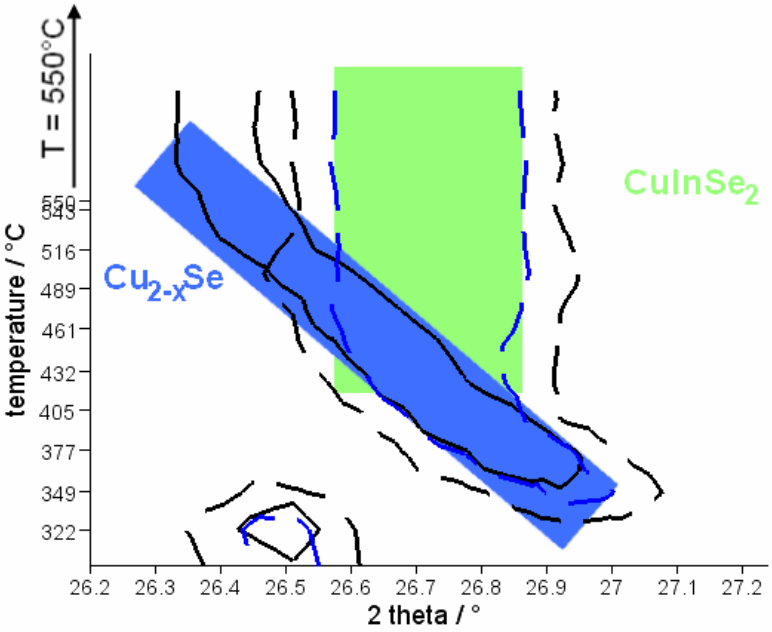

Figure 19.8.: Contour plot of the onset of the dominant peak in the in-situ diffractograms of Mo/Cu-Se and Mo/In-Se/Cu/Se. The heating up and the first three scans at $550\,°C$ are shown. The black lines show the contour of the measured data at $150\,counts$ and the blue line is the contour at $300\,counts$. The solid line belongs to the Mo/Cu-Se stack and the dashed one to Mo/In-Se/Cu/Se. The coloured boxes suggest the phases that are involved in the contour. The plot is a magnified excerpt of the measurement in figure 19.7.

At this point the same problem arises as for the completely electrodeposited precursor in figure 19.5. It is again not possible to distinguish the phases $CuInSe_2$, $CuIn_3Se_5$ and $Cu_{2-x}Se$ clearly. A closer look into the evolution of XRD reflections around the onset of $CuInSe_2$ is given in figure 19.8. The contour of the main peak for the Mo/In-Se/Cu/Se stack is overlaid with the contour of the simple Mo/Cu-Se stack. This time the $Cu_{2-x}Se$ peak can completely describe the peak shift of the full precursor below $400\,°C$. Although the contour of the full precursor is a little bit broader due its higher countrate there is no convexity at low temperatures as it has been observed for the Mo/In-Se/Cu-Se precursor in figure 19.6. Also the kink at $490\,°C$ is absent for the Mo/In-Se/Cu/Se precursor. Therefore it is possible to describe the peak evolution by a superposition of a $Cu_{2-x}Se$ and $CuInSe_2$ reflection as it is visualised by the coloured shading in figure 19.8. There is no need to introduce the $CuIn_3Se_5$ phase in the diffractogram. Considering continuity it can still be accepted that the phase reaction from In_2Se_3 to $CuInSe_2$ involves the presence of an ordered vacancy phase. If it is not observed in the diffractogram it can be concluded that there is a fast conversion from $CuIn_3Se_5$ into $CuInSe_2$ and the content of the ordered vacancy phase is low. A faster $CuInSe_2$ reaction in the Mo/In-Se/Cu/Se stack with the sputtered Cu layer in comparison to the completely electrodeposited Mo/In-Se/Cu-Se precursor supports the idea that the latter one is limited by the interface area. The interface area between indium selenide and copper selenide is small in the completely electrodeposited stack. The sputtered Cu and the evaporated Se top layer are

smooth and even if both elements react to copper selenide at the beginning of the heating process a better coverage of the indium selenide can be assumed. Therefore the interface area between In-Se and Cu-Se is larger in the partly sputtered precursor and the reaction of both can proceed faster.

There is still an inconsistency in the contour plots (figure 19.6 and figure 19.8). For the Mo/In-Se/Cu/Se precursor $\mathrm{CuInSe_2}$ sets in at $400 - 430\,°\mathrm{C}$. The $\mathrm{CuIn_3Se_5}$ phase in the completely electrodeposited Mo/In-Se/Cu-Se precursor already sets in at $350\,°\mathrm{C}$. If the reaction between copper selenide and indium selenide is really slower in the latter case, a higher onset temperature is expected, because of two possible reasons. First, the diffusion will become faster with higher temperature. That means for the slower Mo/In-Se/Cu-Se precursor a higher temperature is required to obtain the same reaction rate as for the Mo/In-Se/Cu/Se precursor. Second, the temperature increase is continuous. That means if the process is slower, it will extend to higher temperatures, because it takes longer until the product can be detected in the diffractogram. A repetition of the contour plot with a higher resolution in temperature and angle is required to validate the results and precise the onset temperature of the reaction.

At $550\,°\mathrm{C}$, when the thermal expansion makes it possible to distinguish between $\mathrm{CuInSe_2}$ and $\mathrm{Cu_{2-x}Se}$, the reflections of the latter phase at $26.3\,°$ and $43.8°$ are not observed for the partly sputtered Mo/In-Se/Cu/Se precursor (figure 19.7). The overall composition of the Mo/In-Se/Cu/Se is Cu-rich (Cu/In atomic ratio of 1.14), while the Mo/In-Se/Cu-Se was intended to be stoichiometric. The higher $\mathrm{Cu_{2-x}Se}$ signal of the completely electrodeposited sample can be explained by more copper selenide residuals at the surface, because the reaction is slow. An alternative explanation is a better crystallinity of the copper selenide phases synthesised from a Cu-Se layer instead of a Cu/Se stack. Again some $\mathrm{In_2O_3}$ forms during the annealing.

In summary the behaviour of the Mo/In-Se/Cu/Se is similar to the one of Mo/In-Se/Cu-Se. Cu is not directly diffusing into the indium selenide layer as it might be expected. Instead it is reacting with the molten Se into CuSe which decomposes into $\mathrm{Cu_{2-x}Se}$ around $370\,°\mathrm{C}$. The fact that Cu preferably forms copper selenide instead of reacting with indium selenide is in line with observations by Hergert et al. and Verma et al. from annealing stacked elemental layers. In this case it is also observed that the Cu and In react to their binary selenides first and the actual formation of $\mathrm{CuInSe_2}$ takes place through the binaries [43, 180].

It has been discussed that the reaction kinetics are probably different for the completely electrodeposited Mo/In-Se/Cu-Se precursor and the partly sputtered Mo/In-Se/Cu/Se one. Therefore it is interesting to compare the morphology of both absorbers after annealing to look for a possible difference in the crystallisation. In a first experiment grain size difference between the annealed precursors can be estimated from the SEM picture of their surface and cross section (figure 19.9). The precursors have been annealed in the tube furnace under standard conditions. In order to rule out an effect from the Cu-rich growth conditions, samples with a similar Cu/In ratio are compared. The morphology of the absorbers is similar. At the surface both sample have small grains ($500-1000\,\mathrm{nm}$). Between them are some scattered grains with a lateral extension up to $5\,\mu\mathrm{m}$. The larger grains are a little bit more frequent for the partly sputtered precursor. The cross sections show grains between 1 and $2\,\mu\mathrm{m}$ height. So the different reaction kinetics of both precursor types have no profound consequences on the grain size.

In conclusion the electrodeposited binary selenide stack reacts the following way: In the beginning the electrodeposited copper selenide reacts with amorphous Se into $\mathrm{CuSe_2}$ which undergoes the phase transitions expected from the Cu-Se phase diagram as the temperature increases (section 14.2). The Se-rich $\mathrm{CuSe_2}$ phase is favoured if the annealing is performed in the tube furnace under Se atmosphere instead of the XRD hotstage. The formation of $\mathrm{Cu_2Se}$ by reaction 14.5 coincides with the formation of $\mathrm{CuInSe_2}$. Therefore it is likely that $\mathrm{Cu_2Se}$ and amorphous $\mathrm{In_2Se_3}$ are the relevant binary phases for $\mathrm{CuInSe_2}$ formation under the used conditions. It is expected that an ordered vacancy phase is formed as an intermediate phase. This phase could not be verified directly. Nevertheless a discontinuity in the XRD peak position (figure 19.6) supports the possible presence of an intermediate phase. The higher onset temperature of $\mathrm{CuInSe_2}$ formation observed in the in-

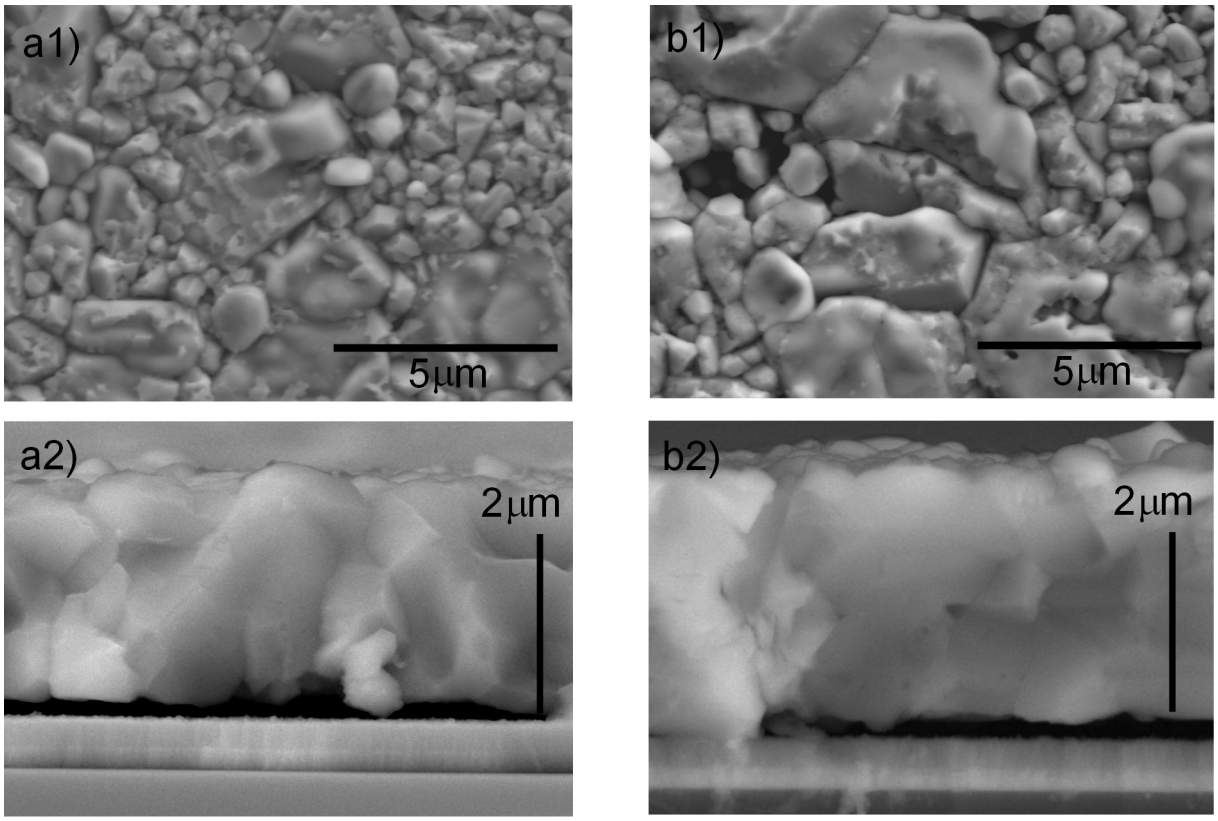

Figure 19.9.: SEM top and cross sections views of absorbers annealed at $550\,°C$ for $30\,\mathrm{min}$ from a) a completely electrodeposited Mo/In-Se/Cu-Se precursor (Cu/In atomic ratio 1.20) b) a Mo/In-Se/Cu/Se precursor where the indium selenide layer has been electrodeposited, the Cu layer sputtered and the Se layer evaporated (Cu/In atomic ratio 1.14). The thicknesses of the Cu and Se layers are adjusted to same Cu/Se ratio as in the electrodeposited Cu-Se layer. The absorbers have been etched in KCN to remove copper selenide phases.

situ experiment compared to the ex-situ measurements and the temperatures reported in literature indicate a slow reaction of the electrodeposited precursors.

If the electrodeposited copper selenide in the precursor stack is substituted by smooth layers of Cu and Se the principal reaction path of the precursor stays the same, because both elemental layers react into copper selenide at the beginning of the annealing. The shape of the XRD reflection at the onset temperature of $\mathrm{CuInSe_2}$ formation does not indicate the presence of an intermediate ordered vacancy phase. It might be concluded that the smooth top layer promotes the diffusion of Cu, because it enlarges the interface area between copper selenide and indium selenide. Therefore the intermediate phase could convert to $\mathrm{CuInSe_2}$ quickly and not show up in the diffractogram. The crystallisation is not significantly improved for the Mo/In-Se/Cu/Se precursor stack.

20. Absorber impurities

Trace element impurities can affect the opto-electronic properties of the $\mathrm{CuInSe_2}$ semiconductor material. It is obvious that their concentration will depend on the details of the preparation procedure, e.g. purity of used chemicals, cross-contamination of shared equipment, or even the care of the operator. It is therefore in most cases not possible to state general impurity levels. Nevertheless one can expect general trends for possible impurity sources. Thus the following examples must not be understood as general valid impurity concentrations but shall indicate trends, where trace impurities can enter in the fabrication process.

20.1. Background

Sodium is the most studied impurity in CIGS, because it leads to an improvement of the solar cell performance [181, 182]. It has several effects on the absorber and solar cell properties, which are reviewed in [15]. The presence of Na during the absorber formation results in a higher V_{OC} and fill factor of the solar cell [183]. It has been proposed that the increase of V_{OC} is caused by a higher effective acceptor density [15]. The conductivity of CIGS increases with the incorporation of Na [184, 185]. A preferred (112)-orientation of the absorber is observed with presence of Na during growth [185]. Na does not change the reaction path of a binary selenide precursor stack during selenisation, but slows down the reaction rate [168]. An effect of Na on the grain size is controversial. Older articles report a larger grain size for Na containing absorbers [184, 185] while newer articles report a decrease in grain size [186, 187]. Smaller grains are also observed if the sodium content is high [183].

Like sodium also potassium can increase the absorber conductivity and the hole carrier density. However the effects are less pronounced than for Na. For caesium no significant change in comparison with an undoped reference sample was seen [184].

The diffusion of impurities from the substrate into the absorber has been studied in order to identify alternative substrates, e.g. metal foils. Different metal precursor layers have been deposited below, the Mo backcontact layer of the substrate to study the impurity diffusion into the absorber. The elements V, Ti, Al, and Ni showed a comparatively low diffusion (concentration in the absorber $< 100\,\mathrm{ppm}$) and did not reduce the solar cell efficiency a lot. In contrast, Mn and Fe led to a concentration above 10% in the absorber which destroyed the solar cell. The impurity concentration could be significantly reduced if the Mo layer thickness acting as a diffusion barrier was increased [188]. A different study could not detect diffusion through the Mo backcontact for Fe and Mn but only for Ti and Na [189]. That means the results probably depend on the detailed material properties of the Mo backcontact.

A different motivation to study the effects of impurities in CIGS, is the idea to form a homo-junction solar cell in CIGS by external doping. For this purpose impurities are introduced by ion bombardment with successive annealing. It has been shown that n-type $\mathrm{CuInSe_2}$ can be converted to p-type conduction by N, P, Sb, Bi, He, Ne and O incorporation [190, 191]. p-type $\mathrm{CuInSe_2}$ can be converted n-type by Br, Cl, and Zn incorporation [192].

Procedures to determine trace element concentrations in $\mathrm{CuInS_2}$ have been developed by Hwang et al. and Hung et al. [193, 194]. They combine wet chemical methods, electrochemical purification and atomic absorption spectroscopy or neutron activation analysis. The concentration of Ag in $\mathrm{CuInS_2}$ single crystals grown by iodine transport was between $0.8\,\mathrm{ppm}$ and $2\,\mathrm{ppm}$ [193, 194]. The elemental Cu source was the main origin of contamination [194].

In a first approach Calixto et al. studied the effect of contamination in the $CuInSe_2$ coelectrodeposition process by using $InCl_3$ of different purities (98.5% versus 99.999% purity). There was no significant difference in the composition of the precursor [195]. Dharmadasa et al. hypothesise a possible contamination of the $CuInSe_2$ deposition bath by the use of Ag/AgCl and calomel reference electrodes [196]. For this reason they move to a two-electrode set-up. In thin film CdTe solar cells already a Ag impurity concentration below $5\,\mathrm{ppb}$ can decrease the performance of the device [197].

A possible electrochemical fabrication of Pt micro-particles resulting from an anodic dissolution of the counter electrode has been observed in [198]. Pt particles deposited on the working electrode after keeping it at $-1.2\,\mathrm{V}$ (vs. Ag/AgCl) in a stirred $1\,\mathrm{M}\ H_2SO_4$ solution for $6\,\mathrm{h}$.

20.2. Results and Discussion

The effect of the background electrolyte was studied for the electrodeposited copper selenide layer. In this case a $232\,\mathrm{mmol/kg}\ LiCl$ solution has been chosen as background electrolyte. Table 20.1 lists the Li concentration obtained by ICP-MS for several samples. While most samples are below the quantification background of the ICP-MS, the single Cu-Se layer contains a significant amount of Li ($206 \pm 79\,\mathrm{ppm(atomic)}$). This contamination results from the background electrolyte. Although one would expect finding a higher Li contamination in all electrodeposited samples that contain a Cu-Se layer, this is not observed (table 20.1). If there was another electrodeposition step after the Cu-Se layer it could be cleaned within the further process. But Cu-Se is the final layer before the annealing. A possible explanation is the water rinsing after the Cu-Se layer is taken out of the bath. Obviously it has not been as thoroughly for the single Cu-Se layer as for the complete stacks. The difficult cleaning of the Cu-Se is caused by its porous morphology (see figure 9.2). The pores bind the background electrolyte by capillary forces. Only a careful water rinsing can wash it out again. Thus it can be concluded that impurities resulting from the bath will in generally be higher for rough and porous layers.

In the present electrodeposition set-up a platinum sheet is applied as counter electrode and an Ag/AgCl electrode as reference electrode. Table 20.1 lists the silver and platinum contents of several electrodeposited and physical vapour deposited samples. For both elements the contamination is lower for the PVD samples. It seems as if reference and counter electrode increase the corresponding impurity level in the electrodeposited film. This result is further supported by the single electrodeposited Cu layer. In this deposition the Ag/AgCl reference electrode had been replaced by a Hg/HgO reference. Consequently the silver contamination is lower in this sample compared to the other electrodeposited samples. Although it is likely that the electrodes are responsible for the Ag and Pt contamination, the results could also be explained by impurities in the pH buffer solution. In all cases except the copper deposition the pH was adjusted by a buffer made from sulfamic acid and potassium biphthalate. The purity of these chemicals was 99.99% and 99.95%, but no further information on their Ag or Pt contamination is available.

In conclusion three sources of contamination have been identified in the presented electrodeposition process. The salt of the background electrolyte can cause trace impurities in the plated film, if the sample is not cleaned carefully enough after the electrodeposition. It is especially an issue of porous layers like copper selenide. The use of an Ag | AgCl reference electrode is the probable cause for an incorporation of silver up to $37 \pm 15\,\mathrm{ppm}$. The platinum incorporation in the low ppm range is probably caused by the counter electrode.

	Ag	error	Pt	error	Li	error
	ppm (at)	ppm (at)	ppm (at)	ppm (at)	ppm (at)	ppm (at)
PVD						
BAG/Mo/PVD	0.2*	0.4*	0.0*	4.1*	28*	15*
SLG/Mo/PVD(1)	0.2*	0.3*	0.0*	4.1*	32*	17*
SLG/Mo/PVD(2)	0.2*	0.2*	0.0*	1.5*	21*	12*
ED						
BAG/Mo/$CuInSe_2$	7	3	0.9	3.0	23*	17*
SLG/Mo/$CuInSe_2$	32	12	0.1*	2.7*	37*	28*
BAG/Mo/In-Se/Cu-Se	6	3	2.1	1.5	18*	16*
SLG/Mo/In-Se/Cu-Se	37	15	0.6*	0.5*	14*	18*
BAG/Mo/In-Se(1)	16	7	2.8	2.2	49*	32*
BAG/Mo/In-Se(2)	3	2	3.3	2.9	21*	29*
SLG/Mo/In-Se	7	3	3.7	3.4	24*	31*
BAG/Mo/Cu-Se	12	5	0.2*	7.1*	206	79
BAG/Mo/Cu	0*	4*	1.6*	3.0*	43*	67*

Table 20.1.: Silver, platinum, and lithium impurities in absorbers, precursor and single electrodeposited layers. The impurities have been measured by ICP-MS. Values marked with * are below the quantification limit of the ICP-MS apparatus and cannot be interpreted quantitatively. The first 3 samples have been prepared in a PVD 3-stage-process [130]. The electrodeposited (ED) $CuInSe_2$ absorbers have been obtained by annealing Mo/In-Se/Cu-Se precursor stacks. Soda-lime glass (SLG) and boro-aluminosilicate glass (BAG) substrates have been used.

21. Conclusion

The prerequisite for a scientific study of having samples of controlled chemical composition was demonstrated by EDX measurements. It has been verified that the annealing of an electrodeposited stoichiometric Mo/In-Se/Cu-Se precursor leads to $\mathrm{CuInSe_2}$ chalcopyrite. If the precursor has an overall Cu-rich composition, the copper excess forms $\mathrm{Cu_{2-x}Se}$ phases at the surface of the $\mathrm{CuInSe_2}$, as it is expected from the phase diagram. If the precursor composition is Cu-poor, it is possible that the reaction is incomplete and an ordered vacancy compound is left at the backside of the absorber.

It has been observed that the tetragonal splitting between the (220) and (204) XRD reflections increases with Cu/In ratio. The increase is higher than it is expected from bulk samples. An explanation is a change of strain in the thin film absorber for different Cu/In ratios. In this case not the tetragonal distortion of the unit cell but the strain is the main cause for the splitting of the XRD reflections. As it has been suggested in the motivation of the electrodeposited binary selenide precursors (section 2.3) the grain size of the absorber is larger than for a coelectrodeposited sample annealed under the same conditions. The same is true for the crystal coherence length. Grain size and coherence length can further be enhanced if the background gas pressure during the annealing is increased to $1000\,\mathrm{mbar}$. The higher background pressure increases the effective selenium partial pressure, because it slows down the outdiffusion of selenium from the reaction zone due to the reduced mean free path.

At the beginning of the annealing the electrodeposited copper selenide reacts to $\mathrm{CuSe_2}$ and with increasing temperature follows the phase transitions expected from the Cu-Se phase diagram. If the electrodeposited copper selenide layer is replaced by a smooth copper film capped with selenium the process is similar. Copper and selenium will react to copper selenide and follow the phase transitions expected from the Cu-Se phase diagram as the temperature increases. No crystalline indium selenide is observed in the reaction, because its crystallisation temperature is above the onset of $\mathrm{CuInSe_2}$ formation. Under equilibrium conditions, when the temperature is constant, $\mathrm{CuInSe_2}$ sets in between $250\,°\mathrm{C}$ and $350\,°\mathrm{C}$. In accordance with the quasibinary $\mathrm{In_2Se_3}$-$\mathrm{Cu_2Se}$ section of the Cu-In-Se phase diagram and supported by similar experiments in literature [169] it can be assumed that Cu-Se diffusion into the indium selenide converts it into an ordered vacancy compound. Further Cu-Se diffusion leads to the formation of $\mathrm{CuInSe_2}$. A discontinuity in the peak position might be an experimental confirmation of the ordered vacancy compound but the superposition of $\mathrm{CuInSe_2}$, $\mathrm{Cu_{2-x}Se}$, and the possible ordered vacancy phase makes the interpretation of the XRD diffractograms difficult at that point.

The porous morphology of the electrodeposited copper selenide leads to a small interface area with the indium selenide and slows down the diffusion between both. This was concluded from SEM cross sections and the late onset of $\mathrm{CuInSe_2}$ in the in-situ XRD experiments. The slow diffusion between indium selenide and copper selenide causes the long residence time of copper selenide on the surface, where it undergoes the phase transitions from the Cu-Se phase diagram. It seems that the reaction of the precursor where the porous copper selenide has been replaced by a smooth copper film capped with selenium sets in earlier, because the interface with the indium selenide layer is larger. The sintering of the electrodeposited copper selenide particles influences the interface area and thus the diffusion kinetics. It is a complex effect dependent on several factors (e.g. stacking density of the copper selenide platelets), which can explain the variability observed in the annealing process. The reaction of a Cu-poor precursor stack can be incomplete, but also counter-examples have been observed. The slow diffusion also leads to a longer presence of the intermediate ordered vacancy compound. That is a possible reason, why the phase is observed in the present experiments but has not been reported in similar experiments in literature.

Finally it has been shown that elements from the electrodeposition bath and the electrodes, can induce impurities in the absorber layer. The magnitude of these impurities was observed to be multiple times higher in the electrodeposited material than the vacuum deposited material. The implications on opto-electronic properties including device performance for absorber layers containing an ordered vacancy compound at the back contact, and the effect of different background annealing pressures will be explored in part III.

Part III.

Optoelectronic Absorber and Device Characterisation

22. Introduction

The third part in this thesis studies the performance of solar cells prepared from absorber layers grown from electrodeposited binary selenide precursors. The influence of Cu-rich, stoichiometric, and Cu-poor growth conditions are studied (table 16.1). In chapter 18 it has been observed that a higher background gas pressure during annealing improves grain and crystallite size. In the following it will be examined, if this also leads to a better solar cell performance.

At the beginning the photoluminescence of the absorber is studied, because it provides information on the optoelectronic quality of the absorber material without the need to complete the solar cell. It has been reported in literature that the observed radiative recombination transitions in $\mathrm{CuInSe_2}$ depend on the composition of the absorber [199, 200, 201, 202, 203, 204]. This will be compared to the present absorbers.

JV characteristics of the completed solar cells are taken to determine the conversion efficiency, because this is the measure of practical relevance. The characteristics also provide first information on loss mechanisms for the solar cells prepared from the absorbers in table 16.1. The loss mechanisms are studied in more detail by different characterisation techniques. Temperature dependent JV measurements are applied to study interface recombination. Quantum efficiency measurements identify current losses. Voltage biased quantum efficiency measurements show if the current losses are connected to an incomplete collection of charge carriers or a loss mechanism that is independent of the location of charge carrier generation (e.g. interface recombination or a photocurrent barrier).

23. Background

23.1. Band structure of a $\mathrm{CuInSe_2}$ thin film solar cell

CIS thin film solar cells are designed as heterojunction solar cells where the p-n junction is formed between different semiconductors. If the band diagrams of two isolated semiconductors are aligned by the vacuum energy level (the lowest energy level, where the electron is no longer bound to the material), there will be an energy offset between the conduction band edges of the two semiconductors and another energy offset between their valance band edges. The equilibrium band diagram of a heterojunction can be constructed from the following conditions: 1) the conduction and valance band offsets at the interface are perceived if the materials are brought into contact; 2) the Fermi level is constant [205]. The typical band diagram of an absorber/buffer/window layer junction is sketched in figure 23.1. The band gaps of the buffer and window layer are large to avoid absorption of light in these layers. The CIS absorber layer is p-type and the window layer n-type. If both materials are brought into contact, electrons from the donors in the n-type material will recombine with holes from acceptors in the p-type material. Therefore donors and acceptors become charged and form a space charge region (SCR), which results in the band bending in the band diagram. (The space charge region in the window layer is narrow due to the high doping density.) The electric field inside the SCR separates the photogenerated electron-hole pairs.

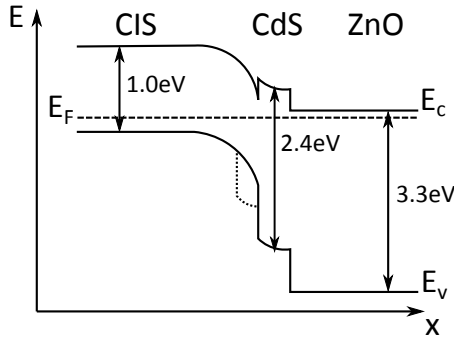

Figure 23.1.: Typical band structure of the absorber/buffer/window layer heterojunction in a CIS thin film solar cell [205]. The junction is at equilibrium. The band gap energies have been taken from [206]. The dotted line shows the valance band edge, for a Cu-poor grown absorber [207].

The CdS buffer layer improves the band alignment. In figure 23.1 the CdS layer causes a spike in the conduction band between the CIS and the window layer [206]. Without the CdS buffer one observes a "cliff" in the conduction band between absorber and window layer. It has been shown that a cliff favours interface recombination and thus reduces V_{OC}. This can be prevented by a small spike below $0.3\,\mathrm{eV}$. If the spike is larger, it limits the short circuit current [208, 209, 210]. Cu-poor absorbers lead to less interface recombination than absorbers grown under Cu-rich conditions, because the valance band edge is lowered (section 23.2) [207].

At the surface of the absorber layer the Fermi-level is close to the conduction band. (This is valid for CIGS absorbers with a small band gap energy, i.e. a low Ga content.) The conductivity of the surface can therefore be inverted to n-type. This inversion of conductivity lowers the density of holes and reduces interface recombination [211].

23.2. Influence of Cu/In ratio on electronic structure

Several electronic properties of the $\mathrm{CuInSe_2}$ absorber depend on its Cu/In ratio. Cu-poor absorbers have a higher defect density than Cu-rich grown films, which leads to a strong compensation of the semiconductor. The strong compensation induces fluctuations of the band edges (chapter 25.1) [200]. It is also accompanied by a lower free charge carrier density [212]. The electrical resistance of the absorber layer increases the less Cu it contains. It is a possible explanation why the parallel resistance in a solar cell is usually higher if the absorber is Cu-poor [212].

The band gap energy is also dependent on the Cu/In ratio. The band gap of $\mathrm{CuInSe_2}$ depends on the Cu/In ratio of the as-grown absorber. It has been shown for PVD grown polycrystalline absorbers that there is a step in E_G from $\approx 0.96\,\mathrm{eV}$ to $\approx 1.01\,\mathrm{eV}$, when going from Cu-poor (Cu/In atomic ratio < 0.92) to Cu-rich (Cu/In > 1.20) growth conditions. Above this step the band gap changes with composition are small. Similar results are true for epitaxial samples [145].

Solar cells prepared from Cu-rich grown $\mathrm{Cu(In_Ga)Se_2}$ absorbers show strong interface recombination [207, 211]. The lower interface recombination of Cu-poor absorbers can be explained by a band gap widening at the surface. For polycrystalline $\mathrm{CuInSe_2}$ thin films a depletion of Cu in the bulk is connected to an even larger depletion of Cu at the surface [205]. It has been proposed that the band gap widening at the surface of the Cu-poor grown absorber is caused by an ordered vacancy phase (dotted line in figure 23.1) [206, 213]. An alternative explanation for the lower interface recombination of Cu-poor grown solar cells is the formation of a defect layer at the surface formed by the interaction with Cd from the buffer layer [214].

24. Experimental

24.1. Photoluminescence (PL)

The set-up for PL measurements is shown in figure 24.1. The sample is excited with the $514.5\,\mathrm{nm}$ line of an argon ion laser that is focused on the sample. A laser intensity between $1\,\mathrm{mW}$ and $50\,\mathrm{mW}$ is applied. The sample is kept inside a cryostat at $10\,\mathrm{K}$ to allow comparison with previous reported literature results [202, 199]. The photoluminescence signal is focused into a spectrograph which spatially splits up the spectrum by a dispersive grating. The complete spectrum is recorded at once by a InGaAs detector. A notch filter in front of the spectrograph removes the wavelength range of the laser radiation and protects the detector.

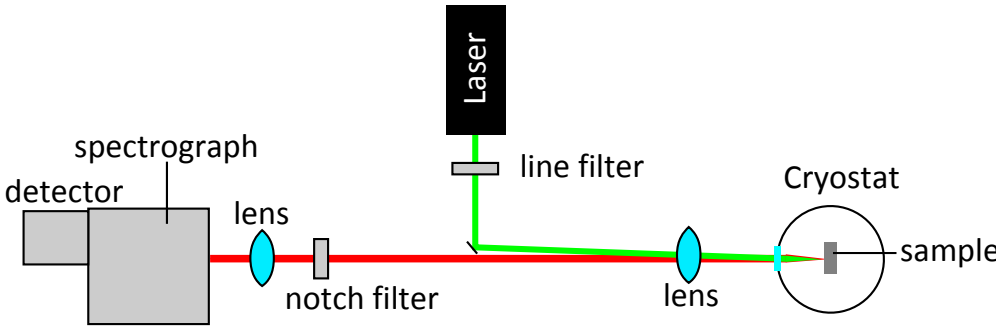

Figure 24.1.: Photoluminescence set-up.

The quantitative PL measurements which have been recorded to determine the band gap in table 27.1 were measured in the same set-up at room temperature. The quantification of the set-up was done with a calibration lamp of known intensity.

24.2. Solar cell fabrication

The CdS buffer layer and the ZnO window layer with the grids have been deposited on the absorber to complete the solar cell.

Directly before the buffer deposition the absorbers were etched in a 5% potassium cyanide solution for two minutes to clean the surface and remove copper selenide phases if present. CdS was deposited by chemical bath deposition [215]. A solution containing $0.42\,\mathrm{g/l}$ $\mathrm{CdSO_4}$, $0.76\,\mathrm{g/l}$ $\mathrm{(NH_2)_2CS}$, and $10\,\%\mathrm{(vol.)}$ $\mathrm{NH_4OH}$ (28% solution) was prepared at $67\,^{\circ}\mathrm{C}$. The absorbers were immersed in this solution for $420\,\mathrm{s}$, which results in a $70\,\mathrm{nm}$ thick CdS film. For technical reasons the Cu-rich sample "ED-Cu-rich-10mbar" was only covered with a $50\,\mathrm{nm}$ thick CdS film.

The further processing of the windows layer was done at the Helmholtz Zentrum Berlin. A $130\,\mathrm{nm}$ thick intrinsic ZnO layer followed by a $540\,\mathrm{nm}$ thick aluminium doped ZnO layer were deposited by rf-sputtering. Afterwards a grid of $10\,\mathrm{nm}$ thin Ni covered by $2\,\mu\mathrm{m}$ Al was added as front contacts of the cells. The area of the cells was about $0.5\,\mathrm{cm}^2$. The backcontact was prepared by scratching off the absorber down to the Mo layer at a spot close to the solar cell. Indium spots were painted with a soldering iron on the blank Mo substrate to assure a good contact.

24.3. (Temperature dependent) current-voltage measurements

Current density - Voltage (JV) characteristics have been measured in a home-built set-up. A halogen lamp (ANSI code: ELH) with a dichroic reflector was used as illumination source. The light intensity at the position of the sample was adjusted to $100\,\mathrm{mW/cm^2}$ with a certified solar cell. The solar cell sample was placed on a peltier element to prevent a warming due to the illumination. The cell was contacted in a four point geometry (two contacts at the front and two at the back) to allow a correction of the contact resistance. A computer controlled current-voltage-source was used to scan the voltage bias and record the current response.

The used set-up underestimates current densities. This has been checked in our group by comparing the JV characteristics of the same PVD grown solar cell measured in our set-up to the one which has been obtained in a sun simulator at the "Fraunhofer-Institut für Solare Energiesysteme ISE". In the illuminated JV characteristic the current density is 10% higher in case of the sun simulator. The JV characteristics presented in this thesis and the values derived from them have been corrected by multiplying the measured current density by 1.1.

Temperature dependent JV measurements have been performed in a similar set-up. This time the sample was placed inside a cryostat, allowing temperatures down to $100\,\mathrm{K}$.

24.4. (Voltage biased) quantum efficiency measurements

Quantum efficiency (QE) measurements record the current response of the solar cell depending on the wavelength of the illumination. It is a useful method to identify current loss mechanisms in the solar cell (section 27.1). Quantum efficiency was measured by a lock-in technique (figure 24.2), because the signal response is low (ca. $1\,\mu\mathrm{A}$). The sample solar cell is illuminated on a $1-2\,\mathrm{mm}$ broad spot by a monochromatic light beam. The illumination is chopped to provide a clock signal for the lock-in amplifier. Front and back contact of the solar cell are connected to a potentiostat which amplifies the current signal and allows to apply a DC voltage bias between the contacts. A software controls the scanning through the light spectrum and the voltage bias applied at the potentiostat. The current response at each wavelength is recorded. In order to relate the current response to the quantum efficiency a Si or InGaAs solar cell with a calibrated quantum efficiency is measured under the same conditions.

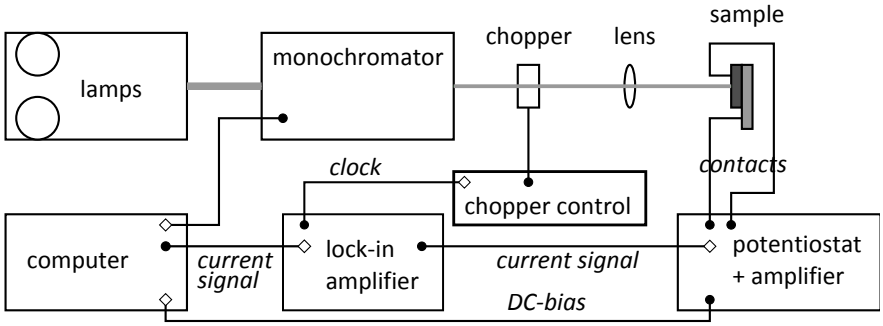

Figure 24.2.: Set-up for QE measurements. The light beam is represented by the grey line from the lamps to the sample. The signal cables are marked with an open symbol at the input and a filled symbol at the output.

25. Photoluminescence

25.1. Background

Photoluminescence (PL) provides a method to observe the radiative recombination processes in a semiconductor and conclude on their defect levels within the bandgap. It is thus a suitable technique to examine the optoelectronic quality of the absorber layer.

In a photoluminescence set up the electrons are excited by a laser into the conduction band leaving behind holes in the valance band. Afterwards a fast thermalisation brings the electrons close to the conduction band edge and the holes close to the valance band edge. Different radiative recombinations are now possible (figure 25.1) [208, 202]:

- Band-to-band transition: An excited electron recombines with a hole from the valance band.
- Excitonic transition: Due to their opposite charges an electron and a hole can form an exciton. In a simple way it can be described by analogy to the hydrogen model. The transition energy is therefore reduced by the binding energy of the exciton.
- Free-to-Bound transition: An electron of the conduction band can recombine with a hole in an acceptor or a hole from the valance band can recombine with an electron in a donor.
- Donor-Acceptor (DA) transition: An electron of a donor state can recombine with a hole of an acceptor state. The remaining donor and acceptor are now charged positive and negative, respectively. The attractive Coulomb force between them causes a binding energy that must be considered in the transition energy.

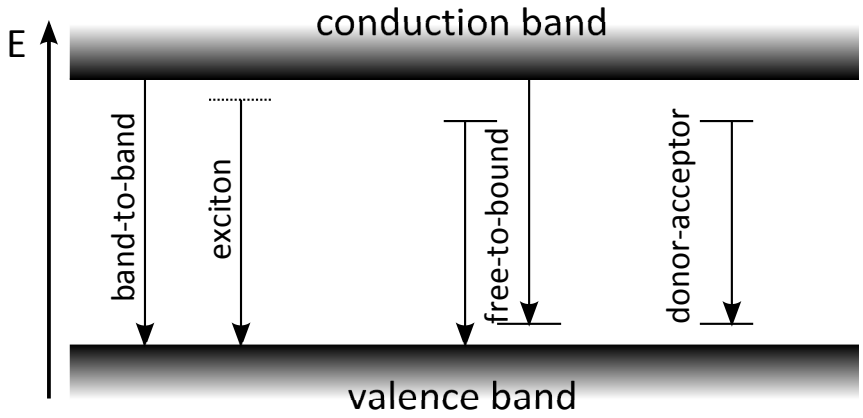

Figure 25.1.: Radiative transitions in a semiconductor. Scheme taken from [208].

A way to distinguish between the possible radiative recombination mechanisms is a variation of the laser excitation intensity I_{exc}. The transition energy E_{PL} and also the transition intensity I_{PL} show different dependencies on I_{exc} for the different types of transition. In this context it is helpful to introduce the energy shift coefficient β and the intensity exponent k which describe the dependency of the corresponding variable on the excitation intensity I_{exc} [208, 202]:

$$E_{PL}(I_{exc}) = E_{PL}(I_0) + \beta \log_{10}(I_{exc}/I_0) \tag{25.1}$$

$$I_{PL} \propto I_{exc}^{k} \tag{25.2}$$

The typical values of β and k for the different transition types are summarised in table 25.1.

transition type	β	k	remarks
Band-to-Band	0	≈ 2	[1]
Excitonic	0	$1-2$	
Free-to-Bound	0	< 1	
Donor-Acceptor (weak comp.)	few $\mathrm{meV/decade}$	< 1	
Donor-Acceptor (strong comp.)	$> 10\,\mathrm{meV/decade}$	≈ 1	

[1] $k = 2$ is only valid in case of low carrier injection and negligible competitive recombination mechanisms

Table 25.1.: Energy and intensity dependence of radiative transitions with excitation intensity I_{exc} [208, 202, 216]. The coefficients β and k are defined in equations 25.1 and 25.2. In case of donor-acceptor transitions it is distinguished between weakly and strongly compensated semiconductors.

The observed photoluminescence transitions in $\mathrm{CuInSe_2}$ are composition dependent. PL spectra of epitaxial $\mathrm{CuInSe_2}$ absorbers in dependence on their Cu/In ratio have been presented in [199, 202]. In these samples distinct donor-acceptor transitions are observed for near-stoichiometric and Cu-rich material. The first transition (DA2) is dominant at Cu excess (Cu/In > 1.05). It is located around $0.97\,\mathrm{eV}$ (at $10\,\mathrm{K}$). In the near stoichiometric range ($0.94 <$ Cu/In < 1.05) another transition (DA1) dominates around $0.99\,\mathrm{eV}$. A weak peak is observed around $0.94\,\mathrm{eV}$. It can either be interpreted as a phonon replica of the DA2 transition or as a separate donor-acceptor transition (DA3). The latter interpretation is supported by analogous observation for $\mathrm{CuGaSe_2}$ [199, 208]. For Cu-poor samples (Cu/In < 0.91) a broad asymmetric peak is observed. This peak is interpreted as a donor-acceptor transition in a highly compensated semiconductor [200]. Such a semiconductor has a high density of ionised donors and acceptors that attract and repel the free charge carriers. These Coulomb potentials cause statistical fluctuations of the conduction and valance band edge. Therefore the transition energy is not well-defined any more but shifted and broadened. If the excitation intensity is increased, the free charge carrier density in the bands is raised. The free charge carriers can shield the Coulomb potentials and reduce the band edge fluctuations. Thus the transition energy in a highly compensated semiconductor shows a more pronounced dependency on excitation intensity than for a weakly compensated one (see table 25.1).

In addition to the donor-acceptor transitions also excitonic transitions and phonon replicas are observed for Cu-rich and near-stoichiometric epitaxial samples. In a phonon replica a phonon has been excited in the optical transition process. Therefore the energy of the initial optical transition is reduced by the energy of the phonon. For $\mathrm{CuInSe_2}$ the energy of a longitudinal optical phonon is about $29\,\mathrm{meV}$ [202]. Excitonic transitions and phonon replicas require a supreme crystal quality, because grain boundaries and crystal defects can break the excitonic bond or reduce the coupling between electronic and lattice system [217, 202].

25.2. Results and Discussion

Figure 25.2 shows photoluminescence spectra of the $\mathrm{CuInSe_2}$ absorbers obtained from electrodeposited binary selenide precursors. Previous studies on epitaxial and polycrystalline thin films have demonstrated that the observed transitions depend on the Cu/In ratio of the absorber [199, 200, 201, 202, 203, 204]. In the following a Cu-poor, a stoichiometric, and a Cu-rich $\mathrm{CuInSe_2}$ film (see table 16.1) are compared and it is tested if the results from literature can be transferred to the electrodeposited absorbers.

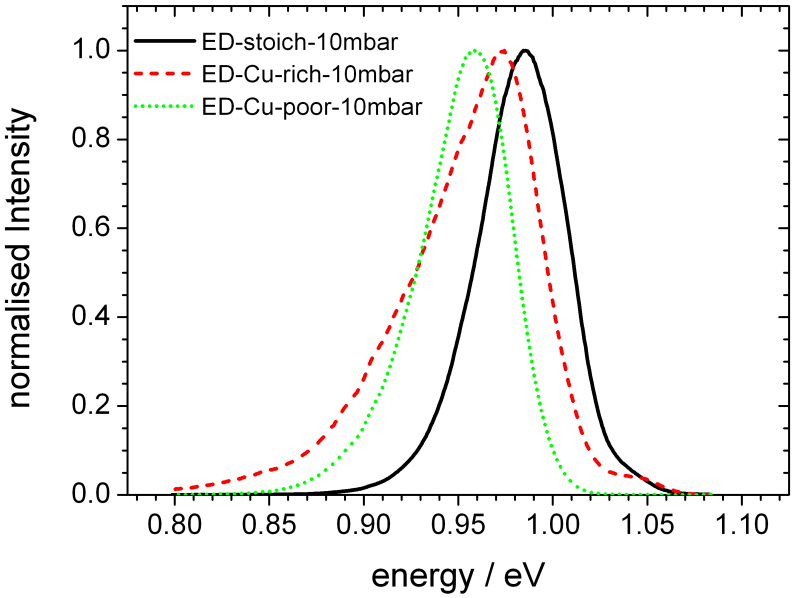

Figure 25.2.: Photoluminescence spectra of $\mathrm{CuInSe_2}$ absorbers with different Cu/In ratios (compare table 16.1). The spectra have been recorded at a temperature of $10\,\mathrm{K}$ and $50\,\mathrm{mW}$ laser excitation power.

In case of a Cu-poor grown film only one broad peak is observed at $0.959\,\mathrm{eV}$ (figure 25.2, "ED-Cu-poor-10mbar"). The broad and asymmetric shape is the typical sign for a strongly compensated semiconductor (see section 25.1). This result is further supported by the energetic shift of the peak with increasing laser excitation intensity (figure 25.3). The high β value of $19\,\mathrm{meV/decade}$ is in the typical range observed for strongly compensated $\mathrm{CuInSe_2}$ absorbers (compare with table 25.1). In case of the near-stoichiometric absorber (ED-stoich-10mbar in figure 25.2) the energetic shift $\beta = 13\,\mathrm{meV}$ is less pronounced, but still high enough to assume a strongly compensated semiconductor. The reduced degree of compensation for the near-stoichiometric absorber compared to the Cu-poor one is also seen from the energetic position of the transition peak at $0.985\,\mathrm{meV}$. It is already close to the energy of the DA1 transition (see section 25.1). The small tail on the high energy side of the peak can be a weak excitonic transition.

The results are similar to the ones reported for epitaxial films (section 25.1, [199]). In both cases Cu-poor samples show strong compensation. Epitaxial samples with a composition close to stoichiometry show a DA1 transition in their photoluminescence spectra. The near-stoichiometric absorber in figure 25.2 is still strongly compensated. There are two possible explanations. First, taking into account the accuracy of the EDX (Cu/In atomic ratio ± 0.05) it is possible that sample "ED-stoich-10mbar" is not stoichiometric but slightly Cu-poor, although the atomic Cu/In ratio measured by EDX was 0.98. Second, it is possible that the defect concentration which causes the compensation is higher in case of the electrodeposited absorbers.

The Cu-rich grown sample "ED-Cu-rich-10mbar" in figure 25.1 is probably not strongly compensated, although it has a broad and asymmetric shape. The value $\beta = 3\,\mathrm{meV/decade}$ indicates only a low compensation (figure 25.3). That is supported by a weak excitonic peak around $1.05\,\mathrm{eV}$. It is usually not observed for highly compensated semiconductors (compare to the Cu-poor and near-stoichiometric spectrum in figure 25.2). The main peak position ($0.972\,\mathrm{eV}$) is close to the values expected for a DA2 transition being the dominant one at high Cu-excess growth conditions. If the absorber is not compensated, the peak asymmetry must be explained by a different cause. A typical explanation is the existence of several phonon replicas of the main DA2 peaks [218]. In the present

case a phonon replica cascade is unlikely, because it does not provide a sufficient fit of the asymmetry and requires a very good crystal quality [202]. It is more likely that at least one further defect transition is present in the low energy side of the peak. This defect could be the DA3 transition that has been proposed in [208]. The photoluminescence signal of the further defect(s) needs to be weak and wide to describe the asymmetry, therefore a broad energy distribution of the defect level(s) must be assumed.

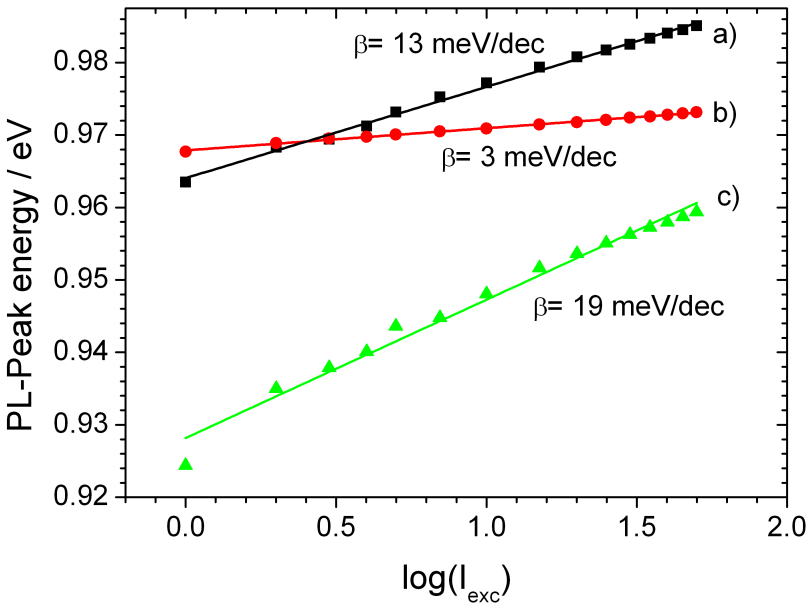

Figure 25.3.: Energy shift of the PL maximum with respect to the laser excitation intensity I_{exc}. The absorbers a) "ED-stoich-10mbar", b) "ED-Cu-rich-10mbar", c) "ED-Cu-poor-10mbar" from table 16.1 are shown.

The electrodeposited absorber which has been annealed at $1000\,\mathrm{mbar}$ background gas pressure shows sharp peaks in the PL spectrum (figure 25.4, sample "ED-stoich-1000mbar"). The highest peak at $0.975\,\mathrm{eV}$ can be assigned to the DA2 transition. The shoulder on its low energy side is probably a phonon replica, because the energy difference to the DA2 transition is close to the energy of a longitudinal optical phonon in $\mathrm{CuInSe_2}$ $(29\,\mathrm{meV})$ [202]. Otherwise it can also be the DA3 transition. The peak at about $1.04\,\mathrm{eV}$ can be ascribed to an excitonic transition, because $k = 1.2$. The presence of an exciton and a possible phonon replica confirms the high crystal quality of the material [217].

Another absorber (labelled "repeat") has been prepared under similar condition as sample "ED-stoich-1000mbar". A near-stoichiometric electrodeposited binary selenide precursor was annealed at $1000\,\mathrm{mbar}$ background gas pressure[1]. The Cu/In atomic ratio of the absorber was determined by EDX to be 1.03 for sample "ED-stoich-1000mbar" and 0.99 for sample "repeat". The PL spectrum of this new absorber is different (figure 25.4, sample "repeat"). The main peak at $1.001\,\mathrm{eV}$ is close to a DA1 transition. The shoulder at lower energies can either be assigned to a phonon replica or a DA2 transition. There are different possible explanations for the different PL spectra of the similar prepared absorbers. It is possible that the actual composition difference is larger than it is assumed from the EDX measurements. This has been discussed before in the context of sample "ED-stoich-10mbar". Taking into account the accuracy of the EDX (atomic Cu/In ratio ± 0.05) and

[1] After the annealing sample "repeat" was cooled down to room temperature within $1\,\mathrm{h}$, while the cooling process for sample "ED-stoich-1000mbar" took about $3\,\mathrm{h}$. In both cases the cooling was slow and it is not expected that the difference influences the absorber properties.

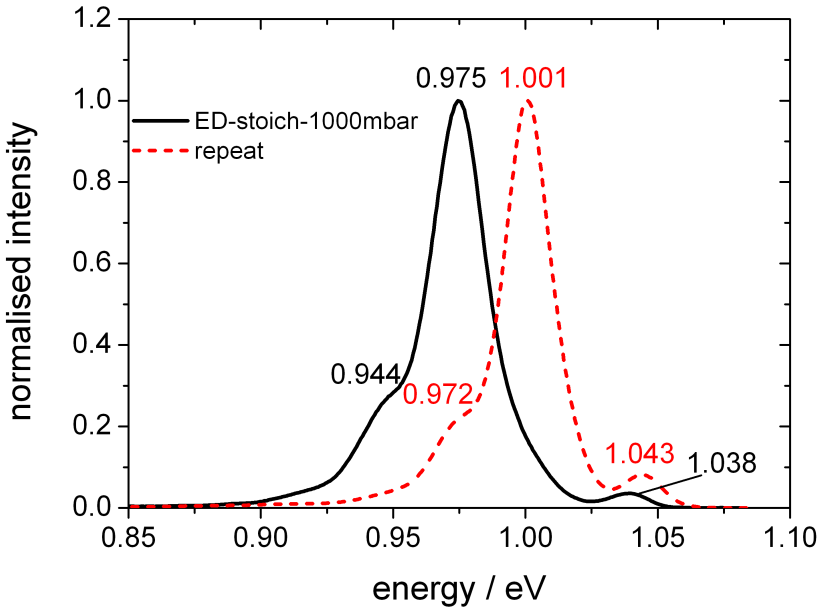

Figure 25.4.: Photoluminescence spectra of two $CuInSe_2$ absorbers annealed at $1000\,\mathrm{mbar}$ background gas pressure. Both samples "ED-stoich-1000mbar" and "repeat" have been prepared in a similar way from precursors with a Cu/In ratio close to 1. The energy of the transitions is noted.

the fact that the EDX measurements have been performed on different days, the composition of sample "ED-stoich-1000mbar" might actually be slightly Cu-rich. It has been reported in literature that Cu-rich growth conditions favour the DA2 transition [199]. The porous morphology of the electrodeposited copper selenide provides a second explanation. If its porosity varies between the precursors, the sintering process during the annealing can change. This can effect the interdiffusion between the copper selenide and indium selenide layer (see discussion at the end of chapter 19.2.1). Although the overall composition is the same, the Cu concentration being effectively involved in the growth of $CuInSe_2$ can then change between different samples. Both interpretations explain the different DA-transitions by an effective difference in Cu content during the growth.

In conclusion it has been shown that in case of absorbers prepared from electrodeposited binary selenide precursors the photoluminescence spectrum is not only dependent on the precursor composition but also on the annealing conditions. The Cu-poor grown absorber is strongly compensated which is in line with observations in literature on epitaxial grown samples [199]. The Cu-rich grown absorber is dominated by the DA2 transition which has also been reported for epitaxial samples [199]. However the energetic distribution of the defects seems to be broader for absorbers prepared from electrodeposited binary selenide stacks and low energy transitions (e.g. DA3) are more pronounced. The interpretation of near-stoichiometric samples is difficult, because differences between the samples or a deviation from results reported in literature might be an issue of an insufficient composition control. EDX measurements in chapter 16 showed a sufficient composition control to distinguish between the Cu-poor, near-stoichiometric, and Cu-rich growth conditions studied in this thesis (table 16.1). A more accurate composition control (e.g. the precise repetition of a sample) is unfortunately not possible in the current process. It must be studied if the lack of reproducibility is caused by the precursor formation or during the annealing process. A higher background gas pressure during annealing significantly improved the quality of the semiconductor.

26. (Temperature dependent) Current-Voltage characterisation

26.1. Background

26.1.1. Diode Equation

The performance of a solar cell is given by its JV characteristic, which is the current density response J under standard illumination versus the applied voltage V. The characteristic performance values open circuit voltage V_{OC}, short circuit current density J_{SC}, fill factor FF, and efficiency η can be obtained from the measured curve [219]. An ideal solar cell can be described by the diode equation with an additional photocurrent density J_{ill}.

$$J = J_0 \left(\exp\left(\frac{eV}{A \cdot k_B T} \right) - 1 \right) - J_{ill} \tag{26.1}$$

The saturation current density J_0 is a measure for the recombination and generation current densities in a solar cell in the dark at $V = 0$. The diode factor A depends on the mechanism of recombination (e.g. $A = 1$ for radiative recombination, $A = 1 - 2$ for defect related recombination [220, 205]). For a real solar cell equation 26.1 is extended by the series resistance R_S and the parallel resistance R_P[219]:

$$J = J_0 \left(\exp\left(\frac{(V - R_S J) \cdot e}{A \cdot k_B T} \right) - 1 \right) + \frac{V - R_S J}{R_p} - J_{ill} \tag{26.2}$$

An evaluation of the parameters V_{OC}, J_{SC}, FF, J_0, A, R_S, and R_p helps to identify the the main efficiency loss mechanisms in the solar cell[1]. The parameters are not independent, e.g. V_{OC} and J_0 are both an indicator of recombination and connected by

$$V_{OC} \approx \frac{A k_B T}{e} \ln\left(\frac{J_{ill}}{J_0} \right) \tag{26.3}$$

which is derived from the diode equation 26.1.

26.1.2. Temperature-dependent JV measurements

Non-radiative recombination is an important efficiency loss mechanism, because it reduces V_{OC}. In an ideal solar cell radiative recombination takes place in the quasi neutral region. Additional defect related recombination paths can occur in a real solar cell. They can be located in the quasi-neutral region, in the space charge region or at the buffer interface. Interface recombination can often be identified by temperature dependent JV characterisation [222, 211]. The saturation current density J_0 in equation 26.2 is temperature dependent. Most of the temperature dependence can be separated into an Arrhenius factor with the activation energy E_a, while the remaining J_{00} has only a weak temperature dependence

$$J_0 = J_{00} \cdot \exp\left(-\frac{E_a}{A \cdot k_B T} \right) \tag{26.4}$$

[1] 26.2 is an implicit equation. The software "ivgen" which is part of the "ivfit" package [221] allows an easy computation.

Combining equations 26.1 and 26.4 leads to [222, 211, 205]

$$V_{OC} \approx \frac{E_a}{e} - \frac{Ak_BT}{e} \ln\left(\frac{J_{00}}{J_{ill}}\right) \tag{26.5}$$

Assuming A, J_{00}, and J_{ill} to be constant with temperature the activation energy E_a can be obtained by a linear extrapolation of a V_{OC} versus T plot for $T \to 0$. The activation energy E_a depends on the recombination path. In case of bulk recombination E_a equals the band gap E_G. If the activation energy E_a is below the band gap energy interface recombination is present[211, 220]. However

26.1.3. Anomalies in the JV characteristic

JV characteristics can show anomalies which are not explained by the diode equation 26.2. An excellent list of anomalies and there causes is given in the book of Scheer and Schock [205].

26.1.3.1. Roll-over

"Roll-over" denotes if the forward current does not follow the exponential behaviour expected from the diode equation 26.2 but saturates above a certain forward voltage bias.

A "roll-over" can be caused by a back contact barrier [223, 205]. In this case it is necessary to extend the classical diode circuit of real solar cell by a second reverse diode. This second diode must be in series with the main diode to cut off the forward current. It has its own series resistance R_{S2}, parallel resistance R_{P2} and a reverse illumination current density J_{ill2}. The series resistance R_{S2} can be absorbed in the total series resistance R_S of the complete diode. The resulting circuit is given in figure 26.1a. The implicit equation of the JV characteristic is complicated and will only be discussed qualitatively in the following.

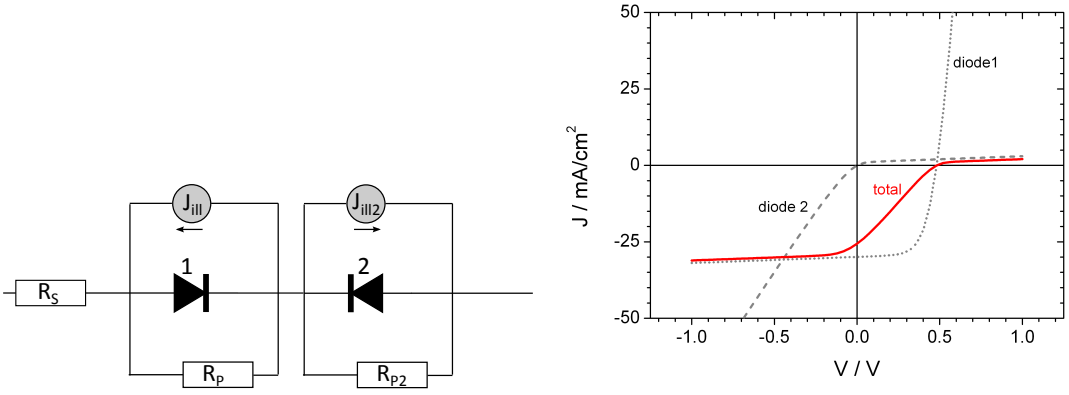

(a) Electrical circuit

(b) JV characteristic

Figure 26.1.: Electrical circuit and corresponding JV characteristic of a solar cell with a reverse np-junction at the back contact. The calculation in 26.1b has been done with the electric circuit simulation software "Micro-Cap 9.0". The circuit parameters are $R_S = 1\,\Omega\mathrm{cm}^2$, $R_P = R_{P2} = 500\,\Omega\mathrm{cm}^2$, $J_0(\text{diode1}) = 1\,\mu\mathrm{A/cm}^2$, $J_0(\text{diode2}) = 1\,\mathrm{mA/cm}^2$, $J_{ill} - J_{ill2} = 30\,\mathrm{mA/cm}^2$.

Both photocurrent densities J_{ill} and J_{ill2} are opposite to each other. It is expected that the absolute value of J_{ill} will be much higher, because most of the light is absorbed at the front of the absorber layer. A correct comparison of the photocurrents requires the knowledge of the space charge width for both junctions to decide how charge carriers created in the middle of the absorber will distribute between the front and backcontact junction. Assuming voltage independent photocurrents

the JV characteristic will shift $(-J_{ill} + J_{ill2})$ under illumination. Under reverse voltage bias diode 2 is in forward direction and will have a negligible effect on the diode characteristic of the main diode 1 (figure 26.1b). If the total current becomes positive, diode 2 will be in reverse direction. That means above the saturation current density of diode 2 (J_{02}) the current will flow through the shunt resistance R_{P2} and the JV characteristic above V_{OC} will be linear with the slope determined by R_{P2} (and R_S, which is always present but probably lower than R_{P2}). In the intermediate voltage range where the current starts to rise exponentially both diodes will contribute to the JV characteristic. Thus a continuous transition from a diode 1 dominated circuit to a R_{P2} dominated circuit will result.

Another explanation of the "roll-over"-effect can be a forward current barrier at the absorber buffer interface [205]. In the band diagram in figure 26.2c electrons flowing in forward direction from the window layer into the absorber have to overcome a spike in the conduction band. As long as the spike is small it has negligible effect on the solar cell efficiency. If the spike is too large it can cut off the forward current.

26.1.3.2. Kink

If the JV characteristic shows a "kink" the current saturates at intermediate forward voltage bias. At higher forward voltage bias the current rises again.

A kink can be caused by a photocurrent barrier [205]. If the voltage bias is close to V_{OC} the barrier in the conduction band can cut off the photocurrent (figure 26.2b). This causes the "saturation" of J at intermediate bias V. Under forward voltage bias the forward current can pass and J rises again (figure 26.2c).

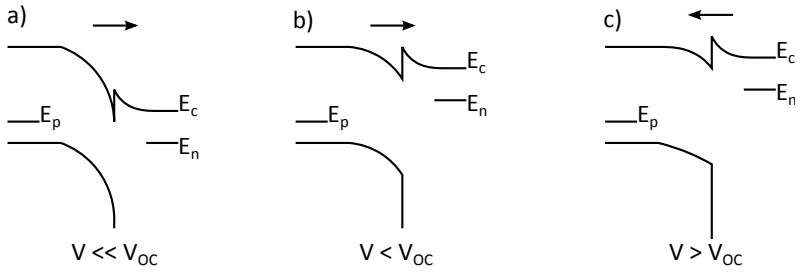

Figure 26.2.: Band structure of an illuminated heterojunction with a conduction band offset at different applied voltage bias V. a) under strong reverse voltage bias, b) V close to V_{OC}, but still under reverse current, c) under forward voltage bias. E_p and E_n denote the Quasi-Fermi-levels in the bulk.

26.2. Results and Discussion

26.2.1. JV characteristic at room temperature

The $\mathrm{CuInSe_2}$ absorbers in table 16.1 have been completed into solar cells and their JV characteristics are shown in figures 26.3 and 26.4. The characteristic parameters are listed in table 26.1. R_S, R_P, A and J_0 were obtained by fitting the JV characteristics with the diode model of a real solar cell (equation 26.2). The fitting was done by the software "ivfit" [221]. A best efficiency of 5.5% has been obtained from the stoichiometric absorber which has been annealed at low background gas pressure.

In comparison with a $\mathrm{CuInSe_2}$ solar cell grown in a PVD 3-stage process open-circuit voltage V_{OC}, short-circuit current density J_{SC}, and fill factor are about $20 - 30\%$ lower (table 26.1). The low V_{OC} is an indication for high recombination. This is also seen in the significantly higher saturation current density J_0 for the binary selenide solar cells which is linked to the V_{OC} by relation 26.3. Temperature dependent JV measurements (section 26.2.2) will show strong interface recombination

		electrodeposited binary selenide					PVD Cu-poor	coelec.
	sample	a	b	c	d	e		[21]
	atomic Cu/In	0.98	1.47	0.92	0.94	1.03		
	pressure / mbar	10	10	10	500	1000		
V_{OC}	V	0.34	0.26	0.33	0.31	0.18	0.50	0.40
J_{SC}	$\mathrm{mA/cm^2}$	30.9	32.2	28.3	29.4	16.3	38.1	31.2
FF		0.52	0.49	0.35	0.46	0.26	0.68	0.52
$eff.$	%	5.5	4.1	3.3	4.2	0.8	12.9	6.7
fit - illuminated curve								
R_p	$\Omega\mathrm{cm^2}$	281	76		162		335	290
R_S	$\Omega\mathrm{cm^2}$	0.9	0.7		0.9	10	0.5	2.0
A		2.3	1.8		2.7		1.5	2.0
J_0	$\mu\mathrm{A/cm^2}$	86	98		337		0.1	12
fit - dark curve								
R_p	$\Omega\mathrm{cm^2}$	930	287		477		12700	2000
R_S	$\Omega\mathrm{cm^2}$	1.1	0.9		1.1	14	0.6	2.9
A		2.0	1.5		2.3		1.6	2.3
J_0	$\mu\mathrm{A/cm^2}$	21	16		84		0.2	6.6
J_{SC} determined from quantum efficiency spectrum								
$\hat{J}_{SC}$	$\mathrm{mA/cm^2}$	34.1	38.3	28.1	31.0	21.5	41.2	

sample labels according to table 16.1

a: ED-stoich-10mbar
b: ED-Cu-rich-10mbar
c: ED-Cu-poor-10mbar
d: ED-stoich-500mbar
e: ED-stoich-1000mbar

Table 26.1.: JV characteristic and calculated parameters of thin film solar cells prepared from the absorbers in table 16.1. The PVD sample has been prepared in a 3-stage-process (section 15.1.4). The parameters of the coelectrodeposited solar cell are taken from [21]. V_{OC}, J_{SC}, FF and efficiency were directly determined from the JV characteristic. R_S, R_P, A, and J_0 have been obtained from a fit of the dark and illuminated curve with equation 26.2 by the software *ivfit* [221]. In case of "ED-stoich-1000mbar" the resistance has been determined from the slope of the JV-curve. The last row shows the $\hat{J}_{SC}$ (active area) determined by integrating the quantum efficiency spectrum.

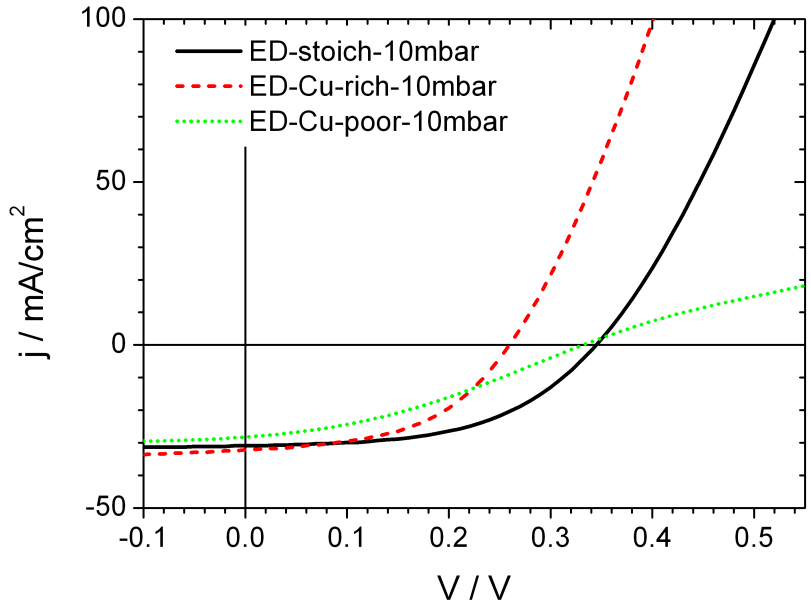

Figure 26.3.: JV-characteristic of solar cells prepared from electrodeposited binary selenide precursors with different Cu/In ratios. The composition of the absorbers is given in table 16.1.

for the stoichiometric solar cell prepared from electrodeposited binary selenide precursors. The loss of V_{OC} is the main reason why solar cell "ED-stoich-10mbar" has a lower performance than the coelectrodeposited sample reported by Dale et al. [21]. The coelectrodeposited sample has been prepared under Cu-poor (Cu/In $= 0.79$) growth conditions, which usually results in a Cu-poor surface composition. Therefore the coelectrodeposited sample benefits from a reduced interface recombination which allows a higher V_{OC} (section 23.2).

The lower J_{Sc} of the binary selenide solar cells is caused by an incomplete charge carrier collection as it will be shown in quantum efficiency measurements (figure 27.2). A low fill factor is often caused by a high R_S and a low R_P. For the binary selenide samples the resistances are not the dominating limitation of the fill factor. If the IV-curve of these cells is calculated by the diode equation 26.2 taking the better resistances of the PVD sample, the fill factor will only improve from 0.52 to 0.54. The main limitation of the fill factor is the high saturation current J_0, i.e. again the high recombination in the devices. The diode factor A of the stoichiometric cells (ED-stoich-10mbar and ED-stoich-500mbar) is above 2. This can be an indication for tunnelling enhanced recombination [211]. A diode factor above 2 can also be caused by spatial fluctuation in the activation energy of the dominant interface process (probably interface recombination in case of "ED-stoich-10mbar") [205].

The Cu-rich grown solar cell (ED-Cu-rich-10mbar) shows a lower efficiency of 4.1% compared to the stoichiometric one (table 26.1). While J_{SC} is similar, V_{OC} drops. It will be shown in figure 26.6 that the Cu-rich absorber has an enhanced interface recombination. Another reduction of V_{OC} can be caused by a reduced parallel resistance that indicates the appearance of shunts (e.g. copper selenide phases along the grain boundaries [212]). The parallel resistance of the Cu-rich absorber is less than the one of the stoichiometric absorber (table 26.1). However a calculation from the diode equation 26.2 shows that the change of R_P from $281\,\Omega\mathrm{cm}^2$ to $76\,\Omega\mathrm{cm}^2$ causes a reduction in V_{OC} of less than $0.01\,\mathrm{V}$ and therefore being negligible.

The Cu-poor grown solar cell has similar J_{SC} and V_{OC} as the stoichiometric one. Its shape however cannot be described by the exponential shape of the diode equation. In forward bias direction a "roll-over" of current is observed, which is often a sign for a back contact barrier (section 26.1.3.1). The

composition depth profile of the absorber (figure 16.1b) suggests the formation of a copper vacancy compound at the backcontact of the absorber. The copper vacancy compounds $CuIn_3Se_5$ and $CuIn_5Se_8$ are usually n-type doped[2] [225, 224] and thus form a reverse n-p junction at the back of the absorber. Thus the incomplete reaction of the binary selenide precursor stack limits the solar cell performance of the Cu-poor device due to the formation of a reverse np-junction at the backside of the absorber which acts as a barrier for the holes. The proposed circuit in 26.1a can explain, why the Cu-poor cell is not more efficient than the stoichiometric one. The main loss of efficiency is attributed to the low fill factor. It is reduced by the parallel resistance R_{P2} that is connected in series to the first diode, when the back contact diode changes from forward to reverse direction. At this point the R_{P2} adds up to the series resistance R_S and reduces the fill factor.

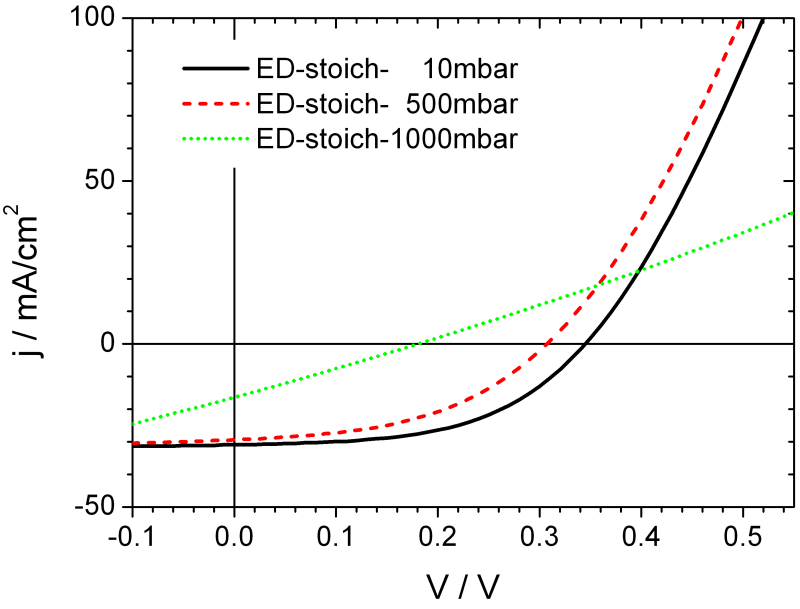

Figure 26.4.: JV-characteristic of solar cells prepared from stoichiometric binary selenide precursors. The samples have been annealed at $10\,\mathrm{mbar}$, $500\,\mathrm{mbar}$ and $1000\,\mathrm{mbar}$ background gas pressure. The composition of the absorbers is given in table 16.1.

Increasing the background gas pressure during the annealing from $10\,\mathrm{mbar}$ to $500\,\mathrm{mbar}$ leads to a small loss of efficiency (figure 26.4). It has been shown that an annealing pressure of $1000\,\mathrm{mbar}$ leads to larger grains, a longer lattice coherence length and a better electronic structure of the absorber. Therefore one would expect a higher solar cell efficiency, but the opposite is observed. The JV characteristic has degenerated into a line meaning a resistive behaviour of the cell. The resistance is about $10 - 14\,\Omega\mathrm{cm}^2$. The reason for this becomes clear in the XRD diffractogram (figure 17.2b). There is no Mo reflection visible any more but only a $MoSe_2$ phase. Obviously the higher Se pressure that was confined by the high background gas pressure has not only led to a better crystallisation of the absorber film but also to a nearly complete selenisation of the back contact.

Table 26.1 lists the short circuit current density $\hat{J}_{SC}$ which has been calculated by integrating the external quantum efficiency spectra of the solar cells (figure 27.2). In the used QE set-up (section 24.4) there is no shading of the solar cell grids, because only a small spot between the grids is probed. Therefore it is expected that $\hat{J}_{SC}$ is about 5% higher than J_{SC} which has been determined from the JV characteristic and includes shading from the grids. This is true for sample "ED-stoich-500mbar" and the Cu-poor PVD sample (The percentage of the grids is a little bit higher for the PVD sample,

[2] It has been reported that $CuIn_3Se_5$ single crystals have p-type conductivity. Thin films synthesised from these targets by laser ablation show n-type conductivity [224].

because the total area was $0.39\,\mathrm{cm}^2$ instead of $0.50\,\mathrm{cm}^2$). For the other samples $\hat{J}_{SC}$ is $10-32\%$ higher than J_{SC}, except for sample "ED-Cu-poor-10mbar" where J_{SC} is higher than $\hat{J}_{SC}$. It means that the solar cells are not laterally uniform and $\hat{J}_{SC}$ measured in the middle of the solar cell deviates from J_{SC} being an average of the complete solar cell.

In conclusion, a best efficiency of 5.5% has been obtained for solar cells prepared from electrodeposited binary selenide absorbers. The solar cells suffer from a low V_{OC} due to strong non-radiative recombination. The photoresponse fluctuates across the cell which can be connected to the variation in crystallisation that has been observed after the annealing (section 16). The device prepared from a Cu-poor grown absorber is probably limited by a reverse np-junction at the backside of the absorber due to the formation of a n-type ordered vacancy compound at the backside. The ordered vacancy compound is a result of an incomplete reaction of the precursor stack (section 16). The solar cell prepared from the absorber annealed at $1000\,\mathrm{mbar}$ background gas pressure has a low performance, because the Mo backcontact has been selenised in the annealing process.

26.2.2. Temperature dependent JV characteristic

Temperature dependent JV characteristics have been recorded in order to study the possible recombination paths (figures 26.5 - 26.8). The Cu-rich grown solar cell (ED-Cu-rich-10mbar, figure 26.5) shows the expected increase of V_{OC} with lower temperatures. A plot of V_{OC} versus T confirms the linearity of equation 26.5 (figure 26.6). The intercept at $T \to 0$ is $E_a = 0.63\,\mathrm{eV}$. This is below the bandgap of $1.02\,\mathrm{eV}$ which has been determined by quantitative photoluminescence measurements (table 27.1). Therefore it can be concluded that interface recombination is important. High interface recombination is typically observed for Cu-rich grown $\mathrm{CuInSe_2}$ solar cells prepared by coevaporation (section 23.2)[226, 207]. It is also evident from figure 26.5 that the photocurrent decreases for lower temperatures. This can be a problem of an insufficient charge carrier collection (see section 27.1). Under the assumption of complete ionisation of the dopant within the space charge region its width is independent of temperature, because it is only determined by the dopant density and the voltage drop over the space charge region. Then the reduced carrier collection is due to a decrease in the electron diffusion length. The electron diffusion coefficient D_n is given by the Einstein relation $D_n = \frac{k_B T}{e}\mu_n$ and the electron mobility μ_n. The temperature dependence of μ_n is specific for each sample. Even for samples where μ_n increases with lower temperature the pre-factor $\frac{k_B T}{e}$ usually dominates and the diffusion coefficient at $200\,\mathrm{K}$ is lower than at room temperature [227]. Scattering at ionised impurities and grain boundaries decreases the mobility with lower temperature while scattering at optical phonons increases it [228]. Therefore in addition to the pre-factor $\frac{k_B T}{e}$ a high density of ionised impurities or grain boundaries can further decrease D_n with lower temperature. A reduced diffusion length at low temperatures can cause insufficient carrier collection explaining the decrease in short circuit current with lower temperature in figure 26.5.

The stoichiometric solar cell (ED-stoich-10mbar, figure 26.7) shows a kink in the JV-characteristic for temperatures below $200\,\mathrm{K}$. Such a kink is also observed in coevaporated Cu-poor $\mathrm{Cu(In_Ga)Se_2}$ solar cells [229, 230]. It might be explained through the presence of a photocurrent barrier (section 26.1.3.2). Extrapolating the V_{OC} for $T \to 0$ leads to an activation energy of $0.80\,\mathrm{eV}$ (figure 26.6) which is lower than the band gap of $0.99\,\mathrm{eV}$ (table 27.1). Thus interface recombination can also be identified for the near-stoichiometric case.

As it has already been observed at room temperature the Cu-poor sample shows a current roll-over due to a backcontact barrier (ED-Cu-poor-10mbar, figure 26.8). If the forward voltage (corresponding to a reverse voltage for the diode at the backcontact) is sufficiently high, a current break-through of the reverse diode will occur and the current will rise again. For the Cu-poor absorber the current break-through is only observed close to room temperature. At lower temperatures the forward current stays limited by the parallel resistance R_{P2} (figure 26.1a). The short circuit current density of the Cu-poor grown solar cell is increasing with temperature. As for the Cu-rich grown solar cell this can be a sign of a low diffusion coefficient leading to an incomplete charge carrier collection. It can also be an effect of a temperature dependent parallel resistance, because also the slope of the JV

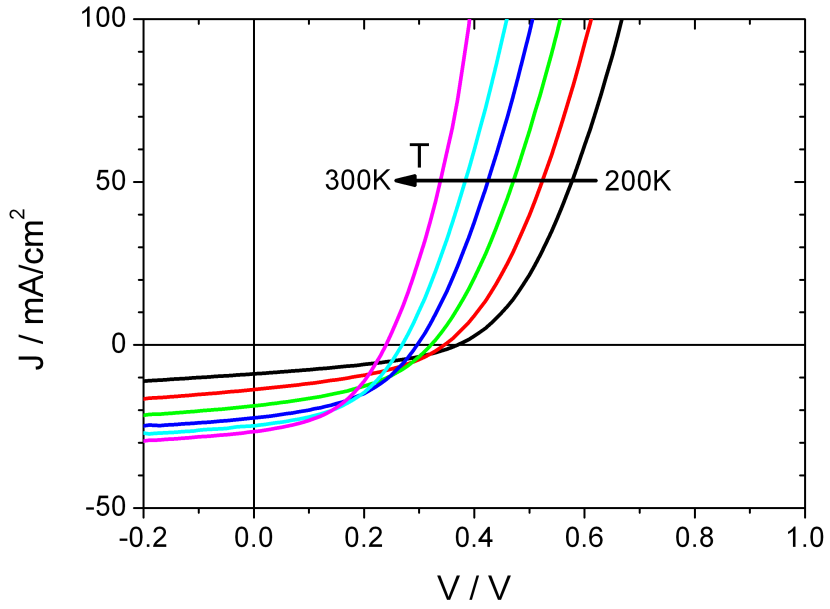

Figure 26.5.: Temperature dependent JV characteristics of the Cu-rich solar cell (ED-Cu-rich-10mbar)

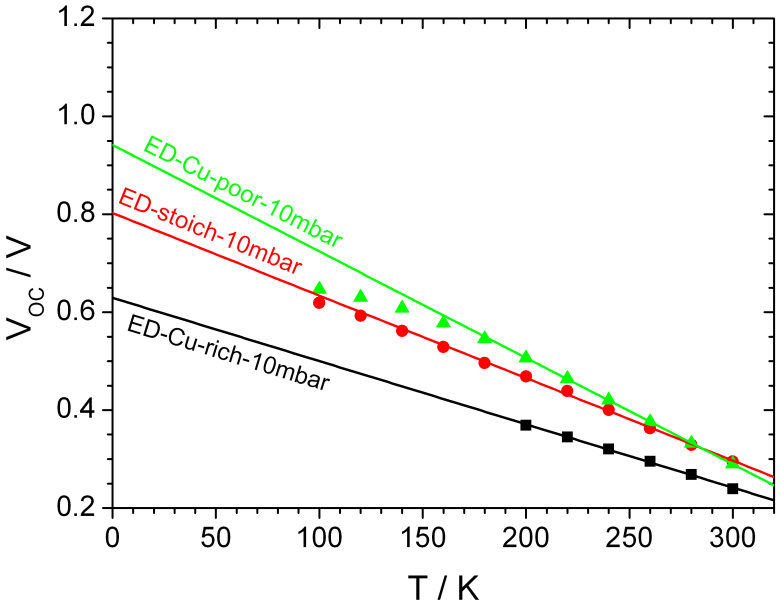

Figure 26.6.: Open circuit voltage V_{OC} as a function of solar cell temperature T with a linear extrapolation to $T \to 0$

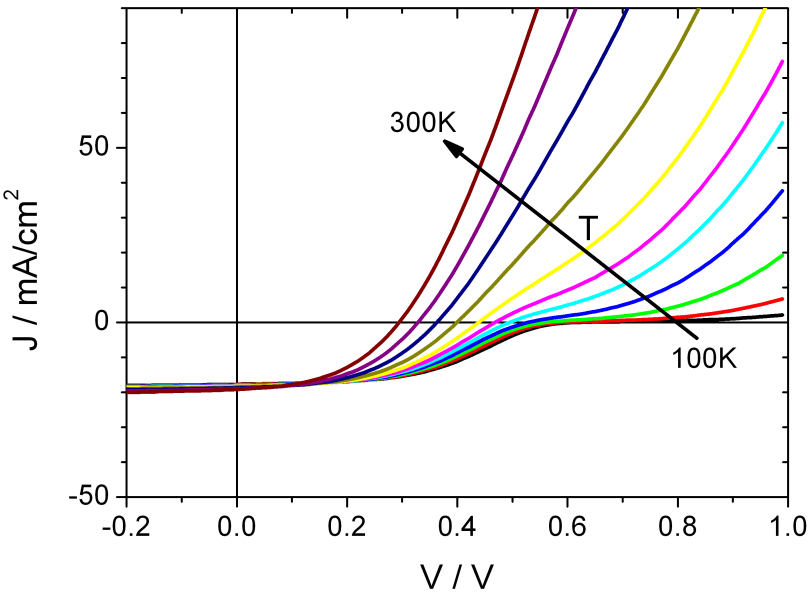

Figure 26.7.: Temperature dependent JV characteristics of the stoichiometric solar cell (ED-stoich-10mbar)

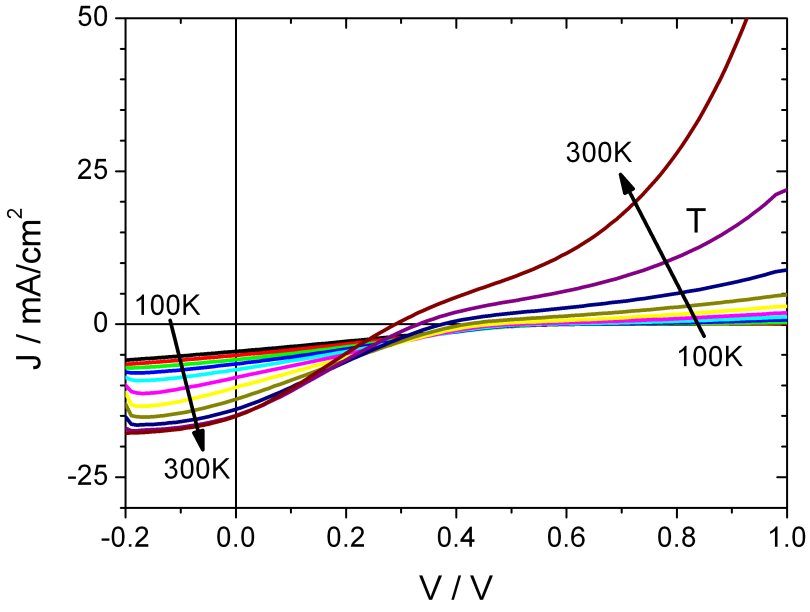

Figure 26.8.: Temperature dependent JV characteristics of the Cu-poor solar cell (ED-Cu-poor-10mbar)

characteristic is changing.

Before extrapolating the V_{OC} for $T \to 0$, it must be considered how the existence of the reverse diode at the back contact effects the V_{OC}. For simplicity it is assumed that the photocurrent of the reverse np-junction is $J_{ill2} = 0$. This is justified, because most charge carriers are generated at the front of the solar cell. At V_{OC} no total current is passing through the solar cell. Due to charge conservation this is not only true for the complete solar cell but also separately for each junction, the one at the back and the one at the front[3]. That means the V_{OC} of the complete solar cell is the sum of the front junction V_{OC} and the back junction V_{OC}. The latter one is zero, because $J_{ill2} = 0$ has been assumed. Then the V_{OC} of the complete solar cell is only determined by the main pn-junction at the front. Therefore it is still possible to perform the temperature dependent V_{OC} evaluation by equation 26.5. The V_{OC} is still linear with temperatures above $180\,\mathrm{K}$ (figure 26.6). At lower temperatures the slope of the forward current in figure 26.8 is so low that already small effects on the current value (e.g. a small J_{ill2}) can shift V_{OC} considerably. It is also possible that the assumption of a temperature independent diode factor A is no longer valid for the low temperature data points. Extrapolation results in an activation energy of $E_a = 0.94\,\mathrm{eV}$. This value is close to the band gap value of $0.97\,\mathrm{eV}$ (table 27.1). E_a might be slightly underestimated due to the non-linearity of the plot in figure 26.6. Since the activation energy is below E_G, it can be concluded that interface recombination is still the dominant mechanism.

In conclusion it has been presented that interface recombination is the dominant recombination mechanism in solar cells prepared from electrodeposited binary selenide precursors. The main limitation in performance between the best solar cell from an electrodeposited binary selenide precursor and a solar cell prepared by coelectrodeposition is the V_{OC}, i.e. recombination losses (table 26.1) . A reduction in the rate of interface recombination is necessary to reach higher efficiencies. Although the measure of recombination rate is the saturation current density j_0 and not the activation energy E_a, a high activation energy is in general expected to be beneficial to reducing interface recombination losses (equation 26.4). The activation energy of the interface recombination decreases from Cu-poor to Cu-rich growth conditions as it has previously been reported for coevaporated samples [226, 207]. Therefore also in case of solar cells prepared from electrodeposited binary selenide precursors Cu-poor growth conditions seem to be a promising route toward higher efficiencies. This presumes, of course, the absence of a reverse junction at the back caused by an incomplete reaction of the precursor. So far the advantage of low interface recombination is not fully active, since the V_{OC} of the Cu-poor prepared solar cell is not higher than for one from a stoichiometric absorber.

[3] This can be seen from circuit 26.1a. If no current is passing through the complete circuit, the current through the connection between both diodes must be zero. This is only possible if for each junction the current is zero, because no current is created in the back contact junction.

27. (Voltage-biased) Quantum Efficiency measurements

27.1. Background

Quantum efficiency (QE) measurements record the photoresponse of the solar cell at varying excitation wavelengths. It can be understood as the number of electrons generated per incident photon. QE measurements allow to distinguish different loss mechanism which reduce the photocurrent. This is mainly based on two principles. First, each solar cell layer (e.g. window or buffer layer) has a typical absorption spectrum that causes a loss of excitation intensity. Second, the wavelength dependency of the absorption coefficient provides information on the spatial location of loss mechanisms within the absorber.

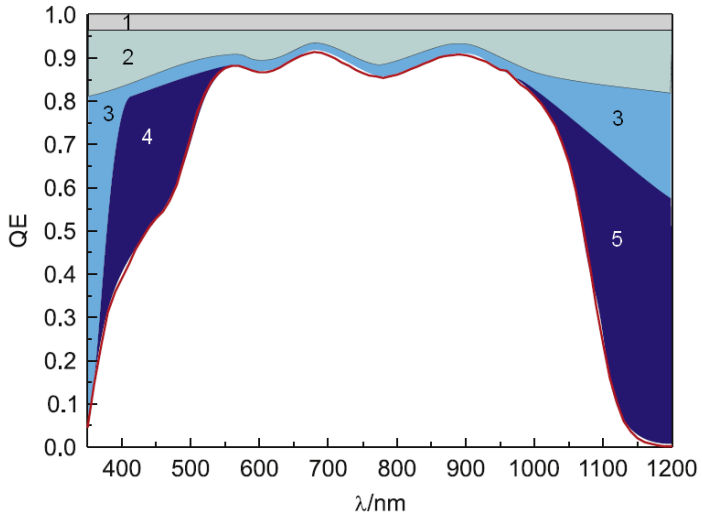

Figure 27.1.: Typical Quantum efficiency losses in thin film Cu(In,Ga)Se_2 solar cells. The loss mechanisms a)-e) are discussed in the text. The graph has been adopted from [6].

Figure 27.1 shows a typical QE spectrum of a Cu(In,Ga)Se_2 solar cell and assigns its main losses [6, 231]:

1. Shading of the front contact grid. (This is not observed in our QE set-up where the illumination spot is between the grid fingers). Transmission factor: T_G
2. Surface reflection R
3. Absorption of the ZnO window layer A_{TCO}
4. Absorption of the CdS buffer layer A_{CdS}
5. Insufficient absorption and charge carrier collection within the absorber. The band gap of the absorber can be determined on this side.

One distinguishes the external and internal quantum efficiency (EQE and IQE). EQE is of practical relevance, because it relates the current output of the complete device to the illumination intensity.

IQE is focused on the absorber layer. It relates the current to the intensity that has been absorbed in the absorber layer. IQE and EQE are linked through the optical losses 1. - 4. [231]

$$EQE = T_G\,(1-R)\,(1-A_{TCO})\,(1-A_{CdS})\cdot IQE \tag{27.1}$$

Equation 27.1 is valid in the absence of photoconductive effects (e.g. if a light bias is applied). Otherwise a correction factor $\Gamma\,(\lambda, V, I)$ must be added.

The IQE can be approximated by the Gärtner equation [232, 231, 205, 21]

$$IQE\,(\lambda, V) = 1 - \frac{\exp\left(-\alpha(\lambda)W(V)\right)}{\alpha(\lambda)L+1} \tag{27.2}$$

$\alpha(\lambda)$ is the wavelength dependent absorption coefficient, $W(V)$ the voltage dependent width of the space charge region (SCR) and L is the diffusion length of the minority carriers. In the derivation of equation 27.2 minority charge carriers contribute to the photocurrent if they are either generated within the SCR or if they diffuse into the SCR, because they are generated within $W(V)+L$ distance from the junction. An incomplete carrier collection can be studied by QE measurements under a voltage bias. The voltage bias makes it possible to control the carrier collection by changing the SCR width $W(V)$. In case of a p-type semiconductor [233, 234]:

$$W(V) = \sqrt{\frac{2\varepsilon\varepsilon_0}{eN_A}\,(V_B - V)} \tag{27.3}$$

V_B is the built-in potential of the junction and V the applied voltage bias. N_A is the acceptor concentration and ε the specific dielectric constant of the absorber material. If a high reverse voltage bias (i.e. $V \ll 0$) is applied, the SCR width is increased and the carrier collection can be improved.

Beside the change in SCR width there are additional factors which can cause a change of IQE with an applied voltage bias [205]. These effects are not covered by equation 27.2.

- The voltage bias changes the electric field at the interface and thus effects interface recombination.
- A potential barrier in the conduction band at the junction interface can limit the photocurrent. If a small reverse voltage bias is applied the photocurrent barrier can limit the current density (figure 26.2b). A high reverse bias will increase the band bending and the photocurrent can pass the barrier (figure 26.2c).

In all cases the IQE increases under reverse voltage bias and decreases under forward bias.

27.2. Results and Discussion

EQE spectra measured under short circuit conditions are shown in figure 27.2. The reference spectrum of a PVD sample allows to identify the loss mechanisms presented in figure 27.1. Below $370\,\mathrm{nm}$ the absorption of the ZnO window layer cuts off the spectrum to shorter wavelength. Between $400\,\mathrm{nm}$ and $500\,\mathrm{nm}$ absorption of the CdS buffer layer causes a typical shoulder. The oscillations between $500\,\mathrm{nm}$ and $1200\,\mathrm{nm}$ result from interferences in the window layer, which modulate the reflectance of the solar cell. Above $1000\,\mathrm{nm}$ absorption of the ZnO window layer might reduce the photocurrent. At wavelengths above ca. $1300\,\mathrm{nm}$ the spectrum is cut off by the bandgap of the absorber. The slope on the high-wavelength side of the spectrum is determined by absorption in the $\mathrm{CuInSe_2}$ and carrier collection. The QE spectrum of the Cu-rich binary selenide solar cell (ED-Cu-rich-10mbar in figure 27.2) is close to the Cu-poor PVD reference. The main difference is the higher band gap E_G in case of the electrodeposited sample (see table 27.1). The band gap of the electrodeposited samples seems to be independent of their growth composition, if it is determined from a simple extrapolation

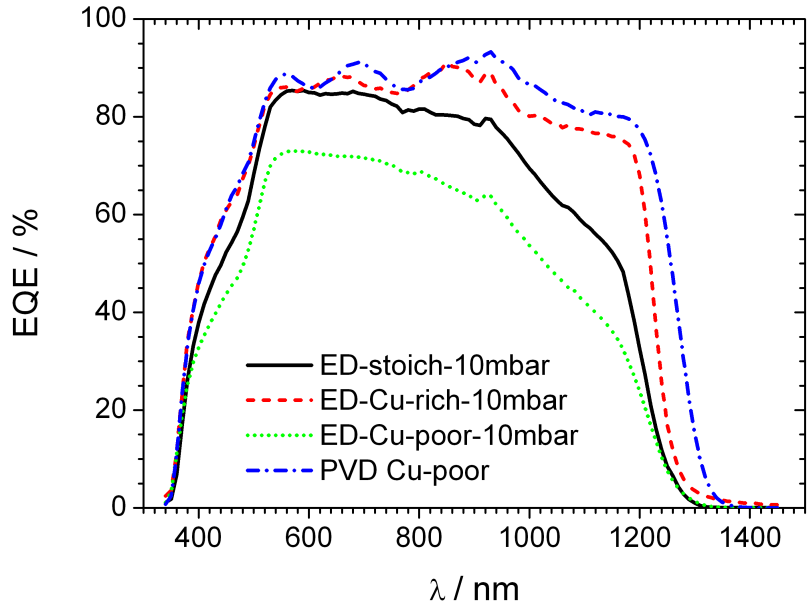

Figure 27.2.: EQE spectra of solar cells prepared from electrodeposited binary selenide precursors under Cu-poor (ED-Cu-poor-10mbar), stoichiometric (ED-stoich-10mbar) and Cu-rich (ED-Cu-rich-10mbar) growth conditions. For comparison the spectrum of a Cu-poor PVD solar cell is added.

of the EQE spectrum (figure 27.2 and table 27.1)[1]. This result is an artifact of the imprecise band gap determination and does not longer hold, if a more accurate method is used to determine E_G (table 27.1). The E_G values from fitting quantitative photoluminescence spectra show the expected increase with higher Cu/In ratio. They correspond to the band gap values that have been reported for polycrystalline $\mathrm{CuInSe_2}$ absorbers prepared by PVD (section 23.2) [145].

The major EQE loss for the stoichiometric sample (ED-stoich-10mbar in figure 27.2) is at wavelengths above $900\,\mathrm{nm}$, that means at long wavelengths penetrating deeper into the absorber. It is therefore likely that this loss is caused by a limited minority carrier collection length which results from a small SCR width $W(V)$ and/or a small diffusion length L (see equation 27.2). The spectrum of the Cu-poor solar cell (ED-Cu-poor-10mbar in figure 27.2) shows the same loss feature above $900\,\mathrm{nm}$. In this case the photocurrent losses are larger than for the stoichiometric sample. The losses between $500\,\mathrm{nm}$ and $800\,\mathrm{nm}$ are not due to incomplete carrier collection in the Cu-poor prepared solar cell but caused by wavelength independent loss mechanisms as it will be shown in the following.

More information on the incomplete carrier collection can be obtained from voltage biased EQE measurements. If a reverse voltage bias is applied, the SCR becomes wider and more electrons can be collected. Figure 27.3 shows the EQE spectrum of the Cu-poor grown sample under reverse bias. The largest effect of the reverse bias is seen in the wavelength range of CdS absorption. A higher EQE in this range is mainly an artifact of the measuring technique. For some samples it can even exceed 1 at high reverse bias. The spectra have been measured under chopped illumination with a lock-in amplifier. In reverse bias the current of the solar cell is given by its saturation current, the photocurrent, and the current through the parallel resistance. CdS is photoconductive [237];

[1]The bandgap can also be determined from the extrapolation of $(\ln(1-QE))^2$ plotted versus the photon energy E. This evaluation procedure results from the relations $\alpha^2 \propto (E-E_g)$ (for direct semiconductors) [235] and $QE \sim 1-\exp(-\alpha W)$ (approximation from equation 27.2). α is the absorption coefficient, E_g the band gap, QE the quantum efficiency and W the width of the space charge region. For the given spectra it is difficult to determine the energy range that is included in the linear fit. Therefore a direct extrapolation of the QE spectra has been preferred.

	Cu/In	EQE		Quant PL
	atomic	band gap / eV	error / eV	band gap / eV
PVD Cu-poor	0.92	0.94	±0.02	0.96
ED-Cu-poor-10mbar	0.92	0.98	±0.01	0.97
ED-stoich-500mbar	0.94	0.98	±0.01	0.96
ED-stoich-10mbar	0.98	0.98	±0.03	0.99
ED-stoich-1000mbar	1.03	0.99	±0.23	1.02
ED-Cu-rich-10mbar	1.47	0.98	±0.05	1.02
PVD Cu-rich	1.55	1.00	±0.06	1.02

Table 27.1.: Band gaps determined from EQE spectra by linear extrapolation of the high-wavelength side to $EQE = 0$. The samples correspond to the ones from table 16.1 and the atomic Cu/In ratio before KCN etching has been noted. In the last column the band gaps have been determined from a quantitative photoluminescence (PL) spectrum fitted by Planck's generalised law. A description of this method can be found in [236]. The band gaps determined by EQE refer to room temperature, while the sample temperature in the PL experiment is assumed to be about $350\,\mathrm{K}$ due to the focused illumination.

therefore the parallel resistance changes with the chopped illumination and the subtraction of the dark current fails in the wavelength range where CdS absorbs light. But also outside of the CdS absorption range the quantum efficiency rises under reverse bias. The wavelength dependence of the EQE increase gives insight into its mechanism. For this it is easier to normalise the EQE at reverse bias with the EQE at $0\,\mathrm{V}$, as it has been done in figure 27.4.

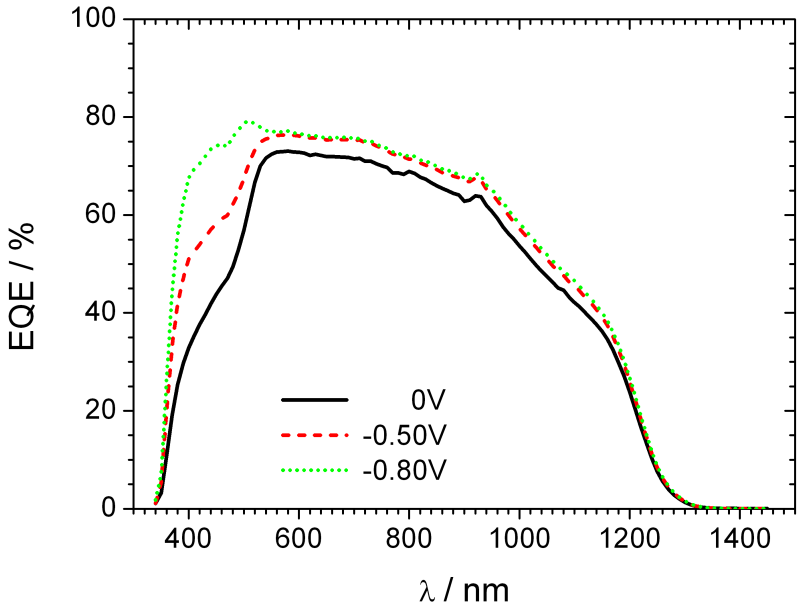

Figure 27.3.: EQE spectra of solar cell "ED-Cu-poor-10mbar" prepared from a Cu-poor precursor. A reverse bias of $-0.50\,\mathrm{V}$ and $-0.80\,\mathrm{V}$ has been applied to the cell.

The Cu-poor grown PVD solar cell has a constant $EQE\,(-0.50\,\mathrm{V})\,/EQE\,(0\,\mathrm{V})$ ratio of 1. That means the combination of diffusion length and SCR width at short circuit conditions is already appropriate to allow a complete carrier collection. Further voltage dependent influences on the EQE (e.g. interface recombination or a photocurrent barrier) are also low. The solar cell from the electrodeposited Cu-rich sample has a EQE ratio below 1, i.e. the EQE is decreasing with reverse

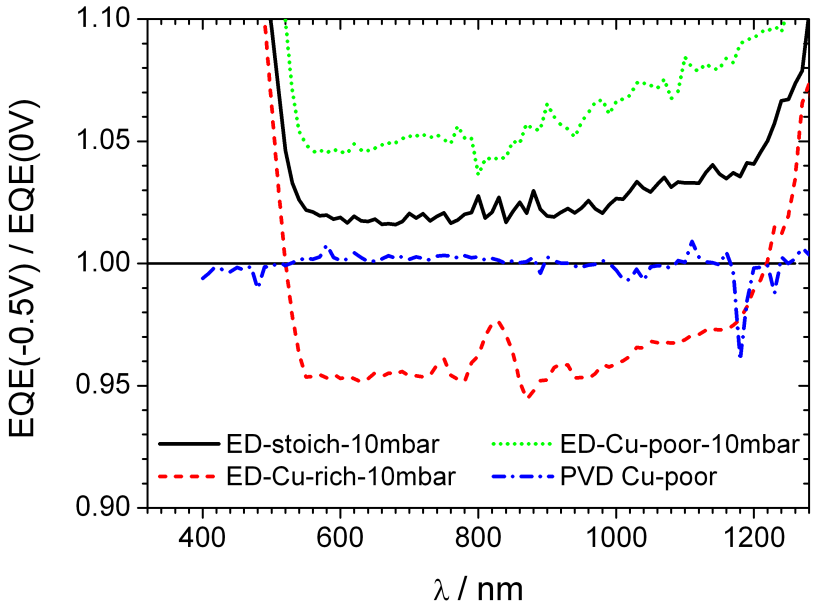

Figure 27.4.: EQE recorded at $-0.50\,\mathrm{V}$ reverse voltage bias normalised with the EQE at $0\,\mathrm{V}$. The samples correspond to the ones given in table 16.1. The sharp rise below $600\,\mathrm{nm}$ is attributed to the photoconductivity of CdS. The curve of ED-Cu-rich-10mbar has been smoothed.

voltage bias. This behaviour is unconventional, because the major voltage dependent processes that act on the EQE (e.g. widening of the SCR, interface recombination or photocurrent barrier) lead to an increase of EQE under reverse bias (section 27.1) [205]. The effect has been reproduced with a new reference measurement of the illumination spectrum. Therefore it cannot simply be explained by an incorrect calibration. Nevertheless it is likely that the reduced EQE under reverse voltage bias is an artifact or error of the measurement (e.g. a measured variable being out of range).

The $EQE\left(-0.50\,\mathrm{V}\right)/EQE\left(0\,\mathrm{V}\right)$ ratio of the other solar cells (ED-stoich-10mbar, ED-Cu-poor-10mbar) is above 1 which corresponds to the conventional EQE behaviour under reverse bias. The ratio increases with longer wavelengths. This is expected for a widening of the SCR which has the strongest effect on charge carriers generated deeper in the bulk. That means the solar cell prepared from Cu-poor and near-stoichiometric binary selenide precursors suffer from incomplete charge carrier collection, either due to a narrow space charge region and/or due to a short diffusion length.

The absorption coefficient of short wavelengths is high (e.g. $\alpha = 6.9 \cdot 10^4\,\mathrm{cm}^{-1}$ at $\lambda = 700\,\mathrm{nm}$ [238]) . Most photons are already absorbed in the top few hundred nanometres of the absorber. Therefore the charge carriers are generated in the SCR without the need of a reverse voltage bias. In this wavelength region the $EQE\left(V\right)/EQE\left(0\,\mathrm{V}\right)$ ratio is expected to be 1 if incomplete carrier collection is the only loss effect. At short wavelengths the observed $EQE\left(V\right)/EQE\left(0\,\mathrm{V}\right)$ ratio is nearly constant but different from 1. Therefore an additional voltage dependent photocurrent loss mechanism exists, which is not wavelength dependent. Voltage dependent interface recombination or a photocurrent barrier in the conduction band are possible examples for such processes (section 27.1) [205]. It has already been shown in chapter 26 that the solar cells fabricated from electrodeposited binary selenide precursors are limited by interface recombination and thus it is a probable explanation for the wavelength independent current losses. In the case of coelectrodeposited solar cells Guillemoles et al. have reported a decrease of spectral response with forward voltage bias that is independent of the wavelength. They explain it by interface recombination [25]. Besides interface recombination it is likely that the reverse diode at the backside will lead to a wavelength dependent loss for the Cu-poor

fabricated solar cell. Figure 26.1 shows that a reverse diode decreases the short circuit voltage and will therefore also result in a lower EQE at $0\,\mathrm{V}$. Under reverse voltage bias the reverse diode at the back will be in forward direction and the spectral response increases.

In summary Cu-rich growth conditions lead to a favourable quantum efficiency for solar cells prepared from electrodeposited binary selenide stacks, because the spectrum is less affected by losses at wavelengths above $900\,\mathrm{nm}$ usually assigned to an incomplete carrier collection. Also the higher band gap of Cu-rich absorbers improves the utilisation of the solar spectrum. It has been demonstrated that the Cu-poor and stoichiometric prepared solar cells suffer from incomplete carrier collection. This can be caused by a high defect density in the absorber which decreases the width of the SCR. The interface recombination which has already been identified in the temperature dependent JV measurements is another cause of current loss.

28. Conclusion

A power conversion efficiency of 5.5% was achieved for the solar cell prepared from the electrodeposited binary selenide precursor with a stoichiometric Cu/In ratio. This is a better efficiency than any solar cell reported in the academic literature based on the selenisation of a stack from indium selenide and copper selenide. The best solar cell in this thesis balances the advantages and disadvantages of the Cu-poor and Cu-rich grown absorbers.

The solar cell prepared from a Cu-rich grown absorber exhibits good charge carrier collection similar to a PVD grown solar cell. It suffers from high interface recombination reducing V_{OC}. This is in general observed for solar cells prepared from Cu-rich absorbers [207]. In contrast to epitaxial grown Cu-rich absorbers the photoluminescence signal of the absorber is broad. It is not a sign for a compensated semiconductor but indicates several defect transition with a broad energy distribution.

Photoluminescence shows the Cu-poor grown absorber is a highly compensated semiconductor, as has already been reported before [200, 199]. The main solar cell performance limitations of the Cu-poor device are caused by poor charge collection and a low fill factor. The low fill factor is caused by a reverse n-p junction at the backside of the absorber due to an incomplete reaction of the precursor stack leaving behind a n-type ordered vacancy compound. There are three reasons for the poor charge collection. Firstly the reverse n-p junction at the back acts as a charge carrier barrier. Secondly the carriers have a low diffusion length and/or a small space charge region. Evidence for this effect is seen in the wavelength dependent charge carrier collection. Thirdly, there may be interface recombination. Although the activation energy for interface recombination is higher for the solar cell prepared from a Cu-poor absorber than the solar cell prepared from a stoichiometric absorber, this benefit is not fully active and the open circuit potential is similar to the cell from the stoichiometric absorber.

A higher background gas pressure during annealing does not only enlarge grain size and crystal coherence length of the absorber (chapter 18), but also provides a superior semiconductor quality. This was confirmed by the appearance of an exciton and a phonon replica in the photoluminescence spectrum. Unfortunately the solar cell prepared from this absorber has an efficiency below 1%. The high Se partial pressure, which is maintained longer by the higher background gas pressure, does not only improve the crystallisation of the absorber but also causes a massive selenisation of the Mo back contact. The massively selenised molybdenum forms a highly resistive contact destroying the device.

In conclusion the solar cells from the Cu-poor grown absorber and the one annealed at high background gas pressure show comparatively easy possibilities for improvement. The reverse n-p junction at the backcontact of the Cu-poor absorber can be avoided, if the precursor can be reacted completely. This can be either done by increasing the annealing temperature slightly (this is limited by softening point of the glass substrate) or annealing for a longer time. Care must be taken with either of the above methods though, not to produce thicker layers of molybdenum selenide. Taking into account that high efficient CIGS solar cells are grown Cu-poor [10], a completely reacted Cu-poor grown absorber is a promising candidate for a further improvement of the presented solar cell performance. The absorber annealed at $1000\,\mathrm{mbar}$ background gas pressure has a high potential for an efficient solar cell, because it has proved a superior semiconductor quality in photoluminescence. The annealing process must be further optimised, by shortening the annealing time for example, to keep the high Se partial pressure necessary for the potent crystallisation but not selenising the Mo backcontact. An improvement of the solar cell from a Cu-rich grown absorber is expected to be more challenging. This solar cell was limited by interface recombination, which is a more complex issue than an incomplete reaction or a selenised contact. Nevertheless solar cell efficiencies of about $10\,\%$ have been reached for Cu-rich grown $\mathrm{CuInSe_2}$ solar cells [239], showing that despite the interface

recombination an improvement of efficiency is possible.

Overall it was shown that electrodeposited binary selenide stacks could be annealed to form working devices with higher efficiencies than those previously reported in the literature. Structural and opto-electronic properties of the absorber layers and devices were measured, and suggestions for improvements have been given.

29. Outlook

Since this thesis covers the complete fabrication process from the electrodeposition of the precursor to the characterisation of the final solar cell, it has not been possible to study all questions in detail. Several interesting problems pertaining to both the electrodeposition and annealing processes are still open and provide starting points for further studies.

It has been pointed out in the part on electrochemistry that different mechanisms for the electrodeposition of indium selenide are proposed in literature. At high bath temperature and low ion concentrations selenium induces the deposition of indium as it has been suggested by Massaccesi et al. [1] and confirmed in this thesis. At room temperature and high ion concentrations, it was proposed that indium induces the deposition of selenium [57]. It is interesting to study the intermediate regime at moderate temperatures and medium concentrations to identify the reason for the change in the deposition mechanism. One can expect that the phase transition of the electroplated Se with higher bath temperature from amorphous to hexagonal and the accompanied change in its electrical properties provide an explanation for this behaviour.

Selenium precipitation is the main side reaction in the electrodeposition process of indium selenide even at In^{3+} excess. Its quantification by ICP-MS as it was done in chapter 10.2.4 is time consuming. Moreover the necessity for a large amount of precipitation causes a depletion of the bath and can thus change the balance between the reaction rates. Se precipitation forms by a reaction between Se^{2-} and Se^{4+}. The first species can be oxidised by a rotating ring disc electrode (RRDE) [57]. The RRDE is a RDE where the inner electrode is surrounded by a second ring electrode. The ring electrode can reduce/oxidise solved species that have been created at the inner electrode, e.g. Se^{2-}. Therefore a RRDE should be an easy way to obtain quantitative information on the Se precipitation. This allows to verify the hypothesis in figure 10.8 that a higher In^{3+} excess in the bath favours Se precipitation.

The electrochemical part in this thesis can be extended further to the electrochemistry of gallium selenide. While there are several recipes for the electrodeposition of elemental indium from aqueous solutions [240], the plating of elemental gallium is much more difficult. Electrodeposition of gallium selenide could shift the inset of gallium incorporation more positive. First experiments of gallium selenide electrodeposition have recently been reported [35, 241]. The electroplating of gallium selenide provides the possibility to synthesise $\mathrm{Cu(In_Ga)Se_2}$ absorbers.

It has been presented in this thesis that the electrodes applied in the electrodeposition process lead to impurities in the completed absorber layer (e.g. silver and platinum). In case of cadmium telluride already trace levels of silver can cause a performance degradation in the solar cell [197]. Therefore it needs to be studied how the detected impurities affect the solar cell properties in case of CIGS and if a different choice of electrodes or electrolyte purification is required.

The electrodeposited binary selenide precursor suffers from the porous morphology of the copper selenide layer in the annealing process. The small interface area with the indium selenide reduces the diffusion and thus requires higher annealing temperatures and longer durations than for smooth precursors with a continuous interface. It is expected that the reproducibility of the annealing can be improved if the sintering process of the copper selenide platelets is avoided. Therefore it is preferred to electrodeposit a compact copper selenide layer on top of the indium selenide. New conditions for the electroplating of a compact copper selenide film must be established. One suggestion is to use pulse plating to allow the diffusion layer to re-establish itself reducing the likelihood of the elongated growth.

Turning to annealing, it has already been discussed in the conclusion of part III that annealing at high background gas pressure results in a superior absorber layer but the concomitant selenisation

of the backcontact destroys the solar cell. Therefore annealing conditions must be worked out, which preserve the high Se partial pressure during the crystallisation but do not cause selenisation of the backcontact. In the used oven an optimisation of the background gas pressure can lead to this result. A more elaborated way is laser annealing. It provides the possibility to supply the energy for the reaction from the surface, while keeping the substrate at low temperature. If the laser annealing is stopped at the right time, it should therefore be possible to react the precursor stack but avoid a reaction of the substrate. Possible drawbacks to this though include an incomplete absorber reaction at the backcontact as it has been observed for the Cu-poor grown absorber, and peeling may occur due to the large temperature gradient causing stress in the films due to different amounts of expansion. First experiments on laser annealing of the presented electroplated binary selenide precursors are recently performed in cooperation with the group of Prof. Scarpulla at the University of Utah.

Finally, several authors have tried to combine the advantages of Cu-rich grown $\mathrm{CuInSe_2}$ (e.g. a larger grain size) with the low interface recombination of a Cu-poor absorber [46, 242, 239]. For this purpose a $\mathrm{In_2Se_3}$ layer is evaporated onto a Cu-rich grown $\mathrm{CuInSe_2}$ absorber to form a copper vacancy compound or a Cu-deficient chalcopyrite layer at the surface. This process can also be imitated by electrodeposition with the results presented in this thesis. After the annealing of a Cu-rich grown precursor another indium selenide layer can be electrodeposited on top of the precursor. This new $\mathrm{In_2Se_3}$ layer would probably have to be grown under illumination to supply the necessary electrons for the reduction of the cations due to the p-type nature of the Cu-rich sample onto which it would be electroplated. A second annealing can convert the electrodeposited indium selenide into a Cu-poor surface.

Appendix

A. Samples and measurements contributed to this thesis

Several persons contributed samples and measurements to this thesis:

- The PVD reference samples "PVD-Cu-poor" and "PVD-Cu-rich" have been prepared by Yasuhiro Aida (TDK corporation / Laboratory of Photovoltaics at the University of Luxembourg [LPV]). He has also contributed the JV characteristics and QE spectra of these samples and determined the underestimation of current density in the JV set-up.
- Most SEM / EDX measurements have been performed by Jean-Christophe Lambrechts (Centre de Recherche Public - Gabriel Lippmann [CRP-GL]), Joffrey Didierjean (CRP-GL), Jean-Luc Biagi (Centre de Recherche Public - Henry Tudor [CRP-HT]) and Dr. Claire Arnoult (CRP-HT).
- The absorber layers have been completed to solar cells by Michael Kirsch (Helmholtz Zentrum Berlin) and coworkers. The CdS buffer layer has been deposited by Yasuhiro Aida (TDK / LPV).
- Cold temperature PL measurements have been performed by Jes Larsen (LPV). The determination of the band gap by quantitative PL measurements was done by David Regesch.
- The temperature dependent JV characteristics have been measured by Tobias Eisenbarth (LPV), Valerie Depredurand (LPV) and Nicole Fèvre (LPV).
- ICP-MS measurements have been performed by Johanna Ziebel (CRP-GL) and Cédric Guignard (CRP-GL).
- The Mo/In-Se/Cu/Se precursors have been deposited by Guillaume Zoppi (Northumbria University). He has also provided the sputtered Mo substrates on soda-lime glass for the impurity analysis.
- AES depth profiles have been measured by Sébastien Francois (CRP-GL), Joffrey Didierjean (CRP-GL) and Jerome Guillot (CRP-GL).
- The sputtered Mo substrates on boro-aluminosilicate glass have been provided by the group of Mike Scarpulla (University of Utah).
- EBSD measurements have been performed by Jörg Schmauch (Universität des Saarlandes).
- The coelectrodeposited $\mathrm{CuInSe_2}$ reference sample has been prepared by Masato Kurihara (TDK / LPV).
- Thomas Schuler (LPV) provided the electrical circuit simulation in figure 26.1b.

B. Acknowledgements

I am deeply grateful to Phillip Dale and Susanne Siebentritt for giving me the opportunity to do my PhD in the field of photovoltaic.

I highly appreciate the profound commitment of Phillip Dale guiding me through my work. His motivation, support and patience as well as the discussion of experiments and results have been a great help. During my work I could always rely on the help of Susanne Siebentritt. I highly value her prodigious expertise and dedication to our group.

I would like to thank Laurie Peter (University of Bath, emeritus), Susan Schorr (Helmholtz Zentrum Berlin), and Roland Sanctuary (University of Luxembourg) for being part of the examination board of my thesis. My thesis has definitely benefited from Laurie Peter's corrections on electrochemistry and Susan Schorr's introduction to X-ray diffraction. I also acknowledge the correction of my thesis by Marc Steichen.

As it has been mentioned before (chapter A) several people have contributed samples and measurements to this thesis. I am very thankful to each of them knowing that this thesis would not be what it is without their help. Although they are not mentioned in chapter A, I would like to add Nathalie Valle and Thierry Girot (both Centre de Recherche Public - Gabriel Lippmann) for Secondary Ion Mass Spectroscopy measurements or support with XRD measurements.

Thomas Schuler and Vicente Reis-Adonis have been a great technical support during my work. For many problems that I faced during the PhD I could benefit from the help and experience of my fellow PhD student Dominik Berg. I sincerely appreciate the support.

Finally I would like to thank the entire LPV group at the University of Luxembourg. I have enjoyed the great cooperation, fruitful discussions and the amusement. Thank you!

The experiments in this thesis have been funded by the "Fonds National de la Recherche Luxembourg" (project number C08/MS/02), TDK corporation and the University of Luxembourg.

C. Reference electrode potentials

For all electrochemical experiments in this thesis a Ag | AgCl | $3\,\mathrm{M}$ KCl reference electrode has been applied. Its potential versus the standard hydrogen electrode (SHE) is $+0.210\,\mathrm{V}$ [243] at room temperature. All potentials stated in this thesis refer to this potential of the Ag | AgCl | $3\,\mathrm{M}$ KCl electrode if the corresponding experiment was performed at room temperature. This includes potentials taken from literature. If the experiment in literature has been done at elevated temperatures, the transformation of potential was still done with the room temperature difference between the electrodes (table C.1). This assumes that all reference electrodes have the same temperature coefficient.

reference electrode	vs SHE at $25\,°\mathrm{C}$	vs Ag | AgCl at $25\,°\mathrm{C}$	Reference
Ag | AgCl | $3\,\mathrm{M}$ KCl at $25\,°\mathrm{C}$	$+0.210\,\mathrm{V}$	0	[243]
Ag | AgCl | $3\,\mathrm{M}$ KCl at $80\,°\mathrm{C}$	$+0.159\,\mathrm{V}$	$-0.051\,\mathrm{V}$	
MSE: Hg | Hg_2SO_4 | K_2SO_4 sat at $25\,°\mathrm{C}$	$+0.65\,\mathrm{V}$	$+0.44\,\mathrm{V}$	[244]
SCE: Hg | Hg_2Cl_2 | KCl sat at $25\,°\mathrm{C}$	$+0.241\,\mathrm{V}$	$+0.031\,\mathrm{V}$	[245]

Table C.1.: Potentials of reference electrodes vs the SHE and a Ag | AgCl | $3\,\mathrm{M}$ KCl. The abbreviations are "mercury/mercurous sulphate electrode" (MSE) and "saturated calomel electrode" (SCE).

The potential of the Ag | AgCl electrode depends on its temperature. It is determined by the standard potential of the Ag|AgCl redox couple and the activity $\mathrm{a}_{\mathrm{Cl^-}}$ of chloride ions:

$$E = E^0(\text{Ag} \mid \text{AgCl}) - {}^{RT}/_{F} \ln(a_{Cl^-}) \tag{C.1}$$

At standard conditions ($25\,°\mathrm{C}$ and activities of $1\,\mathrm{mol/l}$) $E^0(\text{Ag} \mid \text{AgCl}) = +0.2223\,\mathrm{V}$ [68]. The activity of a $3\,\mathrm{M}$ KCl solution at $25\,°\mathrm{C}$ can now be calculated from equation C.1 with the known potential of an Ag | AgCl | $3\,\mathrm{M}$ KCl electrode; it is $\mathrm{a}_{\mathrm{Cl^-}} = 1.60\,\mathrm{mol/l}$. The temperature dependency of E^0(Ag | AgCl) is

$$E^0/\mathrm{V} = 0.23695 - 4.8564 \cdot 10^{-4} \times T - 3.4205 \cdot 10^{-6} \times T^2 - 5.869 \cdot 10^{-9} \times T^3 \tag{C.2}$$

for temperatures T (in °C) from $0\,°\mathrm{C}$ to $95\,°\mathrm{C}$ [68]. Assuming that the activity $\mathrm{a}_{\mathrm{Cl^-}}$ is temperature independent, it is possible to calculate the reference potential of the Ag | AgCl | $3\,\mathrm{M}$ KCl at $80\,°\mathrm{C}$ by equation C.1. One obtains $E(\text{Ag} \mid \text{AgCl}) = +0.159\,\mathrm{V}$ for a $3\,\mathrm{M}$ KCl solution and $25\,°\mathrm{C}$.

Before the experiments the Ag | AgCl | $3\,\mathrm{M}$ KCl reference electrode was checked versus a saturated calomel electrode which can be considered as a stable reference potential. During the experiment the silver chloride reference electrode usually shifted to more negative potentials. A potential shift up to $-20\,\mathrm{mV}$ has been accepted.

D. XRD reference structures

Reference structures for XRD measurements have been taken from the PDF4+ 2009 database of the "International Centre for Diffraction Data" (ICDD).

phase	reference	crystal system	space group	remarks
elements				
Cu	00-004-0836	cubic	$Fm\bar{3}m$ (225)	
Mo	00-042-1120	cubic	$Im\bar{3}m$ (229)	
Se	00-006-0362	hexagonal	P3121 (152)	
binary compounds				
$\gamma - In_2Se_3$	00-040-1407	hexagonal	P61 (169)	
$InSe$	04-003-2450	rhombohedral	R3m (160)	
In_2O_3	04-004-3575	cubic	$Ia\bar{3}$ (206)	
$CuSe_2$-I	04-004-2178	orthorhombic	Pnnm (58)	(1)
$CuSe_2$-II	00-026-1115	cubic	$Pa\bar{3}$ (205)	(2)
CuSe	03-065-3562	hexagonal	P63/mmc (194)	
$Cu_{1.8}Se$	01-088-2045	cubic	$Fm\bar{3}m$ (225)	
$Cu_{1.78}Se$	04-010-6041	cubic	$Fm\bar{3}m$ (225)	
$MoSe_2$	04-004-8782	hexagonal	P63/mmc (194)	
ternary compounds				
$CuInSe_2$	04-005-3912	tetragonal	$I\bar{4}2d$ (122)	
$CuIn_3Se_5$	00-051-1221	tetragonal	$P\bar{4}2c$ (112)	(3)

(1) low-pressure phase [126]
(2) high-pressure phase; stable at atmospheric pressure [126]
(3) The structure of the vacancy compound $CuIn_3Se_5$ is controversial. Beside the noted "P-chalcopyrite" also a stannite structure (space group $I\bar{4}2m$ (121)) has been proposed [129].

Table D.1.: Reference XRD structures used in this thesis. The reference number refers to the ICDD database.

Bibliography

[1] Sylvie Massaccesi, Sylvie Sanchez, and Jacques Vedel. Electrodeposition of indium selenide In_2Se_3. *Journal of Electroanalytical Chemistry*, 412(1-2):95–101, August 1996.

[2] Angus Rockett. Current status and opportunities in chalcopyrite solar cells. *Current Opinion in Solid State and Materials Science*, 14(6):143–148, December 2010.

[3] Martin A Green, Keith Emery, Yoshihiro Hishikawa, Wilhelm Warta, and Ewan D Dunlop. Solar cell efficiency tables (Version 38). *Progress in Photovoltaics: Research and Applications*, 19(5):565–572, August 2011.

[4] Otfried Madelung. *Landolt-Börnstein: Numerical data and functional relationships in science and technology Group III: Crystal and solid state physics*, volume III/41 of *Landolt-Börnstein*. Springer, Berlin-Heidelberg, 2000.

[5] W. Shockley and H.J. Queisser. Detailed balance limit of efficiency of p-n junction solar cells. *Journal of Applied Physics*, 32(3):510–519, 1961.

[6] S. Siebentritt. What limits the efficiency of chalcopyrite solar cells? *Solar Energy Materials and Solar Cells*, 95:1471–1476, 2011.

[7] Masafumi Yamaguchi. Radiation resistance of compound semiconductor solar cells. *Journal of Applied Physics*, 78:1476, 1995.

[8] Jean-François Guillemoles, Leeor Kronik, David Cahen, Uwe Rau, Axel Jasenek, and Hans-Werner Schock. Stability issues of Cu(In,Ga)Se 2 -Based solar cells. *The Journal of Physical Chemistry B*, 104:4849–4862, May 2000.

[9] A. Rockett, F. Abou-Elfotouh, D. Albin, M. Bode, J. Ermer, R. Klenk, T. Lommasson, T. W. F. Russell, R. D. Tomlinson, J. Tuttle, et al. Structure and chemistry of CuInSe2 for solar cell technology: current understanding and recommendations. *Thin solid films*, 237(1-2):1–11, 1994.

[10] Philip Jackson, Dimitrios Hariskos, Erwin Lotter, Stefan Paetel, Roland Wuerz, Richard Menner, Wiltraud Wischmann, and Michael Powalla. New world record efficiency for Cu(In,Ga)Se2 thin-film solar cells beyond 20%. *Progress in Photovoltaics: Research and Applications*, 19(7):894–897, November 2011.

[11] Jehad AbuShama, R. Noufi, S. Johnston, S. Ward, and X. Wu. Improved performance in CuInSe2 and surface-modified CuGaSe2 solar cells. In *Conference Record of the Thirty-first IEEE Photovoltaic Specialists Conference, 2005*, page 299– 302. IEEE, January 2005.

[12] B. Basol, M. Pinarbasi, S. Aksu, J. Wang, Y. Matus, T. Johnson, Y. Han, M. Narasimhan, and B. Metin. Electroplating based CIGS technology for Roll-to-Roll manufacturing. *Twenty third European PVSEC*, page 2137–2141, 2008.

[13] B. M Basol, M. Pinarbasi, S. Aksu, J. Freitag, P. Gonzalez, T. Johnson, Y. Matus, B. Metin, M. Narasimhan, D. Nayak, G. Norsworthy, D. Soltz, J. Wang, T. Wang, and H. Zolla. Status of electroplating based CIGS technology development. In *2009 34th IEEE Photovoltaic Specialists Conference (PVSC)*, page 002310–002315. IEEE, June 2009.

[14] D. Guimard, P. P Grand, N. Bodereau, P. Cowache, J. -F Guillemoles, D. Lincot, S. Taunier, M. Ben Farah, and P. Mogensen. Copper indium diselenide solar cells prepared by electrodeposition. In *Conference Record of the Twenty-Ninth IEEE Photovoltaic Specialists Conference, 2002*, page 692– 695. IEEE, May 2002.

[15] Udai P. Singh and Surya P. Patra. Progress in polycrystalline Thin-Film Cu(In,Ga)Se2 solar cells. *International Journal of Photoenergy*, 2010:1–19, 2010.

[16] O Lundberg, M Edoff, and L Stolt. The effect of Ga-grading in CIGS thin film solar cells. *Thin Solid Films*, 480-481:520–525, June 2005.

[17] D Abou-Ras, G Kostorz, A Romeo, D Rudmann, and A Tiwari. Structural and chemical investigations of CBD- and PVD-CdS buffer layers and interfaces in Cu(In,Ga)Se-based thin film solar cells. *Thin Solid Films*, 480-481:118–123, June 2005.

[18] U Rau. Electronic properties of ZnO/CdS/Cu(In,Ga)Se2 solar cells — aspects of heterojunction formation. *Thin Solid Films*, 387:141–146, May 2001.

[19] R. Bhattacharya, A. M. Fernandez, W. Batchelor, J. Alleman, J. Keane, H. Althani, R Noufi, K. Ramanathan, J. Dolan, F. Hasoon, and M. Contreras. Electrodeposition of CuIn1-xGaxSe2 materials for solar cells: Final report april 1995 - december 2001. Technical report, National Renewable Energy Laboratory (NREL), Golden, CO., 2001.

[20] D Lincot, J Guillemoles, S Taunier, D Guimard, J Sicxkurdi, A Chaumont, O Roussel, O Ramdani, C Hubert, and J Fauvarque. Chalcopyrite thin film solar cells by electrodeposition. *Solar Energy*, 77:725–737, December 2004.

[21] P. J. Dale, A. P. Samantilleke, G. Zoppi, I. Forbes, and L. M. Peter. Characterization of CuInSe2 material and devices: comparison of thermal and electrochemically prepared absorber layers. *Journal of Physics D: Applied Physics*, 41(8):085105, 2008.

[22] R. N. Bhattacharya, A. M. Fernandez, M. A. Contreras, J. Keane, A. L. Tennant, K. Ramanathan, J. R. Tuttle, R. N. Noufi, and A. M. Hermann. Electrodeposition of In-Se, Cu-Se, and Cu-In-Se thin films. *Journal of the Electrochemical Society*, 143:854, 1996.

[23] A Fernandez. Electrodeposited and selenized (CuInSe2) (CIS) thin films for photovoltaic applications. *Solar Energy Materials and Solar Cells*, 52:423–431, April 1998.

[24] Jean François Guillemoles, Alain Lusson, Pierre Cowache, Sylvie Massaccesi, Jacques Vedel, and Daniel Lincot. Recrystallization of electrodeposited copper indium diselenide thin films in an atmosphere of elemental selenium. *Advanced Materials*, 6(5):376–379, 1994.

[25] J. F Guillemoles, P. Cowache, A. Lusson, K. Fezzaa, F. Boisivon, J. Vedel, and D. Lincot. One step electrodeposition of CuInSe2: improved structural, electronic, and photovoltaic properties by annealing under high selenium pressure. *Journal of applied physics*, 79(9):7293–7302, 1996.

[26] D Xia. Electrodeposited and selenized CIGS thin films for solar cells. *Journal of Non-Crystalline Solids*, 354:1447–1450, February 2008.

[27] J.L Xu, X.F Yao, and J.Y Feng. The influence of the vacuum annealing process on electrodeposited CuInSe2 films. *Solar Energy Materials and Solar Cells*, 73(2):203–208, June 2002.

[28] ME Calixto and PJ Sebastian. CuInSe2 thin films formed by selenization of Cu–In precursors. *Journal of materials science*, 33(2):339–345, 1998.

[29] R Caballero and C Guillen. CuInSe formation by selenization of sequentially evaporated metallic layers. *Solar Energy Materials and Solar Cells*, 86:1–10, February 2005.

[30] C. Guillén and J. Herrero. Semiconductor CuInSe2 formation by close-spaced selenization processes in vacuum. *Vacuum*, 67(3-4):659–664, 2002.

[31] A. M. Hermann, M. Mansour, V. Badri, B. Pinkhasov, C. Gonzales, F. Fickett, M. E. Calixto, P. J. Sebastian, C. H. Marshall, and T. J. Gillespie. Deposition of smooth Cu(In,Ga)Se2 films from binary multilayers. *Thin Solid Films*, 361-362:74–78, February 2000.

[32] A Hermann. Low-cost deposition of CuInSe2 (CIS) films for CdS/CIS solar cells. *Solar Energy Materials and Solar Cells*, 52:355–360, April 1998.

[33] C. Guillen and J. Herrero. Improved selenization procedure to obtain CuInSe2 thin films from sequentially electrodeposited precursors. *Journal of The Electrochemical Society*, 143(2):493–498, February 1996.

[34] C. Guillen and J. Herrero. Reaction pathways to CuInSe2 formation from electrodeposited precursors. *Journal of The Electrochemical Society*, 142(6):1834–1838, June 1995.

[35] Serdar Aksu, Jiaxiong Wang, and Bulent M. Basol. Electrodeposition of In-Se and Ga-Se thin films for preparation of CIGS solar cells. *Electrochemical and Solid-State Letters*, 12(5):D33, 2009.

[36] SeJin Ahn, ChaeWoong Kim, JaeHo Yun, JeongChul Lee, and KyungHoon Yoon. Effects of heat treatments on the properties of Cu(In,Ga)Se2 nanoparticles. *Solar Energy Materials and Solar Cells*, 91(19):1836–1841, November 2007.

[37] M Kaelin. CIS and CIGS layers from selenized nanoparticle precursors. *Thin Solid Films*, 431-432:58–62, May 2003.

[38] F Adurodija. Growth of CuInSe2 thin films by high vapour se treatment of co-sputtered Cu-In alloy in a graphite container. *Thin Solid Films*, 338:13–19, January 1999.

[39] F.O. Adurodija, M.J. Carter, and R. Hill. Synthesis and characterization of CuInSe2 thin films from Cu, In and Se stacked layers using a closed graphite box. *Solar Energy Materials and Solar Cells*, 40:359–369, August 1996.

[40] S Zweigart. Studies of the growth mechanism of polycrystalline CuInSe2 thin films prepared by a sequential process. *Journal of Crystal Growth*, 146:233–238, January 1995.

[41] V Alberts, S Zweigart, and H W Schock. Preparation of device quality by selenization of se-containing precursors in atmosphere. *Semiconductor Science and Technology*, 12:217–223, February 1997.

[42] J. Szot and U. Prinz. Selenization of metallic Cu-In thin films for CuInSe2 solar cells. *Journal of Applied Physics*, 66(12):6077–6083, 1989.

[43] F. Hergert, R. Hock, A. Weber, M. Purwins, J. Palm, and V. Probst. In situ investigation of the formation of Cu(In, Ga) Se2 from selenised metallic precursors by x-ray diffraction–The impact of gallium, sodium and selenium excess. *Journal of Physics and Chemistry of Solids*, 66(11):1903–1907, 2005.

[44] L. L. Kerr, S. Kim, S. Kincal, M. Ider, S. Yoon, and T. J. Anderson. Rapid thermal processing of CIS precursors. In *Photovoltaic Specialists Conference, 2002. Conference Record of the Twenty-Ninth IEEE*, page 676–679, 2002.

[45] T. J Anderson, S. S. Li, O. D. Crisalle, and V. Craciun. Fundamental materials research and advanced process development for Thin-Film CIS-Based photovoltaics: Final technical report, 2 October 2001-30 september 2005. Technical report, National Renewable Energy Laboratory (NREL), Golden, CO., 2006.

[46] Sung Chan Park, Doo Youl Lee, Byung Tae Ahn, Kyung Hoon Yoon, and Jinsoo Song. Fabrication of CuInSe2 films and solar cells by the sequential evaporation of In2Se3 and Cu2Se binary compounds. *Solar Energy Materials and Solar Cells*, 69:99–105, September 2001.

[47] Yoshio Hachiuma, Atsuchi Ashida, Nobuyuki Yamamoto, Taichiro Ito, and Yoshio Cho. Characteristics of p-CuInSe2/n-CdS heterojunction prepared by evaporation of Cu2Se and In2Se3. *Solar Energy Materials and Solar Cells*, 35:247–254, September 1994.

[48] Rui Kamada, William N. Shafarman, and Robert W. Birkmire. Cu(In,Ga)Se2 film formation from selenization of mixed metal/metal–selenide precursors. *Solar Energy Materials and Solar Cells*, 94:451–456, March 2010.

[49] A. Romeo, M. Terheggen, D. Abou-Ras, D. L. Bätzner, F. J Haug, M. Kälin, D. Rudmann, and A. N. Tiwari. Development of thin-film cu (In, ga) se2 and CdTe solar cells. *Progress in Photovoltaics: Research and Applications*, 12(2-3):93–111, 2004.

[50] L. Thouin, S. Rouquette-Sanchez, and J. Vedel. Electrodeposition of copper-selenium binaries in a citric acid medium. *Electrochimica acta*, 38(16):2387–2394, 1993.

[51] S. Massaccesi, S. Sanchez, and J. Vedel. Cathodic deposition of copper selenide films on tin oxide in sulfate solutions. *Journal of the Electrochemical Society*, 140:2540, 1993.

[52] Dag Brune, Ragnar Hellborg, Harry J. Whitlow, and Ola Hunderi. *Surface Characterization: A User's Sourcebook*. Wiley-VCH, November 1997.

[53] Dominique Drouin, Alexandre Real Couture, Dany Joly, Xavier Tastet, Vincent Aimez, and Raynald Gauvin. CASINO v2.42: a fast and easy-to-use modeling tool for scanning electron microscopy and microanalysis users. *Scanning*, 29(3):92–101, June 2007.

[54] U Rau. *Advanced characterization techniques for thin film solar cells*. Wiley-VCH, Weinheim Germany, 2011.

[55] G. Hölzer, M. Fritsch, M. Deutsch, J. Härtwig, and E. Förster. $K_{\alpha 1,2}$ and $K_{\beta 1,3}$ x-ray emission lines of the 3d transition metals. *Physical Review A*, 56(6):4554–4568, December 1997.

[56] Robert Thomas. *Practical Guide to Icp-Ms*. CRC Press, December 2003.

[57] K. K. Mishra and K. Rajeshwar. A voltammetric study of the electrodeposition chemistry in the Cu+ In + Se system. *Journal of electroanalytical chemistry and interfacial electrochemistry*, 271(1-2):279–294, 1989.

[58] Allen J. Bard and Larry R. Faulkner. *Electrochemical Methods: Fundamentals and Applications*. John Wiley & Sons, 1 edition, August 1980.

[59] D. B. Hibbert. *Introduction to electrochemistry*. Macmillan physical science. MacMillan, Basingstoke :, 1993.

[60] P.H. Rieger. *Electrochemistry - Second Edition*. Springer, 2nd edition, November 1993.

[61] Christopher M. A. Brett and Ana Maria Oliveira Brett. *Electrochemistry: Principles, Methods, and Applications*. Oxford University Press, USA, July 1993.

[62] J. Koryta and J. Dvorák. *Principles of electrochemistry*. Wiley, Chichester ;New York, 1987.

[63] R. G. Compton and Craig E. Banks. *Understanding voltammetry*. World Scientific, 2007.

[64] R. C Weast. *CRC handbook of chemistry and physic; 69th edition*. CRC Press, Boca Raton, Florida, 1988.

[65] Antonio Castellanos and International Centre for Mechanical Sciences. *Electrohydrodynamics*. Springer, 1998.

[66] D. Grujicic and B. Pesic. Electrodeposition of copper: the nucleation mechanisms. *Electrochimica Acta*, 47(18):2901–2912, 2002.

[67] Matthias Polzler, Adam H. Whitehead, and Bernhard Gollas. A study of zinc electrodeposition from zinc chloride: Choline chloride: Ethylene glycol. page 43–55, 2010.

[68] Allen J. Bard, Roger Parsons, and Joseph Jordan. *Standard Potentials in Aqueous Solution*. CRC Press, 1st edition, August 1985.

[69] Åke Olin. *Chemical thermodynamics of selenium*. Elsevier, June 2005.

[70] Thomas Engel and Philip Reid. *Physikalische Chemie*. Pearson Studium, 1 edition, June 2006.

[71] F. A. Kroger. Cathodic deposition and characterization of metallic or semiconducting binary alloys or compounds. *Journal of The Electrochemical Society*, 125(12):2028–2034, December 1978.

[72] TJ Beveridge and RG Murray. Sites of metal deposition in the cell wall of bacillus subtilis. *Journal of Bacteriology*, 141(2):876, 1980.

[73] Elinor M. Kartzmark. Double salts of indium trichloride with the alkali chlorides, with ammonium chloride, and with indium sulfate. *Canadian Journal of Chemistry*, 55:2792–2798, August 1977.

[74] W Ho and S Yen. Preparation and characterization of indium oxide film by electrochemical deposition. *Thin Solid Films*, 498:80–84, March 2006.

[75] E. Chassaing, P.-P. Grand, O. Ramdani, J. Vigneron, A. Etcheberry, and D. Lincot. Electrocrystallization mechanism of Cu-In-Se compounds for solar cell applications. *Journal of The Electrochemical Society*, 157(7):D387, 2010.

[76] E. D. Kolb and R. A. Laudise. The solubility of trigonal Se in Na2S solutions and the hydrothermal growth of Se. *Journal of Crystal Growth*, 8(2):191–196, 1971.

[77] R. Piercy and N. A. Hampson. The electrochemistry of indium. *Journal of Applied Electrochemistry*, 5(1):1–15, February 1975.

[78] R. Piercy and N.A. Hampson. The electrochemistry of indium: The metal in relation to other solid metal electrodes. *Surface Technology*, 6(6):437–446, May 1978.

[79] S Wood and I Samson. The aqueous geochemistry of gallium, germanium, indium and scandium. *Ore Geology Reviews*, 28(1):57–102, January 2006.

[80] Pourbaix. *Atlas of Electrochemical Equilibria in Aqueous Solutions*. N A C E International, June 1974.

[81] R. C. Valderrama, M. Miranda-Hernandez, P. J. Sebastian, and A. L. Ocampo. Electrodeposition of indium onto Mo/Cu for the deposition of Cu(In,Ga)Se2 thin films. *Electrochimica Acta*, 53(10):3714 – 3721, 2008.

[82] N. Pentland, J. O'M. Bockris, and E. Sheldon. Hydrogen evolution reaction on copper, gold, molybdenum, palladium, rhodium, and iron. *Journal of The Electrochemical Society*, 104(3):182, 1957.

[83] G. A. Bozhikov, G. D. Bontchev, P. I. Ivanov, A. N. Priemyshev, O. D. Maslov, M. V. Milanov, and S. N. Dmitriev. Electrophoretic method for the determination of diffusion coefficients of ions in aqueous solutions. *Journal of radioanalytical and nuclear chemistry*, 258(3):645 – 648, 2003.

[84] B. Timmer, M. Sluyters-Rehbach, and J. H. Sluyters. On the impedance of galvanic cells: The impedance of the In3+/In (Hg) electrode reaction in KSCN and KCl solution. *Journal of Electroanalytical Chemistry*, 19(1-2):73 – 83, 1968.

[85] Chang Wei, Noseung Myung, and Krishnan Rajeshwar. A combined voltammetry and electrochemical quartz crystal microgravimetry study of the reduction of aqueous Se(IV) at gold. *Journal of Electroanalytical Chemistry*, 375(1-2):109–115, September 1994.

[86] M. Skyllas Kazacos and B. Miller. Studies in selenious acid reduction and CdSe film deposition. *Journal of The Electrochemical Society*, 127(4):869–873, April 1980.

[87] G. Pezzatini, F. Loglio, M. Innocenti, and M.L. Foresti. Selenium(IV) electrochemistry on silver: A combined electrochemical quartz-crystal microbalance and cyclic voltammetric investigation. *Collection of Czechoslovak Chemical Communications*, 68(9):1579–1595, 2003.

[88] J.M. Villalvilla, J.Gonzalez Velasco, and J. Ortega. Kinetic study of the formation of copper selenides by copper selenization. *Materials Chemistry and Physics*, 19(4):341–356, May 1988.

[89] VS Minaev, SP Timoshenkov, and VV Klugin. Structural and phase transformations in condensed selenium. *Journal of Optoelectronics and Advanced Materials*, 7(4):1717–1741, 2005.

[90] Herbert Henkels. Properties of single crystal selenium prepared from a melt. *Physical Review*, 76(11):1737 – 1738, December 1949.

[91] Lev Isaakovich Berger. *Semiconductor materials*. CRC Press, 1997.

[92] Norman Neill Greenwood and Alan Earnshaw. *Chemistry of the elements*. Pergamon, 1985.

[93] S. Cattarin, F. Furlanetto, and M. M. Musiani. Cathodic electrodeposition of Se on Ti electrodes. *Journal of Electroanalytical Chemistry*, 415(1-2):123 – 132, 1996.

[94] A. von Hippel and M. C. Bloom. The electroplating of metallic selenium. *The Journal of Chemical Physics*, 18(9):1243, 1950.

[95] Arthur von Hippel and Mortimer C. Bloom. Electrodeposition of selenium. *U.S. Patent*, 2649409, August 1953. k.

[96] A. K. Graham, H. L. Pinkerton, and H. J. Boyd. Electrodeposition of amorphous selenium. *Journal of The Electrochemical Society*, 106(8):651–654, 1959.

[97] T. Godecke, T. Haalboom, and F. Ernst. Phase equilibria of Cu-In-Se. II. the In-In2Se3-Cu2Se-Cu subsystem. *Zeitschrift für Metallkunde*, 91(8):635–650, 2000.

[98] M. B. Dergacheva, V. V. Chaikin, V. P. Grigoreva, and E. P. Pantileeva. Electrodeposition of $CuSe_x$ compounds onto carbon-containing electrodes. *Russian journal of applied chemistry*, 77(8):1273–1278, 2004.

[99] KR Murali and R.J. Xavier. Characteristics of brush electroplated copper selenide thin films. *Chalcogenide Letters*, 6(12):683–687, 2009.

[100] A. N. Skomorokhov, D. M. Trots, M. Knapp, N. N. Bickulova, and H. Fuess. Structural behaviour of $\beta - Cu_{2-\delta}Se$ ($\delta = 0$, 0.15, 0.25) in dependence on temperature studied by synchrotron powder diffraction. *Journal of Alloys and Compounds*, 421(1-2):64–71, 2006.

[101] D. Lippkow and H. H Strehblow. Structural investigations of thin films of copper-selenide electrodeposited at elevated temperatures. *Electrochimica acta*, 43(14-15):2131–2140, 1998.

[102] Frank Hergert. *Chemical formation reactions for Cu(In,Ga)Se2 and other chalcopyrite compounds - An in-situ x-ray diffraction study and crystallographic models*. Dissertation, University Erlangen-Nuernberg, 2007.

[103] H. Okamoto. In-Se (Indium-Selenide). *Journal of Phase Equilibria and Diffusion*, 25(2):201, April 2004.

[104] M. Valdés, M. Vázquez, and A. Goossens. Electrodeposition of CuInSe2 and In2Se3 on flat and nanoporous TiO2 substrates. *Electrochimica Acta*, 54:524–529, December 2008.

[105] M.R. Asabe, P.A. Chate, S.D. Delekar, K.M. Garadkar, I.S. Mulla, and P.P. Hankare. Synthesis, characterization of chemically deposited indium selenide thin films at room temperature. *Journal of Physics and Chemistry of Solids*, 69:249–254, January 2008.

[106] C. Sanjeeviraja and T. Mahalingam. Structural and optical properties of electrodeposited indium selenide thin films. *Journal of Materials Science Letters*, 11:525–526, 1992.

[107] T. Fujiwara and Y. Igasaki. The effects of pulsing the current in galvanostatic electrodeposition technique on the composition and surface morphology of In-Se films. *Journal of crystal growth*, 178(3):321–334, 1997.

[108] S. Gopal, C. Viswanathan, B. Karunagaran, Sa. K. Narayandass, D. Mangalaraj, and Junsin Yi. Preparation and characterization of electrodeposited indium selenide thin films. *Crystal Research and Technology*, 40:557–562, June 2005.

[109] Y. Igasaki and T. Fujiwara. The preparation of highly oriented InSe films by electrodeposition. *Journal of crystal growth*, 158(3):268–275, 1996.

[110] J. Weszka, P. Daniel, A. M. Burian, A. Burian, M. Elechower, and A. T. Nguyen. Raman scattering in amorphous films of In1-xSex alloys. *Journal of non-crystalline solids*, 315(3):219–222, 2003.

[111] Yuichi Watanabe, Shuichi Kaneko, Hiroshi Kawazoe, and Masayuki Yamane. Imperfections in amorphous chalcogenides. IV. a model of electrical conduction processes in amorphous and crystalline In2Se3. *Physical Review B*, 40(5):3133, 1989.

[112] J Weszka. Raman scattering in In2Se3 and InSe2 amorphous films. *Journal of Non-Crystalline Solids*, 265(1-2):98–104, March 2000.

[113] Y. Oda, M. Matsubayashi, T. Minemoto, and H. Takakura. Crystallization of In-Se/CuInSe2 thin-film stack by sequential electrodeposition and annealing. *Journal of Crystal Growth*, 311(3):738–741, January 2009.

[114] Raghu N. Bhattacharya. Electrodeposited Two-Layer Cu-In-Ga-Se/In-Se thin films. *Journal of The Electrochemical Society*, 157(7):D406, 2010.

[115] A. Kampmann, V. Sittinger, J. Rechid, and R. Reineke-Koch. Large area electrodeposition of Cu(In,Ga)Se2. *Thin Solid Films*, 361:309–313, 2000.

[116] Tong Ren, Rui Yu, Min Zhong, Jingying Shi, and Can Li. Microstructure evolution of CuInSe2 thin films prepared by single-bath electrodeposition. *Solar Energy Materials and Solar Cells*, 95(2):510–520, February 2011.

[117] Juan Rechid. *Elektrische Mikrocharakterisierung von elektrochemisch hergestellten CIS-Solarzellen mittels EBIC*. PhD thesis, University Oldenburg, Oldenburg, 2000.

[118] Bharat Bhushan. *Springer handbook of nanotechnology*. Springer, February 2004.

[119] Yuxia Sun. *Colloidal and electrochemical aspects of copper-CMP.* PhD thesis, ProQuest, 2007.

[120] Tomio Hirono. Process for producing light absorption layer of solar cell. *U.S. Patent*, 5489372, February 1996.

[121] Jonathan J Scragg. *Studies of Cu2ZnSnS4 films prepared by sulfurisation of electrodeposited precursors*. Dissertation, University of Bath, Bath, May 2010.

[122] T. Gödecke, T. Haalboom, and F. Sommer. Stable and metastable phase equilibria of the In-Se system. *Journal of Phase Equilibria*, 19:572–576, December 1998.

[123] J.B. Li, M.C. Record, and J.C. Tedenac. A thermodynamic assessment of the In-Se system. *Zeitschrift für Metallkunde*, 94(4):381–389, 2003.

[124] T. B. Massalski. *Binary Alloy Phase Diagrams*. American Society for Metals (Metals Park, Ohio), 2nd (3 volumes) edition, December 1990.

[125] K. Kohary, V. Burlakov, D. Pettifor, and D. Nguyen-Manh. Modeling In-Se amorphous alloys. *Physical Review B*, 71(18), May 2005.

[126] V. M. Glazov, A. S. Pashinkin, and V. A. Fedorov. Phase equilibria in the Cu-Se system. *Inorganic Materials*, 36:641–652, July 2000.

[127] Billy J. Stanbery. Copper indium selenides and related materials for photovoltaic devices. *Critical Reviews in Solid State and Materials Sciences*, 27:73–117, April 2002.

[128] T. Godecke, T. Haalboom, and F. Ernst. Phase equilibria of Cu-In-Se. i. stable states and nonequilibrium states of the In2Se3-Cu2Se subsystem. *Zeitschrift für Metallkunde*, 91(8):622–634, 2000.

[129] JM Merino, S. Mahanty, M. Leon, R. Diaz, F. Rueda, and JL Martin de Vidales. Structural characterization of CuIn2Se3. 5, CuIn3Se5 and CuIn5Se8 compounds. *Thin solid films*, 361:70–73, 2000.

[130] A. M Gabor, J. R Tuttle, D. S Albin, M. A Contreras, R. Noufi, and A. M Hermann. High-efficiency CuInxGa1-xSe2 solar cells made from (Inx, Ga1-x)2Se3 precursor films. *Applied physics letters*, 65(2):198–200, 1994.

[131] R. Klenk, R. Menner, D. Cahen, and H. W. Schock. Improvement of Cu(Ga,In)Se2 based solar cells by etching the absorber. In *Photovoltaic Specialists Conference, 1990., Conference Record of the Twenty First IEEE*, page 481–486, 1990.

[132] J.R. Tuttle, M. Ruth, D. Albin, A. Mason, and R. Noufi. Experiments on the modification of the bi-layer structure in CdS/CuInSe2 devices. In *Conference Record of the Twentieth IEEE Photovoltaic Specialists Conference, 1988*, page 1525–1530 vol.2. IEEE, 1988.

[133] FO Adurodija, J. Song, KH Yoon, SK Kim, SD Kim, SH Kwon, and BT Ahn. Preparation of CuInSe2 thin films by selenization of co-sputtered Cu–In precursors. *Journal of Materials Science: Materials in Electronics*, 9(5):361–366, 1998.

[134] Jung Woo Park, Gil Yong Chung, Byung Tae Ahn, Ho Bin Im, and Jin Soo Song. Effect of hydrogen in the selenizing atmosphere on the properties of CuInSe2 thin films. *Thin Solid Films*, 245(1-2):174–179, June 1994.

[135] V Alberts. Control of VSe- defect levels in CuInSe2 prepared by rapid thermal processing of metallic alloys. *Thin Solid Films*, 361-362:432–436, February 2000.

[136] A. Jiricka and A. Helebrant. Dissolution of Soda-Lime, silica, and High-Level waste glass by static and Single-Pass Flow-Through tests. *Ceramic Transactions*, 107:309–316, 2000.

[137] Gunarathna Perera and Robert H. Doremus. Dissolution rates of commercial Soda-Lime and pyrex borosilicate glasses: Influence of solution pH. *Journal of the American Ceramic Society*, 74:1554–1558, July 1991.

[138] PerkinElmer. The 30-Minute guide to ICP-MS. 2010. http://www.perkinelmer.com/PDFs/Downloads/tch_icpmsthirtyminuteguide.pdf.

[139] Adam J. Schwartz and Mukul Kumar. *Electron Backscatter Diffraction in Materials Science*. Springer, August 2009.

[140] D. Abou-Ras, U. Jahn, M. Nichterwitz, T. Unold, J. Klaer, and H. -W Schock. Combined electron backscatter diffraction and cathodoluminescence measurements on CuInS2/Mo/glass stacks and CuInS2 thin-film solar cells. *Journal of Applied Physics*, 107(1):014311–014311–8, January 2010.

[141] Yoshio Waseda, Eiichiro Matsubara, and Kozo Shinoda. *X-Ray Diffraction Crystallography: Introduction, Examples and Solved Problems*. Springer, March 2011.

[142] Mois I. Aroyo, Asen Kirov, Cesar Capillas, J. M. Perez-Mato, and Hans Wondratschek. Bilbao crystallographic server. II. representations of crystallographic point groups and space groups. *Acta Crystallographica Section A Foundations of Crystallography*, 62:115–128, March 2006.

[143] Mois Ilia Aroyo, Juan Manuel Perez-Mato, Cesar Capillas, Eli Kroumova, Svetoslav Ivantchev, Gotzon Madariaga, Asen Kirov, and Hans Wondratschek. Bilbao crystallographic server: I. databases and crystallographic computing programs. *Zeitschrift für Kristallographie*, 221:15–27, January 2006.

[144] J. M. Merino, J. L. Martin de Vidales, S. Mahanty, R. Díaz, F. Rueda, and M. León. Composition effects on the crystal structure of CuInSe2. *Journal of applied physics*, 80(10):5610–5616, 1996.

[145] Levent Gütay, David Regesch, Jes K. Larsen, Yasuhiro Aida, Alex Redinger, Sabina Caneva, Susan Schorr, Christiane Stephan, and Susanne Siebentritt. Experimental test of the theoretical feedback loop to stabilize the band gap in chalcopyrites. *to be published*.

[146] Christiane Stephan, Susan Schorr, and H.W. Schock. New structural investigations in the Cu2Se(S)-In2Se3(S)/Cu2Se(S)-Ga2Se3(S) phase diagrams. *Materials Research Society Symposium Proceedings - Thin-film compound semiconductor photovoltaics*, 1165:411–417, 2009.

[147] W. Paszkowicz, R. Lewandowska, and R. Bacewicz. Rietveld refinement for CuInSe2 and CuIn3Se5. *Journal of alloys and compounds*, 362(1-2):241–247, 2004.

[148] Rachel Reena Philip and B. Pradeep. Nonideal anion displacement, band gap variation, and valence band splitting in Cu-In-Se compounds. *Thin Solid Films*, 472(1-2):136–143, January 2005.

[149] Immo M. Kötschau. *Strukturelle Eigenschaften von Cu(In,Ga)(Se,S)2 Dünnschichten*. Dissertation, Institute of Physical Electronics at the University of Stuttgart, Stuttgart, 2003.

[150] M. R. Balboul, H. W. Schock, S. A. Fayak, A. A El-Aal, J. H. Werner, and A. A. Ramadan. Correlation of structure parameters of absorber layer with efficiency of Cu(In,Ga)Se2 solar cell. *Applied Physics A: Materials Science & Processing*, 92(3):557–563, 2008.

[151] Werner Kraus and Gert Nolze. PowderCell for windows, v. 2.4. *Federal Institute for Materials Research and Testing, Berlin, Germany; http://www.bam.de/de/service/publikationen/powder_cell_a.htm*, 2006.

[152] O. Volobujeva, J. Kois, R. Traksmaa, K. Muska, S. Bereznev, M. Grossberg, and E. Mellikov. Influence of annealing conditions on the structural quality of CuInSe2 thin films. *Thin solid films*, 516(20):7105–7109, 2008.

[153] T. Roisnel and J. Rodríquez-Carvajal. WinPLOTR: a windows tool for powder diffraction pattern analysis. In *Materials Science Forum*, volume 378, page 118–123, 2001.

[154] W. Petruk. *Applied mineralogy in the mining industry*. Elsevier, November 2000.

[155] Bertram Eugene Warren. *X-ray diffraction*. Courier Dover Publications, 1990.

[156] N. C. Halder and C. N. J. Wagner. Separation of particle size and lattice strain in integral breadth measurements. *Acta Crystallographica*, 20(2):312–313, February 1966.

[157] D. Balzar. Voigt-function model in diffraction line-broadening analysis. *International Union of Crystallography Monographs on Crystallography*, 10:94–126, 1999.

[158] J. López-García and C. Guillén. Adjustment of the selenium amount provided during formation of CuInSe2 thin films from the metallic precursors. *physica status solidi (a)*, 206(1):84–90, 2009.

[159] R. M German, P. Suri, and S. J Park. Review: liquid phase sintering. *Journal of materials science*, 44(1):1–39, 2009.

[160] D Albin, G Mooney, A Duda, J Tuttle, R Matson, and R Noufi. Enhanced grain growth in polycrystalline CuInSe2 using rapid thermal processing. *Solar Cells*, 30:47–52, May 1991.

[161] Daigao Chen and Deliang Wang. Formation of CuInSe2 from Cu2Se and In2Se3 compounds. *physica status solidi (a)*, 208:2415–2423, October 2011.

[162] D. Abou-Ras, S. Schorr, and H. W. Schock. Grain-size distributions and grain boundaries of chalcopyrite-type thin films. *Journal of Applied Crystallography*, 40(5):841–848, 2007.

[163] U. Rau, K. Taretto, and S. Siebentritt. Grain boundaries in Cu(In,Ga)(Se,S)2 thin-film solar cells. *Applied Physics A: Materials Science & Processing*, 96(1):221–234, 2009.

[164] H. Rau. Vapour composition and critical constants of selenium. *The Journal of Chemical Thermodynamics*, 6(6):525–535, 1974.

[165] S. Kim, W. K. Kim, R. M. Kaczynski, R. D. Acher, S. Yoon, T. J. Anderson, O. D. Crisalle, E. A. Payzant, and S. S. Li. Reaction kinetics of CuInSe2 thin films grown from bilayer InSe/CuSe precursors. *Journal of Vacuum Science & Technology A: Vacuum, Surfaces, and Films*, 23(2):310–315, March 2005.

[166] W. K. Kim, S. Kim, E. A. Payzant, S. A. Speakman, S. Yoon, R. M. Kaczynski, R. D. Acher, T. J. Anderson, O. D. Crisalle, S. S. Li, et al. Reaction kinetics of [alpha]-CuInSe2 formation from an In2Se3/CuSe bilayer precursor film. *Journal of Physics and Chemistry of Solids*, 66(11):1915–1919, 2005.

[167] M. Purwins, A. Weber, P. Berwian, G. Muller, F. Hergert, S. Jost, and R. Hock. Kinetics of the reactive crystallization of CuInSe2 and CuGaSe2 chalcopyrite films for solar cell applications. *Journal of crystal growth*, 287(2):408–413, 2006.

[168] S. C Kim, H. Park, E. W Lee, J. S Han, S. H Lee, C. W Jeon, D. Jung, J. Jeong, and W. K Kim. Role of na in reaction pathways and kinetics of CuInSe2 formation from stacked binary precursors. *Thin Solid Films*, 2011.

[169] J. S. Park, Z. Dong, Sungtae Kim, and J. H. Perepezko. CuInSe2 phase formation during Cu2Se/In2Se3 interdiffusion reaction. *Journal of Applied Physics*, 87(8):3683, 2000.

[170] F. Hergert, S. Jost, R. Hock, and M.jackson Purwins. A crystallographic description of experimentally identified formation reactions of Cu(In,Ga)Se2. *Journal of Solid State Chemistry*, 179(8):2394–2415, 2006.

[171] S. Jost, F. Hergert, R. Hock, J. Schulze, A. Kirbs, and M. Purwins. The formation of CuInSe2 thin film solar cell absorbers from electroplated precursors with varying selenium content. *Solar Energy Materials and Solar Cells*, 91(18):1669–1675, 2007.

[172] S. Jost, F. Hergert, R. Hock, J. Schulze, A. Kirbs, et al. Real-time investigations on the formation of CuInSe2 thin film solar cell absorbers from electrodeposited precursors. *Solar energy materials and solar cells*, 91(7):636–644, 2007.

[173] P Teheran. Evolution of the phases and chemical composition during the formation of CIS thin films prepared by interdiffusion process in selenides layers. *Journal of Crystal Growth*, 183:352–360, January 1998.

[174] A. Chaiken, K. Nauka, G. A. Gibson, Heon Lee, C. C. Yang, J. Wu, J. W. Ager, K. M. Yu, and W. Walukiewicz. Structural and electronic properties of amorphous and polycrystalline In2Se3 films. *Journal of Applied Physics*, 94(4):2390, 2003.

[175] S. N. Grigorov, V. M. Kosevich, S. M. Kosmachev, and A. V. Taran. Crystallization of the amorphous indium selenide films during annealing. *Physics and chemistry of solid state*, 5(4):35–37, 2004.

[176] M. Yudasaka, T. Matsuoka, and K. Nakanishi. Indium selenide film formation by the double-source evaporation of indium and selenium. *Thin Solid Films*, 146(1):65–73, 1987.

[177] M Afifi. Effect of annealing on the electrical properties of In2Se3 thin films. *Vacuum*, 46:335–339, April 1995.

[178] A. Brummer, V. Honkimäki, P. Berwian, V. Probst, J. Palm, and R. Hock. Formation of CuInSe2 by the annealing of stacked elemental layers–analysis by in situ high-energy powder diffraction. *Thin Solid Films*, 437(1-2):297–307, 2003.

[179] I Aviani. Concentration and temperature dependence of the thermal expansion coefficient in the superionic phase of Cu2-xSe. *Solid State Communications*, 64:1317–1319, December 1987.

[180] S. Verma, N. Orbey, R. W Birkmire, and T. W. Russell. Chemical reaction analysis of copper indium selenization. *Progress in Photovoltaics: Research and Applications*, 4(5):341–353, 1996.

[181] J. Hedstrom, H. Ohlsen, M. Bodegard, A. Kylner, L. Stolt, D. Hariskos, M. Ruckh, and H. - W Schock. ZnO/CdS/Cu(In,Ga)Se2 thin film solar cells with improved performance. In , *Conference Record of the Twenty Third IEEE Photovoltaic Specialists Conference, 1993*, page 364–371. IEEE, May 1993.

[182] D. F Dawson-Elli, C. B Moore, R. R Gay, and C. L Jensen. Substrate influences on CIS device performance. In *IEEE Photovoltaic Specialists Conference - 1994, 1994 IEEE First World Conference on Photovoltaic Energy Conversion, 1994., Conference Record of the Twenty Fourth*, volume 1, page 152–155 vol.1. IEEE, December 1994.

[183] A Rockett. Na in selenized Cu(In,Ga)Se2 on na-containing and na-free glasses: distribution, grain structure, and device performances. *Thin Solid Films*, 372:212–217, September 2000.

[184] M. A Contreras, B. Egaas, P. Dippo, J. Webb, J. Granata, K. Ramanathan, S. Asher, A. Swartzlander, and R. Noufi. On the role of na and modifications to Cu(In,Ga)Se2 absorber materials using thin-MF (M=Na, k, cs) precursor layers solar cells. In *Conference Record of the Twenty-Sixth IEEE Photovoltaic Specialists Conference, 1997*, page 359–362. IEEE, October 1997.

[185] M Lammer. Sodium co-evaporation for low temperature Cu(In,Ga)Se2 deposition. *Thin Solid Films*, 387:33–36, May 2001.

[186] R. Caballero, C. A. Kaufmann, T. Eisenbarth, A. Grimm, I. Lauermann, T. Unold, R. Klenk, and H. W. Schock. Influence of na on Cu(In,Ga)Se2 solar cells grown on polyimide substrates at low temperature: Impact on the Cu(In,Ga)Se2/Mo interface. *Applied Physics Letters*, 96:092104, 2010.

[187] D. Rudmann, G. Bilger, M. Kaelin, F.-J. Haug, H. Zogg, and A.N. Tiwari. Effects of NaF coevaporation on structural properties of Cu(In,Ga)Se2 thin films. *Thin Solid Films*, 431-432(0):37–40, May 2003.

[188] P. Jackson, PO Grabitz, A. Strohm, G. Bilger, and HW Schock. Contamination of Cu(In,Ga)Se2 solar cells by metallic substrate elements. In *19th EU Photovoltaic Solar Energy Conference*, page 1936–1938, 2004.

[189] Rainer Dargel, Frank Heinemeyer, Marc Köntges, Jürgen Vogt, and Carla Vogt. Detection of trace impurities in Cu(In, Ga)Se2 thin film solar cells by laser ablation ICP-MS. *Microchimica Acta*, 165:265–270, January 2009.

[190] Shigemi Kohiki, Mikihiko Nishitani, Takayuki Negami, and Takahiro Wada. CuInSe2 homojunction diode fabricated by phosphorus doping. *Applied Physics Letters*, 62:1656, 1993.

[191] R. D. Tomlinson, A. E. Hill, M. Imanieh, R. D. Pilkington, A. Roodbarmohammadi, M. A. Slifkin, and M. V. Yakushev. Changes in the opto-electronic properties of CuInSe2 following ion implantation. *Journal of Electronic Materials*, 20:659–663, September 1991.

[192] Phil Won Yu, Y. S. Park, and J. T. Grant. Electroluminescence in Br-, Cl-, and Zn-implanted CuInSe2 p-n junction diodes. *Applied Physics Letters*, 28:214, 1976.

[193] C Hung. Analytical characterization of CuInS2 semiconductor material. *Talanta*, 31:259–263, April 1984.

[194] H Hwang, L Liu, M Yang, P Chen, J Chen, and C Sun. Determination of trace elements in CuInS2. *Solar Energy Materials*, 7:237–252, September 1982.

[195] M.E Calixto, P.J Sebastian, R.N Bhattacharya, and Rommel Noufi. Compositional and optoelectronic properties of CIS and CIGS thin films formed by electrodeposition. *Solar Energy Materials and Solar Cells*, 59:75–84, September 1999.

[196] I.M. Dharmadasa, R.P. Burton, and M. Simmonds. Electrodeposition of CuInSe2 layers using a two-electrode system for applications in multi-layer graded bandgap solar cells. *Solar Energy Materials and Solar Cells*, 90:2191–2200, September 2006.

[197] Stephen Dennison. Dopant and impurity effects in electrodeposited CdS/CdTe thin films for photovoltaic applications. *Journal of Materials Chemistry*, 4:41, 1994.

[198] P. J Kulesza, W. Lu, and L. R Faulkner. Cathodic fabrication of platinum microparticles via anodic dissolution of a platinum counter-electrode: Electrocatalytic probing and surface analysis of dispersed platinum. *Journal of Electroanalytical Chemistry*, 336(1-2):35–44, 1992.

[199] Susanne Siebentritt, Niklas Rega, Alexander Zajogin, and Martha Ch. Lux-Steiner. Do we really need another PL study of CuInSe2? *Conference on Photo-responsive Materials (Physica Status Solidi C)*, 1(9):2304–2310, August 2004.

[200] I. Dirnstorfer, Mt. Wagner, D.M. Hofmann, M.D. Lampert, F. Karg, and B.K. Meyer. Characterization of CuIn(Ga)Se2 thin films. *physica status solidi (a)*, 168(1):163–175, July 1998.

[201] Mt. Wagner, I. Dirnstorfer, D.M. Hofmann, M.D. Lampert, F. Karg, and B.K. Meyer. Characterization of CuIn(Ga)Se2 thin films. *physica status solidi (a)*, 167(1):131–142, May 1998.

[202] Niklas Rega. *Photolumineszenz epitaktischer Cu(In,Ga)Se2-Schichten*. Dissertation, Freie Universität Berlin, Berlin, May 2004.

[203] G. Masse. Concerning lattice defects and defect levels in CuInSe2 and the I-III-VI2 compounds. *Journal of Applied Physics*, 68(5):2206–2210, September 1990.

[204] J. H. Schön, V. Alberts, and E. Bucher. Structural and optical characterization of polycrystalline CuInSe2. *Thin solid films*, 301(1-2):115–121, 1997.

[205] Roland Scheer and Hans-Werner Schock. *Chalcogenide Photovoltaics: Physics, Technologies, and Thin Film Devices*. Wiley-VCH, 1 edition, April 2011.

[206] D Schmid, M Ruckh, and H Schock. A comprehensive characterization of the interfaces in Mo/CIS/CdS/ZnO solar cell structures. *Solar Energy Materials and Solar Cells*, 41-42:281–294, June 1996.

[207] M. Turcu, O. Pakma, and U. Rau. Interdependence of absorber composition and recombination mechanism in Cu(In,Ga)(Se,S) 2 heterojunction solar cells. *Applied Physics Letters*, 80:2598, 2002.

[208] Susanne Siebentritt and Uwe Rau. *Wide-Gap Chalcopyrites*. Springer, 1 edition, February 2006.

[209] G.B. Turner, R. J. Schwartz, and J. L. Gray. Band discontinuity and bulk vs. interface recombination in CdS/CuInSe2 solar cells. In *Conference Record of the Twentieth IEEE Photovoltaic Specialists Conference, 1988*, page 1457–1460 vol.2. IEEE, 1988.

[210] M. Gloeckler and J.R. Sites. Efficiency limitations for wide-band-gap chalcopyrite solar cells. *Thin Solid Films*, 480-481:241–245, June 2005.

[211] V. Nadenau, U. Rau, A. Jasenek, and H. W. Schock. Electronic properties of CuGaSe-based heterojunction solar cells. Part i. transport analysis. *Journal of Applied Physics*, 87:584, 2000.

[212] A. Virtuani, E. Lotter, M. Powalla, U. Rau, J. H. Werner, and M. Acciarri. Influence of cu content on electronic transport and shunting behavior of Cu(In,Ga)Se2 solar cells. *Journal of Applied Physics*, 99(1):014906, 2006.

[213] I. Kötschau. Depth profile of the lattice constant of the Cu-poor surface layer in (Cu2Se)1-x(In2Se3)x evidenced by grazing incidence x-ray diffraction. *Journal of Physics and Chemistry of Solids*, 64(9-10):1559–1563, September 2003.

[214] A Rockett. Near-surface defect distributions in Cu(In,Ga)Se2. *Thin Solid Films*, 431-432:301–306, May 2003.

[215] M Contreras. Optimization of CBD CdS process in high-efficiency Cu(In,Ga)Se2-based solar cells. *Thin Solid Films*, 403-404:204–211, February 2002.

[216] T. Schmidt, K. Lischka, and W. Zulehner. Excitation-power dependence of the near-band-edge photoluminescence of semiconductors. *Physical Review B*, 45(16):8989–8994, April 1992.

[217] Jacques I. Pankove. *Optical Processes in Semiconductors*. Dover Publications, 2 edition, November 2010.

[218] T. Makino, Y. Segawa, S. Yoshida, A. Tsukazaki, A. Ohtomo, M. Kawasaki, and H. Koinuma. Spectral shape analysis of ultraviolet luminescence in n-type ZnO:Ga. *Journal of Applied Physics*, 98(9):093520, 2005.

[219] Alan L. Fahrenbruch and Richard H. Bube. *Fundamentals of Solar Cells: Photovoltaic Solar Energy Conversion*. Academic Press, May 1983.

[220] R. Scheer. Towards an electronic model for CuIn1 - xGaxSe2 solar cells. *Thin Solid Films*, 519(21):7472–7475, August 2011.

[221] A.R. Burgers, J.A. Eikelboom, A. Schonecker, and W.C. Sinke. Improved treatment of the strongly varying slope in fitting solar cell I-V curves. In *Proceedings of the 25th IEEE Photovoltaic Specialists Conference*, May 1996.

[222] U. Rau and H. W Schock. Electronic properties of Cu(In,Ga)Se2 heterojunction solar cells–recent achievements, current understanding, and future challenges. *Applied Physics A: Materials Science & Processing*, 69(2):131–147, 1999.

[223] J Sites. Quantification of losses in thin-film polycrystalline solar cells. *Solar Energy Materials and Solar Cells*, 75(1-2):243–251, January 2003.

[224] IV Bodnar, VF Gremenok, Y.A. Nikolaev, V.Y. Rud, Y.V. Rud, and EI Terukov. Photosensitivity of thin-film structures based on CuIn3Se5 and CuIn5Se8 ternary semiconductor compounds. *Technical Physics Letters*, 33(2):111–113, 2007.

[225] H. P. Wang, I. Shih, and C. H. Champness. Studies on monocrystalline CuInSe2 and CuIn3Se5. *Thin Solid Films*, 361:494–497, 2000.

[226] M Turcu. Compositional trends of defect energies, band alignments, and recombination mechanisms in the Cu(In,Ga)(Se,S)2 alloy system. *Thin Solid Films*, 431-432:158–162, May 2003.

[227] Peter M. Gorley, Volodymyr V. Khomyak, Yuri V. Vorobiev, Jesús González-Hernández, Paul P. Horley, and Olena O. Galochkina. Electron properties of n- and p-CuInSe2. *Solar Energy*, 82(2):100–105, February 2008.

[228] S M Firoz Hasan, M A Subhan, and Kh M Mannan. Charge-carrier transport mechanism in copper indium di-selenide thin films. *Journal of Physics D: Applied Physics*, 32(12):1302–1305, June 1999.

[229] T. Eisenbarth. *Identification of defects and metastabilities in Cu(In,Ga)Se2 thin film solar cells*. Dissertation, Freie Universität Berlin, Berlin, May 2010.

[230] Tobias Eisenbarth, Thomas Unold, Raquel Caballero, Christian A. Kaufmann, and Hans-Werner Schock. Interpretation of admittance, capacitance-voltage, and current-voltage signatures in Cu(In,Ga)Se2 thin film solar cells. *Journal of Applied Physics*, 107(3):034509, 2010.

[231] S.S. Hegedus and W.N. Shafarman. Thin-film solar cells: device measurements and analysis. *Progress in Photovoltaics: Research and Applications*, 12(2-3):155–176, 2004.

[232] W.W. Gärtner. Depletion-layer photoeffects in semiconductors. *Physical Review*, 116(1):84, 1959.

[233] Simon M. Sze. *Physics of Semiconductor Devices*. Wiley & Sons, 3 edition, October 1982.

[234] Christian Weissmantel and Claus Hamann. *Grundlagen der Festkörperphysik*. Johann Ambrosius Barth, Heidelberg; Leipzig, 4th edition, 1995.

[235] Kiyoshi Takahashi, Akihiko Yoshikawa, and Adarsh Sandhu. *Wide bandgap semiconductors: fundamental properties and modern photonic and electronic devices*. Springer, 2007.

[236] L Gutay and G Bauer. Spectrally resolved photoluminescence studies on Cu(In,Ga)Se2 solar cells with lateral submicron resolution. *Thin Solid Films*, 515:6212–6216, May 2007.

[237] N. R. Pavaskar, C. A. Menezes, and A. P. B. Sinha. Photoconductive CdS films by a chemical bath deposition process. *Journal of The Electrochemical Society*, 124(5):743–748, May 1977.

[238] P. D. Paulson, R. W. Birkmire, and W. N. Shafarman. Optical characterization of CuIn[1-x]Ga[x]Se2 alloy thin films by spectroscopic ellipsometry. *Journal of Applied Physics*, 94(2):879, 2003.

[239] Valerie Depredurand, Yasuhiro Aida, Jes Larsen, Tobias Eisenbarth, Alain Majerus, and Susanne Siebentritt. Surface treatment of CIS solar cells grown under cu-excess. In *Conference Record of the 37th IEEE Photovoltaic Specialists Conference, 2011*, 2011.

[240] F.C. Walsh and D.R. Gabe. The electrodeposition of indium. *Surface Technology*, 8(2):87–99, February 1979.

[241] TP Gujar, VR Shinde, J.W. Park, H.K. Lee, K.D. Jung, and O.S. Joo. Electrodeposition of photoactive 1D gallium selenide quantum dots. *Electrochimica Acta*, 54(2):829–834, 2008.

[242] D Lee. Characterization of cu-poor surface on Cu-rich CuInSe2 film prepared by evaporating binary selenide compounds and its effect on solar efficiency. *Thin Solid Films*, 410(1-2):171–176, May 2002.

[243] Binghe Wang and Eric V. Anslyn. *Chemosensors: Principles, Strategies, and Applications*. John Wiley and Sons, July 2011.

[244] R. Holze. *Leitfaden der Elektrochemie*. Vieweg+ Teubner, 1998.

[245] Waldfried Plieth. *Electrochemistry for materials science*. Elsevier, January 2008.